UNIVERSITÉ DE GRENOBLE

LAPP-T-2011-03

THÈSE

Pour obtenir le grade de

DOCTEUR DE L'UNIVERSITÉ DE GRENOBLE

Spécialité : **Physique des Particules**

Présentée par

Louis Hélary

Thèse dirigée par **Nicolas Berger**
et codirigée par **Isabelle Wingerter-Seez**

préparée au sein du **Laboratoire d'Annecy-le-Vieux de Physique des Particules**
et de l'**École Doctorale de Physique de Grenoble**

Recherche de Technicouleur avec l'expérience ATLAS. Développement d'outils et étude des performances du calorimètre à argon liquide.

Thèse soutenue publiquement le **9 Décembre 2011**,
devant le jury composé de :

M. Henri Bachacou
CEA - Saclay, Examinateur
M. Nicolas Berger
LAPP - Annecy-le-Vieux, Directeur de thèse
M. Yannis Karyotakis
LAPP - Annecy-le-Vieux, Président
M. Kenneth Lane
Boston University, Examinateur
M. Emmanuel Monnier
CPPM - Marseille, Rapporteur
M. Yves Sirois
LLR - Palaiseau, Rapporteur
Mme. Isabelle Wingerter-Seez
LAPP - Annecy-le-Vieux, Directeur de thèse

UNIVERSITÉ DE GRENOBLE

LAPP-T-2011-03

PhD Thesis

Submitted in fulfillment of the requirements for the degree of

DOCTEUR DE L'UNIVERSITÉ DE GRENOBLE

Specialty : **Particle Physics**

Prepared by

Louis Hélary

Thesis supervised by **Nicolas Berger and Isabelle Wingerter-Seez**

Prepared at the **Laboratoire d'Annecy-le-Vieux de Physique des Particules**

Search for Technicolor with the ATLAS experiment. Tool development and performance study of the ATLAS Liquid Argon Calorimeter.

Thesis publicly defended the 9^{th} **December 2011**,
In front of the comity :

Mr. Henri Bachacou
CEA - Saclay, Examinateur
Mr. Nicolas Berger
LAPP - Annecy-le-Vieux, Directeur de thèse
Mr. Yannis Karyotakis
LAPP - Annecy-le-Vieux, Président
Mr. Kenneth Lane
Boston University, Examinateur
Mr. Emmanuel Monnier
CPPM - Marseille, Rapporteur
Mr. Yves Sirois
LLR - Palaiseau, Rapporteur
Mme. Isabelle Wingerter-Seez
LAPP - Annecy-le-Vieux, Directeur de thèse

Remerciements

> "I believe that a scientist looking at nonscientific problems is just as dumb as the next guy."
> **Richard Phillips Feynman**.

Je voudrais tout d'abords remercier Yannis Karyotakis de m'avoir accueilli au Laboratoire d'Annecy-le-Vieux de Physique des Particules pendant presque quatre ans, que ce soit pendant mon stage, ma thèse, où pour mon après-thèse. Durant ma thèse j'ai pu bénéficier du soutien financier du CNRS, de l'Assemblée des Pays de Savoie, de l'Université de Savoie, de l'Université de Lyon et de l'Université de Grenoble et je les en remercie tous. Merci aussi aux personnels administratifs du laboratoire pour leur disponibilités, merci en particulier à Claudine, Chantal, Marie-Claude et Brigitte.

Je souhaiterais ensuite remercier profondément Emmanuel Monnier et Yves Sirois d'avoir accepté d'être les rapporteurs de ma thèse, de l'avoir lue et de m'avoir donné beaucoup de conseils pour l'améliorer. I would also like to deeply thank Kenneth Lane for having come from Boston to be part of the thesis committee, for having read my thesis, for the many discussions we had during the last four years and finally for the support he provided me after my thesis ! Je tiens ensuite à remercier Henri Bachacou d'avoir accepté de faire partie de mon jury et d'avoir vu à de nombreuses reprises mes présentations sur la technicouleur, au JRJC, au PAF et dans ATLAS. Merci également pour le soutien qu'il m'a apporté après ma thèse et j'espère qu'on se recroisera en montagne ! Enfin, je vais remercier collectivement Nicolas Berger, Yannis Karyotakis et Isabelle Wingerter Seez d'avoir accepter de compléter le jury et donc par la force des choses d'avoir lu le manuscrit.

Je remercie le groupe ATLAS du LAPP de m'avoir accueilli et fait partager sa vision de la recherche. Merci a tout ceux du groupe que j'ai pu croiser et avec lesquels j'ai pu travailler durant ces quatre années ici ou au CERN. Merci donc à Ludovica, Alain, Nicolas B., Tetiana, Lucia, Marco, Oanh, Mohamed, Sabine, Corinne, Stéphane, Mayuko, Houry, Rémi, Jessica, Vincenzo, Nicolas M., Guy, Elisabeth, Julie, Helenka, Emmanuel, Teddy, Maud, Dimitra et Isabelle ; et aux membres passés, Olivier, Mathieu, Michele, Thibault, Iro, Paolo, Sandrine, Jean-François, Julien L., Julien M., Margar, Pierre-Antoine, Philippe, et Gilles. Merci plus particulierement aux différentes personnes avec lesquelles j'ai partagé mon bureau ici au LAPP : Nicolas M., Margar, Mathieu, Houry et Marco. Je remercie également chaleureusement mes deux directeurs de thèse pour leur encadrement, leur implication et pour m'avoir supporté jusqu'à la fin de ce travail. Merci donc à Nicolas Berger et Isabelle Wingerter-Seez pour leurs conseils et les discussions que nous avons pu avoir durant ces quatre ans.

Je voudrais ensuite remercier les différentes personnes avec lesquelles j'ai pu travailler et qui m'ont donné des conseils au CERN durant ces quatre années et notamment pour le travail accompli sur la calorimètre à argon liquide. Merci donc à la communauté ATLAS LAr pour son accueil, ses explications, et son enthousiasme au travail, et merci plus particulierement à Jessica, Benjamin, Olivier et Guillaume.

Je vais ensuite remercier les personnes avec qui j'ai pu durant mes deux premières années de thèses enseigner à l'université de savoie au Bourget du Lac. Merci à Damir Buskulic et Gwenael Gaborit pour m'avoir encadré dans cette délicate activité qu'est l'enseignement. Merci également à Vincent pour l'organisation des salles du batiment Iseran. Enfin merci aux jeunes avec qui j'ai pu enseigner en TP et en TD, prendre des pauses et nous faire payer des cafés par les étudiant(e)s : Sean Bailly, Julien Labbé et Julien Morel. Enfin merci aux étudiant(e)s que j'ai pu croiser d'avoir écouté (avec attention) mes explications farfelues.

Je vais ensuite remercier tout les jeunes du laboratoire avec lesquels nous avons tenté de maintenir une vie sociale dans cette belle ville d'Annecy. Merci donc à : Julien Labbé, Julien Masbou, Julien Morel (pour les soirées pâtes-projecteur, les soirées cordes-déprime et pour m'avoir enmené de nombreuses fois en montagne), Thimothé, Timur (pour les débats politiques), Florent, Florian, Mathieu (pour les shifts en salle de contrôle, le partage de bureaux et pour les meetings au bâtiment 1 avec le sieur Morel), Laura, Olivier (pour l'organisation pendant les deux premières années ici), Caroline (toi aussi), Magali, Ambroise, Michele (pour m'avoir laissé ton appartement au début de ma thèse), Gwenaële, Loïc, Benedicte, Iro, Armand, Sean, Ludovica (pour cette dernière année), Dimitra, Guillaume Chalons, Guillaume Drieu (pour les apéros à la poire), Daniel, Walter, Maud, Jessica et les petits jeunes qui proposent de sortir tout les week-ends Guilhem et Laurent ! Also many thanks to Plamen for the three years we have lived together in this nice apartment ! Merci également à tout les autres que j'ai pu croiser durant ces quelques années ici et que j'oublie de citer !

Je voudrais ensuite remercier les différentes personnes qui m'ont accueilli et guidé vers la physique des hautes énergies durant mes études. Merci au groupe CMS de Lyon à l'IPNL de m'avoir donner l'occasion de faire ce stage pendant ma licence où j'ai commencé à jouer avec PYTHIA et ROOT et en particulier merci a Stéphane Perriès de m'avoir encadré. Je voudrais également profondément remercier Imad Laktineh et Luisa Arabito de m'avoir accueilli pendant pratiquement un an, quand j'étais en première année de master à Lyon sur l'expérience OPERA. Je me souviendrais pendant longtemps de la forte odeur d'huile et de l'humidité insoutenable du laboratoire de scanning des émulsions d'OPERA et surtout des nombreuses discussions que nous avons eu à ce moment-là. J'en profite aussi pour remercier les copains de fac que j'ai rencontré à Lyon et qui m'ont aidé à obtenir mes examens de l'époque, merci Davide, Robert, Laetitia et les autres !

Enfin je vais finir par remercier les personnes qui m'ont apporté leur soutien affectif et matériel durant et surtout à la fin de ma thèse. Merci donc à Ludovica, mon père Jean-Louis, ma mère Hermina, ma soeur Saskia, ma soeur Anna, mon futur beau-frère Manuel et mon petit frère Adrien. Merci également à toutes celles et tout ceux qui ont fait ou feront l'effort de lire ce manuscrit !

"A ma grand-mère, Marie-Louise, qui nous a quitté durant la rédaction de ce manuscrit."

List of acronyms and note about the figures

Acronyms

Symbols:

η**:** Pseudo rapidity.
θ**:** Polar Angle.
ϕ**:** Azimuth angle.
K_T**:** Algorithm used for jet reconstruction.
Anti-K_T**:** Algorithm used for jet reconstruction.
E_T**:** Transverse energy.
p_{T}**:** Transverse momentum.
$p_{\mathrm{T}}^{\mathbf{EM}}$**:** Transverse momentum at the EM Scale.
$p_{\mathrm{T}}^{\mathbf{part}}$**:** Transverse momentum at the parton level.
$p_{\mathrm{T}}^{\mathbf{calo}}$**:** Transverse momentum at the reconstructed level.
$\sigma^{\mathbf{reso}}$**:** Jet Energy resolution at reconstructed level.
$\sigma^{\mathbf{part}}$**:** Jet Energy resolution at truth level.
$\langle p_T \rangle$:mean p_{T}: $\frac{p_{\mathrm{T}}(1)+p_{\mathrm{T}}(2)}{2}$
ΔR**:** Spatial distance in detector: $\sqrt{\Delta\eta^2 + \Delta\phi^2}$
$\Delta\phi_{12}$**:** Angular difference between two leading jet in the transverse plan.
$|y|$**:** Rapidity
ΔN**:** Noise term increase for JER.
1D-2D: 1 Dimension-2 Dimensions.
w_{s3}**,** F_{side}**,** ΔE **and** E_{Ratio} :Shower Shape variable used for photon identification
$E_T^{\mathbf{cone}(30)}$**:** Isolation variable in a cone $\Delta R = 0.3$, for electron and photon.
***W+X*:** Monte Carlo sample, with real $E_{\mathrm{T}}^{\mathrm{miss}}$.
***Z+X*:** Monte Carlo sample, without real $E_{\mathrm{T}}^{\mathrm{miss}}$.
X_0**:** EM interaction length.
λ_i**:** Nuclear interaction length.

A:

ADC: Analog to Digital Converter
ALPEH: Apparatus for LEP Physics at CERN
ATLAS: A Toroidal LHC Apparatus.
ALICE: A Large Ion Collider Experiment.

B:

BEHGHK: Brout-Englert-Higgs-Hagen-Guralnik-Kibble mechanism also known as Higgs mechanism.
Bkg: Background.
BPTX: Beam Pickup Trigger system.

C:

CB: Calibration Board.
CERN: Centre Européen pour la Recherche Nucléaire.
CDF: Collider Detector at Fermilab (Tevatron experiment).
CL: Confidence Level.
CL_s**:** Confidence Level Signal.
CL_b**:** Confidence Level Background only.
CM: Center of Mass.
CMS: Compact Muon Solenoid
CSC: Cathode Strips Chambers.
CTP: Central Trigger Processor

D:

D∅: Experiment at the Tevatron.
d∅: Impact parameter.
DAC: Digital to Analog Converter.
DELPHI: DEtector with Lepton, Photon and Hadron Identification (LEP - CERN).
DESY: Deutsches Elektronen-SYnchrotron.
DONUT: Direct Observation of the NU Tau (Fermilab experiment).
DQ: Data Quality.
DSP: Digital Signal Processor.

E:

EF: Event Filter.
EM: Electro Magnetic.

EMB: Electro Magnetic Barrel calorimeter.
EMBA: Electro Magnetic Barrel calorimeter side A.
EMBC: Electro Magnetic Barrel calorimeter side C.
EMEC: Electro Magnetic End Cap calorimeter.
EMECA: Electro Magnetic End Cap calorimeter side A.
EMECC: Electro Magnetic End Cap calorimeter side C.
EMJES: Electro Magnetic Jet Energy Scale.
EMScale: Electro Magnetic Scale, calorimeter cells without calibration.
ETC: Extended TechniColor.
eV: electron Volt.
EW: ElectroWeak.

F:

FCal: Forward Calorimeter.
FCalA: Forward Calorimeter side A.
FCalC: Forward Calorimeter side C.
FEC: Front End Crate.
FCNC: Flavor Changing Neutral Current.
FEB: Front End Board.
FPGA: Field Programmable Gate Array.
FSR: Final State Radiation.
FT: Feed Through.

G:

G4: Geant4, software to simulate interaction particle matter.
GCW: Global Cell Weighting.
GeV: Giga electron Volt.
GS: Global Sequential.

H:

HEC: Hadronic End Cap calorimeter.
HECA: Hadronic End Cap calorimeter side A.
HECC: Hadronic End Cap calorimeter side C.
HEP: High Energy Physics.
HLT: High Level Trigger.
HV: High Voltage.
HVPS: High Voltage Power Supply.
HV Trips: High Voltage Trips.

I:

IP: Interaction Point.
ID: Inner Detector.
ISR: Initial State Radiation.
IR: Infra Red.

J:

JES: Jet Energy Scale.
JES: Jet Energy Resolution.

L:

L1Calo: Level1 Calorimeter trigger.
L3: LEP experiment at CERN.
LAr: Liquid Argon.
LCW: Local Cluster Weighting.
LEP: Large Electron Positron collider.
LHC: Large Hadron Collider.
LHCb: Large Hadron Collider Beauty.
LHCf: Large Hadron Collider Forward.
LO: Leading Order.
LSTC: Low Scale TechniColor.
LVL1: Level 1 trigger.
LVL2: Level 2 trigger.

M:

MB: Mother Board.
MBTS: Minimum Bias Trigger Scintillator.
MC: Monte Carlo.
MDT: Monitoring Drift Tubes.
MET-$E_{\mathrm{T}}^{\mathrm{miss}}$: Missing Transverse Energy.
MeV: Mega electron Volt.
ML: Maximum Likelihood.
MTC: Minimal TechniColor.
MS: Muon Spectrometer.

N:

NDF: Number of Degree of Freedom.
NLO: Next Leading Order.
NNLO: Next to Next Leading Order.

O:

OF: Optimal Filtering.
OFC: Optimal Filtering Coefficient.
OPAL: Omni-Purpose Apparatus for LEP.
OTx: Optical Transmitters.
ORx: Optical Receiver.

P:

PDF: Parton Density Function.
***pdf*:** Probability Density Function.
PS: Pre-Sampler or Proton Synchrotron.
PU: Processing Unit.

Q:

QCD: Quantum Chromo-Dynamics.
QED: Quantum Electro Dynamics.
QFT: Quantum Field Theory.

R:

RF: Radio Frequency.
RoI: Region of Interest.
ROD: Read Out Driver.
RPC: Resistive Plate Chambers.

S:

SB: Summing Board.
SCA: Switched Capacitor Array.
SCT: Semi Conductor Tracker.
SI: International units System.
SM: Standard Model.
SPS: Super Proton Synchrotron.
SR: Soft Radiation.
SUSY: SUper SYmmetry.

T:

TBB: Trigger Board Builder.
TC: TechniColor.
TeV: Tera electron Volt.
Topo-clusters: Topological clusters of calorimeter cells.
TOTEM: TOTal Elastic and diffractive cross section Measurement.
TGC: Thin Gap Chambers.
TRT: Transition Radiation Tracker.
TT: Trigger Tower.
TTC: Trigger Timing Control.

U:

UA1-UA2: experiments at the CERN Sp$\bar{p}$S discovered W and Z bosons.

V:

Var: Variance.
VEV: Vacuum Expectation Value.

Z:

ZDC: Zero Degree Calorimeter.

Note about the figures

All the figures taken in books, publications or on the web are referenced in their caption. The other figures were done by the author.

The ATLAS experiment has a policy about labels on the figures:

- "ATLAS": means that the figure appears in peer-reviewed article.
- "ATLAS Preliminary": means that the figure was approved by the collaboration, but does not appear in a peer-reviewed article.
- "ATLAS Work In Progress": means that the figure was done by a student and represent its work within the collaboration.

Contents

Introduction

"Ce tout petit changement avait été une révolution."
Victor Hugo, *Les Misérables.*

The last three years have been rich in development for High Energy Physics on colliders. In 2008, the Large Hadron Collider commissioning started, followed rapidly by an incident that caused the shutdown of the machine for one year. In 2009-2010, the LHC was restarted, the commissioning was short allowing to reach a center of mass energy of $\sqrt{s} = 7$ TeV, followed by 9 months of data taking, providing an integrated Luminosity of about $\mathcal{L} \approx 50$ pb^{-1} to the experiments. In 2011, the first fb^{-1} was provided to the LHC experiments, while in the US, the Tevatron was shut down after almost 20 years of data taking, leaving the LHC alone in the search for the Higgs boson.

This particle is the last missing piece in the Standard Model of particle physics, a theoretical framework explaining physics at the subatomic scale. The SM has predicted the existence of several particles before they were effectively discovered. In the first Chapter of this thesis, an introduction to the SM is given. This introduction summarizes the success of the SM and explain the generation of the masses *via* the Higgs mechanism. The shortcomings of the SM are also presented. In particular as the SM Higgs boson has not been observed up to now an alternative model, called TechniColor, allowing the generation of the masses is presented.

The ATLAS experiment is one of the six experiments placed around the LHC rings. It has been designed for the search of the Higgs boson and new physics phenomena. In the first part of the second Chapter of this thesis, the LHC accelerator is presented. The different steps that have been reached since the start of the machine, the current and nominal parameters are summarized. In the second part of this Chapter, the ATLAS experiment is presented. The functioning of the different sub-systems and their performances are given.

The beginning of my thesis in 2008 corresponds to the end of the installation of the ATLAS detector in the underground cavern. This timing has allowed me to participate to almost all the activities related to the experiment: commissioning of the detector, data taking, reconstruction and performances of the detector and finally conducting a search for new physics phenomena.

The LAr calorimeters are introduced in details, in the third Chapter of this thesis. A good understanding of the LAr calorimeters is crucial, since they provide the measurement of electrons, photons, jets and the missing transverse energy. The combined commissioning of the LAr calorimeters within the full ATLAS detector started in 2008 and was continued up to the beginning of the collisions in 2010. The end of the Chapter is focused on my involvement in the data quality and the Monitoring of the LAr calorimeters.

In the fourth Chapter of this thesis, jet reconstruction is presented in details. Using the full 2010

data-set, corresponding to an integrated luminosity of $\mathcal{L} \approx 50$ pb^{-1} of pp collision data at $\sqrt{s} = 7$ TeV, the jet energy resolution is retrieved with two different data-driven techniques. The jet energy resolution is then tested in non nominal calorimetric regions in order to discover an eventual effect.

Finally the last Chapter of this thesis presents a search for new physics in the $W\gamma$ finale state, using the first part of the 2011 data-set, corresponding to an integrated luminosity of $\mathcal{L} = 2.04$ fb^{-1} of pp collision data at $\sqrt{s} = 7$ TeV. No resonance searches have been conducted in this final states at the LHC. One uses the Low Scale TechniColor model as a benchmark model to study the existence of new physics in this final state.

Chapter 1

The Standard Model of Particle Physics and its extension

"Il y a trop de choses à comprendre en même temps."
Louis Ferdinand Céline, *Voyage au bout de la nuit.*

Introduction

This chapter is a theoretical introduction to physics at the subatomic scale. In particular, an introduction to the Standard Model framework is presented in the first section. In the second section, the generation of mass within the Standard Model is introduced. The third section is dedicated to the study of the shortcomings of which the Standard Model suffers, and one possible model to cure them: Technicolor. Finally the last section presents current experimental constraints. The first sections have been written with the helps of these books [1, 2, 3, 4, 5].

1.1 The Standard Model

Developed since the early 60's, the Standard Model (SM) [6, 7, 8] of particle physics is a powerful framework describing physics at the subatomic scale. It is a relativistic Quantum Field Theory (QFT), which uses local symmetry groups (or gauge groups) to introduced the interactions between particles. The SM is a theory invariant under the gauge group $SU(3)_C \times SU(2)_L \times U(1)_Y$.

The SM describes three of the four interactions known in nature: The Strong interaction described by the group $SU(3)_C$, and the Electromagnetic and Weak interactions described by the group $SU(2)_L \times U(1)_Y$, as a unified Electroweak interaction. The way the Gravitational force acts at the subatomic scale is not known yet.

In QFT particles are described by fields. The particles of matter have half integer spins ($S = n/2$), and are called fermions. Fermion interactions are conducted via the exchange of integer spin-1 particles called bosons.

In this section, the formalism of the SM will be introduced.

1.1.1 Quantum field theory

QFT [1, 2] is a mathematical framework which allows the application of quantum mechanics to systems containing an infinite number of degree of freedoms. It is particularly useful in particle physics, where the evolution of a reaction is continuous in time, and thus contains an infinite number of parameters.

In QFT the particles are represented by fields and their evolution is governed by a Lagrangian. Using the Euler Lagrange equation, one can derive the equation of motion for the system.

The Gauge group is used to model the interactions. Noether's Theorem [9] states that to any continuous transformation of a system leaving the Lagrangian invariant, an associated quantity is conserved. This point is used to describe the conservation of quantum quantities such as energy, momentum, charge, etc.

In particle physics the groups used to explain the interactions are Unitary Lie Groups, generally written $SU(N)$. If ψ is a field, its transformation under the group $SU(N)$ is:

$$\psi \rightarrow \psi' = V\psi$$

Where V is a N dimensional squared matrix, and $VV^\dagger = 1$.

One can also write V under the form:

$$V = e^{i\alpha_a T_a}$$

Where α_a represents the transformation and T_a form a representation of the Lie Group, and satisfies the Lie Algebra:

$$[T_a, T_b] = iC_{abc}T_C$$

It should be noted that there are $N^2 - 1$, T_a in a $SU(N)$ gauge group. The C_{abc} are called the structure constant of the group.

One can distinguish global symmetries (α_a), which are space time independent and the local (gauge) symmetries ($\alpha_a(x)$), which depend on the space time coordinates.

1.1.2 Fermions

Fermions are half integer spin particles ($S = 1/2$); they follow Fermi-Dirac statistics: two fermions cannot be in the same quantum state. Massive fermion are represented by a four-parameter Dirac spinor which can be decomposed into two two-dimensional Weyl spinor representing the left-handed and right-handed helicity states of the Fermions

$$\psi = \begin{pmatrix} \psi_L \\ \psi_R \end{pmatrix}.$$

To obtain the left and right spinors we use the chiral projector operator P_L and P_R:

$$\begin{cases} \psi_L = P_L\psi = \frac{1}{2}(1-\gamma^5)\psi \\ \psi_R = P_R\psi = \frac{1}{2}(1+\gamma^5)\psi \end{cases}$$

The motion of free fermions is governed by the Dirac Lagrangian

$$\mathcal{L}_D = \bar{\psi}(i\gamma^\mu\partial_\mu - m)\psi \tag{1.1}$$

Fermions are classified by the following quantum numbers depending on how they interact in the SM:

1. The electromagnetic charge written Q, summarizes the interaction under $U(1)_{EM}$.
2. The weak isospin charge is generally written I, summarizes the interaction under $SU(2)_L$.
3. At this point it's also interesting to introduce the hypercharge given by the Gell-Mann Nishijima relation [3]:

   $$Y = 2(Q - I_3) \tag{1.2}$$

   Where I_3 is the third component of the weak isospin. The hypercharge determines the interaction of the particle under $U(1)_Y$.
4. And finally the Color charges written C, which determine the interaction in $SU(3)_C$.

Fermions can be split into two different families: the leptons which are sensitive only to the electroweak interactions and the quarks which are sensitive to both the strong and electroweak interactions.

The discovery of parity violation in β decays [4] led to the idea that the weak interaction only affects left handed fermions. This leads to defining left handed fermions to be doublets of the weak isospin gauge group $SU(2)_L$, while the right handed fermions are defined to be singlets.

For the strong interaction, the gauge group is $SU(3)_C$, and the quarks are defined to be color triplets.

Table 1.1 summarizes the main properties of each SM fermions. As one can see the quark and leptons are classified in three generations, which increase with their masses. It's also noticeable that all the normal matter is only made up of fermions from the first generation. Second generation fermions can be detected in cosmic rays, but the third generation is visible only in colliders. Each fermion possesses an anti particle, with the opposite gauge quantum numbers. They have all been seen experimentally, the last two being the top quark at Tevatron in 1994 by the CDF and D$\emptyset$ experiments [10, 11], and the ν_τ in 2000 by the DONUT experiment [12].

Generation	First	Second	Third
Leptons	ν_e $Q=0$ mass$< 2\times10^{-6}$ MeV	ν_μ $Q=0$ mass<0.19 MeV	ν_τ $Q=0$ mass<18.2 MeV
	e $Q=-1$ mass$=0.511$ MeV	μ $Q=-1$ mass$=105.7$ MeV	τ $Q=-1$ mass$=1.777$ GeV
Quarks	u $Q=\frac{2}{3}$ mass$=1.7-3.3$ MeV	c $Q=\frac{2}{3}$ mass$=1.27$ GeV	t $Q=\frac{2}{3}$ mass$=171.2$ GeV
	d $Q=-\frac{1}{3}$ mass$=4.1-5.8$ MeV	s $Q=-\frac{1}{3}$ mass$=101$ MeV	b $Q=-\frac{1}{3}$ mass$=4.2$ GeV

Table 1.1: Fermions of the Standard Model with their charge and mass. [13]

Leptons

Leptons couple only via the electroweak interactions. They are classified into left-handed doublets and right-handed singlets of isospin. As neutrinos couple only via the weak interaction in the SM, right-handed neutrinos are usually not considered. Lepton representations under $SU(2)_L$ are:

$$\begin{pmatrix} \nu_e \\ e^- \end{pmatrix}_L, \begin{pmatrix} \nu_\mu \\ \mu^- \end{pmatrix}_L, \begin{pmatrix} \nu_\tau \\ \tau^- \end{pmatrix}_L, e^-_R, \mu^-_R, \tau^-_R.$$

This means that under $SU(2)_L$, a left-handed electron and an electronic neutrino are "the same particle".

The neutrinos are mass-less in the SM. However the detection of neutrino oscillations [13] have shown that they should have a mass of the order of the eV. It is however unknown whether neutrinos are Majorana particles, with identical left-handed and right-handed states, or Dirac particles with separate right handed degrees of freedom.

Quarks

Quarks couple through the electroweak and strong interactions. Their representation under $SU(2)_L$ is:

$$\begin{pmatrix} u \\ d \end{pmatrix}_L, \begin{pmatrix} c \\ s \end{pmatrix}_L, \begin{pmatrix} t \\ b \end{pmatrix}_L, u_R, d_R, c_R, s_R, t_R, b_R.$$

Results [13], have shown that weak interactions in the quark sector do not conserve flavor. For example a u quark can transform to an s quark by the exchange of a W. This means that the quarks mass states are not eigen-states of flavor, but are a linear combination of the mass states. This formalism has been introduced by Cabibbo, Kobayashi and Maskawa [14, 15]:

$$\begin{pmatrix} d' \\ s' \\ b' \end{pmatrix} = V_{CKM} \begin{pmatrix} d \\ s \\ b \end{pmatrix} \quad ,$$

Where the V_{CKM} matrix gives the mixing between the quark generations.

$$V_{CKM} = \begin{pmatrix} V_{ud} & V_{us} & V_{ub} \\ V_{cd} & V_{cs} & V_{cb} \\ V_{td} & V_{ts} & V_{tb} \end{pmatrix} \quad .$$

It can be described by four real parameters: three angles α, β, γ, and a complex phase. The latter gives the source of CP violation in the SM.

The quark color charge can take three values and three anti values written: $r, \bar{r}, g, \bar{g}, b, \bar{b}$. For example the representation of the quark u under $SU(3)_C$ will be:

$$\begin{pmatrix} u_r \\ u_g \\ u_b \end{pmatrix}_C$$

Due to the confinement properties of QCD, the quarks cannot exist as free particles. They exist as bound states, either of a quark-antiquark pair forming a mesons or a three-quark system forming a baryon.

1.1.3 Bosons

In QFT forces are described as an exchange of particles between the particles of matter. This is a major difference compare to classical physics where forces were assumed to act instantaneously. The exchanged particles are integer spin particles ($S = 1$) called gauge bosons. The forces are described as gauge groups [1]. Of the four forces known in nature: gravitational, electromagnetic, weak and strong, only the last three are included in the SM. Table 1.2 gives a summary of the properties of SM bosons, and which force they mediate.

EW			QCD
γ $Q = 0$	Z^0 $Q = 0$	$W^{\pm}$ $Q = \pm 1$	g $Q = 0$
m= 0 GeV	m= 91.1876 GeV	m= 80.399 GeV	m= 0 GeV $n = 8$

Table 1.2: Bosons of the Standard Model with their charge and mass.[13]

The notion of photon is known since the beginning of the 20^{th} century. The electroweak gauge bosons, W and Z, were predicted by the SM [6, 7, 8] before they were discovered experimentally in 1983 by the $UA1$ and $UA2$ collaborations at the CERN $SP\bar{P}S$ accelerator [16, 17]. There are eight gluons carrying the QCD interaction. They are mass-less within the SM. They were discovered in 1979 by the Tasso Collaboration at DESY [18].

1.1.4 Electroweak model

Quantum Electro Dynamics

Quantum electrodynamics [1] is the first theory which explained an interaction in terms of a gauge group. It was developed in the 40's, and used the $U(1)_{EM}$ gauge group to describe electromagnetism. $U(1)$ has only one generator: $T_a = 1$.

As a starting point, let's recall the Dirac Lagrangian of free particles (Eq. 1.1):

$$\mathcal{L}_D = \bar{\psi}(i\gamma^\mu \partial_\mu - m)\psi$$

This Lagrangian is invariant under a global $U(1)$ transformation:

$$\psi \rightarrow \psi' = e^{-i\alpha}\psi,$$

but if we require a local gauge transformation, *i.e.* a transformation which depends on the coordinates

$$\psi \rightarrow \psi' = e^{-i\alpha(x)}\psi,$$

then the Dirac Lagrangian is no longer conserved:

$$\mathcal{L}_D = \bar{\psi}(i\gamma^\mu \partial_\mu - m)\psi + \bar{\psi}(\gamma^\mu \partial_\mu \alpha(x))\psi.$$

In order to preserve the symmetry, an extra term is introduced in the Lagrangian, involving a gauge field A_μ :

$$\mathcal{L}_D = \bar{\psi}(i\gamma^\mu\partial_\mu - m)\psi + ie\bar{\psi}(i\gamma^\mu A\mu)\psi.$$

with the A_μ transforming under $U(1)$ as:

$$A_\mu \to A'_\mu = A_\mu + \frac{1}{e}\partial_\mu \alpha x$$

This makes the Lagrangian invariant under gauge transformations as well. Alternatively, one can rewrite the Lagrangian in terms of the covariant derivative operator

$$\mathcal{D}_\mu = (\partial_\mu + ieA_\mu)$$

which has the property that the covariant derivative $\mathcal{D}_\mu\psi$ of ψ transforms in the same way as ψ:

$$\mathcal{D}_\mu\psi \to e^{-i\alpha(x)}\mathcal{D}_\mu\psi$$

The dynamics of this gauge fields A_μ, can be described in terms of the electromagnetic tensor

$$F_{\mu\nu} = \partial_\mu A_\nu - \partial_\nu A_\mu$$

so that the full Lagrangian, invariant under $U(1)_{EM}$ gauge transformation, reads

$$\mathcal{L}_{QED} = \bar{\psi}(i\gamma^\mu\mathcal{D}_\mu - m)\psi - \frac{1}{4}F_{\mu\nu}F^{\mu\nu} \tag{1.3}$$

This Lagrangian describes the electromagnetic interactions. The A_μ field represents the photon. Any term such as $m^2A_\mu A^\mu$ that would give a mass to the photon is forbidden by gauge invariance, in accordance with the known mass-less-ness of the photon.

The weak interaction

The weak force [2] is represented by a gauge group $SU(2)_L$. The fundamental representation of the corresponding Lie algebra is:

$$T_a = \frac{\tau_a}{2}$$

Where the τ_a are the Pauli Matrices. The algebra commutation rules for this group are given by: $[\frac{\tau_a}{2}, \frac{\tau_b}{2}] = i\epsilon_{abc}\frac{\tau_c}{2}$. Where ϵ_{abc} is the permutation symbol. There are $N_L^2 - 1 = 3$ generators in this group.

The invariance of the Lagrangian under a local transformation of $SU(2)_L$:
$\psi'_L(x) = e^{i\vec{\tau}.\frac{\alpha(\vec{x})}{2}}\psi_L(x)$ can be restored by introducing a triplet of gauge fields

$$W^\mu(x) = (W_1^\mu, W_2^\mu, W_3^\mu) \tag{1.4}$$

The dynamics of this triplet are given by the term $-\frac{1}{4}W^{\mu\nu}W_{\mu\nu}$ in the Lagrangian, with

$$W_{\mu\nu} = \partial_\mu W_\nu - \partial_\nu W_\mu - gW_\mu \wedge W_\nu.$$

The covariant derivative is

$$D_\mu = (\partial_\mu + ig\frac{\vec{\tau}}{2}.W^\mu).$$

The physical gauge bosons are linear combination of the fields introduced in 1.4 :

$$\begin{cases} W^+ &= \frac{1}{\sqrt{2}}(W_1 - iW_2) \\ W^- &= \frac{1}{\sqrt{2}}(W_1 + iW_2) \\ W^0 &= W_3 \end{cases} \tag{1.5}$$

The weak interaction acts as a charged current interaction ($W^\pm$) and as the neutral current interaction (W^0).

Electroweak unification

The next step in the development of the theory is the unification [1] of the weak and electromagnetic interactions in a single electroweak (EW) interaction. This is introduces through the invariance of the Lagrangian under the gauge group $SU(2)_L \times U(1)_Y$.

A new gauge boson B_μ associated with the $U(1)_Y$ group, whose dynamics are given by the term $\frac{1}{4}B^{\mu\nu}B_{\mu\nu}$ in the Lagrangian, with

$$B_{\mu\nu} = \partial_\mu B_\nu - \partial_\nu B_\mu.$$

The coupling constant associated with the $U(1)_Y$ interaction is denoted g', and the covariant derivative for the combined $SU(2)_L \times U(1)_Y$ group is thus

$$D_\mu = (\partial_\mu + ig\frac{\vec{\tau}}{2}.W^\mu + ig'\frac{1}{2}Y_L B_\mu). \tag{1.6}$$

The neutral sector of the interaction is composed of the two states W^0 and B, which can mix. As will be detailed below, one can consider in particular the basis obtained by a rotation of θ_W, called the weak mixing angle [1] or Weinberg angle, defined by

$$\begin{cases} \cos\theta_W &= \frac{g}{\sqrt{g^2+g'^2}} \\ \sin\theta_W &= \frac{g'}{\sqrt{g^2+g'^2}} \end{cases} \tag{1.7}$$

Where g and g' are respectively the electromagnetic and weak coupling constant. The corresponding gauge degrees of freedom as

$$\begin{cases} W^+ &= \frac{1}{\sqrt{2}}(W_1 - iW_2) \\ W^- &= \frac{1}{\sqrt{2}}(W_1 + iW_2) \\ Z^\mu &= \cos\theta_W W_3^\mu - \sin\theta_W B_\mu \\ A^\mu &= \sin\theta_W W_3^\mu + \cos\theta_W B_\mu \end{cases} \tag{1.8}$$

As explained below, the field A^μ is associated to the photon and mediates the electromagnetic interaction. The field (Z^μ) is associated to the Z boson and mediates the neutral current of the weak interactions. The fields $(W^\pm)$ are associated to the W bosons and mediate the charged currents.

The EW Lagrangian is therefore given by:

$$\mathcal{L}_{EW} = i\bar{\psi}_L\gamma^\mu(D_\mu)\psi_L + i\psi_R\gamma^\mu(\partial_\mu + ig'\frac{1}{2}Y_L B_\mu)\psi_R - \frac{1}{4}(F_{\mu\nu}F^{\mu\nu} + B_{\mu\nu}B^{\mu\nu}) \tag{1.9}$$

No mass terms can be introduced in this Lagrangian without explicitly breaking the $SU(2)_L$ symmetry.

1.1.5 Quantum chromo-dynamics

The theory of Quantum Chromo-Dynamics [2] (QCD) theory is a description of the strong interactions built by a gauge theory using the group $SU(3)_C$. In this group there is $N_C^2 - 1 = 8$ generators associated with gauge bosons: the gluons. The corresponding coupling constant is referred to as g_s.

As mentioned in sections 1.1.2 and 1.1.3, only quarks and gluons are sensitive to the strong interaction. The same procedure as in section 1.1.4 will be used. One imposes the invariance of the Dirac Lagrangian (Eq. 1.1) under the local symmetry $SU(3)_C$, introducing a new gauge field G_a^μ for the gluons and an associated term $-\frac{1}{4}G_a^{\mu\nu}G^a_{\mu\nu}$ in the Lagrangian explaining its dynamics, with

$$G_a^{\mu\nu} = \partial^\mu G_a^\nu - \partial^\nu G_a^\mu - g_s f^{abc} G_b^\mu G_c^\nu$$

The covariant derivative is

$$D_\mu = (\partial_\mu + igT_a G_a^\mu)$$

Finally the QCD Lagrangian is:

$$\mathcal{L}_{QCD} = \sum_f \bar{\psi}_f \gamma_\mu i D^\mu \psi_f - \sum_f m_f \bar{\psi}_f \psi_f - \frac{1}{4} G_a^{\mu\nu} G^a_{\mu\nu} \tag{1.10}$$

Where the sum runs over the flavor of the quarks. The mass terms cannot be included in the SM since they break explicitly the $SU(2)_L$ symmetry.

At high energy the theory becomes perturbative, leading to the asymptotic freedom of QCD. This property means that the strong coupling constant is inversely proportional to the energy. At low energy quarks and gluons are free and interacts weakly with each others. At high energy the interaction is strong and can be described by perturbative theory.

Renormalization

At this point one needs to talk about the renormalization [2] of the theory. Figure 1.1 gives the Feynman diagrams of a quark quark interaction by the exchange of a gluon, at the tree level (a), in the first order in perturbation theory as a correction on the propagator (b), and on the correction on the vertex (c). One can see that if we go in perturbation theory there are many diagrams that contribute.

The principle of renormalization is to note that the contributions from particles in the loops with sufficiently high momentum can be fully taken into account by a redefinition of the parameters of the Lagrangian. This is the case in particular for the coupling constants. One thus introduces a cutoff scale μ, and considers the contributions from loop momenta above μ to be included in the definition of the couplings. This means that the coupling constants are dependent on the chosen scale μ, and is said to be *running*. The expression of α_s can be written as a function of the momentum transfer (Q):

$$\alpha_S(Q^2) = \frac{\alpha_S(\mu^2)}{1 + C\frac{\alpha_S(\mu^2)}{4\pi}\ln(\frac{Q^2}{\mu^2})}$$

For a gauge theory $SU(N_c)$, one has $C = -\frac{2}{3}N_f + \frac{11}{3}N_c$. Where N_f represents the number of fermion flavors. One can notice that for lower values of N_c, we have $C < 0$ and the coupling constant increases with energy (*i.e.* decreases as the separation between the interacting fermions increases). This is the case in particular for electroweak interactions. However for higher values of N_c, and in particular for QCD, we have $C > 0$ and the coupling constant decreases with energy. This is referred to as *asymptotic freedom*, and conversely leads to an interaction strength that increases with separation; this is thought to be the mechanism underlying the confinement of quarks.

One can introduce the scale Λ_{QCD} (usually called the scale of QCD) above which QCD starts to be perturbative:

$$\Lambda^2_{QCD}(\mu_R) = \mu_R^2 e^{(\frac{-4\pi}{\alpha_S(\mu_R^2)C})}$$

The evolution of the coupling constant as a function of Q can then be re-expressed as

$$\alpha_S(Q^2) = \frac{36\pi}{C\ln(\frac{Q^2}{\Lambda^2_{QCD}})} = \frac{6\pi}{23\ln(\frac{Q^2}{\Lambda^2_{QCD}})}.$$

Figure 1.2 gives the evolution of the coupling constant of the electromagnetic, weak and strong interactions, giving the expected energy dependencies.

1.2 Mass generation in the Standard Model

Now that the general theoretical landscape of the SM has been introduced, one can turn to the remaining issue of how to generate masses without losing the benefits of gauge invariance. Two mechanisms are presented.

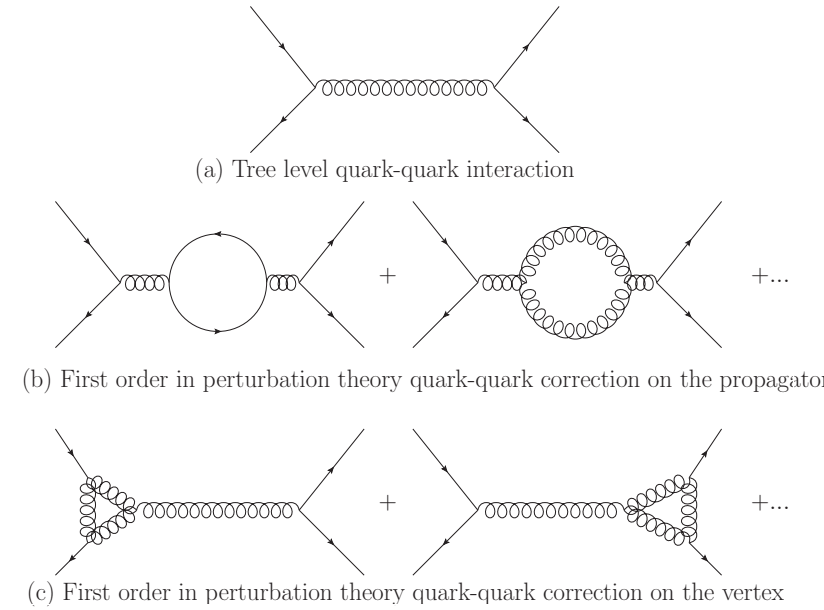

(a) Tree level quark-quark interaction

(b) First order in perturbation theory quark-quark correction on the propagator

(c) First order in perturbation theory quark-quark correction on the vertex

Figure 1.1: Tree and first Order perturbation theory quark-quark *via* gluon interaction.

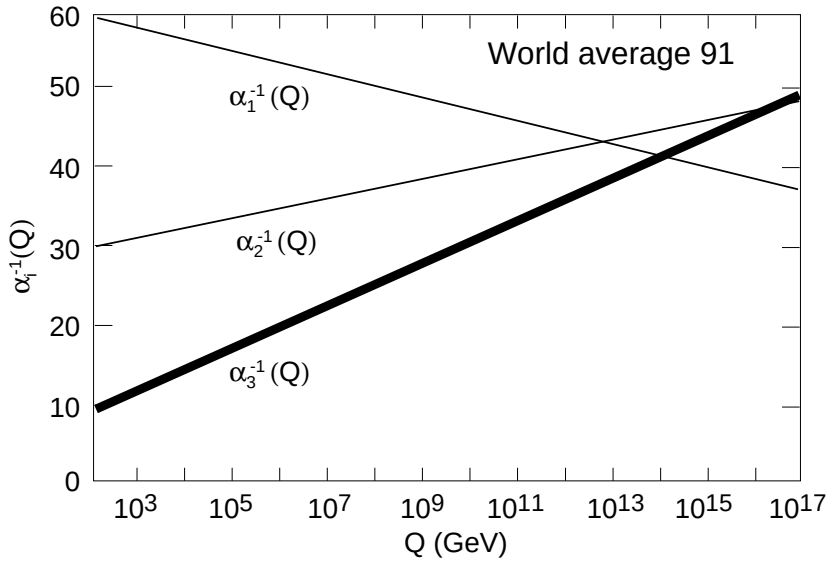

Figure 1.2: Evolution of the SM inverse coupling constants: EM(α_1), weak(α_2) and strong(α_3) [13].

1.2.1 Higgs mechanism

Spontaneous electroweak symmetry breaking

The first mechanism found to explain the electroweak symmetry breaking and thus gives the mass to the W and Z bosons is the BEHGHK mechanism also known as the Higgs mechanism. It has been introduced independently by Brout and Englert [19], by Higgs [20] and by Guralnik, Hagen, and Kibble [21] in 1964.

The basic idea is to introduce a new complex scalar field generally written:

$$\phi_H = \frac{1}{\sqrt{2}} \begin{pmatrix} \phi^+ \\ \phi_0 \end{pmatrix} \tag{1.11}$$

With a hypercharge $Y = -\frac{1}{2}$.

One can add to the Lagrangian the term

$$\mathcal{L}_{Higgs} = (D_\mu \phi)^\dagger (D^\mu \phi) - V(|\phi|^2) \tag{1.12}$$

which is invariant under a local gauge transformation of $SU(2)_L \times U(1)_Y$; D_μ is the covariant derivative (see Eq. 1.6). The Higgs potential $V(|\phi|^2)$ is given by:

$$V(|\phi|^2) = \mu^2 |\phi|^2 + \lambda |\phi|^4 \tag{1.13}$$

Where λ and μ are such that $\lambda > 0$ and $\mu^2 < 0$.

A graphical representation of the Higgs potential in the real plane using this parameterization is given in fig 1.3. One can see that the fundamental state at $\phi = 0$ is not the minimum of the potential and does not correspond to the true vacuum of the theory. The true vacuum occurs for $|\phi| = v$, where v is called the Vacuum Expectation Value (VEV) of ϕ and given by $v = \sqrt{\frac{-\mu^2}{\lambda}}$. v is continuously degenerate in the complex plane. A parameterization of the Higgs field around v is given by:

$$\phi(x) = \frac{e^{\theta^a(x)} I_a}{\sqrt{2}} \begin{pmatrix} 0 \\ v + h(x) \end{pmatrix}$$

where the "angular" degrees of freedom θ^a give the direction of the VEV, and $h(x)$ is the degree of freedom along v. One can impose that the vacuum state corresponds to

$$\phi_H = \frac{1}{\sqrt{2}} \begin{pmatrix} v \\ 0 \end{pmatrix}$$

This choice breaks spontaneously the symmetry $SU(2)_L \times U(1)_Y$ to a $U(1)_{EM}$ invariance. The Goldstone Theorem [22, 23] states that when a continuous symmetry is broken, mass-less bosons appears. In this case three Goldstones bosons are created, corresponding to the θ^a fields, and provide the longitudinal modes to the W and Z bosons, which thus acquire masses. The field h remains as "the" Higgs boson.

Adding the Higgs Lagrangian (eq 1.12) to the EW Lagrangian (eq 1.9), it is possible to obtain the masses of the gauge bosons:

$$\begin{cases} M_{W^\pm} = \frac{gv}{2} \\ M_{Z^0} = \frac{M_{W^\pm}}{\cos\theta_W} \\ M_{h^0}^2 = -2\mu^2 = \lambda v^2 = \frac{4\lambda}{g^2} M_{W^\pm}^2 \end{cases} \tag{1.14}$$

The VEV can be parameterized using the mass of the W ($M_{W^\pm}$) and the Fermi constant [2] (G_F). At the lowest order in perturbation theory this relation is valid:

$$\frac{1}{\sqrt{2}} G_F = \frac{g^2}{8 M_{W^\pm}^2} \rightarrow v = \sqrt{\sqrt{2} G_F} \approx 246 \; GeV \tag{1.15}$$

The A_μ field given in Eq. 1.8 remains massless, since it is associated with the unbroken $U(1)_{EM}$ symmetry.

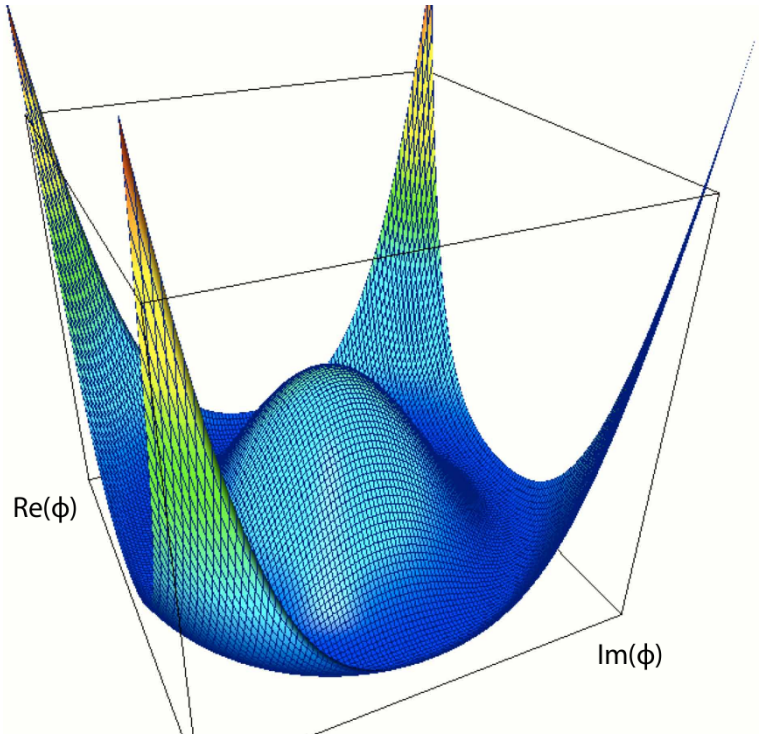

Figure 1.3: Higgs Potential $V(\phi)$ in the real plan, for $\lambda > 0$ and $\mu^2 < 0$ [24].

Yukawa interactions

The Higgs mechanism allows to give mass to the SM bosons. But the introduction of fermions mass term in the SM Lagrangian still breaks explicitly the EW symmetry. A development of the Higgs mechanism to solve this issue leads to the Yukawa interaction [1]. It allows to couple the fermions to the Higgs fields, giving mass to the SM fermions.

The Yukawa Lagrangian for the first generation of fermions is proportional to:

$$\mathcal{L}_{Yukawa} = -\lambda_e \bar{l}_L \phi e_R - \lambda_u \bar{q}_L \bar{\phi} u_R - \lambda_d \bar{q}_L \phi d_R + h.c. \tag{1.16}$$

The mass of the fermions are given by:

$$M_f = \lambda_f \frac{v}{\sqrt{2}} \tag{1.17}$$

Where λ_f is the Yukawa coupling of the fermions to the Higgs fields. For 2 fermion generations, this is replaced by a complex 3x3 mass matrix containing information on both the fermion masses and inter-generation mixing [13].

1.2.2 Quantum chromo-dynamics

Another possible way of breaking the EW symmetry is to use the QCD dynamics [25, 26, 27, 28]. In this section we will see how it is possible. In order to simplify this introduction, one will consider only the up and down quarks. The QCD Lagrangian is invariant under a *chiral* gauge symmetry $SU(2)_L \times SU(2)_R$ in which independent gauge transformations ($SU(2)_L$ and $SU(2)_R$ respectively) are applied to the left- and right-handed fermions.

Due to the confining properties of QCD, the true vacuum of the theory contains $q\bar{q}$ condensates which spontaneously breaks the chiral symmetry to the isospin symmetry,

$$SU(2)_L \times SU(2)_R \rightarrow SU(2)_V.$$

The quark condensate has non-zero vacuum expectation values:

$$\langle 0|q\bar{q}|0\rangle = \langle 0|\bar{q}_L q_R + \bar{q}_R q_L|0\rangle \neq 0$$

Since the condensate is a doublet of $SU(2)_L$ and carries hypercharge $Y = 1$, this leads to the breaking of the EW symmetry in which only a $U(1)$ gauge symmetry remains:

$$SU(2)_L \times U(1)_Y \rightarrow U(1)_{EM}$$

From the Goldstone theorem [22] three mass-less bosons are created, which are eaten by the EW gauge bosons as in the Higgs mechanism. The masses of the gauge bosons are then given by:

$$\begin{cases} M_{W^\pm} = \frac{g}{2} f_\pi \\ M_{Z^0} = \frac{g}{2\cos\theta_W} f_\pi \end{cases} \tag{1.18}$$

Where $f_\pi \approx 92$ MeV is the decay constant of the pion. If we inject this constant in the equations 1.18, we obtain $M_{W^\pm} \approx 30$ MeV and $M_{Z^0} \approx 34$ MeV. Although this is far lower than the values found experimentally (Tab. 1.2), the ratio of the mass of the two bosons is correct (Eq. 1.14):

$$\frac{M_{Z^0}}{M_{W^\pm}} = \frac{1}{\cos\theta_W}$$

Even if this mechanism does not gives the proper mass to the electroweak bosons, it is interesting to notice that it generates these masses dynamically, with no extra interactions.

1.3 Why new physics?

1.3.1 Problems of the Standard Model

The SM is a quite powerful theory which has predicted many particles before their discovery such as the top quark or the EW bosons.

However there is also a certain number of problems in the SM that have no answer or no satisfactory explanation. A non-exhaustive list of these problems is as follows:

- Indirect proof of Dark Matter have been detected through the astrophysical observation [29, 30] but there is no suitable particle content in the SM to account for this observation.
- The Higgs mechanism is introduced in an *ad hoc* way in the SM. It explains how vector bosons and fermions acquire masses but not why. Moreover the SM Higgs boson has not been yet observed experimentally.
- The standard model contains free parameters, which have no theoretical underpinning. They have been introduced by hand in the theory to fit observations.
- The Hierarchy problem: the quadratic corrections to the Higgs mass leads to an unnaturally high mass of the Higgs boson as the cutoff scale of the SM is raised. It is possible to restore the proper Higgs mass, but this requires fine tuning of the SM parameters, which is not intellectually satisfactory.
- There is no explanation to the hierarchy of the fermions masses within the SM. For example the up and down quarks masses are separated by almost six order of magnitude from the mass of the top quark.
- It is known [31] that neutrinos have mass, but the exact nature of the mass terms remains unknown.
- Gravitation is not included in the SM.

The Hierarchy problem in particular suggests that the SM may be a low-energy effective theory of a new fundamental theory, whose validity may not reach much beyond the TeV scale. Two main approaches to extending the SM have been introduced over the years in order to resolve this.

One approach consists of introducing a new symmetry that gives bosonic partners to the known fermions, and fermionic partners to the known bosons. This approach is called SuperSymmetry (SUSY). It will not be developed here.

In the other approach, the EW symmetry breaking and the mechanism to give masses to particles are explained in terms of strong dynamics. In this approach the models are "Higgsless", with no analog of a Higgs boson. One possibility is to introduce a completely new strong sector, along with additional fermions. This is the possibility that will be developed here, in terms of a model called TechniColor (TC).

1.3.2 One possible extension of the Standard Model: Technicolor

Minimal Technicolor models

Minimal models of Technicolor (TC) were first introduced in the mid-1970's by S. Weinberg and L. Susskind [32, 33]. Those models postulate the existence of a new strong gauge interaction to generate the electroweak symmetry breaking, and therefore the masses of the Z and W bosons. If we take $f_\pi = v = 246$ GeV (the value of the EW VEV v) in Eqs. 1.18, we recover the proper mass of the W and Z bosons. This new strong interaction is assumed to be invariant under a $SU(N_{TC})_{TC}$ gauge group[1].

New mass-less fermions sensitive to this interaction are introduced [32, 33], the technifermions. The number of such new fermions is denoted by N_{Tf}. Technifermions are assumed to be only sensitive to the new TC interactions and to the EW interactions. Therefore they are classified in N_D doublet of weak isospin:

$$\begin{pmatrix} Q_U \\ Q_D \end{pmatrix}_L, Q_{U_R}, Q_{D_R}$$

There are as usual $N = N_{TC}^2 - 1$ gauge bosons associated with the TC gauge group, called technigluons.

As for QCD, the theory is invariant under a chiral version of the TC symmetry:

$$SU(N_{TC})_L \times SU(N_{TC})_R$$

which is dynamically broken at a scale Λ_{TC}, analog to the QCD scale. One can also introduce a technipion decay constant F_{π_T}, related to the f_π of QCD by:

$$F_{\pi_T} = \sqrt{\frac{N_{TC}}{3}} \frac{\Lambda_{TC}}{\Lambda_{QCD}} f_\pi \tag{1.19}$$

The VEV v occurring in EW symmetry breaking is related to F_{π_T} and to the number of technifermions doublets N_D by

$$v = \sqrt{N_D} F_{\pi_T}. \tag{1.20}$$

Combining these last two equations one gets

$$\Lambda_{TC} = \sqrt{\frac{3}{N_{TC} N_D}} \frac{v}{f_\pi} \Lambda_{QCD} \tag{1.21}$$

In a simple TC model where $N_{TC} = 4$ and $N_D = 1$, there are two types of technifermion bound states: $Q\bar{Q}$ states called technimesons, and $QQQQ$ modes called technibaryons. The Goldstone bosons originating from the symmetry breaking are technimesons, and it is interesting to note that in particular the EW gauge bosons have a technimeson component through their longitudinal mode.

Their are three main problems with such Minimal TC models:

[1] For $N_{TC} = 3$ the TC model is equivalent to QCD with a higher mass scale.

- These models usually fail the constraints from precision EW measurements. Figure 1.4 gives the results of the SM parameters fit in the plane of the S and T Peskin-Takeuchi parameters [34, 35]. In the SM, one has $S = 0.01 \pm 0.10(-0.08)$ and $T = 0.03 \pm 0.11(+0.09)$ [34, 35]. This is in good agreement with the experimental values, but disagrees with the prediction $S >> 0$ and $T \approx 0$ coming from simple TC models.
- No mechanism can account for technibaryon decays to lighter states, so the lightest one should be stable. Moreover if there exist more than three technimesons, they should give some new massive particles which will have a mass on the order of the SM EW gauge bosons [26]. None of these particles has ever been observed.
- Finally the minimal TC models gives only mass to the SM gauge bosons and not to the SM fermions.

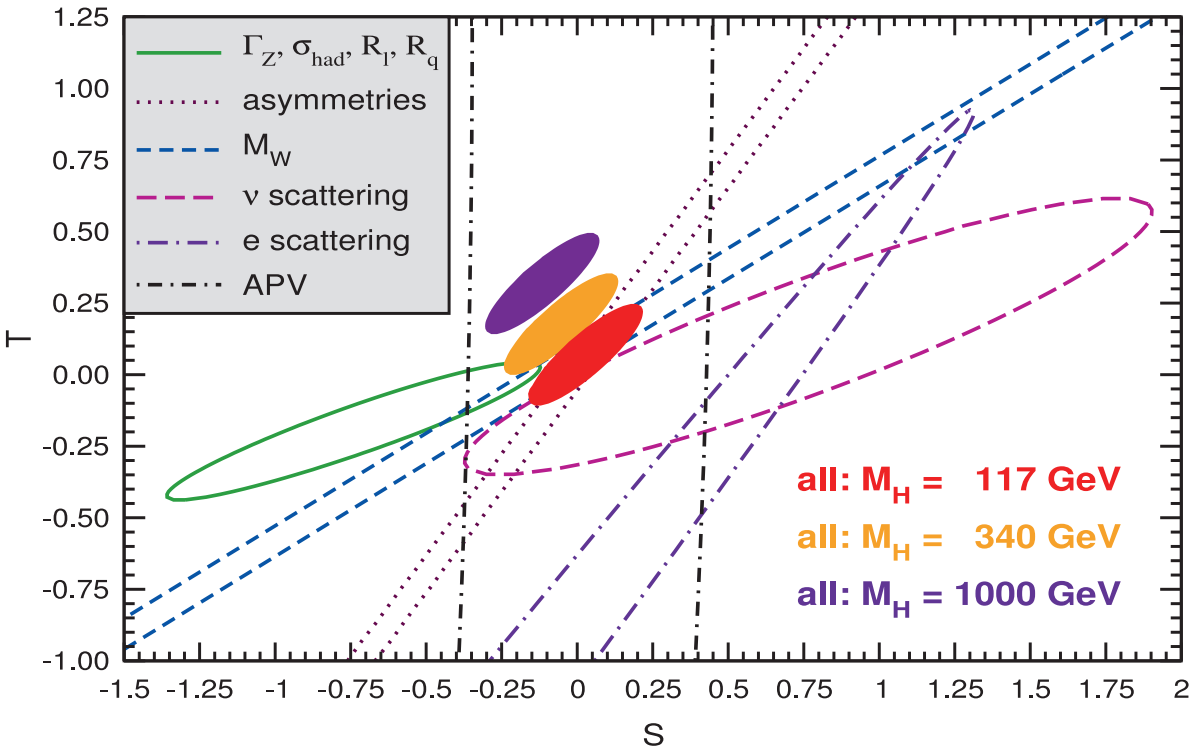

Figure 1.4: Values of the S and T parameters in the SM. The ellipses in the plot show the constraints coming from various sets of observables. The M_H ellipses are given for different Higgs Mass scenario [13].

Extended TC

In order to address how the SM fermions acquire a mass, Extended TC (ETC) [26, 36] was introduced. It consists to introduce a new gauge group, usually assumed to be of the form $SU(N_{ETC})$, which contains the SM group $SU(3)_C \times SU(2)_L \times U(1)_Y$ and the TC group $SU(N_{TC})$. This new group contains the SM, so the interaction of the ETC gauge bosons with the SM fermions will allow them to acquire their mass, after the ETC symmetry is dynamically broken.

An effective ETC Lagrangian can be written:

$$\mathcal{L}_{ETC} = \alpha_{ab}\frac{\bar{Q}\gamma^\mu T^a Q \bar{Q}\gamma_\mu T_b Q}{\Lambda^2_{ETC}} + \beta_{ab}\frac{\bar{Q}\gamma^\mu T^a \psi\bar{\psi}\gamma_\mu T_b Q}{\Lambda^2_{ETC}} + \gamma_{ab}\frac{\bar{\psi}\gamma^\mu T^a \psi\bar{\psi}\gamma_\mu T_b \psi}{\Lambda^2_{ETC}} \tag{1.22}$$

Where ψ represents the fields of SM fermions and Q the fields of techniquarks. The α_{ab}, β_{ab} and γ_{ab} terms represents the different coupling of ETC to the SM and TC fermions.

The α_{ab} term represents the interaction between a techniquark and an ETC gauge boson. The corrections added by this term will raise the masses of the technimesons and solve the problem of the lightest technimeson not being detected. Figure 1.5 gives an example of a Feynman diagram of the interaction of a technipion and an ETC gauge boson.

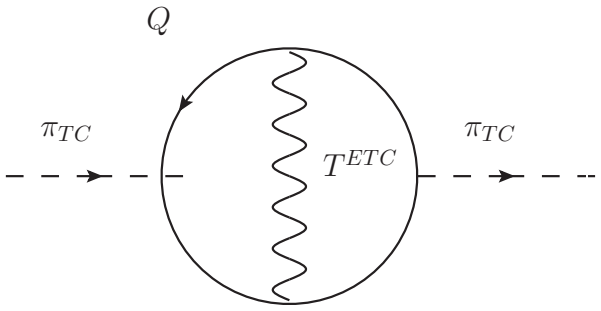

Figure 1.5: Feynman Diagram of the correction to the propagator of a technimeson *via* the exchange of an ETC gauge boson. This diagram leads to scale up the mass of the technimeson.

The β_{ab} term allows the mixing of SM fermions to technifermions and gives the strength of the coupling to the ETC gauge bosons. This term explains the decay of the technibaryons and also the masses of the fermions. Figure 1.6 gives an example Feynman diagram of such interactions. The mass term is proportional to

$$m_f \approx \frac{g_{ETC}^2}{\Lambda_{ETC}^2} < \bar{Q}Q >_{ETC} \approx \beta \frac{N_{TC}\Lambda_{TC}^3}{\Lambda_{ETC}^2} \tag{1.23}$$

One can see using this formula that all the SM fermions masses should be equivalent, in contrast to experimental observation.

One way of solving this problem is to introduce different ETC scales:

$$\Lambda_{ETC}^1 \rightarrow \Lambda_{ETC}^2 \rightarrow \Lambda_{ETC}^3 \rightarrow \Lambda_{TC}$$

Each of this scale corresponds to the dynamical breaking of a different ETC component, and differences in couplings to the different fermion flavors would account for the observed mass hierarchy.

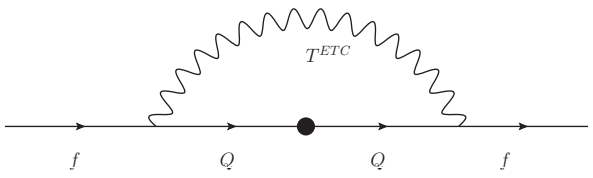

Figure 1.6: Feynman Diagram of the correction to the propagator of a SM fermion *via* the exchange of an ETC gauge boson, allowing the mass of the fermion.

Finally the last term γ_{ab} brings a new problem. Since it allows the coupling of different flavors of SM fermions, it leads to Flavor Changing Neutral Current (FCNC) interactions, which are strongly constrained within the SM. Figure 1.7 gives an example of a Feynman diagram of a FCNC interaction. This term is also proportional to Λ_{ETC}^2, the same parameter which allows to tune the masses of the

fermions. There is therefore a tension between the need to enhanced the mass of the fermions to their proper value and the need to simultaneously suppress the FCNC interactions.

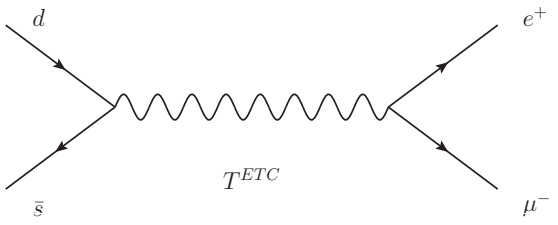

Figure 1.7: Feynman Diagram of the exchange of a quark pair into a lepton pair *via* an ETC gauge boson leading to a FCNC interaction.

Therefore, although ETC is a nice enhancement of minimal TC models, allowing in particular to explain naturally the mass of the fermions and address the problem of the TC bound states not seen, it in brings FCNC interactions and also doesn't address the discrepancy between TC and the precision EW measurements.

Walking TC

The QCD coupling is said to be *running* because of the renormalization of the theory (*cf* 1.1.5). The latest class of TC models takes most of their properties from QCD like models, but they also incorporate a new feature called *walking* coupling constant [36, 26].

The ETC operators that generate the SM fermions mass are subject to renormalization effects by TC of the form:

$$< \bar{Q}Q >_{ETC} = < \bar{Q}Q >_{TC} \, e^{\int_{\Lambda_{TC}}^{\Lambda_{ETC}} \frac{d\mu}{\mu} \gamma_m(\alpha(\mu))}$$

Where $\gamma_m(\alpha(\mu))$ is the operator anomalous dimension, and μ an energy scale moving from Λ_{TC} to Λ_{ETC}.

In a general QCD like theory, $\Lambda_{TC} \equiv \Lambda_{ETC}$, this integral will give something like:

$$< \bar{Q}Q >_{ETC} \approx \ln(\frac{\Lambda_{TC}}{\Lambda_{ETC}})^{\gamma_m} < \bar{Q}Q >_{TC} \tag{1.24}$$

However if we introduce a fixed point where the coupling constant stays constant for a wide energy scale then one obtains

$$< \bar{Q}Q >_{ETC} \approx (\frac{\Lambda_{TC}}{\Lambda_{ETC}})^{\gamma_m(\alpha^C)} < \bar{Q}Q >_{TC} \tag{1.25}$$

where α^C is the value of the coupling at this fixed point. This is now called a *walking* coupling constant, since it varies little over a large energy range. To illustrate this feature figure 1.8 show α_{ETC}, in a QCD like case and in a *walking* TC like case. Now if one reconsiders Eq. 1.23, the mass is dependent on the Λ_{ETC}, and on $< \bar{Q}Q >_{ETC}$, so *walking* allows to release the pressure on the FCNC interactions while moving up the mass of the SM fermions.

In order to construct the *walking* gauge coupling, one need to create a fixed point for the coupling. Two approaches can be used. One can introduce a large number of technifermions N_D, using relation 1.21; this leads to $\Lambda_{TC} \approx 100$ GeV. Alternatively, one introduces two scales of TC, with one being much lower than 250 GeV.

The *walking* feature also makes the S and T parameters of TC not directly calculable from the analogy with QCD, relaxing the constraints from precision EW measurements. Some studies [37] have also shown that walking TC could lead to precision EW predictions values compatible with the SM.

A specific subclass of walking TC models called Low-Scale TechniColor (LSTC) is of particular interest at LHC, since new vector technimeson resonances could give a striking signal.

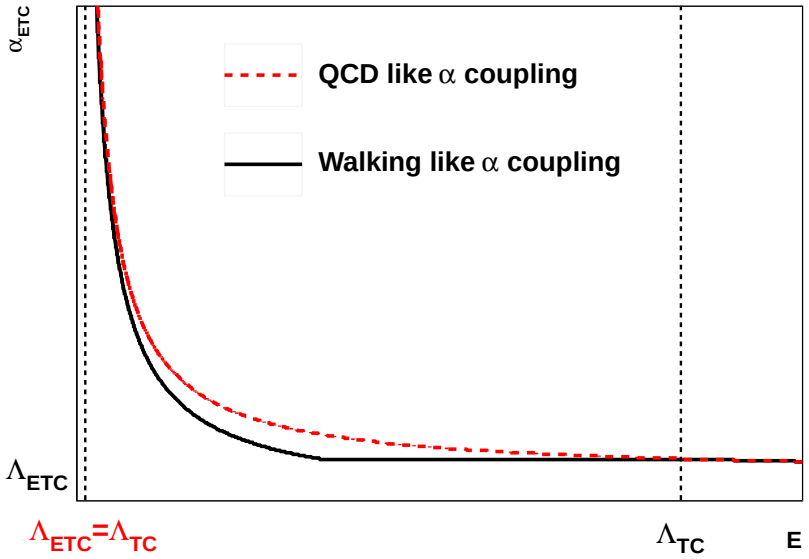

Figure 1.8: Coupling of the ETC theory in a QCD like case (red), and in the presence of a stopping point *walking* case (black).

Phenomenology of the LSTC Straw-man Model

A simple version of an LSTC model called the "LSTC straw-man model" [38, 39, 40, 26] is implemented in PYTHIA [41]. This simplified model was used for most of the LEP and Tevatron LSTC studies. It's also the model we will use as a benchmark to study TechniColor in ATLAS [42].

This models follows the basic principles outlined in the previous sections. The TC group used is $SU(N_{TC})$, and there are N_f technifermions introduced, classified in N_D doublets of weak isospin and carrying an electrical charge.

The lightest isospin doublet of technifermions is a singlet of $SU(3)_C$ and is independent of the other doublets. It gives the dominant effect at low energy. The other doublets might interact under $SU(3)_C$. All the fermions acquire mass via ETC. The masses of the ETC gauge bosons are set around 10^{3-4} TeV to give the correct masses to the fermions and suppress FCNC interactions.

The technipion Π_T, which constitutes the lightest technimesons is identified with

$$|\Pi_{\mathsf{T}}^{\pm,0}>=\sin\chi|W_L^{\pm,0}>+cos\chi|\pi_{\mathsf{T}}^{\pm,0}> \tag{1.26}$$

Where $\pi_{\mathsf{T}}^{\pm,0}$ are the mass eigen-state of the technipion, and $W_L^{\pm,0}$ are the longitudinally-polarized weak bosons W,Z bosons.χ is a mixing angle defined by

$$\sin\chi=\frac{F_{\pi_{\mathsf{T}}}}{VEV}=\frac{1}{\sqrt{N_D}} \tag{1.27}$$

One can label the mesons $\pi_{\mathsf{T}}, a_{\mathsf{T}}, \omega_{\mathsf{T}}, \rho_{\mathsf{T}}$, *etc.*, by analogy with QCD. The mass spectrum is then generally such that, $M_{\rho_{\mathsf{T}}}, M_{\omega_{\mathsf{T}}}, M_{a_{\mathsf{T}}} < 2M_{\pi_{\mathsf{T}}}$. The technimeson decays to technipions are therefore kinematically forbidden, and the technimesons decay mostly to two electroweak gauge boson, the dominant channels at the LHC being $\omega_{\mathsf{T}} \to Z\gamma$, $a_{\mathsf{T}} \to W\gamma$ and $\rho_{\mathsf{T}} \to WZ, W\gamma$. The technimesons can also decay into a lepton pairs, or more complex final states involving a boson and jets. These resonances are therefore expected to be narrow with $\Gamma(\rho_{\mathsf{T}}, \omega_{\mathsf{T}}, a_{\mathsf{T}}) \approx 1$ GeV. The angular distribution of the decay product in this model are expected to be proportional to $1+\cos^2\theta$ or $\sin^2\theta$, allowing precision tests of the theory if a particle is discovered.

In the analysis presented here, we will focus only on one final state: $W\gamma$. In this channel, two resonances contribute to the final state. For the $W\gamma$ channel, ρ_{T} and a_{T} contribute, with a_{T} the

dominant contribution. Figure 1.9 gives the Feynman Diagram of the production of these two final states.

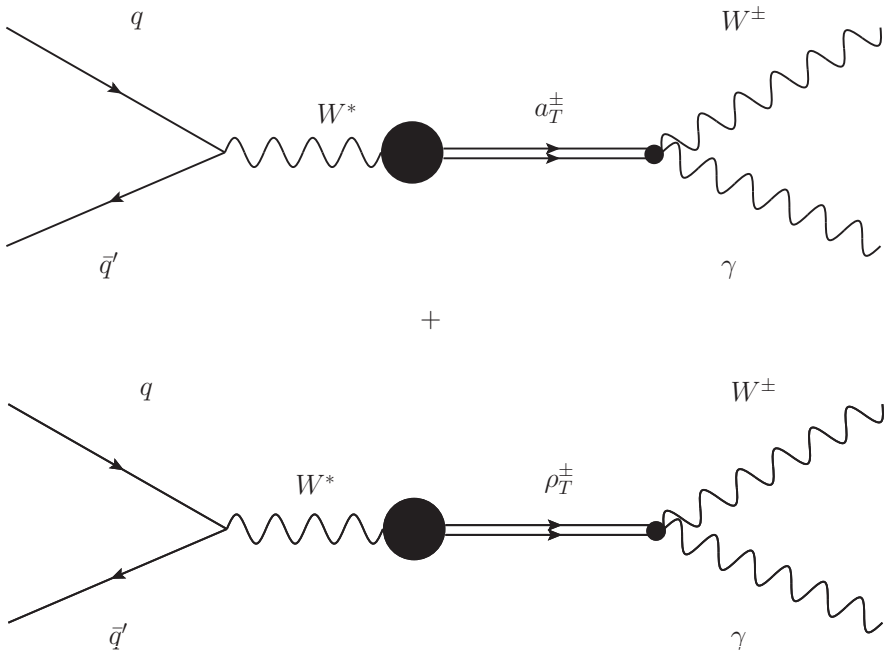

Figure 1.9: Feynman Diagram of the LSTC process giving $W\gamma$ as a final state.

Figure 1.10 gives the cross section of different SM processes as a function of the colliding energy of two protons. On this plot one can see that the production cross section of multi-jets processes at high energy is much larger than the EW processes. For this reason the final states we will look at will be only the one with leptonic decays of the Z and the W.

The following default values of the LSTC parameters were used for the current study:

- The number of techniquark doublets is set to $N_D = 9$. This leads to $F_{\pi_T} \approx 82$ GeV.
- The difference between the techniquark charges is taken to be $Q_U - Q_D = 1$.
- The mixing angle between the techniquarks is taken to be $\sin\chi = 0.333$.
- The ratio of technipion couplings is taken to be $\frac{g_{a_T\pi_T\pi_T}}{g_{\omega_T\pi_T\pi_T}} = 1$.
- The gauge group used is $SU(4)$.

The values of the masses of the resonances are not predicted by the model and are therefore free parameters. By analogy with QCD, it is expected that the ρ_T and ω_T are almost degenerate, with a somewhat higher value for the mass of the a_T. In this study we take the ρ_T and ω_T masses to be exactly equal, and assign a 10% higher value to the mass of the a_T.

The range of interest for these parameters is bounded below by current experimental constraints. As described in Section 1.4.2, this lower bound is $M_{\rho_T} \sim 200$ GeV. The upper bound for the mass scale should be in the order of a few hundred GeV, in order for the theory to naturally describe electroweak symmetry breaking.

1.4 Experimental constraints

All the theoretical results shown in the three previous sections rely on the measurements made over the past century. In this final section a summary of the experimental constraints will be made.

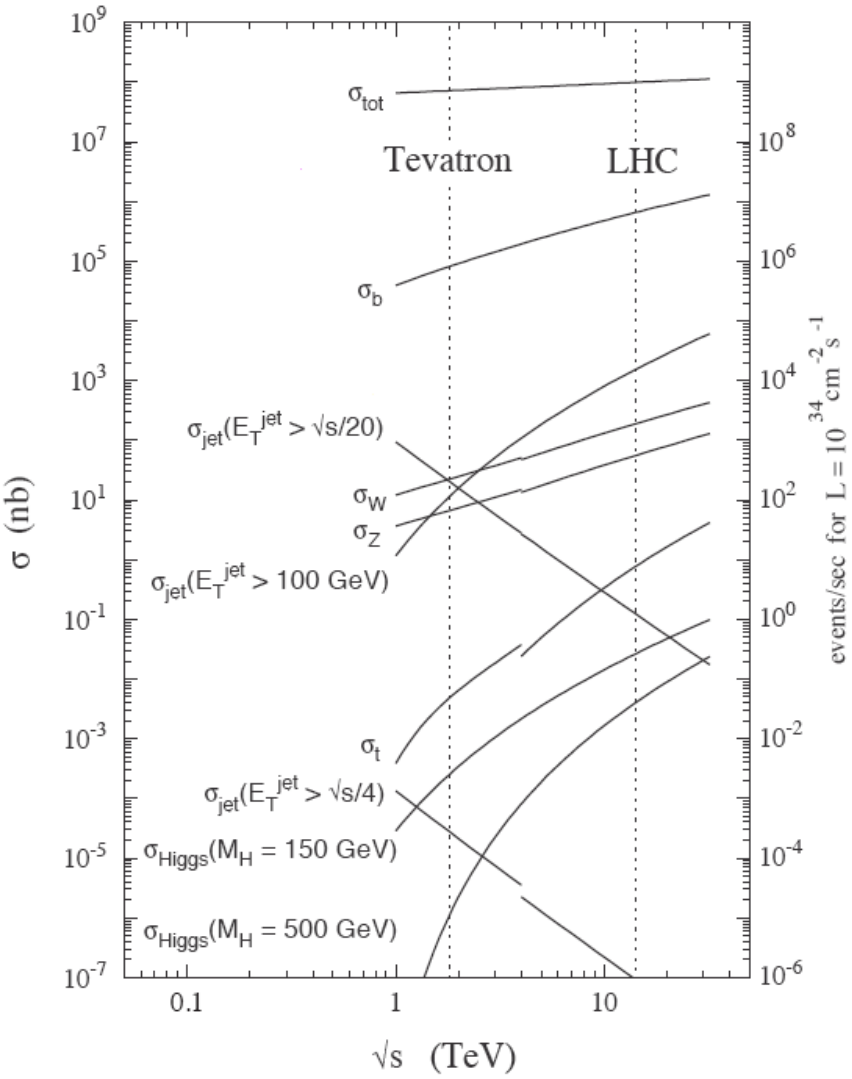

Figure 1.10: Cross-Sections of different SM processes has a function of the $\sqrt{S}$ for a pp collision [43].

1.4.1 Standard Model

Table 1.3 gives a summary of the different SM parameter values, as fitted from experimental measurements by the GFitter collaboration [44, 45]. Many parameters are known to better than to 0.1%, leading to stringent constraints on new models beyond the SM. This table also summarizes the results of two fits done to constrained the Higgs boson mass. Two different approaches have been used. In the first one, all the data available are used (quoted as complete fit). In another approach only the data excluding the direct searches of the Higgs are shown (quoted as standard fit).

Parameter	Input value	Free in fit	Results from global EW fits: *Standard fit*	*Complete fit*	*Complete fit w/o exp. input in line*
M_Z [GeV]	91.1875 ± 0.0021	yes	91.1874 ± 0.0021	91.1877 ± 0.0021	$91.1942^{+0.0168}_{-0.0114}$
Γ_Z [GeV]	2.4952 ± 0.0023	–	2.4960 ± 0.0015	$2.4956^{+0.0015}_{-0.0014}$	$2.4952^{+0.0014}_{-0.0016}$
$\sigma^0_{\rm had}$ [nb]	41.540 ± 0.037	–	41.478 ± 0.014	41.478 ± 0.014	41.469 ± 0.015
R^0_ℓ	20.767 ± 0.025	–	20.742 ± 0.018	$20.741^{+0.018}_{-0.017}$	20.718 ± 0.026
$A^{0,\ell}_{\rm FB}$	0.0171 ± 0.0010	–	0.01641 ± 0.0002	$0.01625^{+0.0002}_{-0.0001}$	$0.01624^{+0.0002}_{-0.0001}$
A_ℓ $^{(\star)}$	0.1499 ± 0.0018	–	0.1479 ± 0.0010	$0.1472^{+0.0010}_{-0.0006}$	–
A_c	0.670 ± 0.027	–	$0.6683^{+0.00044}_{-0.00043}$	$0.6680^{+0.00042}_{-0.00027}$	$0.6679^{+0.00039}_{-0.00022}$
A_b	0.923 ± 0.020	–	0.93469 ± 0.00009	$0.93464^{+0.00007}_{-0.00005}$	$0.93462^{+0.00008}_{-0.00004}$
$A^{0,c}_{\rm FB}$	0.0707 ± 0.0035	–	0.0741 ± 0.0005	$0.0738^{+0.0005}_{-0.0003}$	0.0739 ± 0.0004
$A^{0,b}_{\rm FB}$	0.0992 ± 0.0016	–	0.1037 ± 0.0007	$0.1032^{+0.0007}_{-0.0004}$	$0.1036^{+0.0005}_{-0.0004}$
R^0_c	0.1721 ± 0.0030	–	0.17225 ± 0.00006	0.17225 ± 0.00006	0.17225 ± 0.00006
R^0_b	0.21629 ± 0.00066	–	$0.21578^{+0.00005}_{-0.00008}$	$0.21576^{+0.00007}_{-0.00008}$	$0.21577^{+0.00005}_{-0.00008}$
$\sin^2\theta^\ell_{\rm eff}(Q_{\rm FB})$	0.2324 ± 0.0012	–	0.23141 ± 0.00012	$0.23150^{+0.00007}_{-0.00013}$	$0.23149^{+0.00008}_{-0.00011}$
M_H [GeV] $^{(\circ)}$	Likelihood ratios	yes	$95.7^{+30.6[+75.8]}_{-24.2[-43.7]}$	$120.6^{+17.9[+34.7]}_{-5.2[-6.2]}$	$95.7^{+30.6[+75.8]}_{-24.2[-43.7]}$
M_W [GeV]	80.399 ± 0.023	–	$80.382^{+0.014}_{-0.015}$	$80.370^{+0.005}_{-0.009}$	$80.360^{+0.016}_{-0.024}$
Γ_W [GeV]	2.085 ± 0.042	–	2.092 ± 0.001	2.092 ± 0.001	2.092 ± 0.001
$\overline{m}_c$ [GeV]	$1.27^{+0.07}_{-0.11}$	yes	$1.27^{+0.07}_{-0.11}$	$1.27^{+0.07}_{-0.11}$	–
$\overline{m}_b$ [GeV]	$4.20^{+0.17}_{-0.07}$	yes	$4.20^{+0.16}_{-0.07}$	$4.20^{+0.16}_{-0.07}$	–
m_t [GeV]	173.3 ± 1.1	yes	173.4 ± 1.1	173.7 ± 1.0	$177.4^{+11.8}_{-3.5}$
$\Delta\alpha^{(5)}_{\rm had}(M^2_Z)$ $^{(\dagger\triangle)}$	2749 ± 10	yes	2750 ± 10	2748 ± 10	2729^{+39}_{-55}
$\alpha_s(M^2_Z)$	–	yes	$0.1192^{+0.0028}_{-0.0027}$	$0.1193^{+0.0028}_{-0.0027}$	$0.1193^{+0.0028}_{-0.0027}$
$\delta_{\rm th}M_W$ [MeV]	$[-4,4]_{\rm theo}$	yes	4	4	–
$\delta_{\rm th}\sin^2\theta^\ell_{\rm eff}$ $^{(\dagger)}$	$[-4.7,4.7]_{\rm theo}$	yes	4.7	4.7	–
$\delta_{\rm th}\rho^f_Z$ $^{(\dagger)}$	$[-2,2]_{\rm theo}$	yes	2	2	–
$\delta_{\rm th}\kappa^f_Z$ $^{(\dagger)}$	$[-2,2]_{\rm theo}$	yes	2	2	–

$^{(\star)}$Average of LEP ($A_\ell = 0.1465 \pm 0.0033$) and SLD ($A_\ell = 0.1513 \pm 0.0021$) measurements. The *complete fit* w/o the LEP (SLD) measurement gives $A_\ell = 0.1475 \pm 0.0008$ ($A_\ell = 0.1468^{+0.0008}_{-0.0007}$). $^{(\circ)}$In brackets the 2σ. $^{(\dagger)}$In units of 10^{-5}. $^{(\triangle)}$Rescaled due to α_s dependency.

Table 1.3: Standard Model parameter values from the GFitter collaboration [44]. Two independent fits are conducted, one including the direct searches of the Higgs bosons from Tevatron and LEP, quoted as complete fit, the other one excludes these data and is quoted as standard fit.

Figure 1.11 (a) gives the $\Delta\chi^2$ of the SM fit including all the data versus the mass of the SM Higgs Bosons. Figure 1.11 (b) gives the allowed contour from SM fit of the mass of the top quark versus the mass of the SM Higgs Boson. From these two plots, there is a clear hint, that a SM Higgs boson ,if it exists, should have a small mass value, typically from 115 GeV to 150 GeV. Higher masses can not be excluded, but their value would fit less naturally the current data.

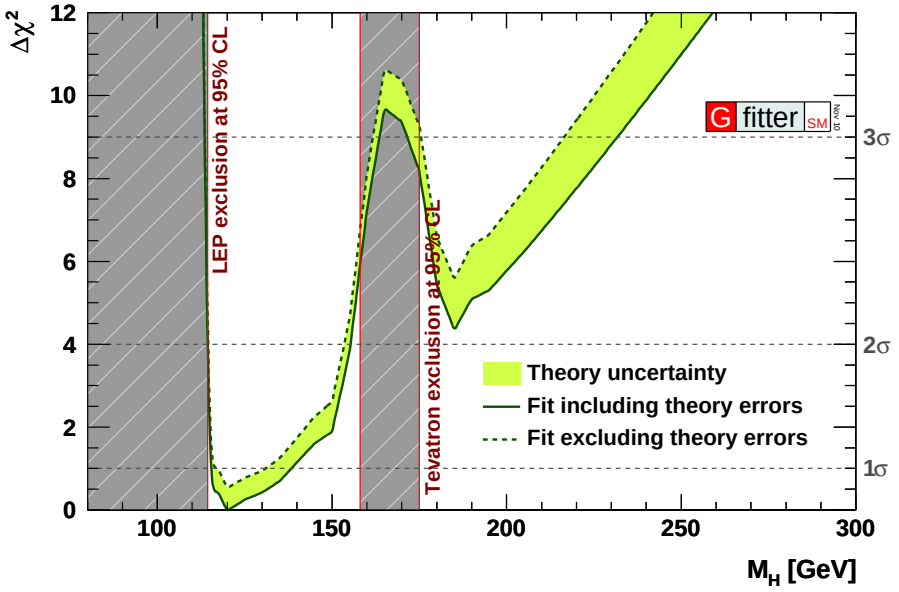

(a) $\Delta\chi^2$ of the SM fit including all data with respect to mass of a SM Higgs.

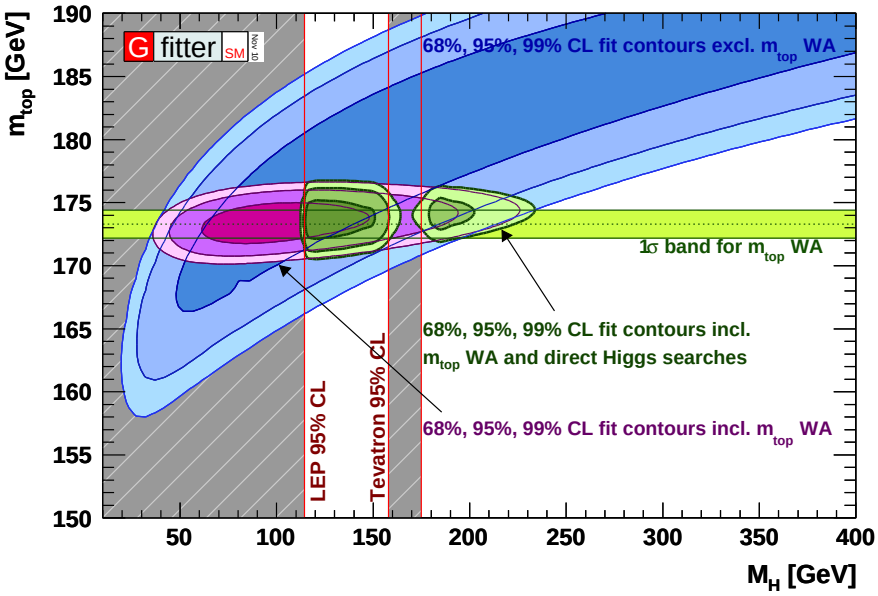

(b) Contours of 68%, 95% and 99% CL obtained from scans of fits with fixed variable pairs m_t vs. M_H . The largest/blue (narrower/purple) allowed regions are the results of the standard fit excluding (including) the measurements of mt. The narrowest/green areas indicate the constraints obtained for the complete fit including all the available data. The horizontal bands indicate the 1σ regions of the current world average of m_t measurements.

Figure 1.11: SM fits from the GFitter Collaboration [44].

1.4.2 Technicolor

The latest limits on LSTC models have been set at the LHC. The ATLAS collaboration studied the production of techniparticles decaying into a lepton pair [46]. Earlier results from Tevatron in different final states also exists, the D$\emptyset$ collaboration studied the production of techniparticles decaying into a WZ pair [47]. The CDF collaboration studied the production of a Wboson in association with a π_{T} [48]. Exclusion results in the plane of ρ_{T} vs. π_{T} masses are shown in Fig. 1.12.

It can also be noticed that recent work from the CDF collaboration [49, 50] leads to an unexplained excess of the di-jet mass spectra at $\approx 3\sigma$ in the $W + jj$ final states. Some studies [51] interpret it as the result of the decay of a ρ_{T} of mass $M_{\rho_{\mathsf{T}}} \approx 290$ GeV decaying into a W and a π_{T} of mass $M_{\pi_{\mathsf{T}}} \approx 160$ GeV. But for now this results have been invalidated by the D$\emptyset$ collaboration [52], and not been seen at the LHC [53, 46]. This point will be tested as a benchmark point in the study presented in the last chapter.

The sensitivity to discover technicolor processes at the LHC was studied at 14 TeV [38, 42] and 10 TeV [39] using a generic detector parameterization and the PYTHIA LSTC models. For the di-leptons final state at 14 TeV, the LSTC models can be discovered up to 1 TeV with less than 5 fb^{-1} of data. For the di-bosons final states at 14 TeV, the $W\gamma$ final state is reachable up to 500 GeV, with less than 10 fb^{-1} of data. As it is described on Chapter 2 and thanks to the very good performances of the LHC, the technimesons could be observed or excluded in these range by the end of 2012.

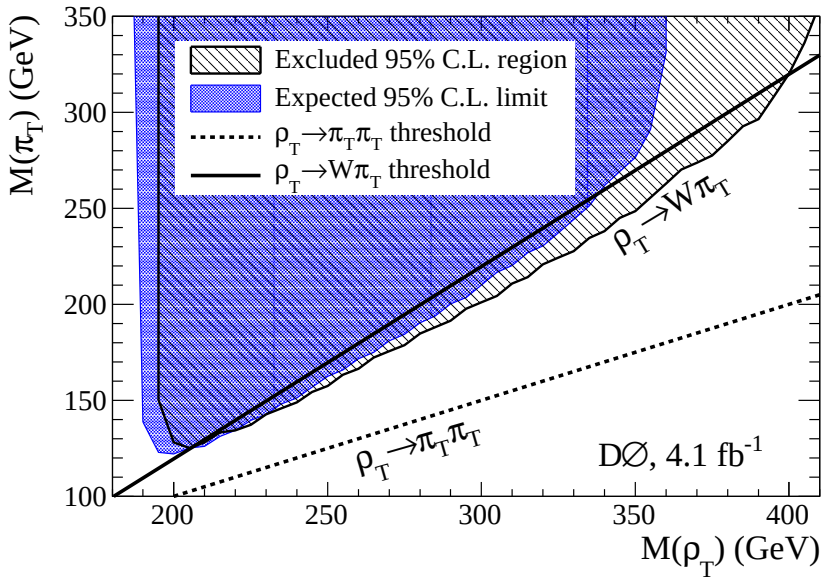

(a) Exclusion in $WZ \to lll\nu$ channel from the DØ collaboration.

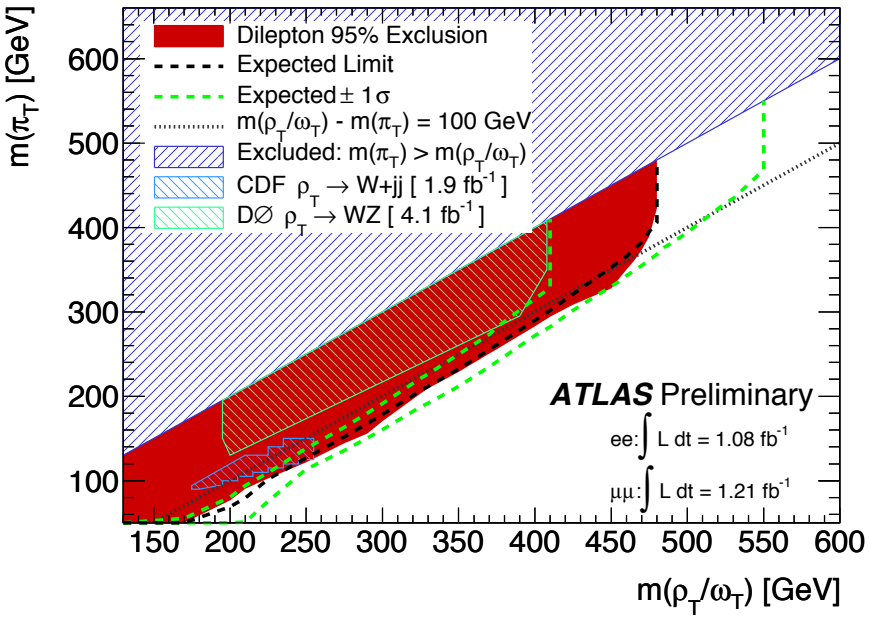

(b) Exclusion in $\rho_T \to ll$ from the ATLAS collaboration, are also quoted the previous exclusion limits from CDF and DØ collaborations in the $W\pi_T \to bql\nu$ channel.

Figure 1.12: Current limits on LSTC from TeVatron data. (a) 95% exclusion region in the plane of ρ_T vs. π_T masses from the DØ collaboration, using 4.1 fb^{-1} of data [48]. (b) 95% exclusion region in the plane of ρ_T vs. π_T masses from the ATLAS collaboration, using 1.08 fb^{-1} and 1.21 fb^{-1} of data. Earlier results from the CDF and DØ collaborations are also displayed [46].

Chapter 2

The Large Hadron Collider and the ATLAS experiment

"Nous allons dans un autre univers."
Voltaire, *Candide ou l'Optimisme*.

Introduction

In the first chapter the theoretical concepts of particle physics were introduced. In this chapter the experimental setup in which this thesis takes place will be presented. In particular in the first section, the CERN accelerator complex and the Large Hadron Collider (LHC) will be described. The second section of this chapter will be dedicated to the presentation of the ATLAS experiment.

2.1 The CERN accelerator complex

2.1.1 Why accelerating and colliding particles?

In order to make a transition from the theoretical concepts of particle physics to the experimental situation, let summarizes why particles are collided, and how it is possible to detect new physics phenomena.

Particle physics is also called High Energy Physics (HEP) because of the Einstein equation:

$$E = \gamma M c^2 \tag{2.1}$$

This equation means that it is possible to create a massive particle if enough energy is brought to create it. As written in Chapter 1, the new phenomena particle physicists are interested to discover nowadays, generally predict the production of particles weighing from one hundred GeV to a few TeV. It means that one has to create an energy source at this scale of energy in order to be able to see these new physical states.

The easiest solution to reach it is obtained by colliding two particles: proton, anti-proton, electrons or positrons, in the center of a detector that will detect the decay products of these collisions.

A schematic summary of the procedure conducted in order to discover a new phenomena in HEP could be:

- Create and accelerate particles at the interesting energy scale.
- Collide these particles in the center of a full coverage detector.
- Analyze the decay products of these collisions.
- Eventually discover new phenomena.

2.1.2 Some history

The CERN accelerators complex is presented in figure 2.1. Its construction started at the creation of CERN in 1954 [54].

The first high energetic accelerator was the Proton Synchrotron (PS), which was built in 1959 to accelerate proton up to 25 GeV.

The second large accelerator was the Super Proton Synchrotron (SPS) which was build in 1971. It was an accelerator designed for a fixed target experiment. The SPS was converted in a collider, at 540 GeV Center of Mass (CM) energy, the $Sp\bar{p}S$[1] in 1981 and housed the UA1 and UA2 experiments that discovered the W and Z bosons in 1983.

In 1981 it was decided to dig a 27 km long circular tunnel to house a new accelerator: the Large Electron Positron collider or (LEP). This accelerator was different from the SPS and the PS, because it was accelerating electrons and positrons and not anymore hadrons. The reason for this choice is due to the nature of the colliding particles. As we saw in section 1.1.2, electrons are leptons and thus are fundamental particles, while protons are hadrons and so are a composite assemblage of quarks and gluons. When hadrons are collided, only two object inside each of it will interact, *ie* two gluons, two quarks, or one quark and a gluon. This means that all the non interacting constituents of the hadrons

[1] Or Super Proton Anti-proton Synchrotron.

will be spectators during the reaction and most of it will be measured in the detector. Moreover as each constituent of the protons has an intrinsic momenta, the energy of the collision will not be known. *A priori* the major points of working with leptons and especially electrons are that the colliding energy is fully known, and the events are much cleaner. LEP was colliding electrons and positron up to a CM energy of 246 GeV.

In 1989 the first beams where circulating in LEP, allowing the precise measurement of the electroweak model by the creation of thousand Z events [55] in the four LEP experiments: ALEPH, DELPHI, L3 and OPAL. The PS and SPS were converted into electron accelerator at this time to be part of the LEP accelerating chain.

The construction of the Large Hadron Collider, or LHC, was decided in 1994. It started in 2001 with the beginning of the LEP decommissioning. The first beams were circulating the 10 September 2008 [56] at 450 GeV. The 21 September 2008 [57] an incident occurred because of a faulty interconnection between two superconducting magnets, damaging the beam pipe. The LHC was finally repaired in 2009, and the beams restarted in November. The first colliding beams at high energy took place short after in 2009 at 2.26 TeV. By the end of the year 2010 [58], 50 pb^{-1} of data at 7 TeV, were recorded by the ALICE, ATLAS, CMS and LHCb experiments. There was also a short heavy ion run at the end of 2010. The 2011 run has allowed to record more than 5 fb^{-1} of data at 7 TeV for the ATLAS and CMS experiments, followed by a short heavy ion run. In 2012, the running conditions should be similar and will allow to collect up to 15 fb^{-1} of data. In 2013, their will be a long shutdown that will allow to reach the nominal LHC Center of Mass Energy of 14 TeV.

2.1.3 The Large Hadron Collider

Why a proton proton collider?

Their are three main reason that leads to the construction of a proton proton collider.

- In a circular collider the particles lose energy due to the Synchrotron effect according to the following formula:

$$\Delta E \propto \frac{E^4}{m^4 R} \tag{2.2}$$

  The energy loses is proportional to the fourth power of the particle energy, inversely proportional to its mass and to the radius of the collider. For instance a 104.6 GeV electron at LEP was loosing 3.5 GeV of energy every time a full lap of the collider was done, whereas at the LHC a 7 TeV proton will lose only 7 keV per cycle. For this reason it was not possible to upgrade LEP to reach higher order of energy.

- The mass of the particle searched at the LHC are not precisely known. Therefore, the accelerator needs to be able to scan a wide energetic range of 100 GeV up to a few TeV, to discover new phenomena.

- The reasons why antiproton are not used like in $S\bar{p}pS$ or TeVatron is due to the luminosity required by the LHC. The anti-protons are created *via* a fixed target experiment, whereas the protons are ionized hydrogen atoms. The antiproton creation process strictly limits the luminosity. Another reason is due to the Parton Distribution Function (PDF). At a 7 TeV or 14 TeV CM energy, the gluon PDF becomes dominant with respect to that of the quarks. Thus at these energies most of the interesting phenomena happens because of gluons fusion processes. For this reason colliding pp or $p\bar{p}$, does not make any differences and as the creation of anti proton limits stringently the luminosity, it is a more convenient choice to collides protons.

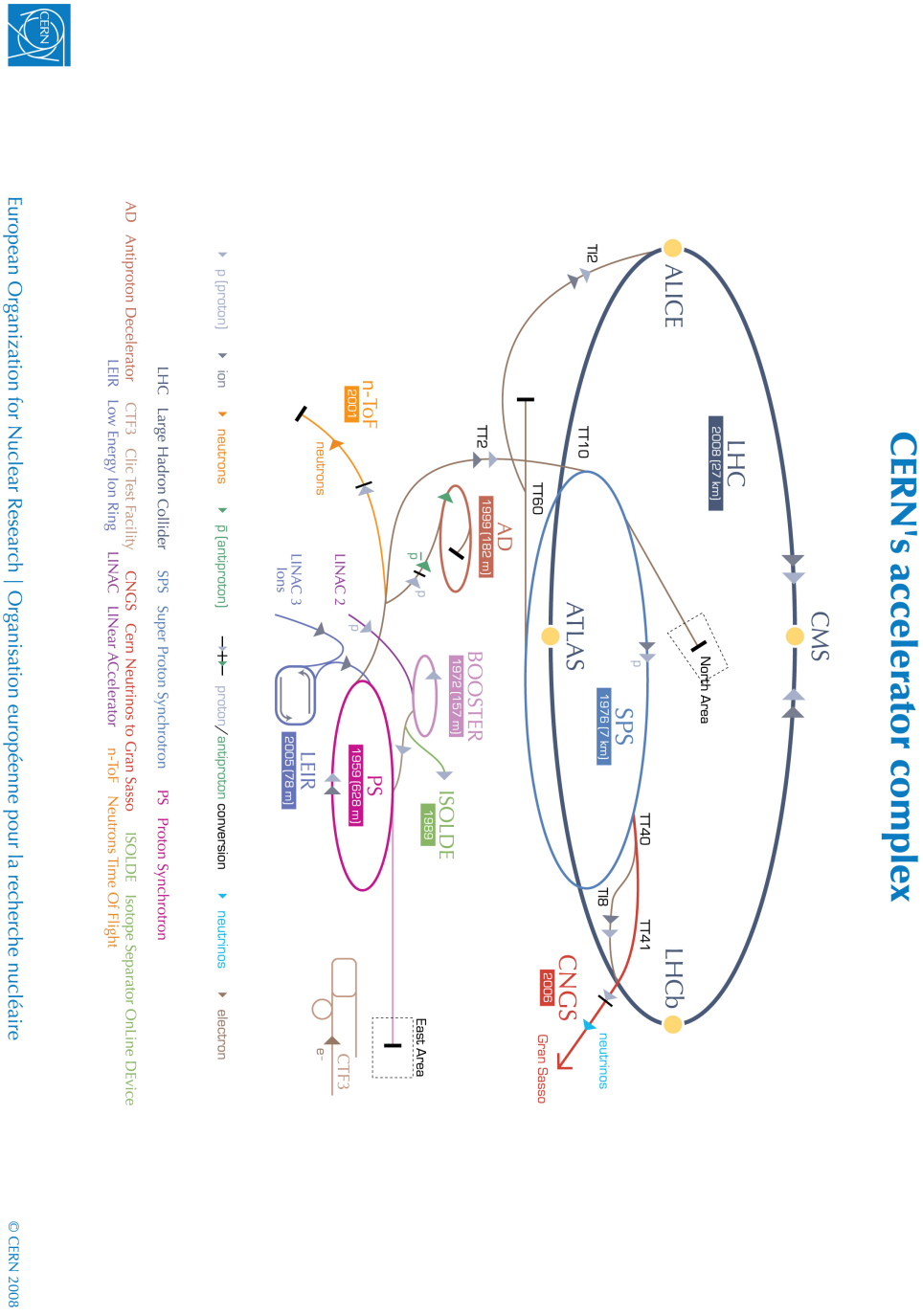

Figure 2.1: The CERN accelerator complex, CERN©.

Accelerator

The LHC [59] is a 27 km long proton proton collider[2], located between France and Switzerland 100 m underground in the place of LEP. LEP was accelerating electrons and positrons, so it was possible to accelerate both particles in the same beam pipe using a common magnetic field.

The situation for the LHC is different because it is accelerating protons. The two beams have to be separated in two beam pipes, each of it having it's own magnetic field. Due to the space constraint in the tunnel, it was decided to use a design of magnet called twin-bore, where both beam pipes are in a single dipole structure.

Figure 2.2 shows the sectional view of one of the 1232 dipoles installed all around the ring. These magnets are composed of a combination of Niobium and Titane (NbTi) and are operated in a superconducting state at a temperature of $\approx 1.9°K$ using super-fluid helium. The dipole magnets are used to maintain each beam in an orbit along the ring. To maintain a proton accelerated to 7 TeV (or 3.5 TeV) in a rotating orbit, the magnetic field required has to be 8.3 Tesla (or 4.2 Tesla) , field which is obtained by running an electrical current in the NbTi wire. Superconducting magnets are used to minimize the current loss by Joule Effect. The acceleration process is achieved using Radio Frequency (RF) cavities. Once beams are accelerated to the desired energy they are collided in the four Interaction Points (IP). In order to collide the beams, quadrupole and triplet magnets are used to focus them at the IP.

The nominal energy of the LHC beams is 7 TeV, giving a total CM energy of 14 TeV. It is now operated in a reduced mode at 3.5 TeV per beam. Given these energies the LHC is the most powerful collider constructed. Before the LHC went into operation the most powerful accelerator was the TeVatron[3] which was operating a proton anti proton collider at a CM energy of 1.96 TeV.

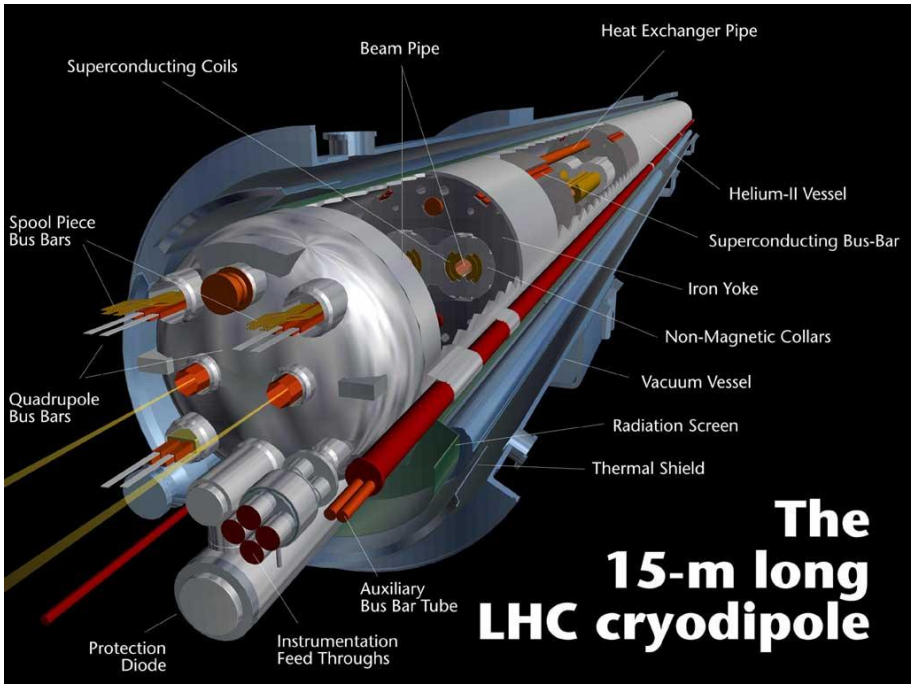

Figure 2.2: Sectional view of one LHC dipole, CERN©.

[2]The LHC is also operated as a Lead Lead collider for a period of one month a year. The energy of each beam is ≈ 5.5 TeV in that case.

[3]The TeVatron worked until the 30 September 2011.

Accelerator chain

The LHC accelerator chain [58, 59] is shown in figure 2.1. The proton are accelerated up to 3.5 TeV this way:

- The hydrogen atoms are ionized and accelerated to 450 GeV up to the SPS. In the SPS, they are gathered in group called bunches.
- Each bunch is injected to the LHC. When the filling of the bunches is finished, they are squeezed by the RF cavities and accelerated up to 3.5 TeV.

Experiments

Their are six experiments installed around the LHC [60]. The experiment position are shown in Figure 2.3. Their list classified by their position on the ring is:

- ATLAS: A Toroidal LHC Apparatus. Located in IP 1. Experiment conceived for the discovery of the Higgs boson, new physics and the precision measurement of the Standard Model.
- LHCf: Large Hadron Collider Forward. Located in IP 1, near the ATLAS experiment. It is dedicated to the study of very forward events.
- ALICE: A Large Ion Collider Experiment. Located in IP 2. Experiment dedicated to the study of heavy ion collisions, and the quark gluon plasma.
- CMS: Compact Muon Solenoid. Located in IP 5. Experiment conceived for the discovery of the Higgs boson, new physics and the precision measurement of the Standard Model.
- TOTEM: TOTal Elastic and diffractive cross section Measurement. Located in IP 5 near CMS. Experiment dedicated to the measurement of the proton proton cross section.
- LHCb: Large Hadron Collider Beauty. Located in IP 8. Experiment dedicated to the study of the B mesons.

2.1.4 LHC operation

Luminosity

The number of events produced each second is given by [59]:

$$N_{\text{process}} = L\sigma_{\text{process}} \tag{2.3}$$

Where L is the luminosity of the machine. The SI units dimension of luminosity is $[L] = [cm]^{-2}[s]^{-1}$. And σ is the cross section of the process. The dimension in SI unit is $[\sigma] = [cm]^2$. The cross section is proportional to an area of interaction between two particles. Proton proton collisions deals with processes of very low cross sections, *cf* Figure 1.10, typically below barn $\approx 10^{-24} cm^2$.

The luminosity of an accelerator which have Gaussian[4] beams is given by:

$$L = f\frac{n_1 n_2}{4\pi\sigma_x\sigma_y} \tag{2.4}$$

Where:

- f is the colliding frequency.
- n_i the number of colliding particles in beam i.

[4]The LHC beams are Gaussian with a width $\sigma_x \approx \sigma_y \approx 16\mu m$ and $\sigma_z \approx 5.6cm$.

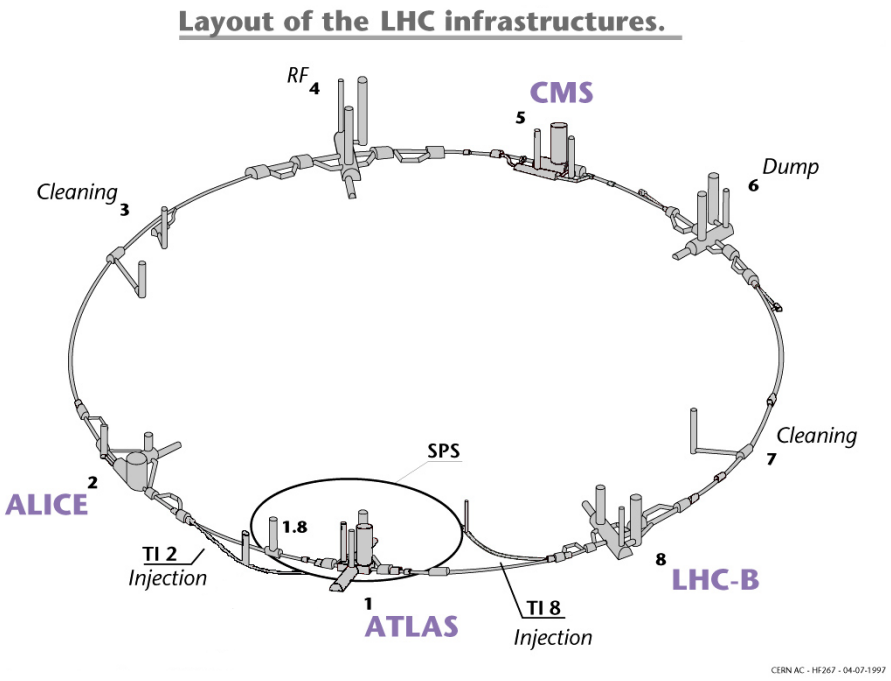

Figure 2.3: Schematic view of the underground LHC complex. The access point and the experiments are visible. CERN©.

- σ_i characterize the Gaussian transverse beam profiles in the horizontal and vertical directions.

Another parameter is introduced, the integrated luminosity over time:

$$L_{\text{int}} = \int L dt \tag{2.5}$$

Equation 2.3 show that if a phenomena has a low cross section, the luminosity required to get a few events needs to be high. The production cross sections of the interesting processes looked at by experiments such as ATLAS and CMS are very low. For example if one looks at Figure 1.10, the production cross sections of the W and Z bosons at a CM energy of 7 TeV, is respectively [61] $\sigma_{\text{prod}}(W) = 10200$ pb and $\sigma_{\text{prod}}(Z) = 970$ pb. The production cross section of the SM Higgs in two photons is expected to be approximately 10 fb.

The nominal instantaneous luminosity[5] given by the LHC to the ATLAS and CMS experiments is $L = 10^{34} cm^{-2} s^{-1}$ leading to an integrated luminosity ≈ 100 fb^{-1} per year.

LHC parameters

For the design luminosity of $L = 10^{34} cm^{-2} s^{-1}$, a bunch charge of 1.1×10^{11} protons and 2808 bunches, the average number of interactions per crossing was estimated to be of the order of 20. The superposition of these interactions to the triggered one, is what is called pile-up. With the current LHC parameters (see Table 2.1) with in particular only about 1400 bunches, a bunch charge of up to 1.3×10^{11} protons, LHC has reached a luminosity of $L = 3.3 \times 10^{33} cm^{-2} s^{-1}$ with the average number of pile-up events is typically 14 with a maximum of 20. To get an idea of the pile-up impact, Figure 2.4 shows an event Display of a $Z \rightarrow ee$ event recorded in 2011, where twenty interactions vertices were reconstructed.

As a comparison the TeVatron [63] reached its instantaneous luminosity peak at $L = 4. \times 10^{32} cm^{-2} s^{-1}$, while the entire RUN II which began in 2001 and stopped in September 2011 have provided about 12 fb^{-1} of data to the CDF and DØ experiments.

[5]For comparison the nominal instantaneous luminosity expected in the LHCb and the ALICE experiments are respectively $L = 10^{32} cm^{-2} s^{-1}$ and $L = 10^{27} cm^{-2} s^{-1}$.

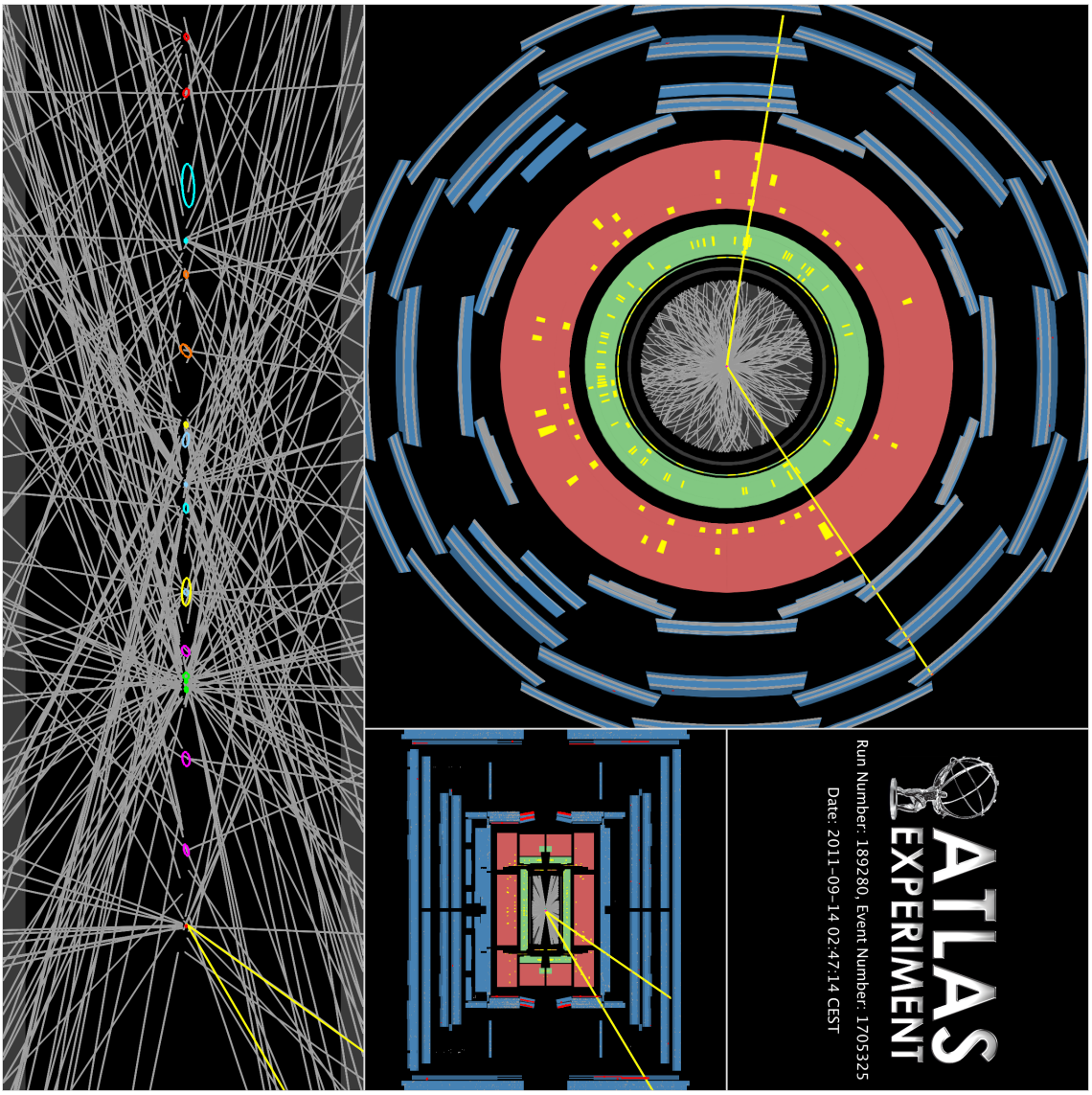

Figure 2.4: Event Display of $Z \rightarrow ee$ event recorded in 2011 by the ATLAS detector. Twenty interactions vertices were reconstructed [62].

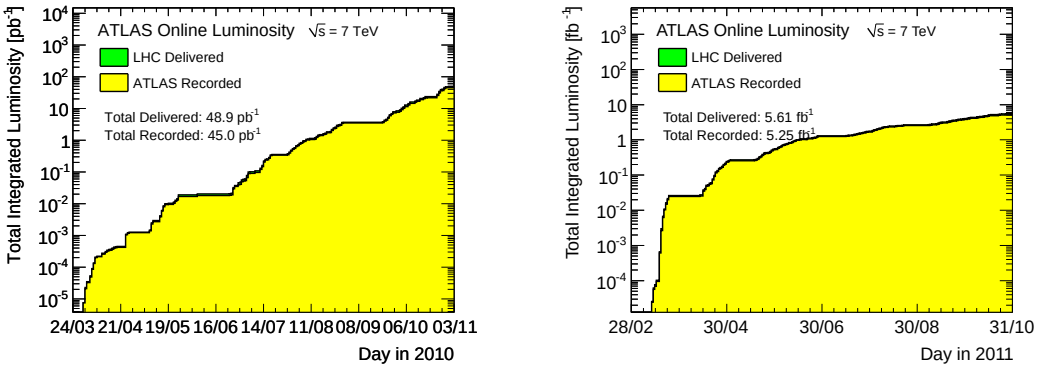

(a) 2010 run.

(b) 2011 run.

Figure 2.5: Total integrated luminosity recorded by the ATLAS experiment in 2010, and up to October 2011 [62].

Table 2.1 recapitulates the LHC run parameters for the nominal running conditions [58, 59, 64] that should takes place in 2014, for 2010 and 2011-2012 runs. Figure 2.5 (a) and (b) show the total integrated luminosity recorded by the ATLAS experiment in 2010 and 2011.

Parameter	2010 run	2011-2012 run	Nominal run
CM Energy	7 TeV	7 TeV	14 TeV
Number of bunches	368	1400	2808
colliding bunches in ATLAS	233	1331	2808
Number of p per bunch	1.1×10^{11}	1.3×10^{11}	1.1×10^{11}
Bunch spacing	150 ns	50 ns	25 ns
Peak Luminosity	$2.07 \times 10^{32}\text{cm}^{-2}\text{s}^{-1}$	$3.65 \times 10^{33}\text{cm}^{-2}\text{s}^{-1}$	$10^{34}\text{cm}^{-2}\text{s}^{-1}$
Integrated lumi per year	50 pb^{-1}	5.6 fb^{-1}	100 fb^{-1}
Number of pileup events	3	17	20

Table 2.1: LHC running conditions for nominal, 2010 and 2011 runs.

2.2 ATLAS

2.2.1 Experiment

Introduction

The ATLAS experiment [65, 66] is one of the six experiments located around the LHC ring. It is located in Switzerland. A cut view of the detector is presented in figure 2.6. The detector is installed in IP1 95m underground. It is 44m long, 22m high and weighs about 7000 tons.

Reference frame and convention

The reference frame of the ATLAS detector is showed in figure 2.7. The center of the detector is chosen to be the center of this reference frame, or the point (0,0,0), it also coincides with the interaction point. ATLAS is divided into two sides: the A side on the direction of Geneva and the C side in the direction of the Jura. The z axis is taken to be the beam axis, the positive direction of this axis is on the A side and the negative on the C side. The transverse plan (x,y) is defined such as y is the vertical axis, defined positive upward to the ground, and the x axis is defined positive when pointing to the center of the LHC ring.

In hadronic colliders the interesting physics processes relies on the transverse energy, because of the uncertainty of the collision energy. For the sake of convenience the transverse plan (x,y) is redefined using two variables: ϕ the azimuth angle, and the rapidity written y:

$$y = \frac{1}{2}\ln(\frac{E + p_z}{E - p_z}) \tag{2.6}$$

The rapidity is a measurement of the particle motion, relatively to the boost along the beam axis. For relativistic objects, the speed is not a Lorentz invariant, while the rapidity is.

In the case where the particle is mass-less, or its mass can be neglected with respect to its energy, the pseudo rapidity, η, can be used instead of the rapidity. It is define as:

$$\eta = -\ln\tan(\frac{\theta}{2}) \tag{2.7}$$

Where θ is the polar angle.

The momenta of a particle in the transverse plan is given by:

$$p_{\text{T}} = \sqrt{p_x^2 + p_y^2} \tag{2.8}$$

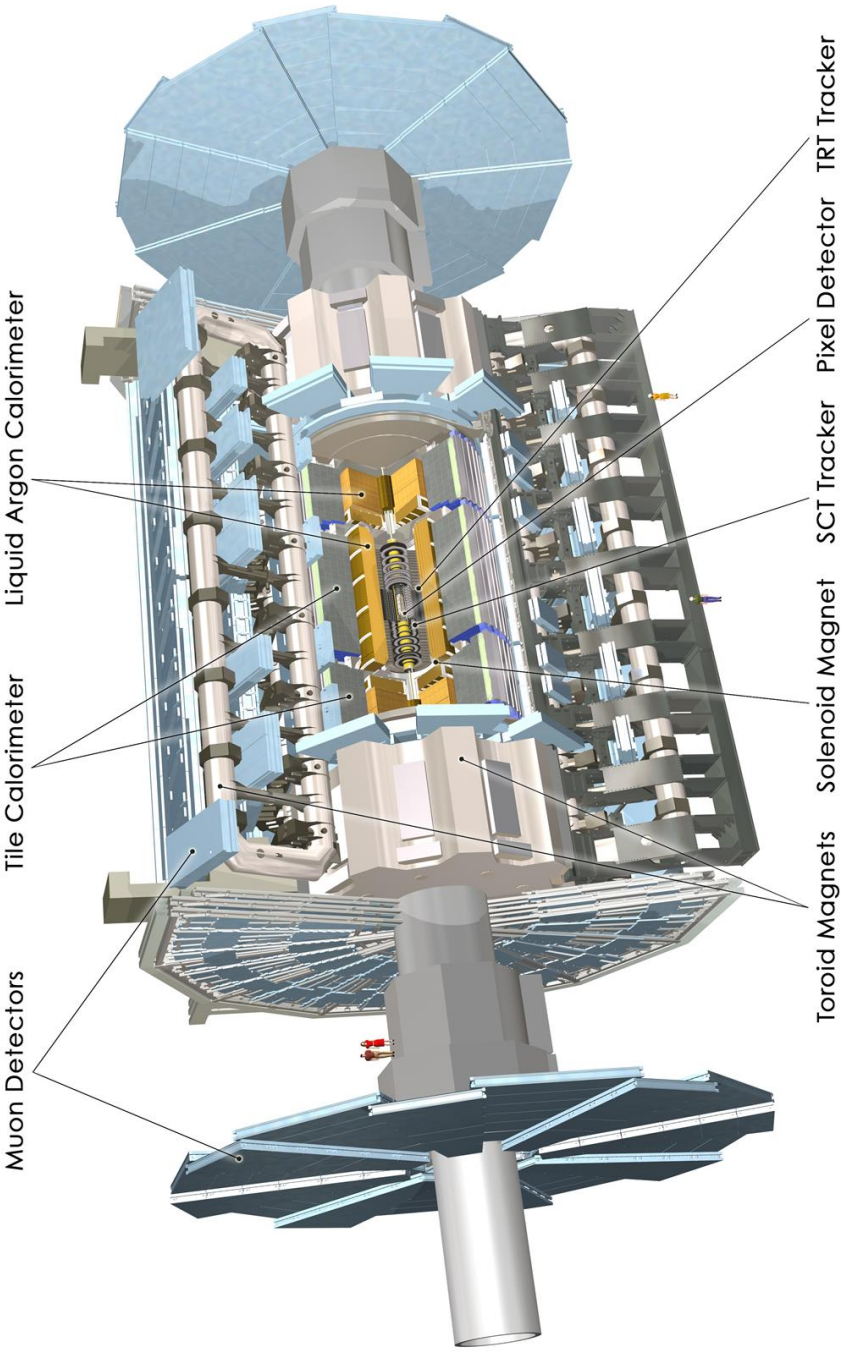

Figure 2.6: The ATLAS Experiment [66].

One defines the spatial distance of two objects in the detector as :

$$\Delta R = \sqrt{\Delta\eta^2 + \Delta\phi^2} \tag{2.9}$$

If a particle escapes from the detector without being detected, like a neutrino, their will be missing energy in the event. It is written $E_{\mathrm{T}}^{\mathrm{miss}}$. The missing transverse energy is defined as the inverse of the vectorial sum, in the transverse plan, of the particles present in the event. Two parameters characterize $E_{\mathrm{T}}^{\mathrm{miss}}$: its azimuth angle ϕ, and the module of the transverse vector.

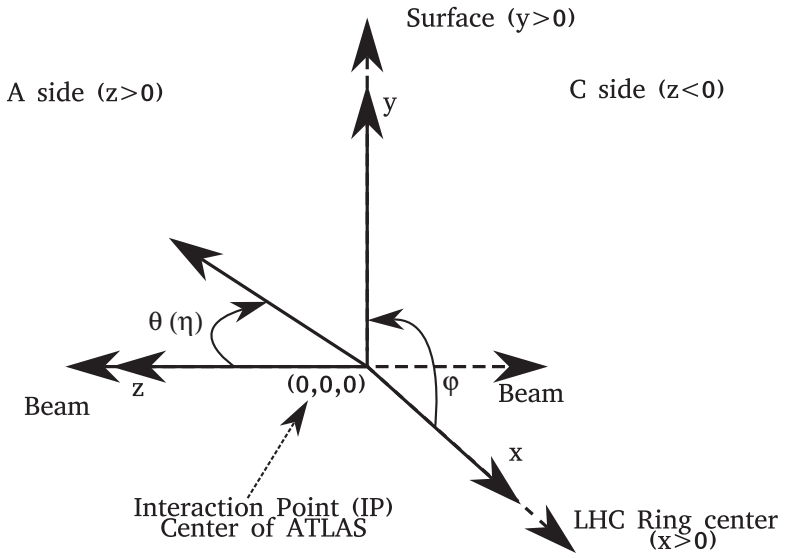

Figure 2.7: Reference coordinates frame used.

Sub detectors

In order to achieve a good granularity and due to the mechanical constraints, the ATLAS detector was build in three parts. A barrel region and two end cap regions that are made with wheels disposed on each side of the barrel closing hermetically the detector.

The ATLAS detector is composed of three main systems:

- The inner detector close to the beam pipe, provides particle tracking. In association with the solenoidal magnetic field, it can be used to provide, particle momenta reconstruction, particle identification, reconstruct the interaction vertex, *etc.*
- The calorimeters collects most of the energy of the electromagnetic particles and jets. They also provides a measurement of the missing transverse energy.
- The Muon Spectrometer combined with the toroidal magnetic field allows a precise measurement of muons momentum.

In hadron collider, selecting events is crucial due to the high collision rate, an high-performance trigger system has been designed to reduces the rate of events from 40 MHz to 200 Hz, in three stages Level1, Level2, and Event Filter. At the Level1, only the calorimeters and Muon Spectrometers are used to trigger the events. In the next steps, all the sub detectors are used.

In this section each of these sub systems will be presented in details.

2.2.2 Magnet system

Figure 2.8 shows an overview of the magnet system. It is composed of one superconductor solenoidal magnet, located in the center of ATLAS, to keep a constant magnetic field in the inner detector. And three superconductor toroidal magnets. One in the barrel region, and two smaller in each end-caps.

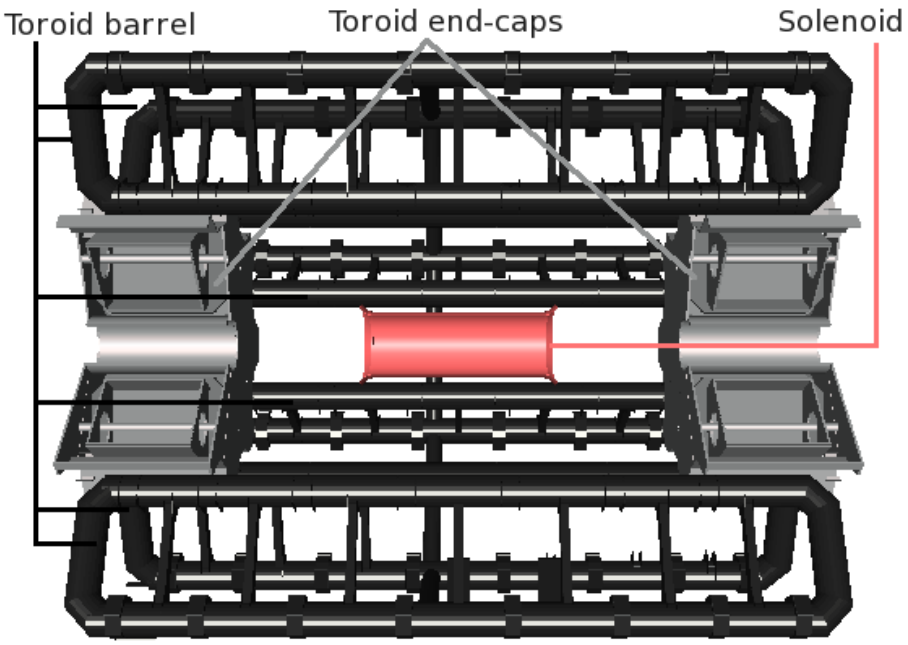

Figure 2.8: Atlas Magnet system. The solenoid magnet is present in the middle of the image. The toroidal magnet barrel are surrounding it. The toroidal end caps magnets are disposed on each side of the solenoid magnet.

Solenoid

In the central region, one superconductor solenoidal magnet provides a constant magnetic field of 2 Tesla which deflects charged particles in the transverse plane. The magnet is composed of a mixture of Al-Cu-NbTi, and is operated at a temperature $T = 4.5°K$, with a current $I = 7.730$ kA. It is 5.8 m long with a diameter of 2.46 m. The thickness of the solenoid is 40 cm. It was optimized in order to minimize the amount of inactive material in front of the calorimeter ($\approx 0.66\ X_O$). It shares the same vacuum vessel as the barrel Liquid Argon electromagnetic calorimeter.

Toroid

In the barrel, eight coils surround the calorimeters, providing a variable magnetic field from 0.15 to 2.5 T. The barrel toroid structure is 9.4 m high at its minimum, and 20.1 m high at its maximum. It is 25.3 m long. Each coils fits in a single vacuum vessel.

In the end caps two smaller toroidal magnets are installed. They provide a variable magnetic field from 0.2 to 3.5 Tesla. The eight coils share the same vacuum vessel, the inner diameter of this structure is 1.65 m, while the outer diameter is 10.7 m. It is 5 m long. The toroidal end cap magnets are displaced at the end of the barrel with a rotation of 22.5° with respect to to the toroid barrel magnet.

The twenty four coils of the toroid system are superconductor and made of a mixture of Al-Cu-NbTi. They are operated at a temperature $T = 4.5°K$, with a current $I = 20.5$ kA.

2.2.3 Inner detector

The Inner detector [67, 68] is the closest detector to the beam pipe. It acts as a tracking system for charged particles. This system is used to identify them, measure their momenta and their impact parameters, and reconstruct the interaction vertex position.

Figures 2.9 (a) and (b) show two sectional views of the Inner Detector. Its dimensions are 6.2 m long and a diameter of 2.1 m. The coverage in pseudo rapidity extend up to $|\eta| < 2.5$. The Inner Detector is divided into three sub detectors: the Pixels, the Semi-Conductor Tracker (SCT), and the Transition Radiation Tracker (TRT).

Pixels

The Pixels detector is the innermost sub-detector. The barrel part is made of three layers located at 50.5 mm, 88.5 mm and 122 mm. In figure 2.9 (b), these layers are visible in green. The first layer is also called b-layer[6]. In the end caps, the pixel detector is composed by three discs located at different |z| position along the beam axis: 49.5, 58 and 65 cm.

The pixel detector is made of 1744 pixel modules with a surface 19×63 mm^2. One pixel size is 50×400 μm^2, there are 46080 pixels per module. The fine granularity of this detector allow a very precise measurement of the position of each hit. The nominal space resolutions [69] for the barrel pixels are $\sigma_{R-\phi} = 10$ μm, $\sigma_z = 115$ μm, and for the end caps pixels are $\sigma_{R-\phi} = 10$ μm, $\sigma_R = 115$ μm.

Semi Conductor Tracker

The Semi Conductor Tracker (SCT) is drawn in blue in figure 2.9. The SCT modules are built from two pairs of single-sided silicon micro-strip sensors. Each module is 12.6 cm long, composed of 2 silicon wafer on each side. The modules are made of 768 silicon micro strips with a mean pitch of 80 μm. A total of 4088 SCT modules is used.

The barrel SCT system is made of four coaxial layers placed at radii of 299, 371, 443 and 514 mm. In the end caps, nine discs are placed on each side of the IP along the beam pipe.

Potentially eight measurement points in the central region and eighteen points in the end caps are expected for a high momentum charged particle. The nominal SCT modules spatial resolutions [69] are: $\sigma_{R-\phi} = 17$ μm, $\sigma_z = 580$ μm for the barrel, and $\sigma_{R-\phi} = 17$ μm, $\sigma_R = 580$ μm for the end caps.

Transition Radiation Tracker

The Transition Radiation Tracker (TRT) is sketched in brown in figure 2.9. It is constituted with drift straw of 4 mm diameter containing a gas mixture Xe-CO_2-O_2 and a tungsten wire of 30 μm. When a particle crosses the straw, the gas is ionized and the charged is collected by the wire, giving a space point in the transverse plan. The straw made of polyimide material are covered with a polyurethane material. When an electron or hadron crosses the polyimide-polyurethane straw interface, a transition radiation is recorded. This radiation allows a differentiation of the electron and hadrons.

The barrel TRT system is composed of three cylinders, 160 cm long, containing in total 53000 straw, each one being 144 cm long. The TRT end caps system is made of six independent wheels, containing 130000 straws, which are 37 cm long.

The TRT system only provides a measurement of ϕ in the barrel, but the system, collect about 36 points per tracks. The nominal space resolution [69] of the TRT is $\sigma_{R-\phi} = 130\mu$m.

Tracking Performances

The three sub-systems should give for the central region about forty points, three for the pixels, eight for the SCT and thirty six for the TRT. Using these points and the 2 T magnetic field, it is possible to reconstruct the particle trajectory, and to measure their momenta.

[6] Due to its position, the b-layer, allow a measurement of displaced vertex, and so to tag the electrons coming from the b-quarks decays.

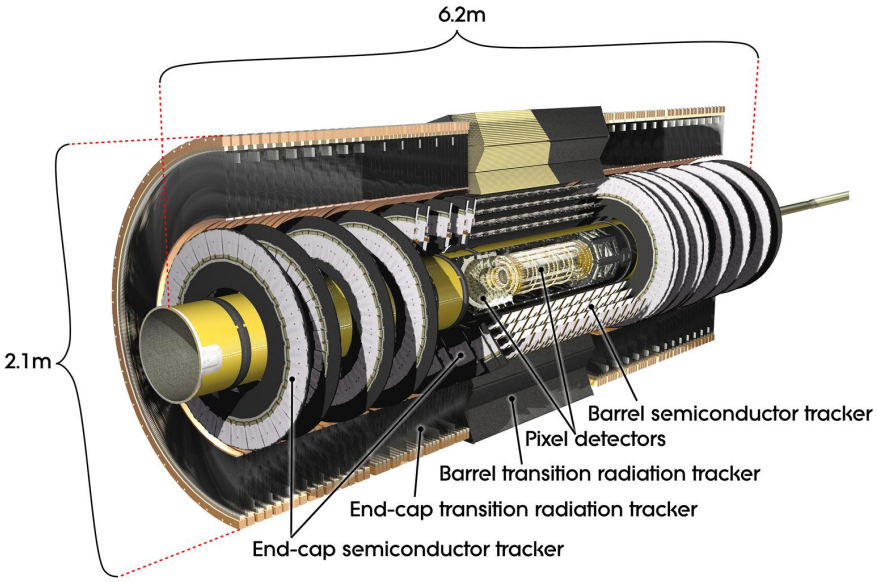

(a) The Atlas Inner Detector. The central and end caps region are visible.

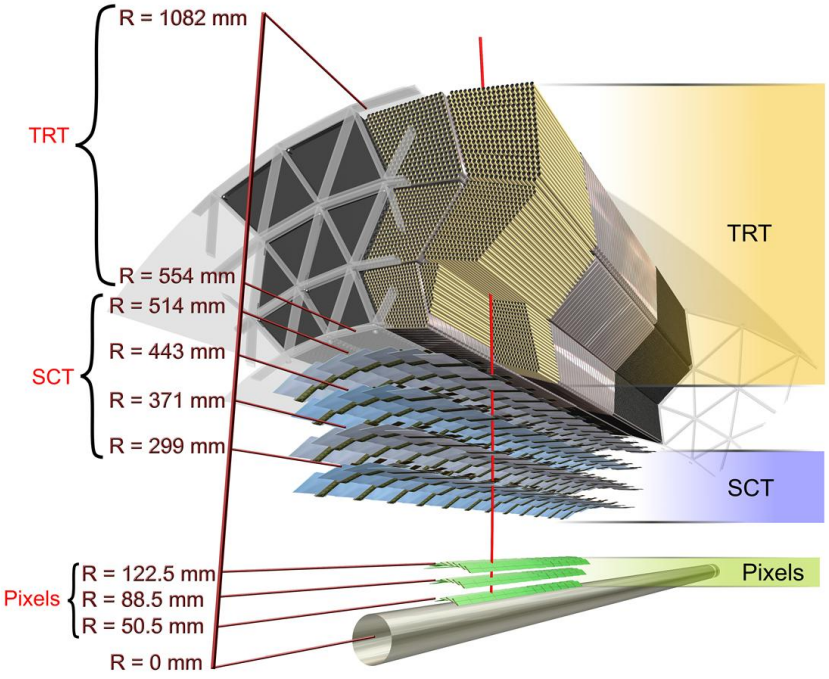

(b) Sectional view of the barrel Inner Detector. The straight line in the middle of the figure represent a 10 GeV track with $\eta = 0.3$.

Figure 2.9: The ATLAS Inner Detector [66].

The tracking and vertexing performance has been tested using cosmics and collisions data.

Figure 2.10 (a) [70] shows the z vertex resolution as a function of the tracks transverse momenta sum. For vertex build with high energetic tracks, the resolution is better than 600 μm, the nominal value is less than 100 μm.

Figure 2.10 (b) [71] shows the impact parameter $d\emptyset$ resolution as a function of the track p_T, using cosmics data. For high energetic tracks the resolution is better than 30 μm, the nominal value is 15 μm.

Figure 2.10 (c) [72] shows the resolution of the inverse transverse momenta, of muons in the ID as a function of their p_T, in the central region. For high p_T muons this inverse resolution is better than 0.0007 GeV^{-1}.

Some discrepancies between Monte Carlo and Data can be seen in figure 2.10 (b) and (c), the calibration procedure are being worked on after the data taking.

For example, figure 2.10 (d) [73] shows the improvement of the difference between the track pseudo rapidity and the cluster pseudo rapidity, for electrons coming from W and Z bosons decay in the central region, after and before the alignment corrections between the calorimeter and the ID are computed.

The performances of the tracking are already in fair agreement with the nominal expected values. They are improving fast thanks to the accumulation of statistics.

Table 2.2 gives the number of readout channels, and the overall operating fraction at the beginning of 2011 run [74] for each ID sub detector.

Sub-detector	Number of Channels	Operating Fraction
Pixels	80 M	97.2%
SCT	6.3 M	99.2%
TRT	350 k	97.5%

Table 2.2: Operating fraction of the sub detector in the inner detector [74].

2.2.4 Calorimeters

The ATLAS calorimeters [75] are sampling calorimeters. They are presented in figure 2.11. They are installed around the inner detector. They can be divided into five sub-systems. The Electromagnetic Barrel (EMB) which is a lead Liquid Argon (LAr) Calorimeter, with a coverage of $0 < |\eta| < 1.475$, the Electromagnetic End Caps (EMEC), which are also lead LAr Calorimeter and whose coverage extent to $1.375 < |\eta| < 3.2$. The hadronic Tile calorimeter, which is steel and scintillating tiles calorimeter with a coverage of $0 < |\eta| < 1.7$, the Hadronic End Caps (HEC), which are copper LAr calorimeters covering $1.5 < |\eta| < 3.2$. And finally the Forward Calorimeter (FCal), which is a mix copper/tungsten LAr Calorimeters, extending the calorimetric coverage to $3.2 < |\eta| < 4.9$. The LAr Calorimeters are described in details in Chapter 3.

Electromagnetic performances

The electromagnetic calorimeter contains most of the electromagnetic shower of electrons and photons. The calorimetric measurement is destructive, since the particles loose most of their energy in the absorbers.

The relative energy resolution of an EM particle is given by

$$\frac{\sigma_E}{E} = \frac{S}{\sqrt{E}} \oplus \frac{N}{E} \oplus C \tag{2.10}$$

Where the energies are given in GeV in this equation and

- S is the sampling term which describes the statistical fluctuations of the electromagnetic shower. At $\eta = 0$, this term is approximately 10%.

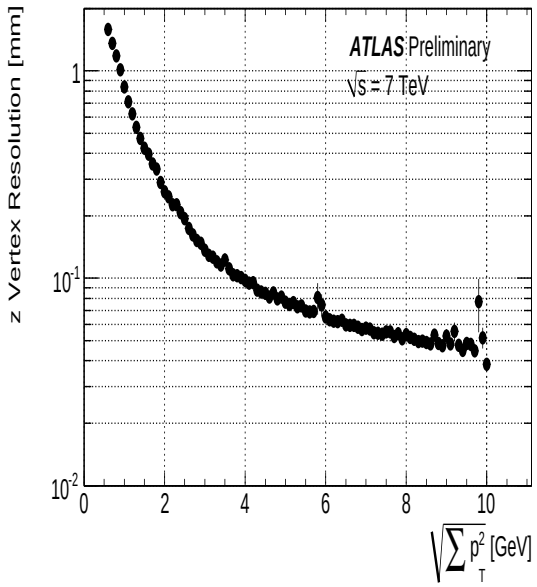

(a) z vertex Resolution as a function of the $\sqrt{\sum p_T^2}$ of tracks, obtained with 2010 collisions data [70].

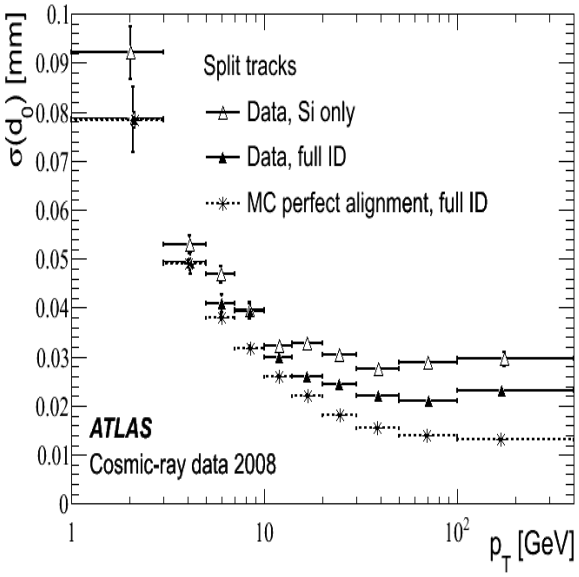

(b) Impact parameter $d\emptyset$ resolution as a function of the track p_T, obtained with 2008 cosmics data [71].

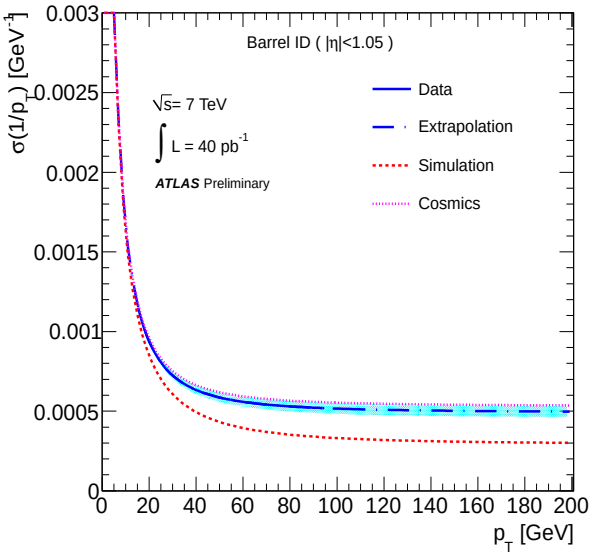

(c) Resolution of the inverse transverse momenta, of muons in the ID as a function of their p_T, in the central region, obtained using 2010 collisions data [72].

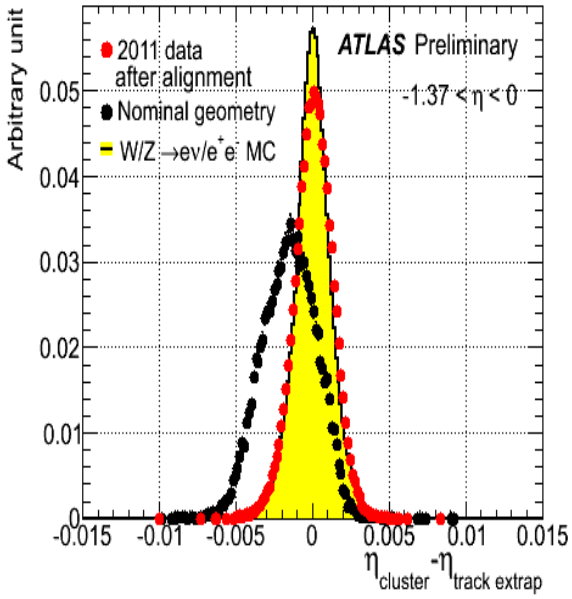

(d) Impact of the Alignment procedure of the Calorimeter and the ID, using electrons from W and Z bosons decay, using 2010 collisions data [73] .

Figure 2.10: ATLAS Inner Detector performance.

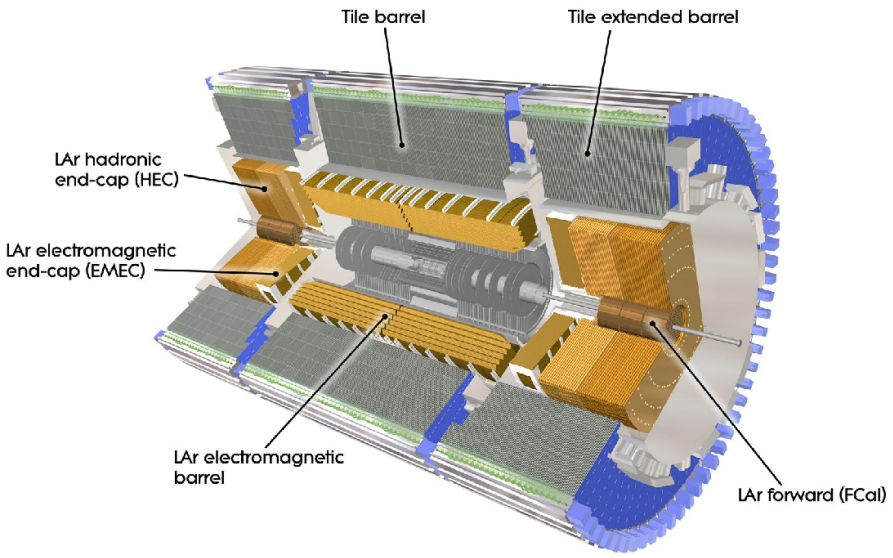

Figure 2.11: Atlas Calorimeter systems [66].

- N is the noise term. It is due to the electronic noise of the preamplifier and the capacitance of the electrodes, and from the pile up. Its value is generally on the order of a few hundred MeV for the measurement of a photon or an electron.
- C is the constant term. It takes into account the non uniformity of the calorimeter, and of its response. At high energy, it is the dominant term of the resolution.

The constant term was estimated in the 2010 data [76], in the EM Barrel, EMEC Outer and inner wheel, and in the FCal. The measurement was obtained by fitting the Z invariant mass and compare the results to the prediction in the Monte Carlo. The results are shown in table 2.3. The measurement gives for the barrel $1.2\% \pm 0.1\%$ (stat) $^{+0.5\%}_{-0.6\%}$ (syst), which is not far from the nominal value which is 0.7%. Some effort are undergoing to improve these results.

EMB	1.2%	±	0.1%	(stat)	$^{+0.5\%}_{-0.6\%}$	(syst)
EMEC Outer Wheel	1.8%	±	04%	(stat)	±0.4%	(syst)
EMEC Inner Wheel	3.3%	±	0.2%	(stat)	±1.1%	(syst)
FCal	2.5%	±	0.4%	(stat)	$^{+1.0\%}_{-1.5\%}$	(syst)

Table 2.3: Constant term of the EM LAr Calorimeter, measured in the 2010 Data.

The di-electron invariant mass, around the Z boson peak, is shown on figure 2.12 (a), and around the J/Ψ peak on figure 2.12 (b). The data corresponds to the full 2010 data set, the Monte Carlo prediction is also shown. The Monte Carlo is found to be in good agreement after all calibrations.

Figure 2.12 (c) shows the energy scale uncertainty as a function of the electron energy, for electron coming from the decay of the J/Ψ meson, Z and W bosons, in 2010 data. The electron energy scale uncertainty about 1% for low energetic electrons is better than 0.5% for higher energies.

Tile calorimeter

The Tile calorimeter [77] is a steel and scintillating tiles calorimeter with a coverage extending up to $|\eta| < 1.7$. The Tile calorimeter is split in three parts. In the central region up to $|\eta| < 0.8$ is the barrel. In the regions $0.8 < |\eta| < 1.7$ the extended barrels complete the coverage. Figure 2.13 shows a sketch of the tile calorimeter segmentation. The tile calorimeter cells are segmented radially in three

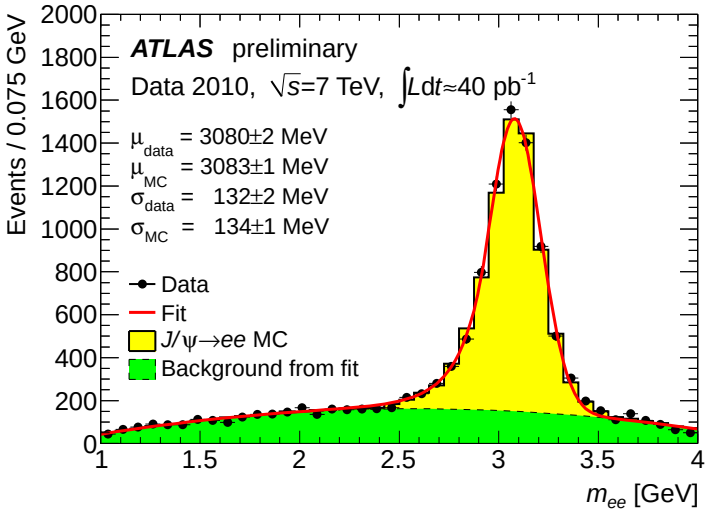

(a) Di-electron invariant mass around the J/Ψ peak, for the full 2010 data sets and the Monte Carlo prediction.

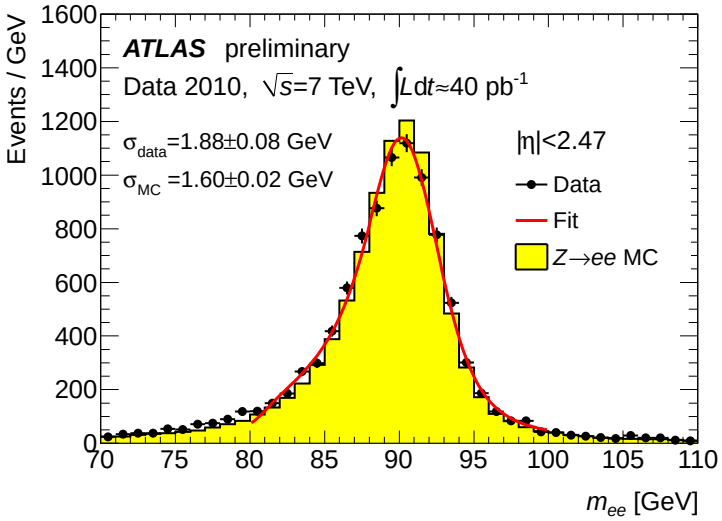

(b) Di-electron invariant mass around the Z peak, for the full 2010 data sets and the Monte Carlo prediction.

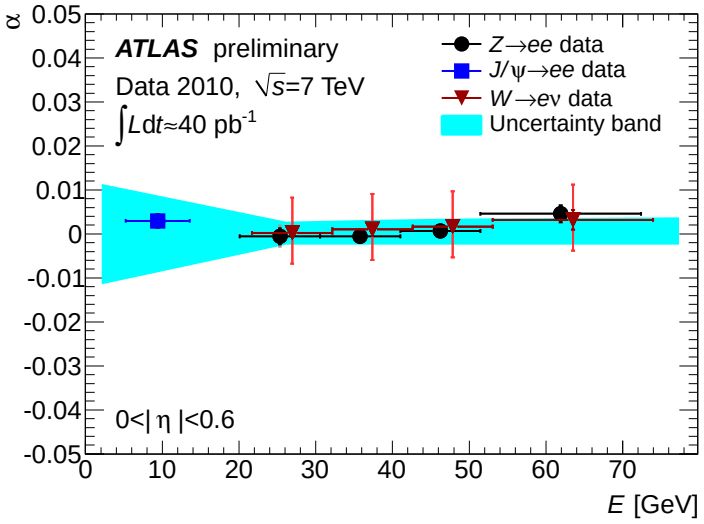

(c) Energy scale uncertainty for electrons coming from the decay of the J/Ψ meson, Z and W bosons, in 2010 data

Figure 2.12: ATLAS EM calorimeter performances [76].

compartments. The cells are pseudo projective in η. Their granularity is roughly $\Delta\eta \times \Delta\phi = 0.1 \times 0.1$ for the two first compartments, and $\Delta\eta \times \Delta\phi = 0.2 \times 0.1$ for the back one.

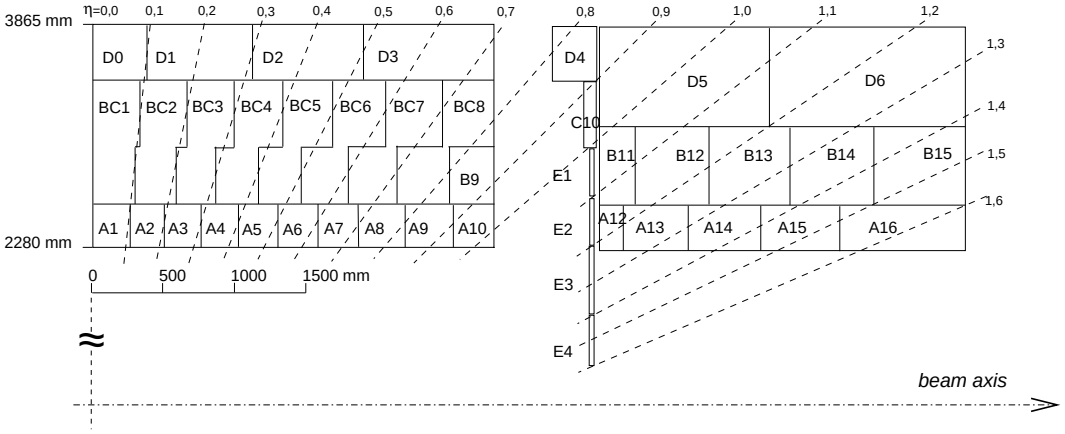

Figure 2.13: Sketch of the Atlas Tile Calorimeter system [66].

The energy resolution of the hadronic calorimeter follows the equation (2.10). It was studied in di-jet event, using *in situ* techniques on the full 2010 data sets [78, 79]. The result is shown on figure 2.14, were the resolution shown is the jet transverse momentum resolution as a function of the jet transverse momentum. This figure was obtained for central jets $|y| < 0.8$, and applying different calibration schema in order to improve the resolution. The difference between Monte Carlo and data is also showed. For central high p_{T} jets, the fractional resolution is better than 9% in the worse calibration schema. The jet resolution will be detailed in Chapter 4.

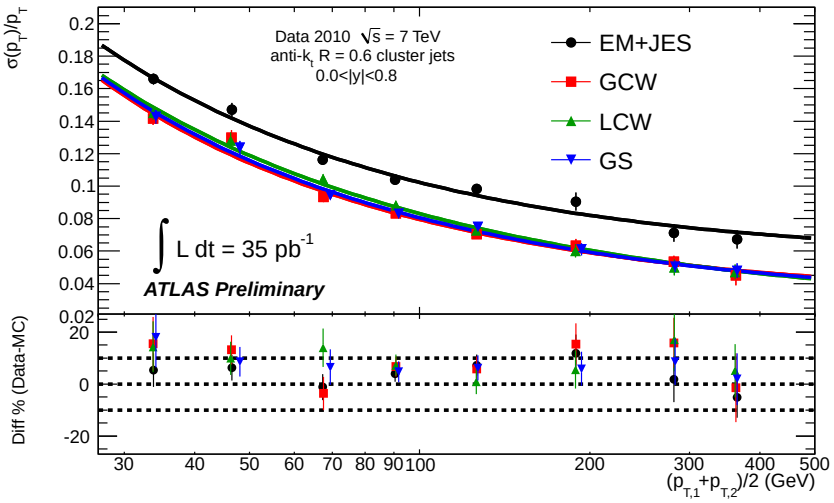

Figure 2.14: Jet transverse momentum resolution as a function of the jet transverse momentum for various jet collections. Fractional jet energy resolution as a function of the average jet transverse momenta for events with two jet in the same rapidity bin for the four different JES strategies in ATLAS: EMJES, Global Cell Weighting (GCW), Local Cluster Weighting (LCW) and Global Sequential (GS) calibrations. The lines correspond to the fits on data for each JES scheme respectively. The lower plot shows the relative difference between Monte Carlo and the data results. The black dotted lines indicate a relative uncertainty of ±10% [62].

The hadronic calorimeter is completed by the LAr end caps calorimeter. This will be described in Chapter 3.

Operational fraction of the calorimeters

Table 2.4 recapitulates the number of readout channels per calorimeter sub-system, and the operating fraction at the beginning of the 2011 run.

Sub-detector	Number of Channels	Operational Fraction
LAr EM Calorimeter	170 k	99.9%
Tile calorimeter	9800	98.8%
Hadronic end-cap LAr calorimeter	5600	99.8%
Forward LAr calorimeter	3500	99.9%
LVL1 Calo trigger	7160	99.9%

Table 2.4: Operating fraction of calorimeters the sub-system [74].

2.2.5 Muon spectrometer

The ATLAS Muon Spectrometer [80] (MS) is presented in figure 2.15. The toroidal magnetic field is used to bend the muon trajectory, and measure their momentum. The coverage of the spectrometer extends up to $|\eta| < 2.7$ while the muon trigger system covers up to $|\eta| < 2.4$.

Monitoring Drift Tubes

The Monitoring Drift Tubes (MDT), provides precise measurement of the muon momenta up to $|\eta| < 2.0$. The MDT are composed of 30 mm Aluminum Tubes, filed with a pressured gas mixture of Argon and CO_2, and a tungsten wire. They are disposed in three layers around the barrel toroidal magnets, and in four layers in the wheel end-caps. The 1163 MDT are covering a total surface about 5500 m^2.

Cathode Strips Chambers

At larger pseudo rapidity $2.0 < |\eta| < 2.7$, the MDT are replaced by Cathode Strips Chambers (CSC). The granularity of the CSC is finer than the one of the MDT because the particle flux increases in this region. The chambers are filed with a gaseous mixture of Argon CO_2 and CH_4. The CSC chambers are located only in the muon wheels end-caps. The 32 chambers cover a surface of 27 m^2.

Resistive Plate Chambers

To trigger the event two independent muon detector are used. The Resistive Plate Chambers (RPC) system is one of the two. It covers the detector up to $|\eta| < 1.05$. This system is made of Bakelite plates immerge in a gaseous mixture of $C_2H_4F_4$, C_4H_{10}, and SF_6. Three layers of RPC are installed between the MDT layers, only in the barrel part. The 1136 chambers cover a surface of 3650 m^2.

Thin Gap Chambers

The second trigger system used at higher pseudo rapidity is composed of Thin Gap Chambers (TGC). They cover the detector in the range $1.05 < |\eta| < 2.4$, and are only located in the end-caps muon wheels. These chambers are filed with a gaseous mixture of CO_2 and n-C_5H_{12}. Their are 1584 TGC covering a surface of 2900 m^2.

Tracking Performances

The muon tracking performances has been measured using cosmic and collisions data.

Figure 2.16 (a) [72] shows the relative transverse momentum resolution of muons in the central region as a function of the muon transverse momentum, Monte Carlo, Cosmic and Collision Data are

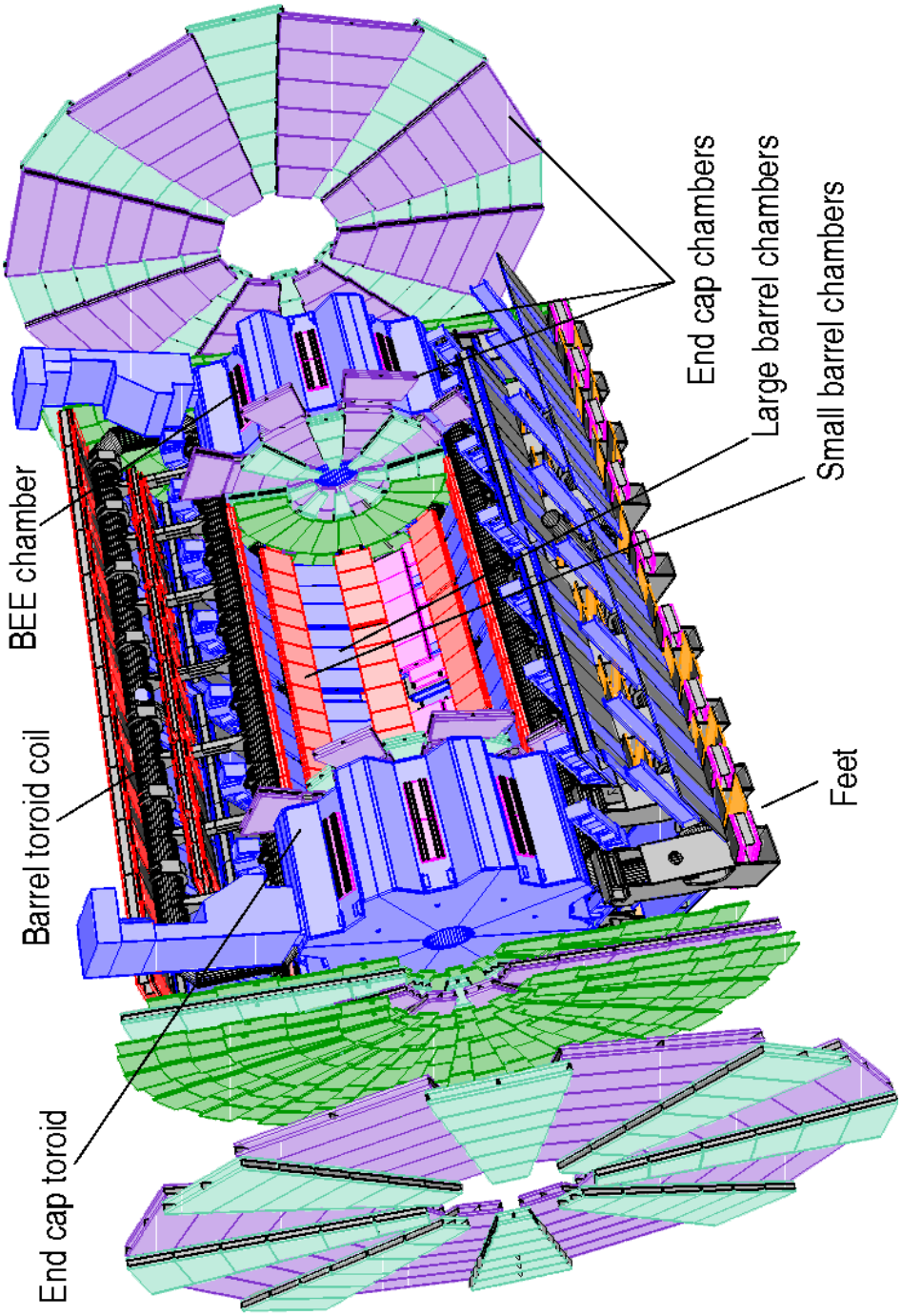

Figure 2.15: Atlas muon spectrometer system [62].

showed, as well as an extrapolation of the resolution for higher p_{T}. The relative resolution measured in the data is better than 5%. The nominal resolution on muons transverse momentum is given by $\frac{\Delta p_{\mathrm{T}}}{p_{\mathrm{T}}} < 10^{-4} \times p(\text{ GeV})$, so for a $p_{\mathrm{T}} = 200$ GeV muon, produced at $|\eta| = 0$, the transverse momentum resolution is about 2%.

Figure 2.16 (b) [81] shows the average deviation of the measured invariant mass from the Z mass world average as function of eta region to which the two combined muons are associated. The error bars showed are statistical only. The mass of the Z is recovered within 2% in the whole η range, and is much less than 1% in the central measurement region.

Figure 2.16 (c) [81] shows the di-muon invariant mass comparison in the Z boson mass range between collision data (dots) and simulation (full histogram), after calibration. A very good agreement is found between data and Monte Carlo.

The performances of the Muon Spectrometer are evolving fast thanks to the statistics increase, and the hard calibration work.

Table 2.5, gives the number of readout channels per muon spectrometer sub-system, and the operating fraction at the beginning of 2011 run.

Sub-detector	Number of Channels	Approximate Operational Fraction
MDT Muon Drift Tubes	350 k	99.8%
CSC Cathode Strip Chambers	31 k	98.5%
RPC Barrel Muon Chambers	370 k	97.0%
TGC End-cap Muon Chambers	320 k	99.1%
LVL1 Muon RPC trigger	370 k	99.5%
LVL1 Muon TGC trigger	320 k	100%

Table 2.5: Operating fraction in the Muon spectrometer sub-systems [74].

2.2.6 Trigger

The Trigger system allows to select potentially "interesting" events, among pp collisions at 20 Mhz[7]. They are selected using three trigger levels. A Schematic description is shown on Figure 2.17.

LVL1

The Level1 (LVL1) trigger system is built of fast custom electronics to identify high p_{T} objects such as electrons, photons, jets, muons, and $E_{\mathrm{T}}^{\mathrm{miss}}$.

Calorimeter triggers is based on trigger tower of granularity $\Delta\eta \times \Delta\phi = 0.1 \times 0.1$ for the EM objects and $\Delta\eta \times \Delta\phi = 0.2 \times 0.2$ for the hadronic objects. For the muon system the RPC and the TGC collects hits information and builds up tracks.

The calorimeter and muons information are sent to the Central Trigger Processor (CTP). There a selection menu is implemented allowing to keep only the events containing objects passing a given set of cuts. Finally if the event is chosen, the Region of Interest (RoI) attributes, such as η, ϕ, E_T threshold, will be kept by the CTP and send to the Level2 (LVL2) trigger.

The LVL1 decision has to be taken in less than 2.5 μs. It reduces the total rate from 40 MHz of collisions to a maximum of 75 kHz.

LVL2

The LVL2 accesses the RoIs information from the CTP, and read the full event granularity from the Read Out Drivers (ROD) in those RoIs. The RoIs information contains about 2% of the event. The LVL2 trigger is essentially made of computers that makes a basic reconstruction of the RoI's to check

[7] 40 Mhz for the nominal LHC parameters.

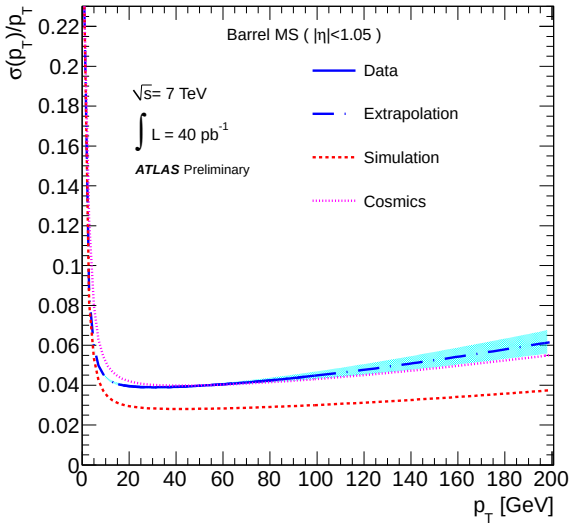

(a) Relative transverse momentum resolution of muons in the central region as a function of the muon transverse momentum, Monte Carlo, Cosmics and 2010 Collisions Data are showed [72].

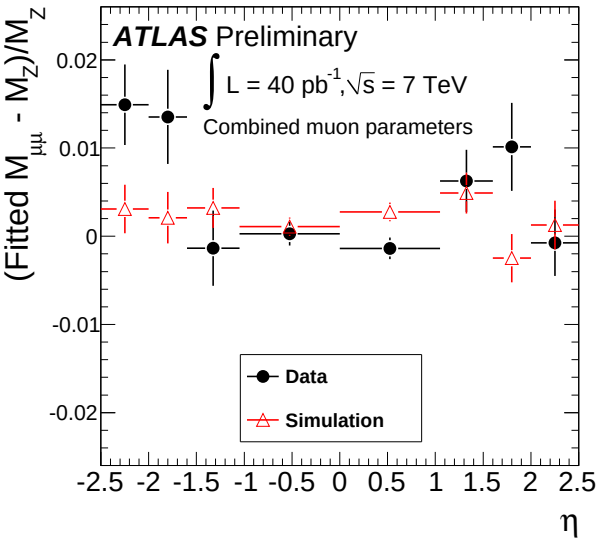

(b) Average deviation of the measured invariant mass from the Z mass world average as function of eta region to which the two combined muons are associated [81].

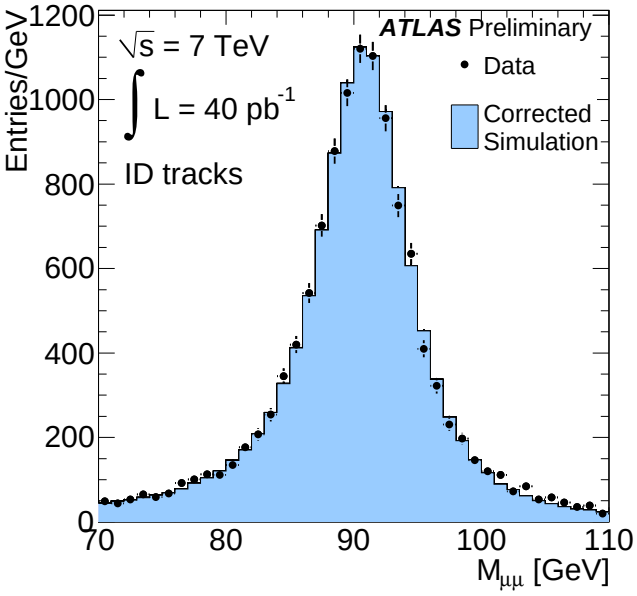

(c) Di-muon invariant mass comparison in the Z boson mass range between collision data (dots) and simulation (full histogram), after calibration [81].

Figure 2.16: ATLAS Muon Spectrometer performance.

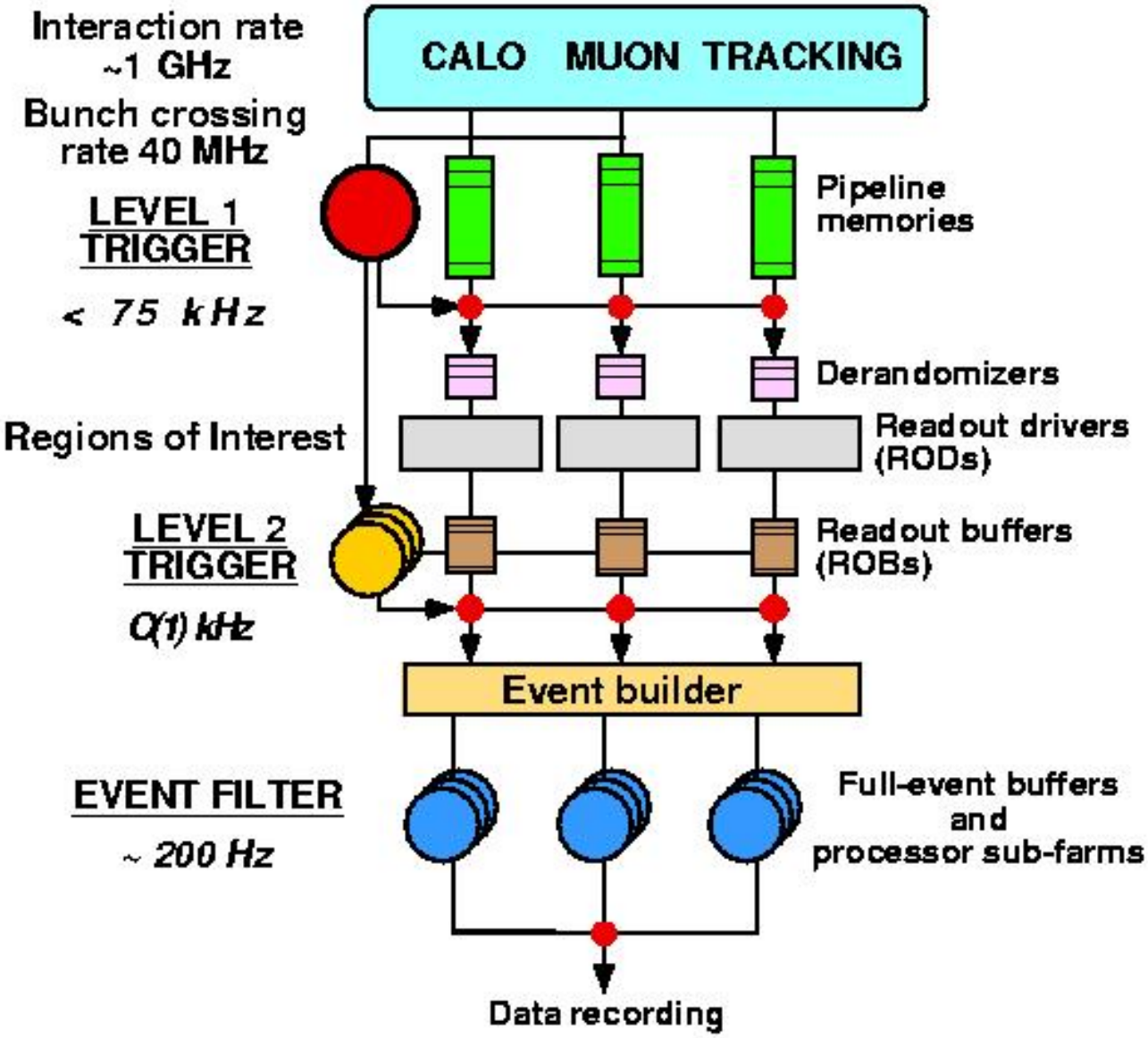

Figure 2.17: Sketch of the ATLAS trigger system [66].

if the objects selected pass a given set of cuts, tighter than at LVL1. It considers information from more than one sub detector.

The LVL2 is designed to reduced the rate from 75 kHz to 3.5 kHz. The processing time of an event fragment is less than 40 ms.

Event Filter

Finally if the event is selected by the LVL2 it is sent to the Event Builder to be analyzed by the Event Filter (EF). At this stage, the whole event is reconstructed using an optimized version of the offline software. If it is selected by the EF, the event is sent to the CERN computing center, or Tier0, to be reconstructed and stored on tape.

The EF reduces the rate from 3.5 kHz to 400 Hz. The processing time of a single event bye the EF is about 4 s. The High Level Trigger or (HLT) is constitutes from the LVL2 and the EF.

Trigger rates on real events

Figure 2.18 (a) [82] shows the rate in kHz, before pre-scale, for different trigger item as a function of the instantaneous luminosity. The highest trigger item is the minimum bias trigger (MBTS), the trigger rate is decreasing when the threshold apply on the object is increased. This figure was obtain on 2010 Collisions data.

Figure 2.18 (b) [82] shows the muon trigger rate for a L1 item, and for EF items as a function of the luminosity. Their is about two order of magnitude between the L1 item $MU0$, and the EF item EF_mu6.

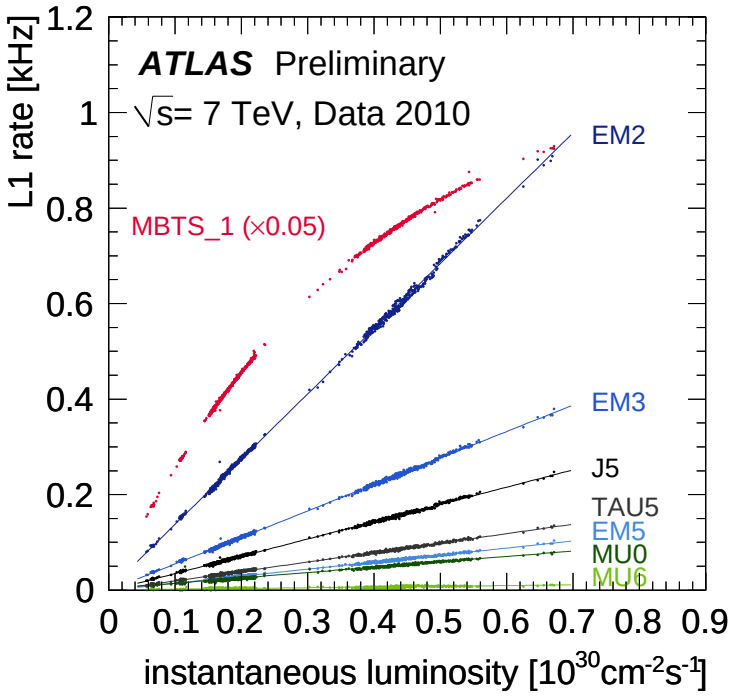

(a) L1 trigger rate as a function of the instantaneous luminosity for different L1 trigger item. [82]

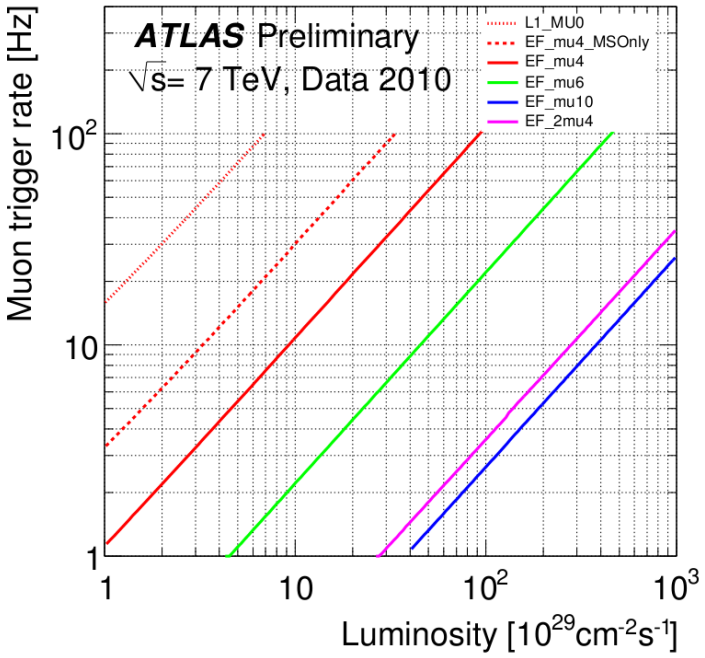

(b) L1 trigger and EF rate as a function of the instantaneous luminosity for different L1 muons trigger item. [82]

Figure 2.18: ATLAS Trigger rates [82].

Chapter 3

The ATLAS Liquid Argon Calorimeters

"Les matelots se précipitèrent à la barre, les ingénieurs à leur machine."
Jules Verne,
Vingt mille lieues sous les mers.

Personal contribution
My PhD work on the detector was focused on the monitoring of the data quality of the LAr calorimeter. I have developed the algorithm presented at the end of this chapter, that allows to check basic properties of the data read out of the calorimeter, such as non-saturation and time-alignment. I was also part of the LAr data quality assessment team for the first two month of collision data in 2010. During this period I was in charge of determining what were the data that could be used for physics analysis and that needed to be discarded.

Introduction

The Liquid Argon [83] (LAr) calorimeters are installed around the Inner Detector. A cut view is shown on Figure 3.1. Their function is to reconstruct electromagnetic particles (electrons or photons), and hadronic particles (pions, kaons, protons, neutrons, *etc*), by measuring their energy, position and time. The calorimeters also measure the transverse missing energy.

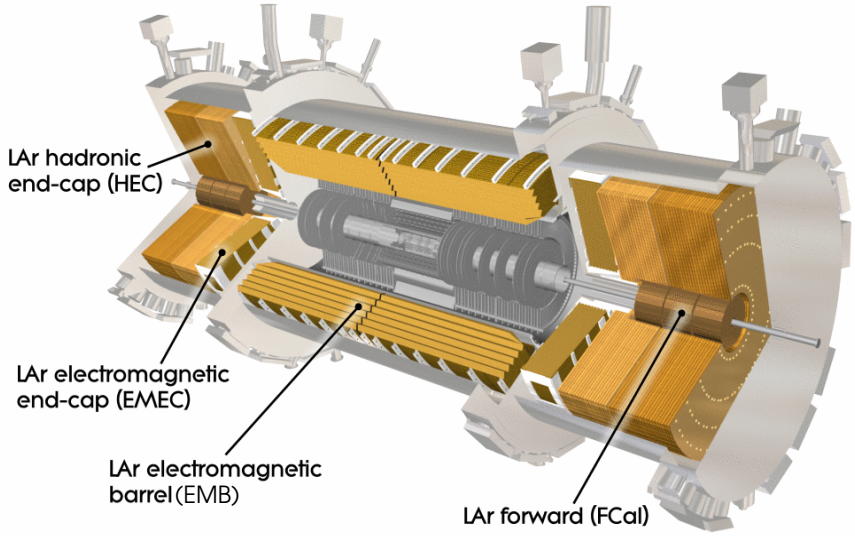

Figure 3.1: Cut view of the LAr Calorimeters. The Inner Detectors and the beam pipe are also visible in the center of the image [66].

The LAr calorimeters are sampling calorimeters. When a particle reaches the calorimeter, it interacts with the absorbers: A shower develops. The ionization energy is measured ultimately in the sensitive medium (Liquid Argon).

- At high energy, the electrons lose energy *via* the radiation of a photon, process called Bremsstrahlung. Photon mainly interact by the creation of electron positron pairs. At low energy, ionization processes are dominant. The electromagnetic shower is characterized by the radiation length (X_0), the distance after which the electron loses $\frac{1}{e}$ of its energy *via* Bremsstrahlung. For photons, the distance for the creation of electron positron pairs is $\frac{7}{9}$ X_0. A 100 GeV electron is contained at 95% in 20 $X_0 \approx 40$ cm of the ATLAS EM Calorimeter, and radially in approximately 3.5 cm.

- For the hadronic particles, the energy is lost *via* the strong interactions with matter. The hadronic shower contains mesons and baryons. An important part, about 30% of the energy, is lost via electromagnetic interactions due to the decay of the π^0. The rest of the energy is lost via nuclear interaction processes, fission, *etc*. For this processes the energy is not necessarily recorded. For these reasons, the hadronic shower is more erratic than the electromagnetic one. It can also be characterized by a parameter called nuclear interaction length: $\lambda_i = \frac{A}{N_A \rho \sigma_{tot}}$, where $\sigma_{tot} \approx 50\ mb$, A is the atomic number, N_A is the Avogadro number, and ρ the density of the medium encountered. λ_i is the length after which the hadronic shower loose $\frac{1}{e}$ of its energy. A 80 GeV pion is contained at 95% in 8 $\lambda_i \approx 85$ cm d'U, and radially in 1.5 $\lambda_i \approx 32$ cm.

The main idea of sampling calorimetry is to develop an electromagnetic or hadronic shower in a dense material, and to sample the energy lost by the particles in the sensitive medium. The calorimeters are made of layers of passive and dense material (lead, copper, tungsten) alternating with active

materials. In the LAr Calorimeters, the active material is Liquid Argon. When a charged particle passes through the LAr gap, the LAr is ionized giving electrons and cations. An electrical field is applied on the LAr gap which makes the ionized LAr electrons drift to the electrode located in its center. The electrons induced a capacitive coupling current in the electrode ($\approx \mu$A) which is measured.

In this chapter, the geometry of the LAr Calorimeters is presented in the first section. In a second section, the electronic readout is presented. The third section is dedicated to the signal treatment and calibrations. Finally the last section present the data acquisition, data quality and the monitoring of the LAr calorimeter. This latter section will be focused on the monitoring algorithm that I have developed during my thesis.

3.1 Geometry

As described in Section 2.2.4 the LAr calorimeters are divided into four different sub-systems, covering the barrel for the electromagnetic part, the end-caps for both the electromagnetic and the hadronic part, and a forward calorimeter allowing coverage up to $|\eta| < 4.9$. The hadronic barrel is a steel/scintillating tiles sampling calorimeter, as described in the previous Chapter.

3.1.1 Electromagnetic calorimetry

The electromagnetic calorimeter is used to reconstruct the energy of photons and electrons. It has also been designed to provide good π^0/γ rejection.

Barrel

The electromagnetic barrel [84] covers the pseudo-rapidity range up to $|\eta| < 1.475$. It is made of two identical half barrels separated at $z = 0$ by a small gap of 4 mm. Each half-barrel weighs 57 tons, is 3.2 m long, and the dimensions of the inner an outer diameters are respectively 2.8 m and 4 m.

One half barrel is made of 1024 layers of lead absorbers. The absorbers are interleaved with an active setup formed of readout electrodes and LAr as ionizing medium. The absorbers and electrodes have a radial accordion-shaped [85] in ϕ. This ensure a full coverage of the calorimeter in ϕ without cracks [66]. Figure 3.2 shows a picture of barrel electrodes and absorbers, the accordion-shape can be seen. Figure 3.3 shows a schematic view of the barrel calorimeter principle. A High Voltage (HV) is applied on both side of the gap creating an electric field which make drift the electrons from the ionization to the electrodes. The electrodes are made of a sandwich of copper and kapton [83]. Each side of the HV electrode is powered by two different HV lines to ensure redundancy.

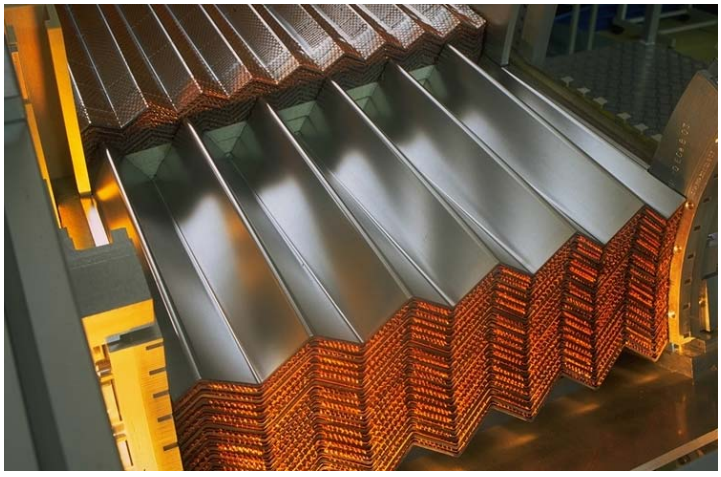

Figure 3.2: Photograph of barrel accordion-shaped electrodes and absorbers [83].

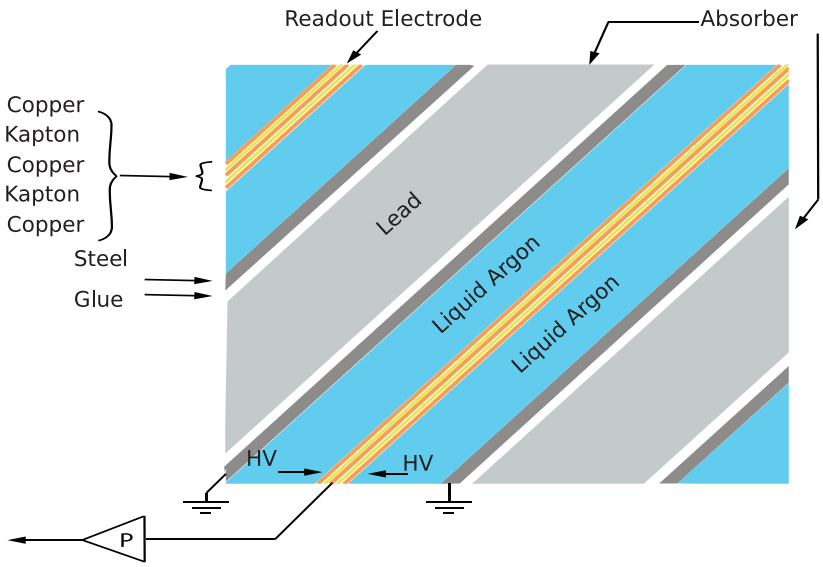

Figure 3.3: Schematic view of the EM LAr calorimeter principle [83].

Each half barrel is made of 16 modules, each one contains 64 pairs of electrodes and absorbers, covering a region $\Delta\phi = 22.5°$. The calorimeter cells are pointing to the interaction point. The cells are divided along three different directions:

- radially the electrodes are divided into three layers.
- azimuthally the electrodes are regrouped in ϕ, to create the readout cells.
- Along z, the cells segmentation is coarser at higher η.

At $|\eta| = 0.8$, the absorber thickness is decreased from 1.5 mm to 1 mm to limit the decrease of the sampling frequency as $|\eta|$ increases. The energy is measured from the drift of the electrons in the LAr gap, for this reason, the LAr gap is constant over the whole barrel with a thickness of 2.1 mm, the electrodes are fed with an electrical HV of 2000 V.

Figure 3.4 shows the number of electromagnetic radiation lengths (X_0) of materials in the ATLAS detector from the beam pipe to the edges of the EM calorimeter in the range $|\eta| < 1.4$. In front of the calorimeter, there are 2.5 X_0 at $|\eta| = 0$, and up to 6.5 X_0 at $|\eta| = 1.4$. In order to estimate the energy lost in the Inner Detector, services and cryostat, two planes of electrodes are inserted in the cryostat in front of the calorimeter. This layer is called the pre-sampler [86].

The segmentation of the LAr calorimeter in the EM barrel is shown in Figure 3.5. Each compartment has a specific purpose and a well defined granularity.

- The pre-sampler (also referred to as PS or layer 0). Its purpose is to estimate the energy lost by the particles in the material located in front of the calorimeter. The cells size is $\Delta\eta \times \Delta\phi = 0.025 \times 0.1$.
- The front (also referred to as layer 1). The cells have a thin granularity in η. Their size is $\Delta\eta \times \Delta\phi = 0.0031 \times 0.1$. This layer is used to differentiate neutral pions, which decay mostly into two photons, from photons. For instance [87] the angular separation of the two photons from a symmetric π^0 decay, is $\Delta\eta_{\gamma\gamma} \approx 0.0135$, assuming that $E_{\pi^0} = 20$ GeV and it is emitted at $\eta = 0$.
- The middle (also referred to as layer 2). It is the deepest layer, from 16 to 18 X_0, it contains most of the electromagnetic shower. The cell size is $\Delta\eta \times \Delta\phi = 0.025 \times 0.025$.

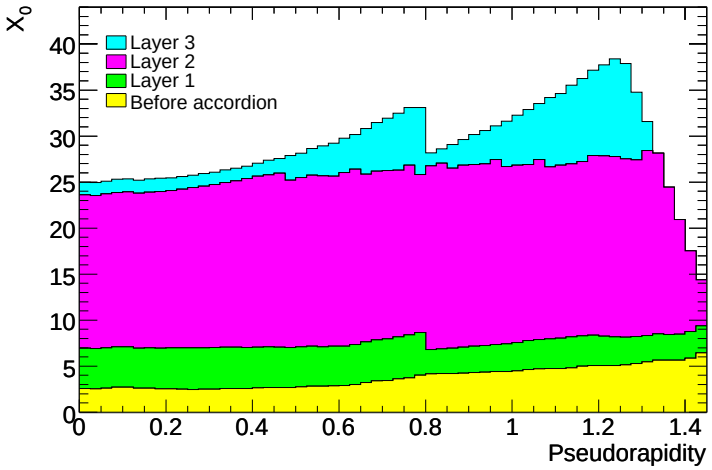

Figure 3.4: Histogram showing the EM interaction length (X_0) as a function of η from the beam pipe to the edges of the EM calorimeter in the barrel region [66].

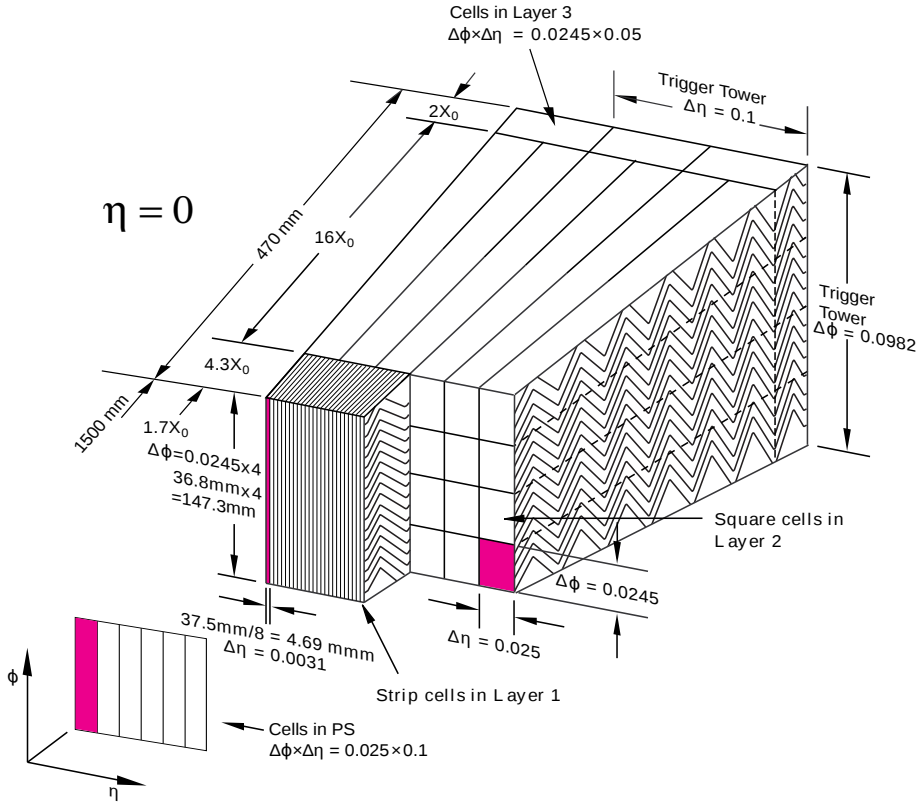

Figure 3.5: Segmentation of the LAr EM barrel calorimeter at $|\eta| = 0$. The size of the cells and interaction length for each layer is quoted [66].

- The back (also referred to as layer 3). The thickness of this layer is 2 X_0 at $|\eta| = 0$. The size of the cells is $\Delta\eta \times \Delta\phi = 0.05 \times 0.025$. This last layer allows to estimate the energy of the EM shower which is not contained within the EM calorimeter.

The arrangement of the electrodes [88] up to $|\eta| < 1.475$ is shown on Figure 3.6.

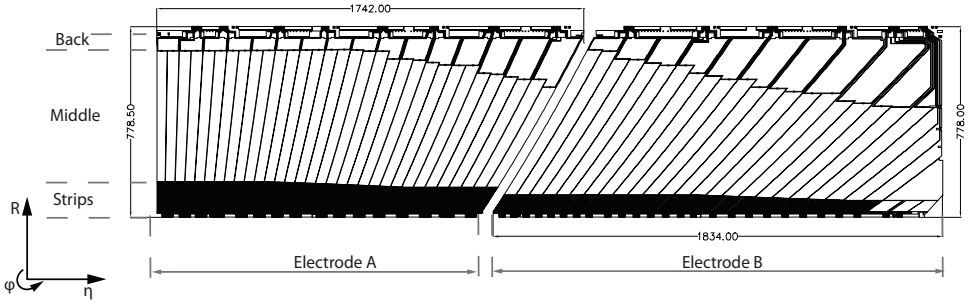

Figure 3.6: Arrangement of the LAr electrodes in the barrel ensuring the coverage up to $|\eta| < 1.4$ [66].

End-Caps

The Electromagnetic End-Caps (EMEC) [89] are composed of two coaxial wheels, the inner and the outer wheels. They are located on each side of the EM barrels, at $|z| \approx 4.3\ m$ in two independent cryostats. Figure 3.7 shows the two types of electrodes for the inner and outer wheels. They cover the region $1.375 < |\eta| < 2.5$, for the outer wheel, and $2.5 < |\eta| < 3.2$ for the inner wheel. The outer wheel is designed for precision measurement in the continuity of the barrel, while the inner wheel provides a good measurement of electrons and photons but with a worse resolution.

The EMEC is also made of accordion shaped electrodes and lead, the electrodes are bent longitudinally. In the inner wheel only the middle and back layers are present. The pre-sampler covers only $1.5 < |\eta| < 1.8$. The cells size are summarized in table 3.3 in section 3.1.5.

In order to keep the response of the calorimeter approximately constant in η, the LAr gap thickness is not constant over the whole η range and the HV applied on the electrodes vary from 2.5 kV to 1.0 kV. The absorber thickness is 1.7 mm at $|\eta| < 2.5$ and 2.2 mm above. The HV parameters and LAr gap thickness are summarized in table 3.2 in section 3.1.5.

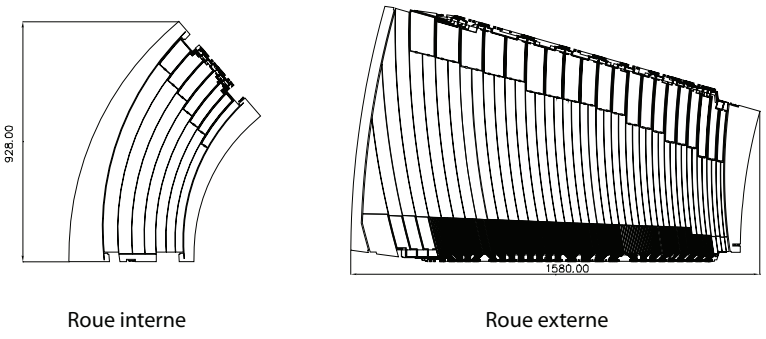

Figure 3.7: Schematic view of the EMEC electrodes in both the inner and outer wheels [66].

3.1.2 Hadronic calorimetry

The hadronic calorimeters must contain the hadronic showers, and provide a good energy measurement of the jets. The hadronic barrel calorimeter is made of steel and scintillating tiles, while the

Hadronic End-Caps (HEC) [90] calorimeters are LAr calorimeters. Figure 3.8 shows the total hadronic interaction lengths (λ_i) present in ATLAS from the beam pipe to the edges of the calorimeter.

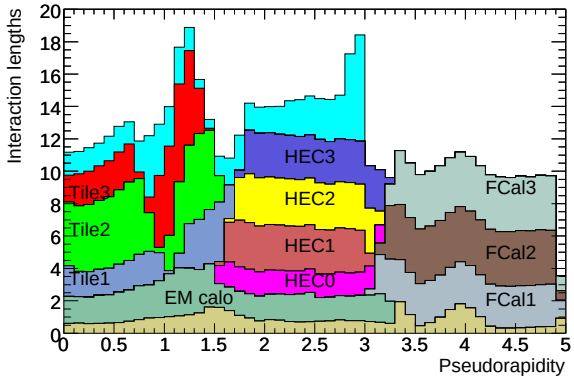

Figure 3.8: Histogram showing the nuclear interaction length (λ) from the beam pipe to the edges of the calorimeters. In cyan is shown the materials present in front of the first active Muon Spectrometer layer [66].

Each HEC is composed of two independent wheels located in the same cryostat as the EMEC. The outer radius of the wheels is 2.03 m. The HEC covers the range $1.5 < |\eta| < 3.2$. Each HEC is composed of 64 identical modules. The HEC geometry, and a HEC module, is shown on Figure 3.9.

Copper is used as the passive medium, its thickness goes from 25 mm in the front wheel up to 50 mm in the rear wheel. The absorber and the electrodes are flat. The LAr gap is constant over the whole η range and is 8.5 mm. For this reason the HV fed to the electrodes is also constant and is 1800 V.

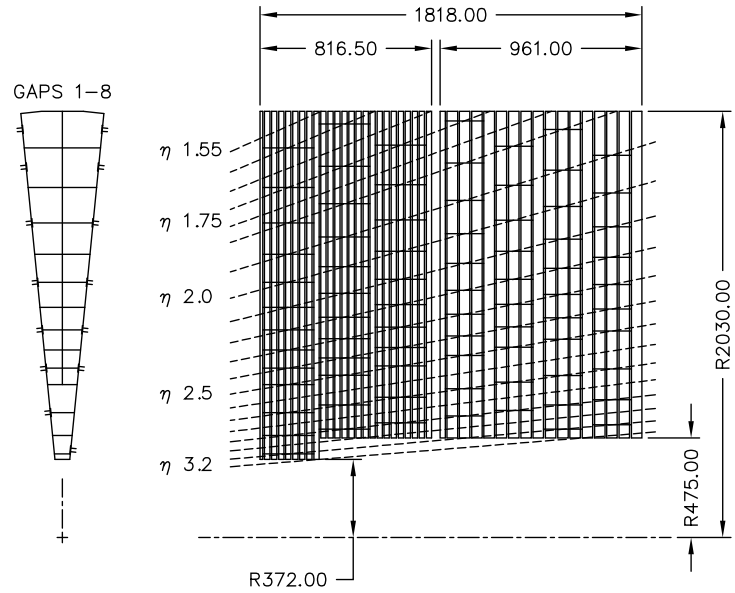

Figure 3.9: Schematic view of the two HEC wheels. One HEC modules is also showed [66].

A schematic view of the HEC electrodes are shown on Figure 3.10. They are different from the electromagnetic calorimeter one, by their structure. The cells have a granularity of $\Delta\eta \times \Delta\phi = 0.1 \times 0.1$ from $1.5 < |\eta| < 2.5$ and $\Delta\eta \times \Delta\phi = 0.2 \times 0.2$ up to $2.5 < |\eta| < 3.2$.

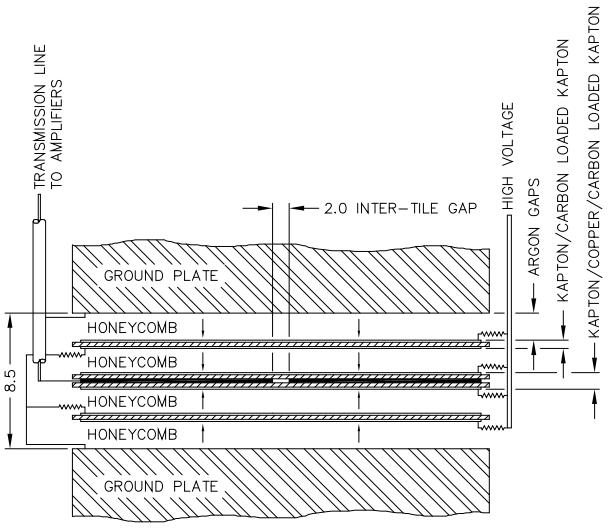

Figure 3.10: Schematic view of one HEC electrode. A preamplifier is located in the cryostat to reduce the electronic noise [83].

3.1.3 Forward calorimetry

The calorimetric coverage is extended up to $3.2 < |\eta| < 4.9$, by two calorimeters, called Forward Calorimeter (FCal) [91], housed in the end caps cryostat inside the HEC and EMEC, close to the beam pipe. The FCal is located at roughly $|z| \approx 4.7\ m$ from the IP.

The FCal is located close to the beam pipe, $|\eta| = 4.9$ corresponds to an angle $\theta = 0.1^{\circ}$, for this reason an high flux of particles is reaching it. The geometry of the detector is different from all the other LAr calorimeters. It is shown in Figure 3.11. The modules are made of a copper or tungsten matrix where rods are installed. The design of the FCal, better leads itself to labeling the cell position in the (x,y) plane than in the (η, ϕ) plane.

Figure 3.12 shows a cut view of one FCal. It consists of three layers. The first one is made of copper for the absorber, it is mainly designed to provide electromagnetic calorimetry at large η. The second and third layers are made of tungsten for the absorber. They are mainly used to provide hadronic calorimetry at large η. A last non-instrumented layer is present which protects the muon chamber placed behind the FCal.

3.1.4 High voltage granularity

The HV granularity [83] in the different LAr sub-detectors is given in Table 3.1. In the HEC and the FCal, one HV line cover the whole η range. Table 3.2 summarizes for each sub-system, the LAr gaps thickness and the nominal HV fed to the electrodes.

3.1.5 Summary of the cells granularity

Table 3.3 summarizes for each sub-system , the number of readout cells and their granularity for each layers.

3.2 Readout electronics

In this section the electronic readout [92] is presented. Figure 3.13 shows a block diagram of the LAr data acquisition.

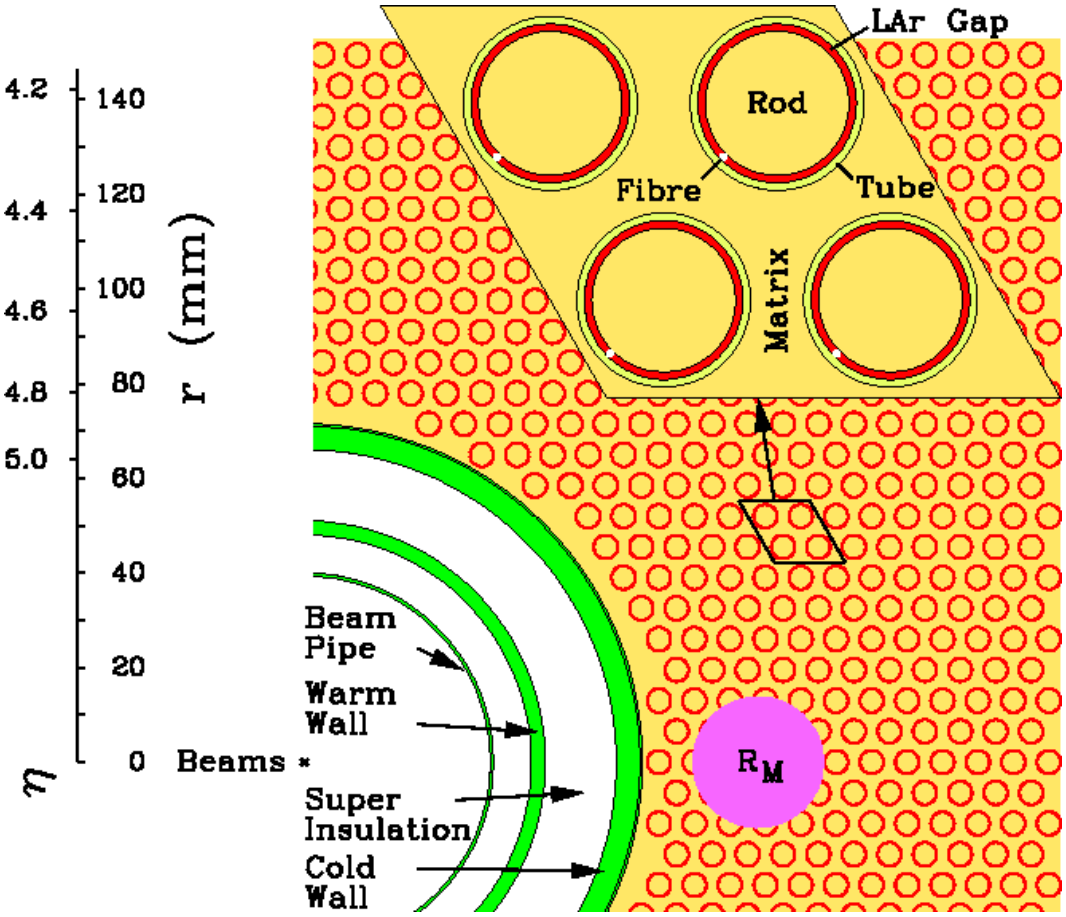

Figure 3.11: The FCal geometry [66].

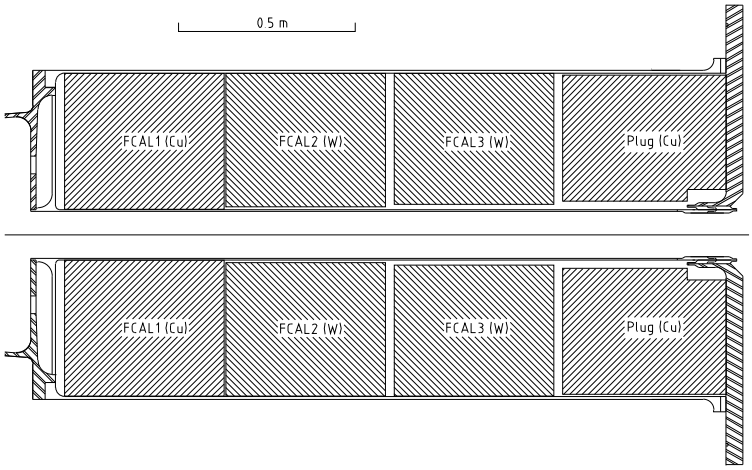

Figure 3.12: Cut view of one FCal. The three modules can be seen. The last layer or "plug" is a shielding [66].

Sub-detector	Size of HV zone $\Delta\eta \times \Delta\phi$	Number of HV Lines
PS Barrel	0.4×0.2	512
EM Barrel	0.2×0.2	896
PS EMEC	0.3×0.2	128
EMEC	0.2×0.2	1024
HEC	1.7×0.2	768
FCal	1.7×0.2	192

Table 3.1: Summary of the LAr HV granularity. For the HEC and the FCal, one HV line feeds the whole η range covered [83].

	range	LAr Gap (mm)	nominal HV (kV)
EMB	$0 - 1.475$	2.1	2
EMEC outer wheel	$1.375 - 1.5$	2.7	2.5
	$1.5 - 1.6$	2.5	2.3
	$1.6 - 1.8$	2.2	2.1
	$1.8 - 2.0$	1.9	1.7
	$2.0 - 2.1$	1.6	1.5
	$2.1 - 2.3$	1.4	1.25
	$2.3 - 2.5$	1.2	1.0
EMEC inner wheel	$2.5 - 2.8$	2.5	2.3
	$2.8 - 3.2$	2.0	1.8
HEC	$1.5 - 3.2$	8.5	1.8
FCal	FCal1	0.3	0.25
	FCal2	0.4	0.375
	FCal3	0.5	0.5

Table 3.2: Summary of the LAr HV properties. The gaps thickness are expressed in mm, the HV in kV [66].

	$\lvert\eta\rvert$ range	layer 0	layer 1	layer 2	layer 3	# cells
EMB	$0 - 1.475$	0.025×0.1	0.0031×0.1	0.025×0.025	0.05×0.025	109568
EMEC	$1.375 - 1.425$	–	0.05×0.1	0.05×0.025	–	640
	$1.425 - 1.5$	–	0.05×0.1	0.025×0.025	–	1837
	$1.5 - 1.8$	0.025×0.1	0.025×0.1	0.025×0.025	0.05×0.025	22300
	$1.8 - 2.0$	–	$0.025/8 \times 0.1$	0.025×0.025	0.05×0.025	12411
	$2.0 - 2.4$	–	$0.025/6 \times 0.1$	0.025×0.025	0.05×0.025	20569
	$2.4 - 2.5$	–	$0.025/4 \times 0.1$	0.025×0.025	0.05×0.025	3737
	$2.5 - 3.2$	–	0.1×0.1	0.1×0.1	–	2250
HEC	$1.5 - 2.5$	–	0.1×0.1	0.1×0.1	0.1×0.1	5632
	$2.5 - 3.2$	–	0.2×0.2	0.2×0.2	0.2×0.2	
FCal	$3.1 - 4.9$	–	2 mm^2	3.5 mm^2	5.6 mm^2	3524

Table 3.3: Cell sizes of the different LAr Calorimeter sub-detectors. The sizes are given in terms of $\Delta\eta \times \Delta\phi$ for all sub-detectors, except for the FCal, where the sizes are in mm^2. [66]

The Front End [93] electronics is located on the detector. It needs to be highly reliable since it can only be accessed during long shutdowns[1].

The Back End [94] consists of all the instrumentation which is located off the detector, and it is mostly located in the counting room of the ATLAS experiment (USA15).

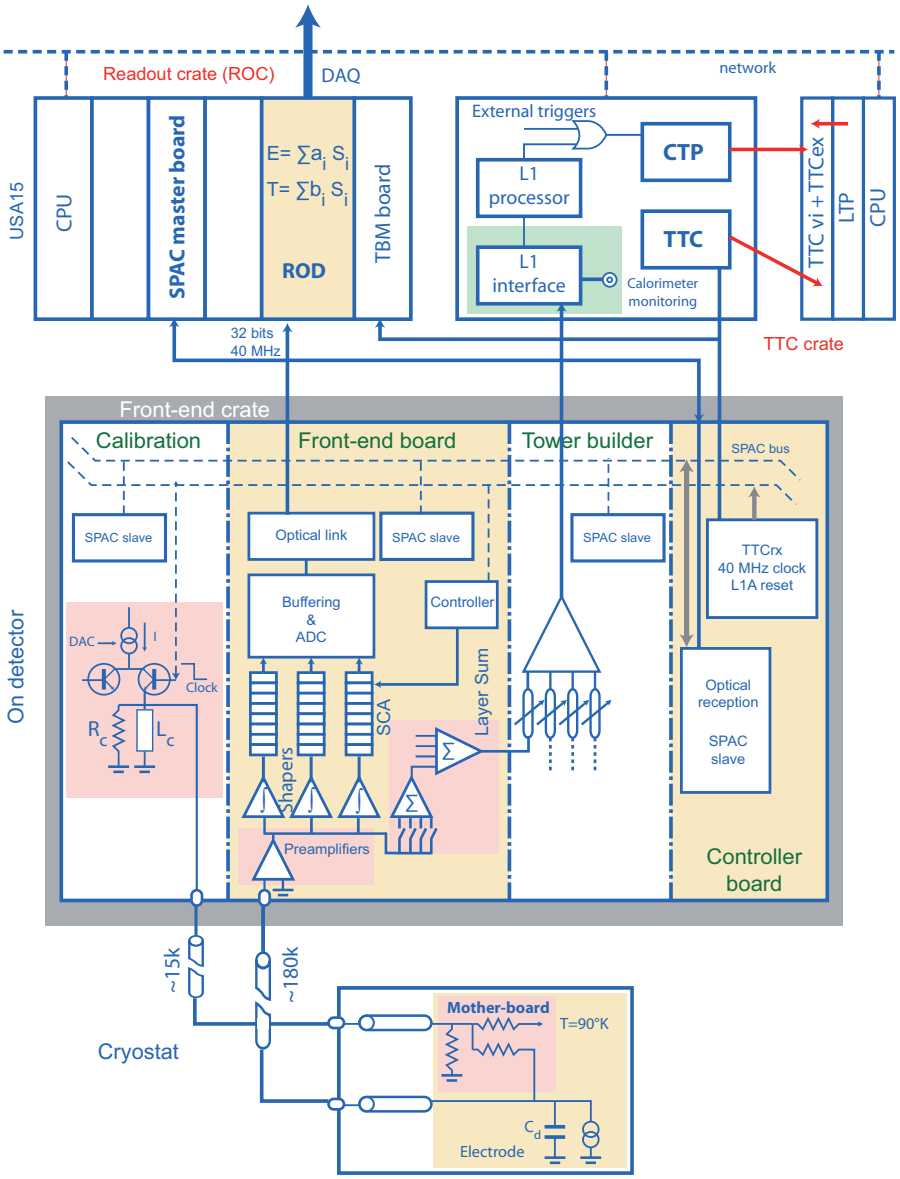

Figure 3.13: Block diagram of the LAr readout chain [66].

3.2.1 Front end electronics

Overview

The treatment of the ionization signal in the Front End Board (FEB) [95] is as follows:

- The signal from the electrodes are summed in the front and the back of the LAr modules by the Summing Boards (SB) which groups cells in ϕ. Figure 3.14 shows a schematic view of three SB and one Mother Board.

[1]Everything which is located inside the cryostat is irreplaceable [83]. For the electronic located outside the cryostat, an opening of ATLAS is required to reach it.

- The cell signal is then transported outside the cryostat *via* the Feed-Through (FT), to FEB. In the case of the HEC, the signal is first pre-amplified[2] inside the cryostat.
- The signal is amplified on the FEB. The treatment in the FEB is shown on Figure 3.15.
  - The signal is shaped using three different gains on the shaper chip, and then sent to the Switched Capacitor Array (SCA), to wait for the L1 trigger accept. If the event is accepted, it is digitized in the Analog to Digital Converter (ADC). It is then sent optically, by the Optical Transmitters (OTx), to the Read Out Driver (ROD) [96] away from the detector.
  - Signals from each layer of a Trigger Tower (TT) are built on the FEB and transmitted to the Trigger Board Builder (TBB) which then align in time and transfer to the L1 Calo processor to select the event in less than 2.5 μs.
- The Front End Crates (FEC) houses ,the FEB, the Calibration Board (CB), the TBB and the Trigger and Timing Control (TTC) control board [93].

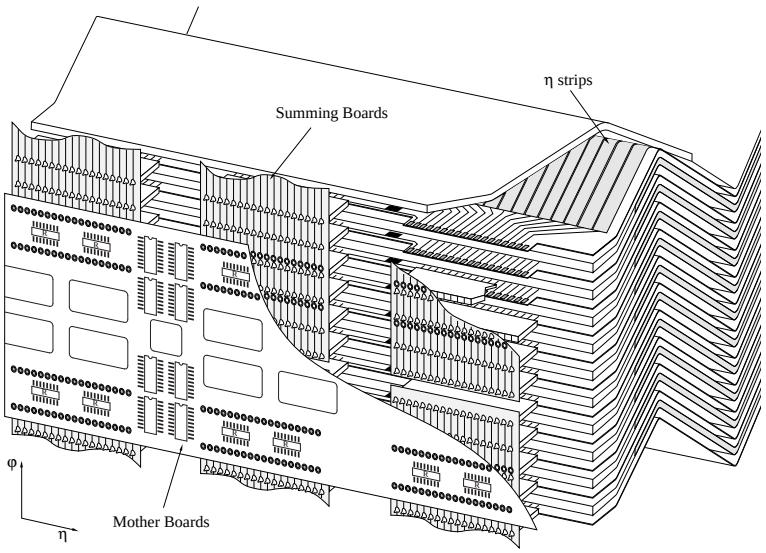

Figure 3.14: Schematic view of a barrel module. The electrodes are summed depending on the layer granularity, to form the readout cells. Are visible the Summing Boards and the Mother Board [66].

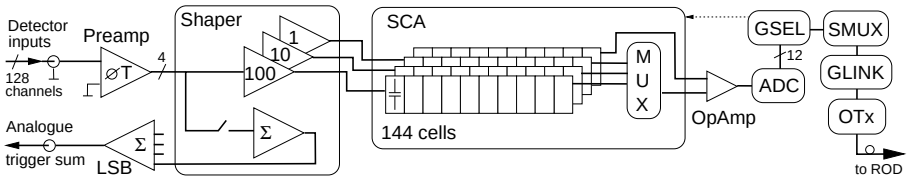

Figure 3.15: Block diagram of the signal treatment within the FEB. The signal arriving from the cryostat comes from the left side of the diagrams and is sent to the back end at the right side of the diagram [66].

[2]The GaAs amplifier are installed on the upper part of the wheels, they provide an optimum signal to noise ratio for the HEC [83]

3.2.2 Trigger

The signal is summed analogically in the Tower Builder [66]. The granularity of each EM tower[3] is $\Delta\eta \times \Delta\phi = 0.1 \times 0.1$. The signal is sent to the L1 processor, located in USA15, where an algorithm seek for maximums passing a defined threshold. Figure 3.16 shows a schematic view of the L1Calo algorithm. It searches for RoI's by computing sums over the different tower in the EM and hadronic calorimeters. An isolation ring can also be computed to account for the occupancy of the event. If some RoI's have been identified, the L1 accept is sent to the FEB in less than 2.5 μs, so that the event is digitized.

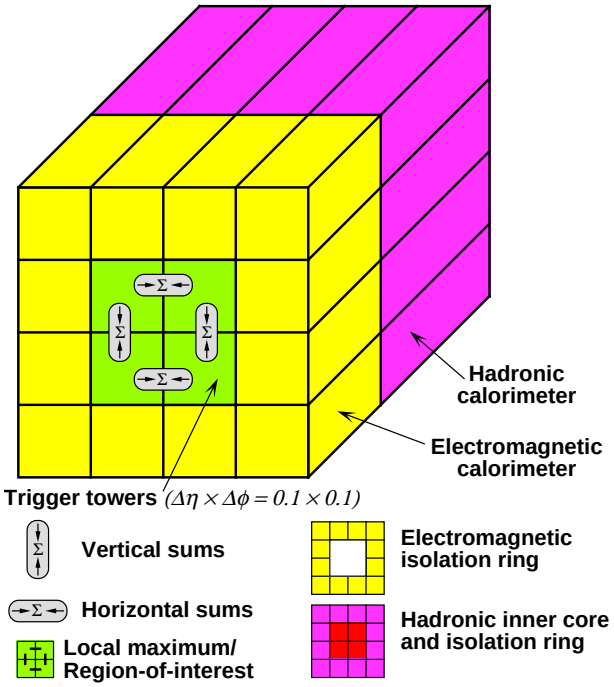

Figure 3.16: The L1 algorithm to find EM RoIs [66].

3.2.3 Back end

The signal coming from the FEBs OTx is received by the optical receivers (ORx) mounted on the Read Out Drivers (ROD). Each ROD collects the signal coming from eight FEBs, and so treats up to 1024 cells. Figure 3.17, shows a schematic view of ROD. The signal is de multiplexed by the inFPGA, and sent to the Processing Units (PU). In each PU, two Digital Signal Processors (DSP) will reconstruct, from the digits, the energy. If the cell energy is greater than a threshold[4] defined at the beginning of the run, the quality factor and the time are also reconstructed. The samples of these high energetic cells are also saved to be able to reconstruct the energy more precisely offline.

Readout structure

For practical reasons, the calorimeter readout was divided into eight[5] independent partitions namely:

- EMBA and EMBC: which regroup the electromagnetic barrel (448+448 FEBs).
- EMECA and EMECC: Which regroup the electromagnetic end-caps (276+276 FEBs).

[3]The hadronic tower granularity is $\Delta\eta \times \Delta\phi = 0.2 \times 0.2$.
[4]This threshold is for most of the recent run three times the electronic noise value.
[5]4 partitions for the A side and 4 for the C side, cf Section 2.2.1.

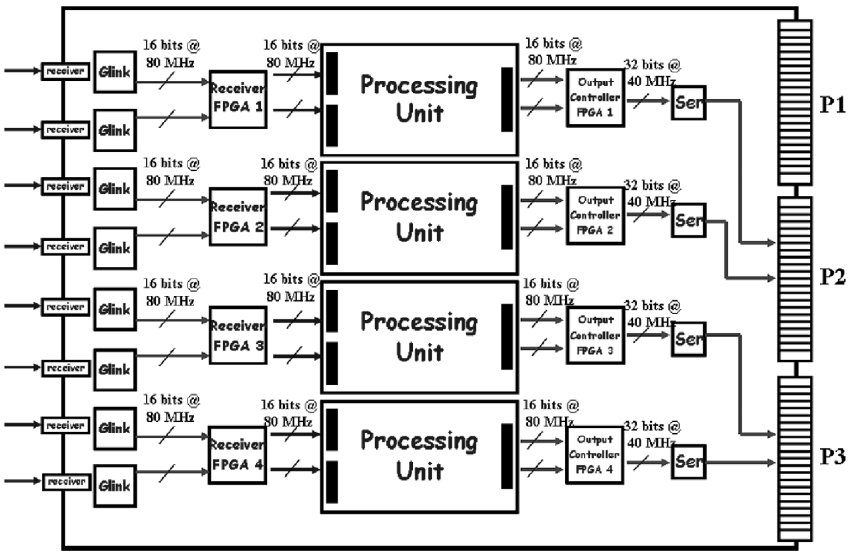

Figure 3.17: Schematic view of a Read Out Driver (ROD) card [24].

- HECA and HECC: Which regroup the hadronic end-caps (24+24 FEBs).
- FCALA and FCALC: Which regroup the forward calorimeters (14+14 FEBs).

The 182468 LAr cells are connected to 1524 FEBs. Each FEB treat at maximum 128 channels. The FEBs are installed outside the cryostat on the FEC. They are connected in the cryostat by the Feed Through (FT). For the barrel their is 64 FT and 50 for the end caps. The FEBs are known *via* their front end crate slot number and FT number. For the end-cap partitions their are at maximum 15 FEBs per FT, and for the barrel 14 FEBs per FT.

3.3 Signal treatment and calibration

The front end and back end treat the signal coming from the electrodes in the cryostat and converts it in energy, time and quality factor. In this section the reconstruction and calibration is presented.

3.3.1 Shaping and digitization

The ionization signal has a triangular shape given by

$$I(t) = \theta(t) I_0 (1 - \frac{t}{\tau_d}) \theta(t - \tau_d) \tag{3.1}$$

Where τ_d is the electrons drift time in the LAr and I_0 is the total intensity over the drift time. Figure 3.18 show the intensity of the triangular signal over time. The barrel drift time[6] is typically on the order of $\tau_d \approx 450\ ns$ [66].

The nominal bunch crossing interval at the LHC will be 25 ns, it is the frequency at which the channel signal is sampled. The signal is pre-amplified, and shaped by a bipolar filter $CR-(RC)^2$. The resulting shaped signal is shown on Figure 3.18. The signal amplitude is recovered in 50 ns, followed by an undershoot which stands for approximately 300 ns. As the bunch crossing frequency is much less than the complete drift time, the calorimeter is affected by the pile-up of the events. The signal bipolar shape allows to cancel in mean the contribution of the out of time pile-up, because the signal integral is null.

[6]For the FCal, the drift time is approximately $\tau_d \approx 60\ ns$.

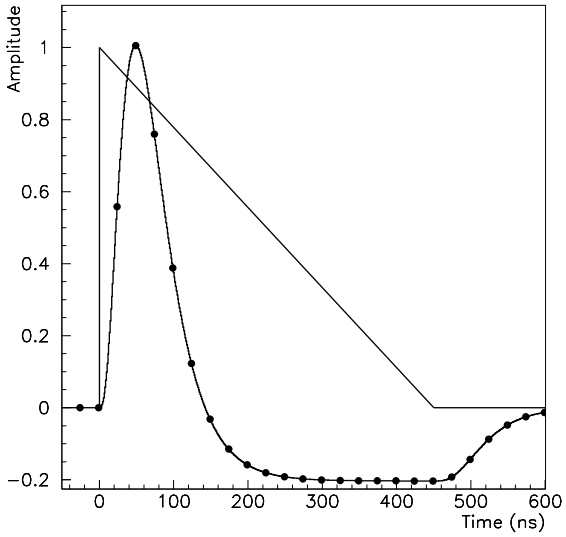

Figure 3.18: The triangular LAr signal. The shaped signal is also showed [66].

The dynamic range of the signal produced covers from about 10 MeV to a few TeV, corresponding to approximately 16 bits, however at the time of the LAr calorimeter construction only 12 bits ADC were existing. For this reason the signal is shaped three times in parallel using different gains. The ratio of the gains are about 100/10/1. The signals shaped are then stored in three switched-capacitor array (SCA), to wait for the L1 Accept. The gain is chosen from the sample with the maximum amplitude. The timing is adjusted so that the maximum sample is the third one for particles coming from the Interaction Point. The gain decision is made from the third sample digitized in the medium gain. The proper timing and saturation of the samples is checked in the monitoring, as this is explained in section 3.4. The signal is sent to a 12 bits Analog to Digital Converter (ADC), where it is digitized. In regular running conditions only five samples (125 ns) are kept, up to thirty two samples (800 ns) can be taken in particular running conditions.

3.3.2 Calibration

The calibration of the acquisition chain is performed during dedicated runs, outside the data taking. A known exponential signal is injected on the readout chain, using Calibration Boards [97]. The intensity of the calibration signal injected, is driven by a Digital to Analog Converter (DAC). The signal obtained after shaping is shown on Figure 3.19, the ionization signal is also shown.
The purpose of the calibration is to:

- Check the connectivity of the electronics.
- Measure the electronic pedestal value of all channels.
- Measure the gain of the electronic.
- Measure and follow the pulse shape of the channels.

Some factors are not measured during calibration runs:

- The factor allowing to convert from μA to MeV. It was determine for each channel during the test beams and from MC simulations. It is also re-calibrated using the electrons coming from Z bosons decays [76].
- The correction factor in case of a reduced HV region, as it will be explained in section 3.3.5, is computed offline.

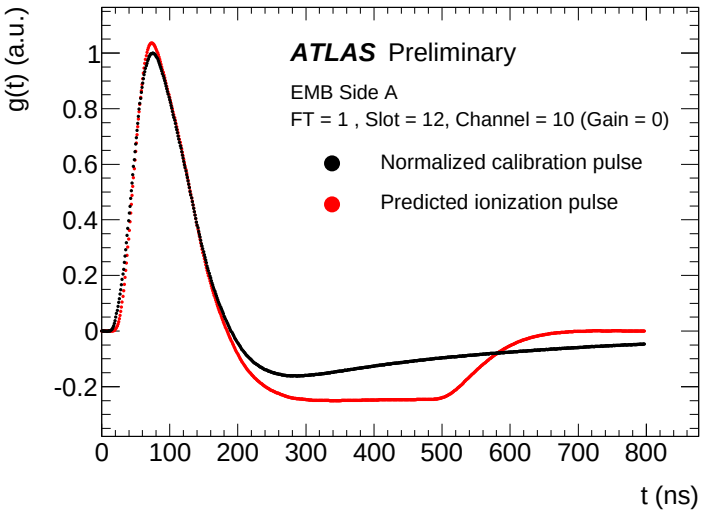

Figure 3.19: The calibration signal of a LAr channel from the barrel is shown in black. The physics pulse is shown in red [62].

3.3.3 Amplitude, time and quality factor calculation

Each DSP processes the data coming from a single FEB. The main purpose of the DSP is to reconstruct the amplitude of the cells using a method called Optimal-Filtering (OF).

The digitized signal is characterized by its maximal amplitude A, measured in ADC count, and the time to which it arrives with respect to the LHC clock, τ, measured in ns.

The OF method provides an unbiased estimator of A and the product $A\tau$, using a linear combination of the samples. The coefficients are called the Optimal Filtering Coefficients (OFC). This method allows to reduce the contribution of the electronic and pile-up noise, by using information from all the samples.

The amplitude is given by the relation [66]

$$A = \sum_{i=1}^{N_s} a_i(s_i - p) \tag{3.2}$$

The time is evaluated using the amplitude and from the relation

$$A\tau = \sum_{i=1}^{N_s} b_i(s_i - p) \tag{3.3}$$

And finally the quality factor, which is a non normalized χ^2 of the expected ionization pulse shape, is given by

$$Q = \sum_{i=1}^{N_s} [s_i - p - A(g_i + g_i'\tau)] \tag{3.4}$$

In these three equations, N_s is the number of samples available, p the pedestal value of the corresponding readout channel, a_i and b_i the OFC, g_i and g_i' are respectively the normalized ionization pulse shape and its derivative with time.

3.3.4 Determination of the energy

The energy is obtained by multiplying the amplitude to a conversion factor:

$$f = F_{\mu A\rightarrow \text{ MeV}} \times F_{DAC\rightarrow\mu A} \times \frac{1}{M_{\text{phys}}/M_{\text{cal}}} \times C_{HV} \times G(\frac{DAC}{ADC}) \quad . \tag{3.5}$$

Where :

- $F_{\mu A \rightarrow \text{ MeV}}$ is a factor allowing to convert the current collected on the electrode in energy.
- $F_{DAC \rightarrow \mu A}$ is a factor allowing to convert the DAC values to a current, it is know up to 0.1%.
- $M_{\text{phys}}/M_{\text{cal}}$, is a factor which takes into account the differences between the calibration signal and the ionization signal.
- C_{HV} is a factor to takes into account the reduced HV regions.
- G is a polynomial function written $G(A) = R_0 + R_1 \times A$, allowing to convert a known analog signal (DAC) to a digital signal in ADC count.

3.3.5 What happen in the case where the HV is reduced

Figure 3.20 shows the ionization signal in the case where the electrode is fed with the nominal HV in gray and in the case where the HV is reduced in blue. The charge collection is equivalent, but the electron drift time is larger in the nominal case.

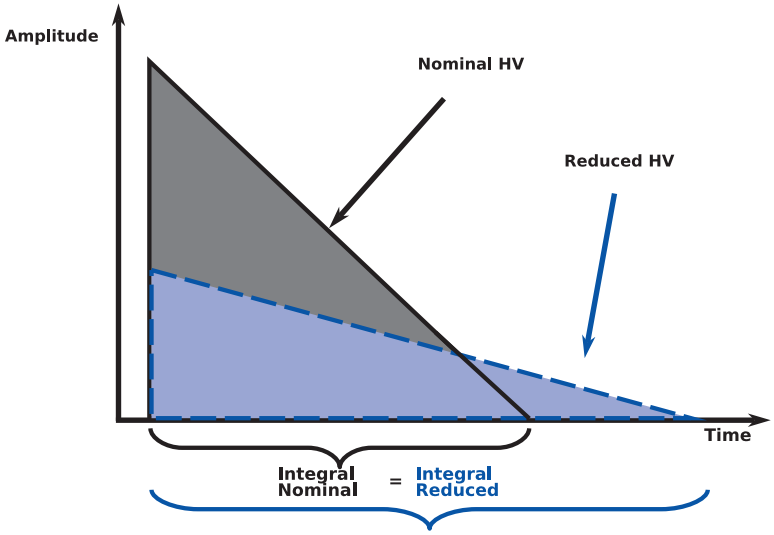

Figure 3.20: The triangular LAr signal in the case where the HV is nominal and non nominal.

Figure 3.21 shows the measured energy of electrons from test beams as a function of the HV fed to the barrel electrodes, for the case of 245 GeV and 100 GeV electrons. If the electrodes are not fed with the nominal HV value, the energy reconstructed has to be corrected by a multiplicative factor [98]. In the barrel, the correction factor can be determined from the fit of these data. The function used is

$$f(U) = a \times U^b \tag{3.6}$$

Where U is in Volt, and f(U) in GeV, the fit gives $a = 13.3 \pm 0.2$ and $b = 0.38 \pm 0.01$ for the barrel.

The correction factor is given by

$$f_{\text{corr}}(U_{\text{red}}) = \frac{f(U_{\text{nom}})}{f(U_{\text{red}})} \tag{3.7}$$

And finally the energy corrected is obtained *via*

$$E_{\text{corr}} = f_{\text{corr}}(U_{\text{red}}) \times E_{\text{meas}} \tag{3.8}$$

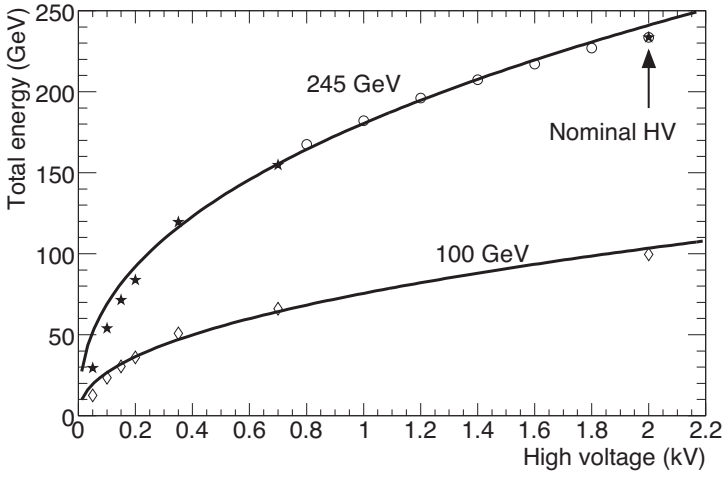

Figure 3.21: Measured electron energy as a function of the HV fed to the electrodes, obtained from test beams, with 245 GeV (open circle) and 100 GeV electrons (diamonds) [98].

Figure 3.22 shows the correction factor computed for the cells in a non nominal HV area in the barrel. Most of the cells have a correction factor of 1 meaning that the HV is nominal.

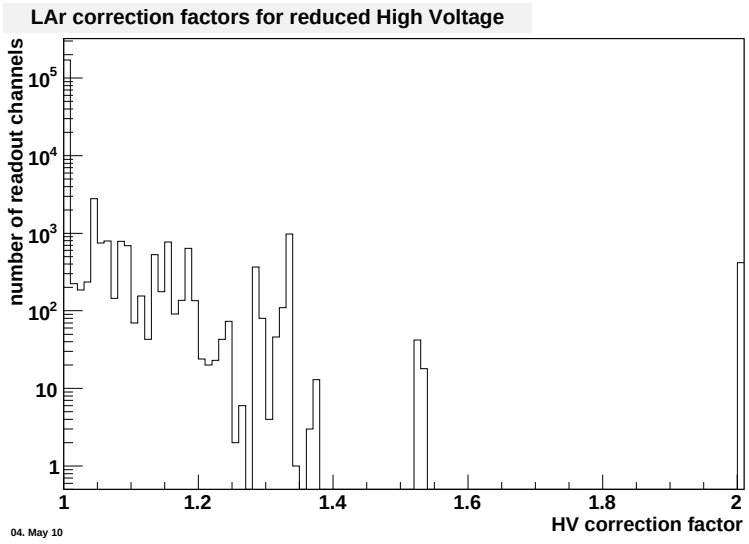

Figure 3.22: HV corrections factor for the Barrel [62] for a 2010 run.

Why are there reduced HV area?

There are at least three different cases that have lead to reduced HV area:

- During the construction of the LAr calorimeter, some HV sector have been found to exceed the maximum current consumption the HV Power Supply is able to provide, for example in the barrel it is about ($\approx 75\ \mu$A) [99]. A dedicated HV power supply was designed to allow an higher current consumption up to 3 mA. Event though this effect is not perfectly understood, it seems to come from impurity in LAr that will make a bridge between the electrode and the anode, leading to a resistive effect. For this reason even if the current consumption may be higher, most of these HV lines are operated at a lower HV value than the nominal one. These HV lines are

said to be in the "Hospital". In the summer 2011, there was 34 HV hospital lines in the barrel and 39 in end caps. They corresponds to most of the entries above one in Figure 3.22.

- The LAr calorimeter has experienced some instability of the HV system, mainly in the EMEC, during LHC collisions. This phenomena is not fully understood, but it occurs when a liquid argon gap is asking for more current than the power supply can provide. The affected line switch off and ramp down to 0 V. The HV modules can detects the trips and automatically ramps up the HV back to nominal.

  Figure 3.23 (a) shows the sequence of events in the case were the auto recovery procedure worked. In the first step the HV is nominal. In the second one the trip starts, the HV is going down. The trip is detected, and in the third step the power supply ramps up to its nominal value. In this case the correction factors are computed at the end of the second step. And they are recomputed every lumi-blocks until the nominal value is reached in the fourth step.

  Figure 3.23 (b) shows the same sequence of events in the case were the auto recovery is switched off. The trip occurred, and the HV is going down to 0 V. In the third step the electrode is only fed by the other HV line. The corrections factors needs to be computed at this point. In the fourth step the ramp up of the HV starts, the correction factor are recomputed every lumi-blocks until the nominal value is reached in the fifth step.

  In both cases the events that were triggered during the ramp down, were not used in the physics analysis, because they contains more noise. In 2010, the events that were triggered during the ramp up were also excluded from physics analysis. However after careful checks, it was shown that during this period the level of noise was under control. In 2011 these events are used in the analysis.

- During 2010 data-taking, the pre-sampler experienced a series of sporadic noise that was correlated to the increase of luminosity. The precise origin of these shortcomings is not known, but at some point, during summer 2010 it was decided to reduce the HV from its nominal value of 2 kV to 1.6 kV. This decision was taken to protect the pre-sampler, since then the situation is more stable.

3.4 Data acquisition and monitoring

The data are taken by the ATLAS experiments depending on the LHC conditions. The running conditions have evolved over the last years.

- In 2008 because of the LHC incident, only beam splashes events and cosmic data were recorded.
- In 2009-2010, the first real collisions were recorded, allowing to retrieve all the standard model physics that was discovered in the last century.
- In 2011 with the luminosity increase, the first competitive searches for new physics at 7 TeV were conducted.

These different running conditions have allowed a deeper commissioning of the different sub-systems along the time. For example the Event Filter was fully commissioned on data before being turn on in the middle of the 2010 run.

The monitoring and the data quality was also developed at the same time to first understand detector related problems, and later on discrepancy in the physics reconstruction.

3.4.1 Data acquisition and event reconstruction

The events are reconstructed using the official ATLAS framework: Athena.

Athena regroups all the software used to perform a physics analysis in ATLAS. It allows:

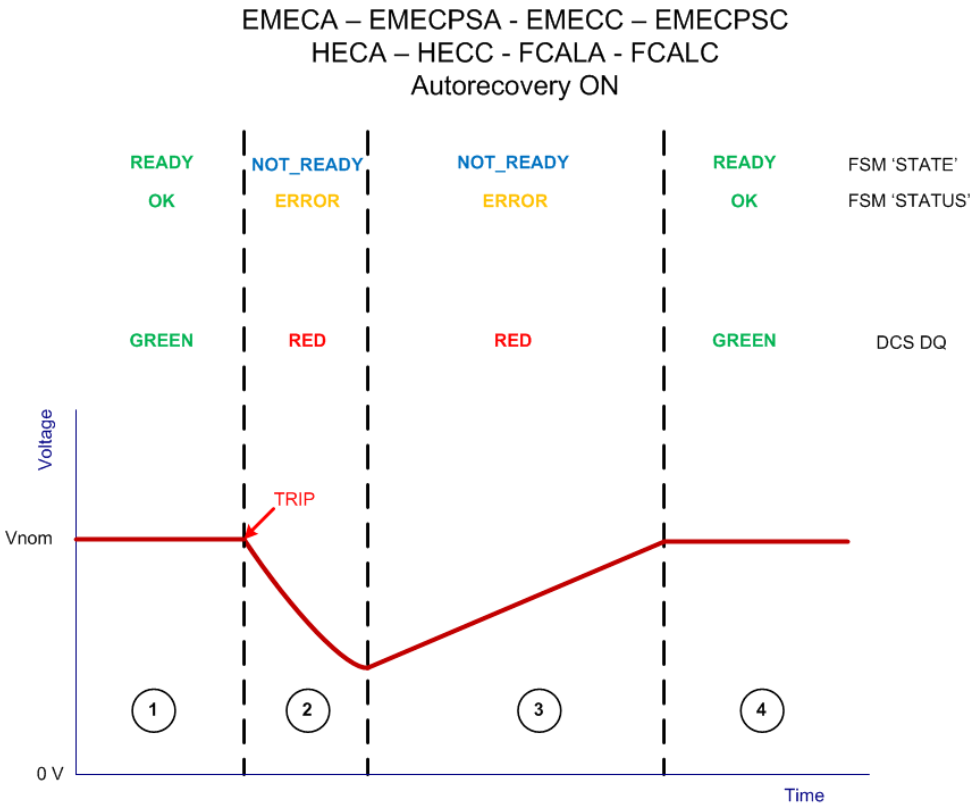

(a) Case were the auto recovery procedure works.

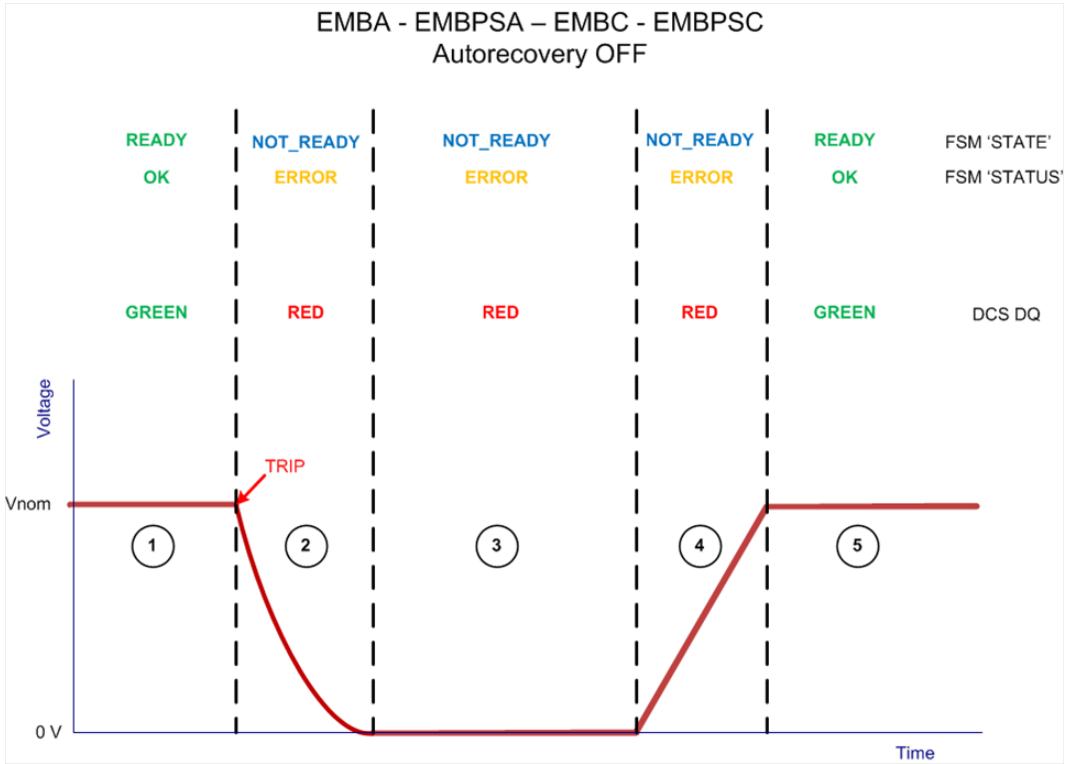

(b) Case were the auto recovery procedure is off.

Figure 3.23: Summary of the LAr HV trips scenario [62].

- To generate events, using almost all the Monte Carlo generator available in HEP.
- It contains the Full Geant 4 [100] simulation of the ATLAS detector.
- The simulated event are also digitized to simulate the electronic response of the detector, and passed through a simulation of the trigger system.
- Finally the reconstruction of the data, allows to pass from the low level detector quantity (ADC count for calorimeter channels, hit points in the tracker,*etc*), to the high level physics objects, such as electrons, photons,*etc*.

During data taking only the reconstruction is used, the other parts are used for Monte Carlo generation.

When data are taken, the events are classified in streams depending on the trigger item that was used to acquire them. This streaming allows an easier determination of the hardware problems that might raised during data taking. The events are also classified by final states this way, which makes physics analysis easier to be conducted.

The events are reconstructed online, using a specific set of calibration constant to check whether the detector conditions or the data integrity are proper. If a dramatic change occurs during data taking, then the run will be stopped, in order to reconfigure the faulty sub-system, or to perform an intervention on it.

Offline the reconstruction of the data is performed in two steps. About 10% of the overall amount of data is reconstructed in a stream called *express stream*. The reconstruction of this stream allows a preview of the *Bulk Processing*, when the full run is reconstructed. This stream allows to compute precise calibration constants that will be applied on the reconstruction of the full run. It also allows to spot and mask noisy segment of the detector, such as calorimeters channel. The determination of the calorimeter noisy channels is made using a dedicated stream called *CosmicCalo*, were the events have been triggered by the calorimeter, but in empty bunches. These allow to see in particular high energy deposition in the calorimeter at a time where we expect not to have some.

The calibration of the *express stream* is made in 36 hours at most. Then the reconstruction of the full run can start, it is called the *bulk processing*. Once the full statistics are processed, the data quality of the run can be assessed. The data are then sent to storage in order to be analyzed.

3.4.2 Data quality

The run is divided in lumi-blocks, which are periods of approximately one minute[7]. A data base is filled at the end of the bulk processing with a list containing the good lumi blocks that will be useful for the physics analysis. The lumi-blocks that are excluded for physics analysis are classified by their defects in order to allow studies of detector related problems.

There is a strong needs to have a robust and reliable monitoring of the data acquisition, that allows to spot without any ambiguity the problems encountered during data taking, and compute corrections factors if needed.

3.4.3 Monitoring

The LAr monitoring consists of several algorithms available in the Athena reconstruction, regrouped in a single package called LArMonTools [101].

This monitoring is used online, allowing to spot directly problems that may cause an interruption of the run if the detector is mis-functioning or if some parameters are wrongly loaded. It is also used offline to spot the problems that were not severe enough to stop the data taking or the one that have passed the vigilance of the shifters.

[7] In 2010 the lumi-blocks were approximately 2 min.

Detector conditions

One of the detector condition that is monitored during data-taking is the HV status. Its monitoring is shown on Figure 3.24. This figure was obtained on a 2011 run, and summarizes the reduced HV regions in this particular run, for the first second and third layer of the EM barrel A. The area in white is the one with a nominal HV value. The sectors in green are the ones with a non nominal HV value. For these sectors, the correction factors are computed offline as explain in Section 3.3.5. They are used in the reconstruction of the energy.

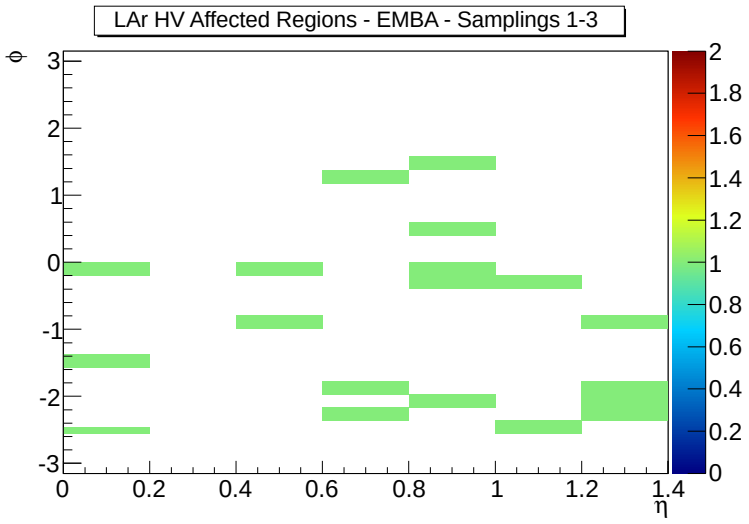

Figure 3.24: Monitoring histogram of the HV conditions obtain for run 179710, which was a 2011 collision run. The histograms show the conditions for the HV zones in barrel A.

Misbehaving Channels

The misbehaving channels [102] are all the cells which have an abnormal status:

- Dead channels.
- Abnormally noisy channels.
- Distorted pulse shape.

They are stored in a dedicated data-base with different flags explaining their pathologies. In most of 2011 run, less than 2000 channels on the 182468 LAr cells were flagged as having a problem. In the cryostat this represents about 1%. On this amount of channels only 42 are dead channels which is about 0.02% of the total amount of LAr cells.

The monitoring of the channels is done offline at the reconstruction level. It monitors the empty bunches, at a time were no collisions are expected and therefore no signal is expected in the LAr calorimeter. If a new bad channel is discovered, and starts to be problematic, it is masked during the reconstruction, and its energy is set to 0. This monitoring is done on a run to run basis. The channels that appear noisy in a large amount of run and the one that are known to misbehaved from calibration runs are kept in this data-base, but their status is checked from time to time. The channels that appears misbehaving in a single run are masked for this run only.

3.4.4 Monitoring of the high energy digits

As said in Section 3.3, the energy, time and quality factor of each cells are reconstructed from the LAr cell samples.

The online reconstruction, performed in the DSP, relies on the proper timing alignment of the ionization pulses, the appropriate description of the pulse shape (OFC) and the correct choice of the electronic gains. The online monitoring "High Energy Digits", provides an essential checks of these conditions.

In order to monitor only the cells where real energy deposition is recorded, they are selected only if $E_{\text{cell}} > 5\sigma_{\text{Noise}}$. The known misbehaving channels are excluded from this monitoring.

The algorithm looks for the maximum and the minimum samples in the 5 available digits. It checks their temporal position, and if they are saturated (*ie* the value of one sample is equal to 4095 ADC counts or the value of the minimum sample is equal to 0 ADC counts).

This monitoring algorithm was designed for hardware commissioning of the LAr calorimeter. For this reasons the hardware segmentation of the calorimeter is used to check problems. It was extensively used during cosmics and beam splashes runs in 2008 and 2009, and during the first collisions in 2010. Now that the detector is more understood, one prefer to relies on higher level objects such as channel clusters and their impact on the jet or photons/electron reconstruction. But this algorithm as also allows to discover more recently detector related problems that were not expected.

Monitoring of the shape

When the cell is selected, the five samples are normalized with respect to the ADC count value of the maximum sample. The normalized shape obtained is added to a profile histogram. This histogram is unique for each sub-partition and run.

The goal of this monitoring is to check whether the average pulse is as expected. If it is not the case, then the energy that is computed by the OF methods will be wrong. As this check is averaging all the pulses of partition in a run, it will allow to detect a coherent problem within the partition, and not a problem affecting a single channel. Having an average pulse shape as expected, means that all the treatment applied to the channels of a single partition, timing setup, pedestal values, *etc*, are fine.

In most of the cases when the average pulse shape is distorted it means that most of the pulses that are entering this histograms doesn't contains an ionization pulse, but that the noise value has increase giving a wrong estimation of the energy. The calibration constant were not propagated into the data-base. This effect was essentially seen during cosmic data-taking in 2008. It is extremely rare in regular conditions.

An example taken from a 2011 run is shown on Figure 3.25. The average pulse shape is shown here is drawn for the EMBA partition. In this case the pulse shape looks as expected: the first sample is almost null, while the third one is almost at one. If everything was perfect, the third sample should be exactly at one in amplitude, and the first one exactly at 0. In 2011 the bunch spacing is 50 ns. This means that if an energy deposition is recorded in the calorimeter due to out of time pile-up, the sample with the maximum amplitude will be the first or fifth one and not anymore the third one. This effect can be seen in Figure 3.28 (c), where two peaks around the main one can be seen at ± 50 ns apart.

Monitoring of the timing

Figure 3.26 shows the sketch of two LAr pulse shapes. In the first case, in black, the pulse is on time, the third sample (75 ns) is the one with the maximum amplitude. In the second case, in blue, the pulse is shifted by 25 ns. The third sample is not anymore the one with the maximum amplitude. The problem in that case, is that the gain switching selection might be wrong, and a saturation will occur at digitization. If the delay is larger than 25 ns, then the energy might not be reconstructed at all.

A histogram automatically produced gives the average temporal position of the maximum amplitude sample within a single FEB. In Figures 3.27 and 3.28 each bin represents a FEB, so 128 LAr cells. The x-axis represents the FEB position on the slot, while the y-axis is the FT number of the FEB.

Figures 3.27 shows a map of the average timing per FEB in Barrel A and C for the first run in 2008 where beam splashes were delivered to ATLAS. A splash event is obtained by stopping the beam

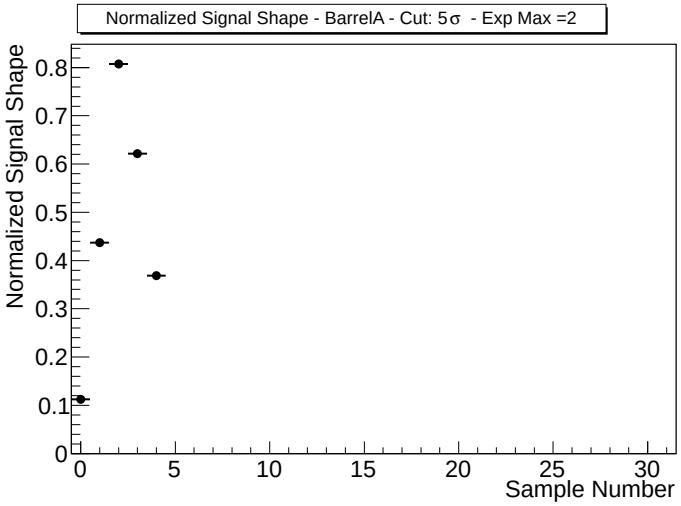

Figure 3.25: Average pulse shape, for barrel A. Monitoring histograms of the High Energy Digits obtain for run 179710, which was a 2011 collision run.

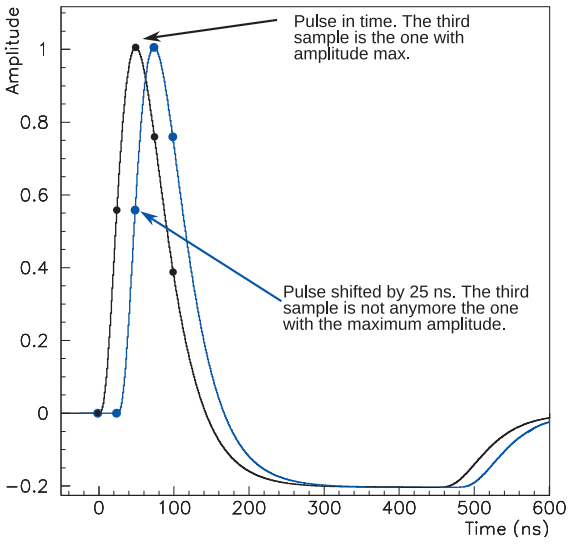

Figure 3.26: Sketch of a LAr pulse shapes. The black one has the proper timing, the blue one is shifted by 25 ns with what is expected.

in a collimator located 140 m upstream from the IP. When the beam, containing 2×10^9 protons, hit the collimator, this creates a shower of secondary particles, muons, pions,*etc* traveling near the speed of light. It will take 150 ns to travel the 44 m of ATLAS, and about 25 ns to cross the full calorimeter. This is a major difference from a collision event, since the particle are produced in the center of the detector and travel in all the directions. Before these beam splashes events only cosmics muons were recorded by the detector. The beam splashes were thus highly expected in the detector, because they were the first beam related events that the detector was recording, and due to the high activity of these events, a huge energy deposition was recorded, allowing to commission further the different detectors.

During this run, the single beam was coming from the C side. The pre-sampler (slot 1) was not recording data properly in the A side due to a configuration problem.

Figures 3.27 (a) and (b) were obtain using the Electrostatic Beam Pick Up Trigger[8] (BPTX), which is a trigger located at 175 m from the IP in ATLAS. The BPTX item was not aligned in time properly with ATLAS at this time, and the signal was recorded by the A side, on the first sample, but not in the C side, because the trigger time correction was not taken into account the particles time of flight. In this case due to the timing difference, the energy was not reconstructed at all in the C side, and poorly in the A side.

It was decided to use a calorimeter based trigger[9] trigger later on. Figures 3.27 (c) and (d) shows the same histograms using this trigger item. The signal was recorded in both sides with approximately 25 ns of difference from the A side to the C side. The timing distribution in both sides is more uniform. But in 2008 the corrections for the timing of each FEBs, such as the cable length, were not precisely computed, explaining the large fluctuation between the FEB timings.

Figures 3.28 shows the same map for a collision runs in 2011. The FEB timing is quite uniform thanks to the timing alignment corrections computed since the beginning of the collisions.

The timing is also checked for the whole partition and for single channels.

Figure 3.28 (c) shows the maximum sample for each selected cell in the barrel A for a 2011 collision run. Three populations can be seen in this histogram. At the third sample which is the expected position of the maximum, and 50 ns after and before it. These last two populations are due to out of time pile-up events, since the bunch spacing in 2011 is 50 ns.

Finally Figure 3.28 (d) shows the percentage of events in a run, where the sample with maximum amplitude is not the third one. This histogram was obtain on the Barrel C on a 2011 run. This fraction of out of time channels is below 0.3% in the worst case. This means that the timing distribution is well under control.

Monitoring of the saturated samples

Figure 3.29 (a) and (b) shows the sketch of a LAr pulse shape, where the digitization is saturated. For Figure 3.29 (a), the maximum amplitude sample value is measured at 4095 ADC count. While for Figure 3.29 (b), the minimum amplitude samples are measured at 0 ADC count. This can occur when the gain switching procedure failed, and the energy of the cell is then not properly reconstructed. The gain switching procedure consist to check the ADC count value of the expected maximum sample in the medium gain.

- If the digit value is $d \lesssim 1400$ ADC count, the high gain is selected.
- If the digit value is $1400 \lesssim d \lesssim 3200$ ADC count, the medium gain is selected.
- If the digit value is $d \gtrsim 3200$ ADC count, the low gain is selected.

The exact switching values where tuned for each channel [87].

The causes of the saturation for a channel can be that the gain switching threshold is too high for this channel, but in most cases, the third sample was not the maximal one, leading to a bad choice.

[8] This trigger item detect the passage of the beam in ATLAS.

[9] *ie* the trigger is fired when activity is recorded in the calorimeter.

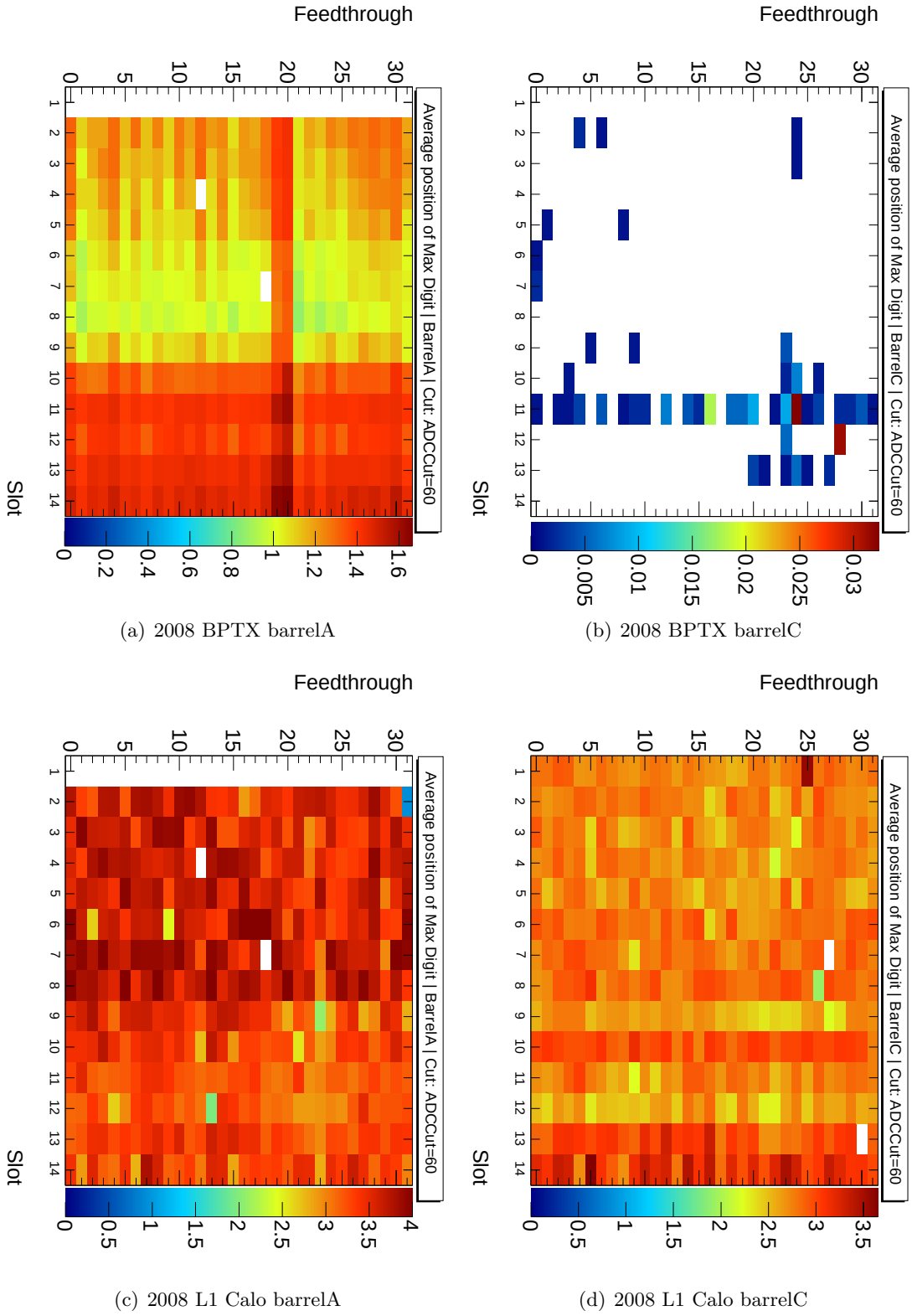

(a) 2008 BPTX barrelA

(b) 2008 BPTX barrelC

(c) 2008 L1 Calo barrelA

(d) 2008 L1 Calo barrelC

Figure 3.27: Monitoring histograms of the High Energy Digits obtain for run 87764, which was the first 2008 run containing beam splash events. The figures represents the average sample max timing per FEB (128 channels).

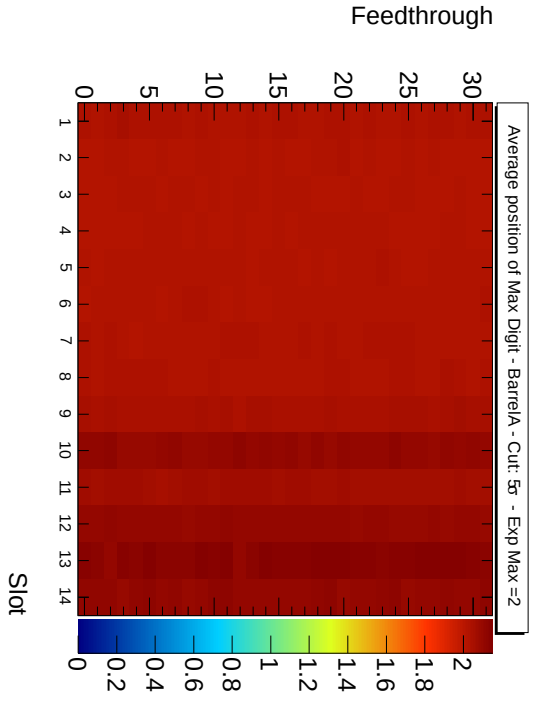

(a) 2011 Barrel A

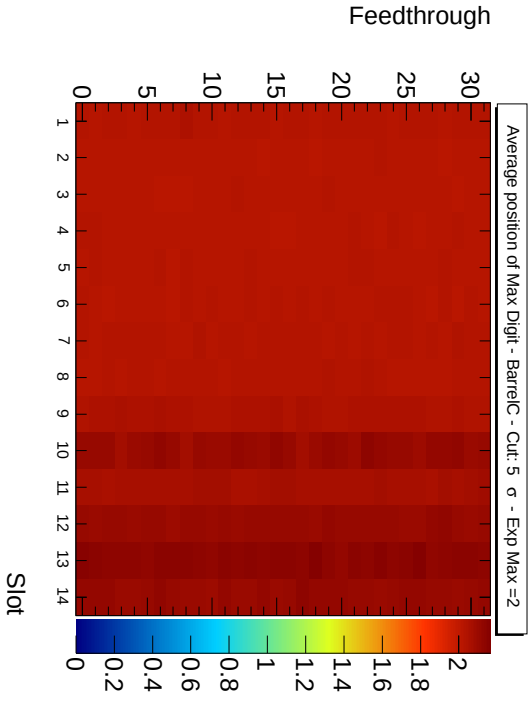

(b) 2011 Barrel C

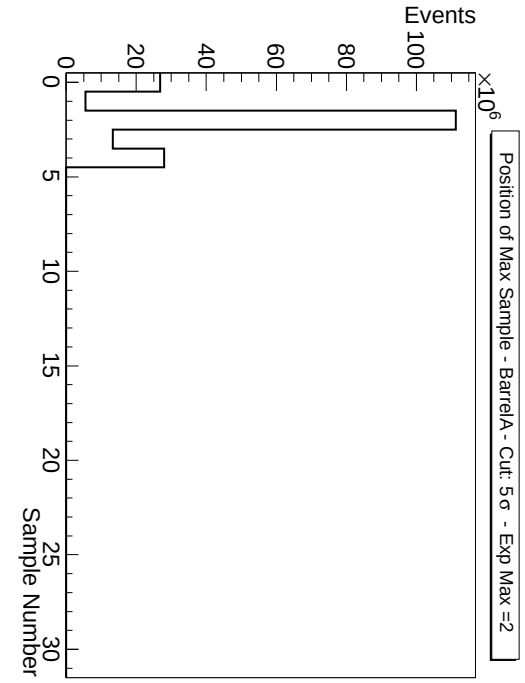

(c) Maximum sample temporal position for the Barrel A

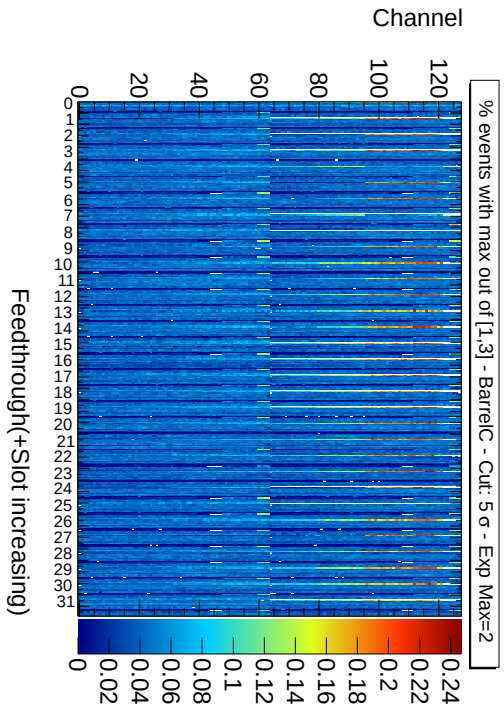

(d) Percentage of channel with their maximum sample not the third one.

Figure 3.28: Monitoring histograms of the High Energy Digits obtain for run 179710, which was a 2011 collision run. The figures (a) and (b) represents the average sample max timing per FEB (128 channels).

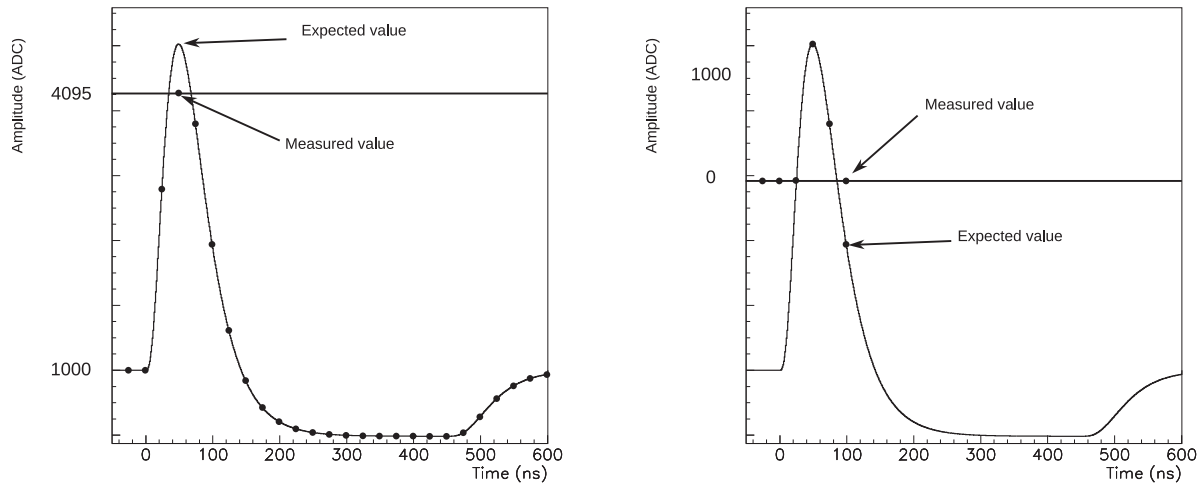

(a) Up saturation.

(b) Down saturation.

Figure 3.29: Sketch of a LAr pulse shape. The digitization is saturated. (a) The expected maximum sample is shown as well as the measured one. (b) The expected minimum samples are shown, as well as the measured one.

The cell saturation is checked *via* four monitoring histograms produced per partition and per run. Two histograms are produced for the upward and downward saturation, one for each FEB, and the other one for each channels.

During 2011 data-taking, the number of saturated FEBs increased in the FCal. The situation was detected thanks to these monitoring plots. The luminosity and the saturation of the FCal channels was correlated. The explanation is that the number of out of time pile-up events was increasing, leading to energy deposition in the FCal, two bunches after the event was triggered. As the gain switching procedure was made on the third samples, which was not anymore the one with the maximum amplitude, one or more sample were found saturated. In order to fix this situation, it was decided that the FCal gain switching will be made only between Medium and Low gain. Figures 3.30 were obtained on two 2011 collisions runs, for FCal A.

Figure 3.30 (a) shows per FEB, the percentage of events where an upward saturated channel was recorded in the run before the medium gain was forced. For the worse FEB, about about 6% of the channels, or 8 channels, are saturated in each event of this run. Figure 3.30 (b) shows the same histograms in the run after the medium gain was forced. The histogram is completely empty now, meaning that the acquisition is not anymore saturated.

Figure 3.30 (c) shows per FEB, the percentage of events where a downward saturated channel was recorded in the run before the medium gain was forced. In the worse FEB, about 53% of the channels, or 68 channels, were downward saturated in this run. Figure 3.30 (d) shows the same plots after the medium gain was forced, again the histogram is empty.

In the hypothetic case were a single channels starts to be abnormally saturated, then the gain switching threshold will be changed, for this channel.

Conclusion

The monitoring of the "High Energy Digits", was essentially made for the commissioning of the LAr calorimeter. For this reasons the histograms gives an output in terms of technical coordinates instead of physics coordinates. This monitoring allows to check that the quantity used by the Optimal Filtering methods, are the one expected:

- The shape of the pulse recorded.

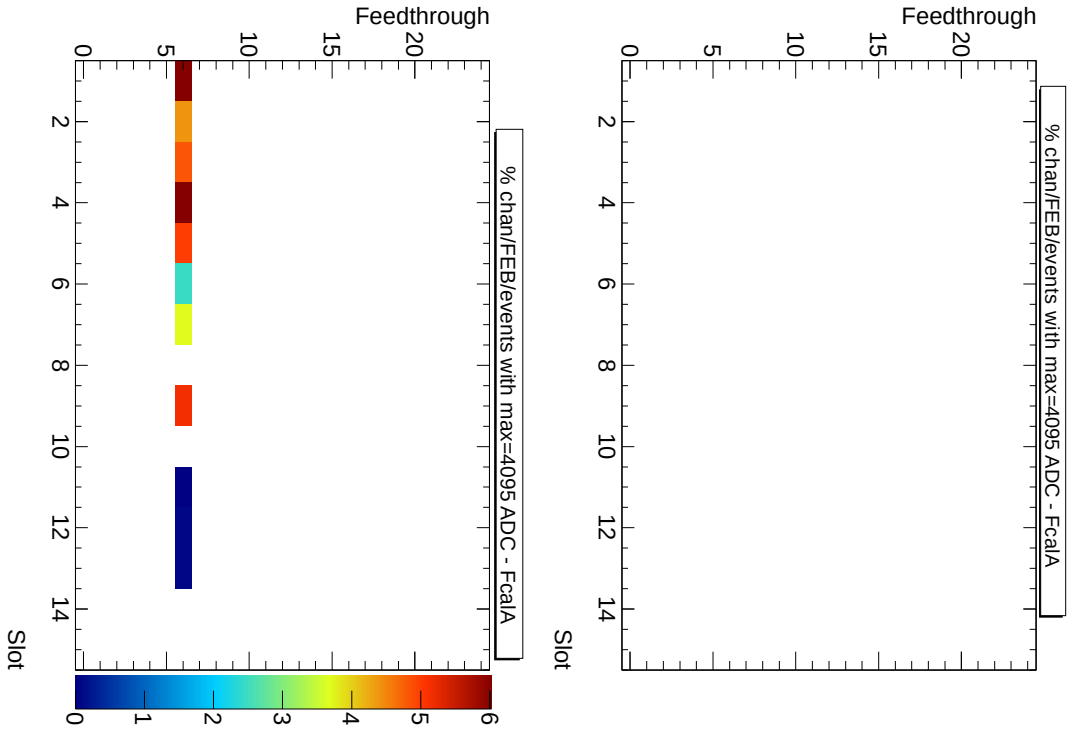

(a) Upward saturation at the FEB level before Medium gain was forced.

(b) Upward saturation at the FEB level after Medium gain was forced.

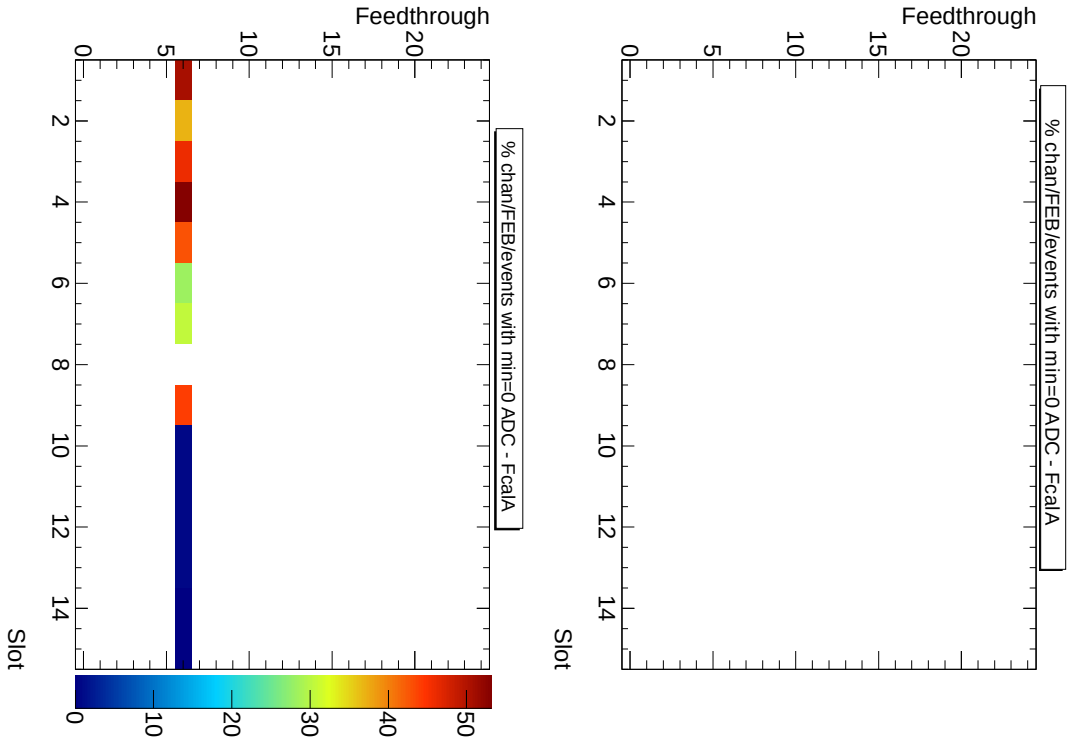

(c) Downward saturation at the FEB level before Medium gain was forced..

(d) Downward saturation at the FEB level after Medium gain was forced.

Figure 3.30: Monitoring histograms of the High Energy Digits obtain for runs 180776 and 182013 which were two 2011 collision runs. Plots were obtained for the FCal A. They show the percentage of saturated channel during these runs.

- The pulse timing.
- The digits value of the samples are not saturated.

This monitoring was extensively used in the first step of the detector commissioning at a time were the detector response was not well known. In particular during the cosmics, beam splash and first collisions, it has allowed to tune the machine parameters to record a proper timing.

Now that the detector is more understood and that more data are recorded, the LAr calorimeter monitoring is more focused on quantities that have a direct impact on the physics reconstruction. For example the noisy channels that induced fake clusters and thus fake jets, photons, electrons or missing transverse energy, are of a bigger interest. The output of this monitoring was still used recently to detect gain saturation related to the out of time pile-up.

Having a strong an reliable monitoring is essential to record proper data and thus conduct physics analysis.

Chapter 4

Jet performance study

"On ne quitte pas une maison qu'on trouve sale. On la nettoie."
René Barjavel, *La faim du tigre.*

Personal contribution
The work described in this chapter follows the analysis described in Reference [79], to recover the jet energy resolution using data driven techniques. The analysis was completely re-implemented within a new analysis framework in order to evaluate the impact of the reduced HV calorimeter regions on the jet energy resolution, since this effect is not included in MC simulation.

Introduction

In the last Chapter, the importance of the knowledge of the detector and data quality was explained. In this Chapter, one will see that understanding the performances of the detector for physics analysis is also important. In the first section the jet reconstruction is introduced. In the second section two data driven techniques to extract the jet energy resolution will be explained. Using these techniques, the jet energy resolution is extracted from the 2010 datasets. Finally in the last section, the jet energy resolution is tested in reduced HV area of the LAr Calorimeter.

4.1 What is a jet?

4.1.1 Theoretical point of view

In chapter one, the confinement nature of QCD was explained. This property means that the physical object created at the end of a reaction needs to carry a null color charge. There are two types of particles that are governed by QCD, the quarks and the gluons. The quarks carry a color charge, while the gluons allows to exchange one charge color to another one, meaning that they carry two net color charges.

When a collision creates a quark or a gluon, the parton fragments giving a shower of particles, the parton shower. This process is calculated with precision using the perturbation theory. The particles are then hadronized. The hadronization process is complicated and not fully understood, but the main idea is that when a quark or a gluon is produced, it gives birth to hadronic particles such as pions, kaons, photons, electrons,*etc.* Because of the QCD scale and the boost of the parton, the particles are emitted in its direction of flight, giving a sizable cone in the detector that is measured. Each particle in the cone taking away part of the momentum of the original parton.

A jet [103] consists of the particles produced by the hadronization of a quark or a gluon. Figure 4.1 shows a schematic view of the hadronization process of a quark. At the end of the shower many particles are detected.

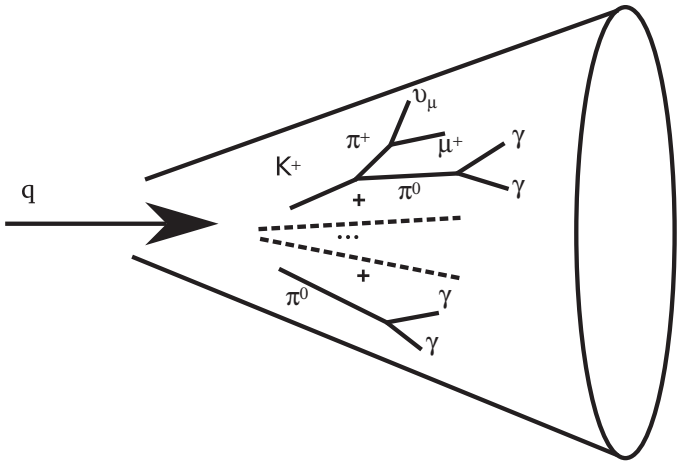

Figure 4.1: Schematic view of a jet originating from the hadronization of a quark.

In an hadronic collider the quarks and gluons giving jets can be emitted at different steps:

- In the hard scatter.

- Due to the other partons of the protons (underlying event).
- Due to the effect of other proton proton interactions in the same bunch crossing and in the nearby ones.

For the hard scatter, one can separate Initial State Radiation (ISR) effects, when extra jets are emitted from the initial state of the process and Final State Radiation (FSR), when jets are emitted from the final state.

Figure 4.2 shows the Feynman diagram of a tri-jet event. Two jets are emitted in the hard process due to a Drell-Yan process. A third jet is emitted due to Final State Radiation.

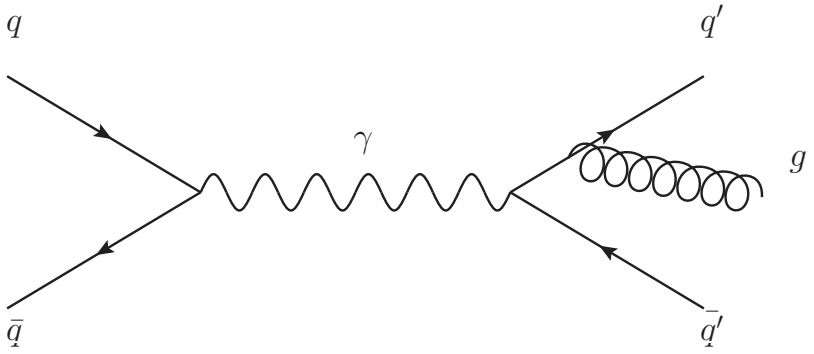

Figure 4.2: Feynman diagram of a Drell-Yan process event giving a di-jet event due to the hard process. A gluon is also emitted because of the FSR.

The production cross section of multi-jet events at the LHC is greater by two order of magnitude than the electroweak processes as it can be seen in Figure 1.10. Due to their higher production cross section and that jets are object composed of particles, they can fake also many established signature and processes.

For studies of processes involving jets, another difficulty arises from the nature of the jets. Due to the complex nature of jets, the interaction of those multi-particles object with the detector needs to be understood and reconstructed such as they can be compared to theoretical predictions. A good jet definition can be applied to experimental measurements, to the output of parton-showering Monte Carlos and to partonic calculations, and the resulting jets provide a common representation of all these different kinds of events. Two key jets attributes needs to be well established and controlled the Jet Energy Scale (JES), and the Jet Energy Resolution (JER).

For all these reasons, a precise measurement of jet properties is crucial in a hadronic experiment.

4.1.2 Jet reconstruction: clustering

Jet are non trivial objects, since they contains many particles, several steps are needed to reconstruct them. The hadronic shower produced energy deposit measured in the trackers and in the EM and hadronic calorimeters. The jets can be reconstructed starting from the tracks left in the ID, in that case they are called track[1] jets they will not be further discussed in this Chapter. Another solution consist to reconstruct them from the calorimeters system, in which case they are called calorimeter jets.

The seeding of calorimeter jets can be done with two main approaches. The most intuitive one, is to divide the full calorimeter into towers of a defined granularity. In ATLAS [65] the typical size of these towers are $\Delta\eta \times \Delta\phi = 0.1 \times 0.1$. Tower passing an energetic threshold are kept, and merged later on. Such algorithm works fine for EM objects since the EM showers are well defined, so their size can be easily estimated, and the tower granularity chosen in consequence. However due to the

[1] In this case the neutral component of the jet is not measured.

more erratic development of hadronic showers, this method leads to an over integration of the number of cells in the jets and thus to much electronic and pile up noise added into it. The tower are however used to trigger events containing jets, with a Trigger Tower size of $\Delta\eta \times \Delta\phi = 0.2 \times 0.2$.

Therefore another approach consists to start from the cells independently, and look for cells passing a 4σ cut of their electronic noise value. These cells would be the seeds of topological clusters [65]. All the neighbors cells passing a 2σ cut are added in the cluster, and finally all the direct neighbors cells are also taken. Figure 4.3 shows a sketch of such 4/2/0 TopoCluster.

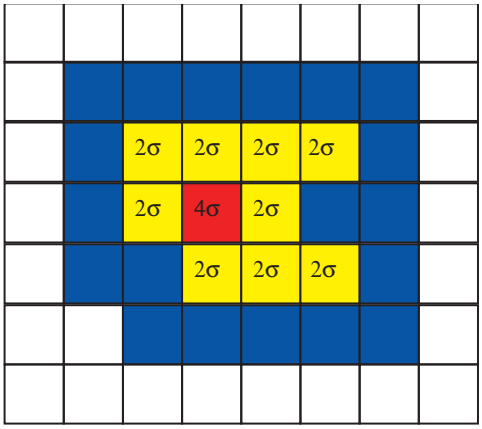

Figure 4.3: Sketch view of a 4/2/0 TopoCluster. The seeding cell with an energy greater than 4σ of the pedestal value is drawn in red. The neighbors cells with an energy greater than 2σ in yellow, and finally their direct neighbors entering in the cluster energy calculation are drown in blue.

The most important ideas of topoclustering are:

- Reduce the noise contribution in the jets, leading to a better estimation of the JES.
- Allow a better connection of particles and clusters within a jet. Leading to a better calibration of the elements within a jet, and could lead to more complicated algorithm such as Particle flow.

In the rests of this study, only jets seeded via the ATLAS standard 4/2/0 topological clusters are considered.

4.1.3 Jet reconstruction: algorithm

The topoclusters are supposed to be equivalent to a single particle contained within a jet. During jet reconstruction, a map containing the position of the clusters and their transverse momenta is built, the jets are seeded from the most energetic topo-cluster in the event, and then constructed by aggregating the lesser energetic ones. This is done such that jets are close as possible to the partons that originate the jet. The jets needs however to be safe with respect to the Infra Red (IR) emissions[2], and need to be calibrated.

There are mainly three families of algorithm currently in use [104].

- Cone Algorithms: These algorithms consists of summing all the clusters contained within a cone of given radius ΔR in the calorimeter. In ATLAS the typical cone size are 0.4 and 0.6. Figure 4.4 (a) shows at generator level of $t\bar{t}$ event the result of such algorithm on the truth particles. The main advantage is that the jets shapes are close to circular, and so easily calibrated. However the most basic cone algorithm are not IR safe. Some more recent algorithms exist to cure the IR problems, but these algorithm are much slower.

[2]IR emissions regroups all the soft gluons emissions that carry little energy compared to the parton. Safe means that the algorithm should find the same number of jets with or without soft emissions.

- K_T algorithm: This algorithm was introduced to correct for collinear and IR divergences. Two parameters are introduced, one proportional to the distance between two objects (clusters or proto jets):

$$d_{ij} = \min(P_{Ti}^2, P_{Tj}^2)\frac{\Delta R_{ij}^2}{R^2}$$

and one to the distance between the object and the beam:

$$d_{iB} = P_{Ti}^2$$

Where P_{Ti}^2 is the transverse momentum of object i. ΔR_{ij}^2 is the distance between the two objects. R is a cut parameter.

These two quantities are computed for all objects, *ie* clusters or proto-jets[3], in the events. If $d_{ij} < d_{iB}$, then the two objects are merged, else the jet is closed.

Figure 4.4 (b) shows at generator level of the same $t\bar{t}$ event the result of this algorithm on the truth particles. Even if it solves collinear and IR problems, the shape of the jets obtained is too irregular to allow an easy calibration of the jets.

- anti-K_T algorithm [105]: It combines most of the advantages of the cone and K_T algorithm. Figure 4.4 (c) shows at generator level of the same $t\bar{t}$ event the result of this algorithm on the truth particle.

The two parameters used in the anti-K_T algorithm are the inverse of the one introduced for the K_T algorithm

$$d_{ij} = \frac{1}{\max(P_{Ti}^2, P_{Tj}^2)}\frac{\Delta R_{ij}^2}{R^2}$$

and,

$$d_{iB} = \frac{1}{P_{Ti}^2}$$

Again these two quantities are computed for all objects in the events. If $d_{ij} < d_{iB}$, then the two objects are merged, otherwise the jet is closed. The anti-K_T algorithm is the preferred algorithm chosen in the ATLAS and CMS experiments, because the resulting jets are IR safe, easily calibrated and fast to compute.

The jets that are used in the rest of this study are seeded from 4/2/0 topo-clusters, and reconstructed using the anti-K_T algorithm with $R = 0.6$ implemented in the FastJet algorithm.

4.1.4 Calibration

The ATLAS calorimeters are non-compensating calorimeters [106]. This means that the response of the calorimeters to the hadronic and electromagnetic part of an hadronic shower is not equal. When the hadronic shower starts, neutral pions are produced, they decay in two photons, giving an important electromagnetic part, about 30% of the energy, the other hadronic particles interacts and lose energy *via* many processes, such as nuclear interactions, excitations, *etc.* The EM and hadronic fractions of the shower need to be evaluated such that both the electromagnetic and the hadronic parts are calibrated independently to recover a proper estimation of the energy. There is also some energy that escapes[4] from the jets and needs to be evaluated from Monte Carlo.

[3] *ie* group of clusters.

[4] For example because of the creation of neutrinos in the shower.

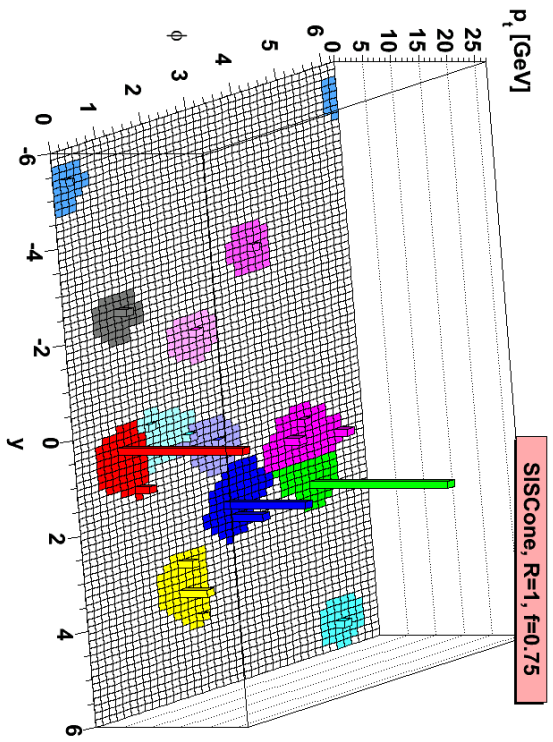

(a) SisCone.

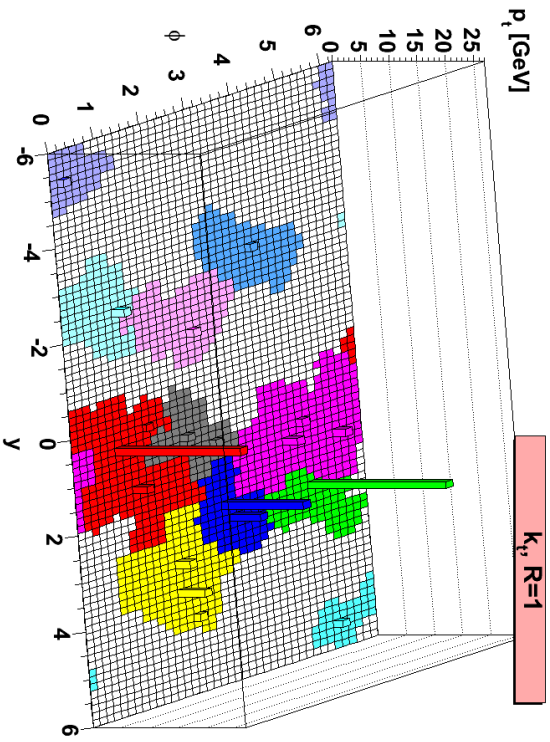

(b) K_T.

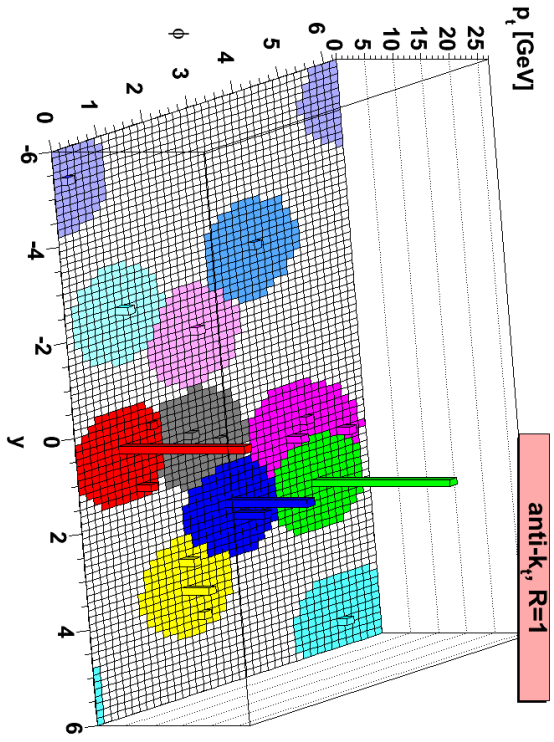

(c) Anti-K_T.

Figure 4.4: η, ϕ map of the truth jets found on a full hadronic $t\bar{t}$ events generated using Herwig, at the generator level. The Cone, K_T, and Anti-K_T algorithm are shown. Figure are extracted from [105].

The calibration process starts by the reconstruction of the jets with the cells calibrated at the EM-scale: this means that the cells are calibrated at the energy of the calorimeter response to electron and photons. The calibration factor to reach the EM-scale were estimated during the tests beams [107]. Due to the non compensation of the calorimeters the jet energy is underestimated by 30% [79].

In ATLAS the jet energy scale is evaluated from test beam data [108] and Monte Carlo [65]. The jets are calibrated to a new scale called EM+JES, by applying a global correction factor, derived from MC. The uncertainty of the JES [109] is estimated to be $\pm 3\%$ at $|\eta| < 0.8$ and $\pm 14\%$ at $3.2 < |\eta| < 4.5$.

In the rest of this study, one is interested by the energy resolution of the jets. It is determined using data-driven techniques considering di-jet events. The jets looked at are calibrated at the EM+JES scale. In most of the di-jet events due to soft radiation effects a third jet can be present. This third leading jet generally has a transverse momentum much less important than the two leading ones. In order to avoid biases of the calibration at low energy, if a third leading jet is present in the event, it is considered at the EM-scale.

4.2 Jet energy resolution

4.2.1 Introduction

Two *in-situ* techniques have been introduced to evaluate the jet energy resolution. The first one is the di-jet balance method, that was used by the $D0$ collaboration [110], the second one is the k_T balance method that was developed by the UA2 [111] collaboration and used by CDF, also known as the bisector technique. One uses these two techniques in order to obtained an independent cross checks of the results

The jet energy resolution is evaluated using events where two jets are produced. These events can originate from Drell-Yan processes, gluon fusion processes, *etc.* The idea is to get events where the jets are balanced, and to use these balance to evaluate the resolution. In order to be independent of biases due to the instrumentation or the kinematics of the events, the jet energy resolution is evaluated for two jets belonging to an equivalent resolution bin. Due to a lack of statistics in the high rapidity bins, this study will focus mainly on the central barrel region ($|y|<0.8$). The two jets are required to belong to this region.

The jet energy resolution is also evaluated in p_T bins, with boundaries at $30, 40, 60, 80, 110$, $160, 210, 260, 310$ and 500 GeV.

The two jets fall in one of these bin if

$$\langle p_T \rangle = \frac{p_T(1) + p_T(2)}{2} \tag{4.1}$$

is in the bin.

Finally, the jet fractional transverse momentum resolution can be parameterized as

$$\frac{\sigma_{p_T}}{p_T} = \frac{N}{p_T} \oplus \frac{S}{\sqrt{p_T}} \oplus C \tag{4.2}$$

Where N is the noise term, which parameterizes mainly the fluctuations due to the pile up and electronic noise within the jet. S is the stochastic term, which parameterizes mainly the stochastic fluctuations in the energy sampled from the jet hadron shower, and C the constant term which parameterizes mainly the non uniformity of the calorimeter responses.

It is interesting to notice that when the fit is performed on data, the three parameters found are almost completely[5] correlated. This means that the meaning of each parameter of this equation, can not be understood as the one described above, but more as a mixture of each. In the rest of this study, the fit is performed free on the truth resolution, then N, S and C are fixed to the truth value, and a overall normalization parameter is left free in the fit on data and MC, to evaluate a systematical shift.

[5]The correlation coefficient between N and S is about 95%, the one between N and C is about 86%, and the one between S and C is about 96%.

The resolution measured are relative resolutions. In the rest of this study, for the data Monte Carlo comparisons, the absolute difference refers to Data-MC, while the relative difference refers to $\frac{\text{Data-MC}}{\text{MC}}$.

4.2.2 Data selection

In this Chapter the jet energy resolution study is revisited to estimate the impact of the reduced LAr HV area on the jet reconstruction. This study focused only on the full data set recorded in 2010[6].

In order to ensure no bias from the trigger, the events are selected if they pass certain trigger items, with an efficiency greater than 99% relative to the offline selection.

Due to the energy reconstruction[7] differences between online and offline, the online jet E_T is significantly lower than the offline jet E_T, and the plateau is always reached far from the online E_T cut. To increase the statistics available for each p_T bin studied the trigger menu chosen is a mix of Level 1, Event filter, single and di-jets items. The complete list of these items can be found in Appendix A.1.

The events are preselected in the analysis, if they pass the following set of cuts:

- The primary vertex is located at |z|<100 mm from the beam spot position.
- One of the Trigger items must have been passed.
- The event contains two or three jets, with $p_T(3) > 7$ GeV.
- The event is requested to be part of a collection of lumi-blocks were the detector was sufficiently nominal to allow data analysis to be conducted.
- The events are excluded, following a set of cuts allowing to remove events due to beam background, cosmic muons, or instrumental energy deposition [114].

In this study, di-jet events generated using the PYTHIA Monte-Carlo generator are used. An upper and lower cut are applied on $\sqrt{s}$, to obtain a regular spectrum. The MC samples are passed through the ATLAS Geant 4 [100] full simulation, where they pass the same reconstruction steps and trigger selection as for the data. The different MC samples are merged using their cross sections and analyzed using the same cuts as the data. The corresponding cross-sections and pre-selection cuts are given in Table 4.1. Figure 4.5 shows the distribution of the leading jet transverse momentum for all the samples as expected the momentum distribution is exponentially decreasing after the merging of the different samples.

Sample name	Cut on $\sqrt{s}$ (GeV)	Cross section
J1	$[17, 35]$	667 pb
J2	$[35, 70]$	41 pb
J3	$[70, 140]$	2.2 pb
J4	$[140, 280]$	87 nb
J5	$[280, 560]$	2.3 nb
J6	$[560, 1120]$	0.03 nb

Table 4.1: MC samples used in the jet energy resolution study.

[6]It corresponds to an integrated luminosity of $\mathcal{L} = 37$ pb^{-1} for the lowest pre-scaled triggers. The uncertainty on the absolute luminosity was evaluated at 3.4% [112, 113].

[7]Analogical sum of the cells energy, EM-scale,*etc.*

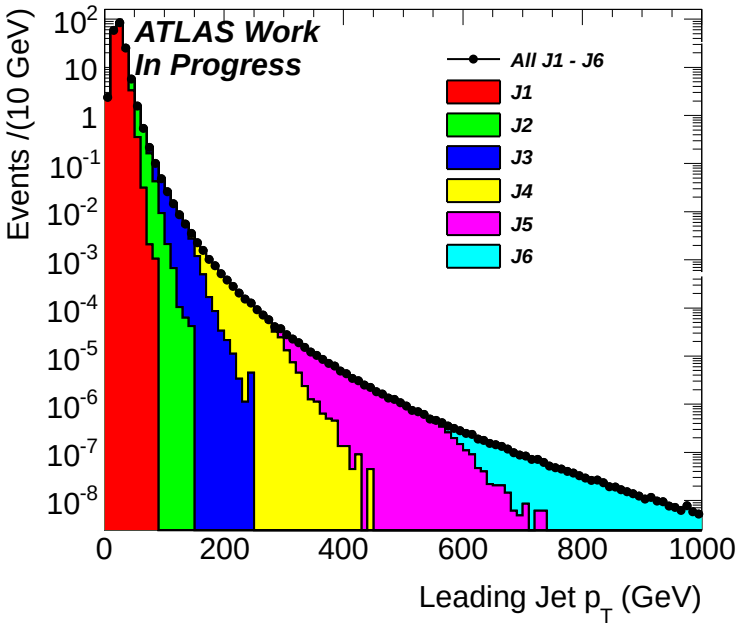

Figure 4.5: Leading Jet p_T from the different Monte Carlo samples.

4.2.3 Di-jet balance

Principe of the techniques

The di-jet balance is a technique allowing to determine the jet transverse momentum resolution. This technique relies on the conservation of momentum in the transverse plane.

In the case of a di-jets event, one can introduce the asymmetry between the two leading jets

$$A(p_T(1), p_T(2)) = \frac{p_T(1) - p_T(2)}{p_T(1) + p_T(2)} \tag{4.3}$$

The variance of this distribution is given by

$$\sigma_A^2 = \frac{4}{(p_T(1) + p_T(2))^4}(p_T^2(1)\sigma_{p_T(1)}^2 + p_T^2(2)\sigma_{p_T(2)}^2) \tag{4.4}$$

where p_T can be understood as the mean value of the jet p_T distributions, and σ_{p_T} is the transverse momentum resolution of the jet.

If the events considered are di-jet events where the two jets have the same p_T at the particle level, and belongs to a bin where their resolutions are equal, Equation (4.4), simplifies as

$$\frac{\sigma_{p_T}}{p_T} = \sqrt{2}\sigma_A \tag{4.5}$$

The fractional transverse momentum resolution can thus be linked to the variance of the asymmetry distribution in the case of a di-jet event, where the two jets belongs to an equivalent resolution bin. This allows an *in-situ* determination of the jet energy resolution.

Data and MC results

The asymmetry distributions are obtained for each $\langle p_T \rangle$ bins described at the beginning of this section. In Equation (4.3), the choice of which jet is the first and the second one is made randomly, to obtain a distribution centered at zero.

The events are selected from the pre-selection described in Section 4.2.2. In addition in order to remove the soft radiation effects, the two jets are required to have $|\Delta\phi_{12}| > 2.4$ and the third leading

jet jet in the event should have a transverse momentum less than $p_T(3)^{\mathrm{EM}} < 10$ GeV at the EM-Scale. The third leading jet does not need to belong in the same $|y|$ bin as the two leading jets; the EM-Scale is chosen to avoid biases coming from the calibration of low p_T jets. Finally the asymmetry distributions are fitted only if they contain more than 50 events.

Figure 4.6 shows the asymmetry distribution obtained from data and MC in the bins $60 < \langle p_T \rangle < 80$ GeV (a) and $80 < \langle p_T \rangle < 110$ GeV (b). The agreement between data and Monte Carlo is fair in these distributions. The same distributions for all the $\langle p_T \rangle$ bins are given in Appendix A.3.1.

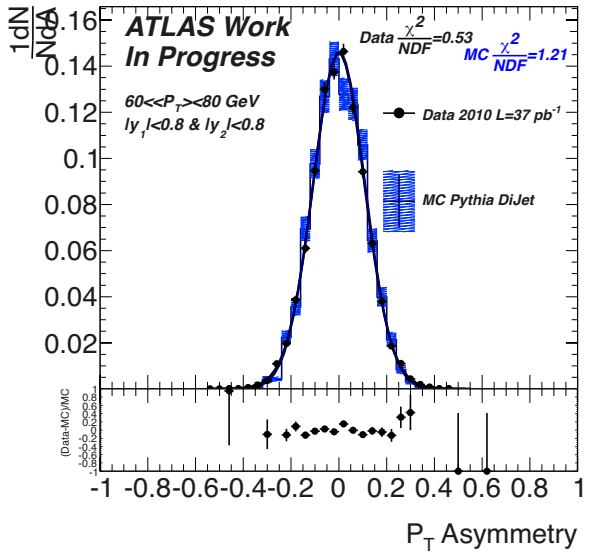

(a) $60 < \langle p_T \rangle < 80$ GeV and $|y| < 0.8$.

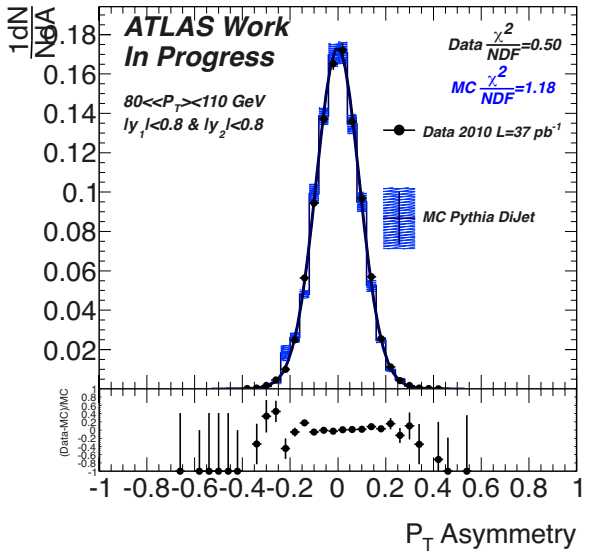

(b) $80 < \langle p_T \rangle < 110$ GeV and $|y| < 0.8$.

Figure 4.6: p_T Asymmetry distributions for the bins $60 < \langle p_T \rangle < 80$ GeV and $80 < \langle p_T \rangle < 110$ GeV, the two jets belongs to the $|y| < 0.8$ bin. The Monte Carlo is shown in blue, the data are in black. The distributions are normalized to their area. The fits to the distributions can also be seen.

In the same Figures, the fits to the distributions are also shown. The asymmetry distributions are fitted using double Gaussian functions, in order to recover the non Gaussian tails of the distributions.

$$\text{Double Gauss} = N(fe^{-0.5(\frac{x-\mu}{\sigma_{G1}})^2} + (1-f)e^{-0.5(\frac{x-\mu}{\sigma_{G1}+\sigma_{G2}})^2}) \tag{4.6}$$

allowing to obtain σ_A. In the case of this double Gaussian function

$$\sigma_A = \sqrt{f \times \sigma_{G1}^2 + (1-f) \times (\sigma_{G1} + \sigma_{G2})^2} \tag{4.7}$$

where f is the relative fraction of the two Gaussian, and σ_{G1}, σ_{G2} are the width of the two Gaussian distributions. The parameters f, σ_{G1}, σ_{G2} are strongly correlated, the covariance matrix is therefore used to propagate properly the uncertainties. N is a normalization parameter.

The fit procedure is repeated for each $\langle p_T \rangle$ bins, to obtain the jet fractional transverse momentum resolution. It is shown in Figure 4.7. Again the data are in black, while the MC is shown in blue. In this figure, only the statistical errors are shown. The agreement between data and MC is good, as shown by the residual distribution below the resolution distributions. In the worse case the relative[8] difference between data and MC is less than 10 %. The resolution function given in Equation 4.2 is fitted. The resolution found in the data seems to be always higher than the one found in MC, the absolute difference obtained with the fit of Equation 4.2 is about 3%. Due to trigger effects, the number of events is not monotonically decreasing in a $\langle p_T \rangle$ bin. The mean value of $\langle p_T \rangle$ in a bin is taken as the $\langle p_T \rangle$ value. For this reason, the points for data and Monte Carlo are not centered in the middle of the $\langle p_T \rangle$ bins

[8] In this study, relative difference will refer to $\frac{\text{data-MC}}{\text{MC}}$, and absolute difference to data-MC.

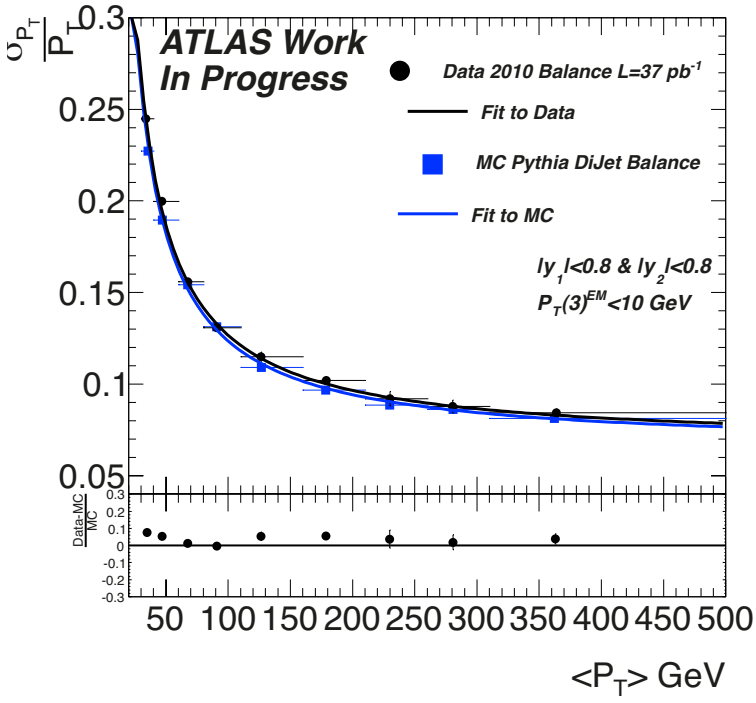

Figure 4.7: Jet fractional transverse momentum resolution for jets belonging in the $|y| < 0.8$ bin. Data are in black, MC is in blue. The residual are also shown.

Soft radiation effect

The resolution measured with the balance method is valid if the two leading jets have almost the same transverse momentum. In the case of a di-jet event, where one of the two jets emits a gluon due to FSR, the balance of the two jets is spoiled. In general the imbalance due to soft radiation increases the resolution measured with the balance method.

The cuts applied in the previous subsection[9] can up to a certain point limit the soft radiation effect. However the presence of a 10 GeV jet in a $\langle p_T \rangle \approx 30$ GeV event, does not have the same impact on the jet balance as on a $\langle p_T \rangle \approx 500$ GeV event. Moreover due to the jet reconstruction inefficiency, and the detector acceptance, the absence of a third energetic jet doesn't mean that the event selected is a real di-jet event.

In order to illustrate this effect, the fractional transverse momentum is drawn as a function of the cut on the third leading jet $p_T(3)^{\mathrm{EM}}$, for each $\langle p_T \rangle$ bin.

Figure 4.8 (a) shows this distribution for the bin $30 < \langle p_T \rangle < 40$ GeV. The first observation that can be made is that on this particular $\langle p_T \rangle$ bin, the disagreement between data and MC is quite strong. However the shape of the two distribution looks similar, even if the data is scaled up compare to MC. The resolution is increasing as expected from 3 GeV up to around 12 GeV. In this case the two jets carry a $p_T \approx 30$ GeV, the presence of a third jet with a $p_T \approx 10$ GeV clearly spoils the imbalance of the event.

If the resolution is evaluated using a 10 GeV cut on the third leading jet, it will be clearly over estimated. In order to remedy the soft radiation problem, the distributions on Figure 4.8 are used to extrapolate the resolution in the case where the third leading jet $p_T(3) \to 0$. This extrapolation is achieved using a first order polynomial function to get the intercept. In order to evaluate a systematic effect due to the shape of this curve, a second order polynomial fit is also conducted to recover the intercept.

Figure 4.8 (b) shows the same distributions for the bin $60 < \langle p_T \rangle < 80$ GeV. The gradient of the

[9] $\Delta|\phi| > 2.4$ and $p_T(3)^{\mathrm{EM}} < 10$ GeV.

curve is still important, showing the interest to extrapolate the intercept, or the ideal case where no jets are present in the event.

Finally Figure 4.8 (c), shows this distribution for the bin $160 < \langle p_T \rangle < 210$ GeV. As expected the gradient of the curve is much less pronounced than in the previous cases, the asymmetry distribution is less spoiled by the presence of a low $p_T(3)$ jet. In these last two $\langle p_T \rangle$ bins the difference between data and MC is reduced compared to the first one.

The distributions shown in Figure 4.8, are given for all $\langle p_T \rangle$ bins in Appendix A.3.1. The relative size[10] of the soft radiation correction for the MC, is given in Table 4.2.

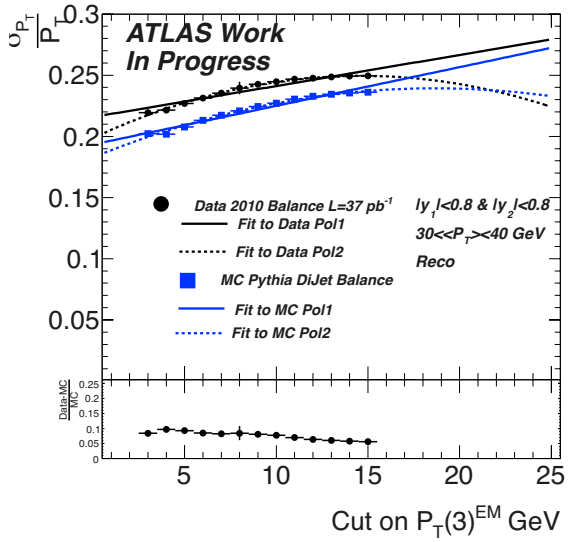

(a) $30 < \langle p_T \rangle < 40$ GeV and $|y| < 0.8$.

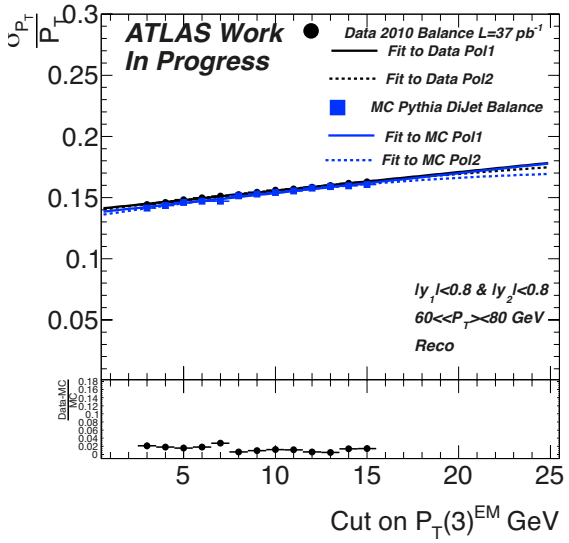

(b) $60 < \langle p_T \rangle < 80$ GeV and $|y| < 0.8$.

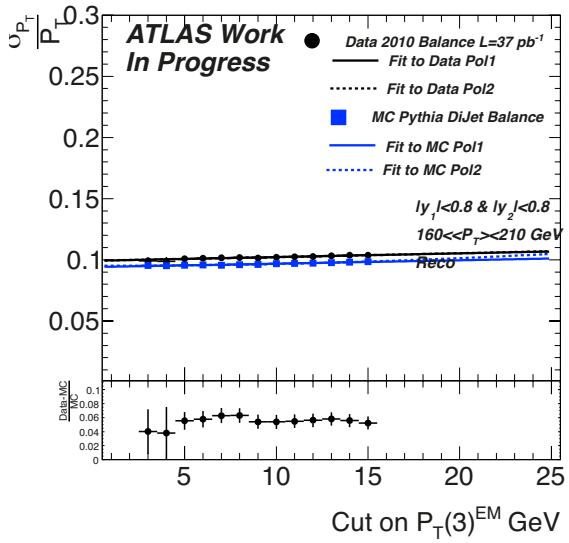

(c) $160 < \langle p_T \rangle < 210$ GeV and $|y| < 0.8$.

Figure 4.8: Jet fractional transverse momentum resolution as a function of the third jet $p_T(3)$, for the bin $30 < \langle p_T \rangle < 40$ GeV, $60 < \langle p_T \rangle < 80$ GeV and $160 < \langle p_T \rangle < 210$ GeV. The two jets belong to the rapidity $|y| < 0.8$ bin. Monte Carlo is shown in blue, data in black. A first and second order polynomial fit are conducted on data and MC to correct for the soft radiation effect.

The jet fractional transverse momentum resolution after the soft radiation correction is shown for data and MC in Figure 4.9. In this figure statistical and systematical errors due to the difference of

[10] *ie*: The relative difference between MC in Fig. 4.8 and Fig. 4.7.

the shape are shown. Again the agreement between data and MC is good, the relative difference is less than 20% in the worse case, but it is compatible within errors in most of the bins. As expected the resolutions measured are now better than in Figure 4.7. The absolute difference between MC and data after the soft radiation correction is measured about 5%.

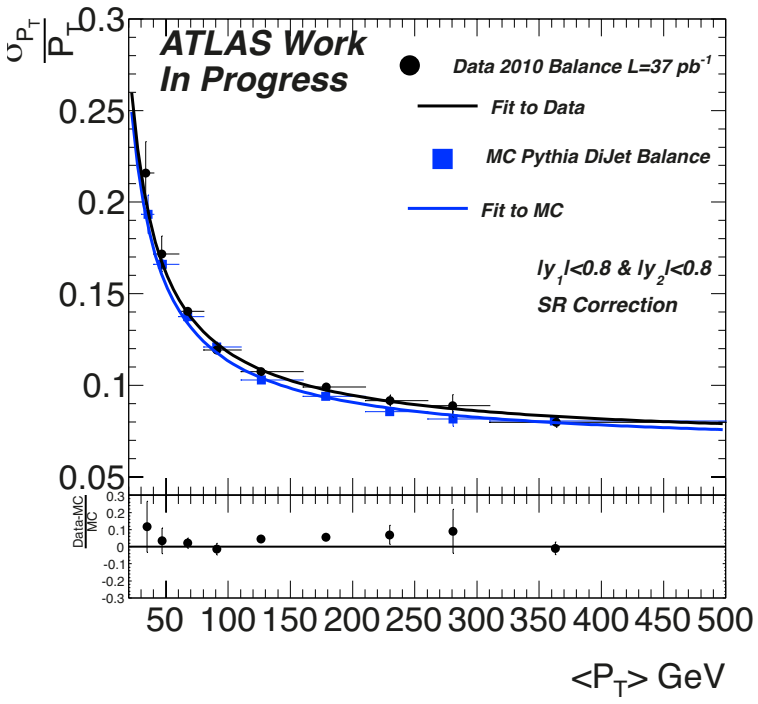

Figure 4.9: Jet fractional transverse momentum resolution for jets belonging in the $|y| < 0.8$ bin. Data are in black, MC is in blue. The residual are also shown. The errors bars ar statistical and systematical.

Particle imbalance correction

The resolution measured by this method includes by construction a contribution from the fact that the jets are not exactly balanced at the truth level, due to parton shower effects. In order to measure energy resolution effects only, this contribution needs to be subtracted. Its value is estimated from MC.

The anti$-K_T$ jet algorithm is run over the reconstructed quantities on the MC, and also at the truth particle level, on the particles coming from the hadronization of the partons. It is thus possible to run the same analysis on the truth level jets to evaluate the contribution of the truth imbalance. The truth asymmetry distributions are fitted using the double Gaussian functions introduced in Equation (4.6), and then evaluated in term of the cut on the third truth jet $p_T(3)$. It is expected that the presence of a soft third jet in the event spoils the imbalance of the event. In most of the case the presence of another soft jet is due to out-of cone showering in the truth jet.

These distributions are then fitted using a first order polynomial function to recover the intercept, or the case of a real di-jet event. The systematic on the shape is determined using a second order polynomial function. This is shown on Figure 4.10.

For the low $\langle p_T \rangle$ bins, the truth imbalance effect is important. For example in Figure 4.10 (a) the bin $40 < \langle p_T \rangle < 60$ GeV is shown, and the effect is around 11%.

For the high $\langle p_T \rangle$ bins, as shown on Figure 4.10 (b) for the bin $210 < \langle p_T \rangle < 260$ GeV, this effect is less important leading to an effect on the order of 2%.

The distributions shown in Figure 4.10, are given for all $\langle p_T \rangle$ bins in Appendix A.3.1. The size of the imbalance correction and their errors are given in Table 4.2.

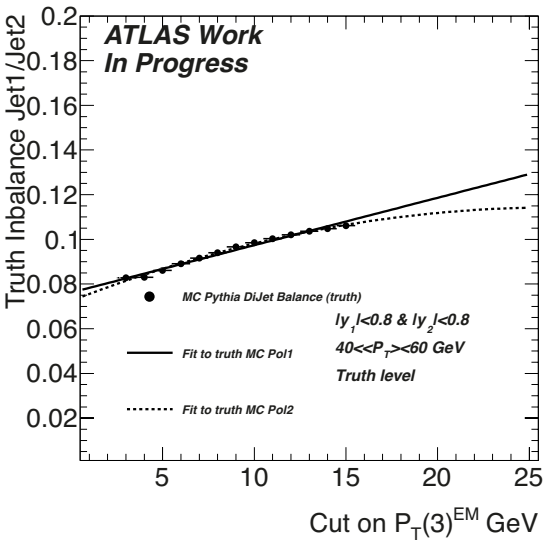

(a) $40 < \langle p_T \rangle < 60$ GeV and $|y| < 0.8$.

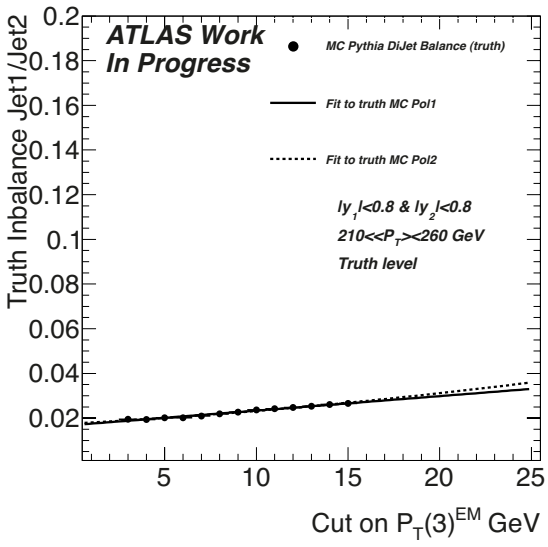

(b) $210 < \langle p_T \rangle < 260$ GeV and $|y| < 0.8$.

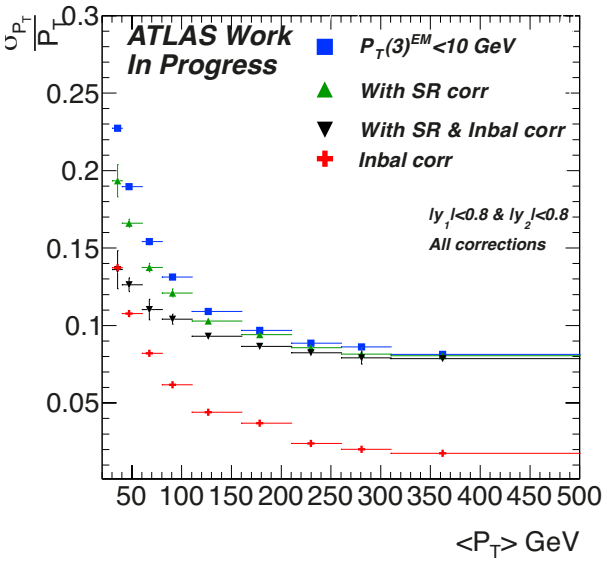

(c) Fractional resolution obtained on MC with a cut on third jet $p_T(3)^{EM} < 10$ GeV (blue), after the soft radiation correction(green), and after the soft and imbalance correction(black).

Figure 4.10: (a) and (b) p_T Truth Asymmetry distributions for the bin $40 < \langle p_T \rangle < 60$ GeV and $210 < \langle p_T \rangle < 260$ GeV, the two jets belongs to the $|y| < 0.8$ bin. The fits to the distributions can also be seen.

The truth imbalance correction is taken into account by subtracting it in quadrature to the resolution obtained after the evaluation of the soft radiation effect. Figure 4.10 (c) shows the fractional transverse momenta resolution obtained on MC with a cut on the third jet $p_T(3)^{\mathrm{EM}} < 10$ GeV in blue, after the soft radiation correction in green, and after the imbalance correction in black. The

size of the imbalance correction is also shown in red. One can observe that the resolution is getting better after each step. Most of the corrections are applied to suppress the soft radiation correction, as a consequence, the effects of these corrections is larger at low p_T, than it is at high p_T.

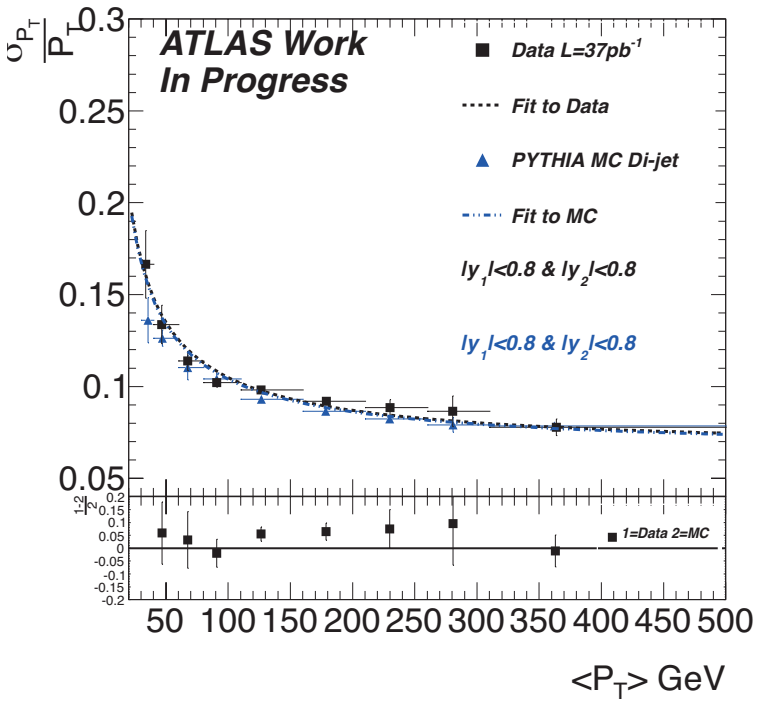

Figure 4.11: Jet fractional transverse momentum resolution for jets belonging in the $|y| < 0.8$ bin after all corrections. Data are in black, MC is in blue. The residual are also shown. Statistical and systematical errors are showed.

$\langle p_T \rangle$ bin	Relative size of SR effect	Imbal. Corr.	Syst. $\Delta\phi$
$[30, 40]$	0.149 ± 0.046	0.137 ± 0.0003	0.001
$[40, 60]$	0.124 ± 0.014	0.108 ± 0.0003	0.001
$[60, 80]$	0.108 ± 0.019	0.082 ± 0.0002	0.004
$[80, 110]$	0.078 ± 0.020	0.062 ± 0.0002	0.001
$[110, 160]$	0.057 ± 0.004	0.044 ± 0.0002	0.0001
$[160, 210]$	0.029 ± 0.011	0.037 ± 0.0002	0.0000
$[210, 260]$	0.032 ± 0.020	0.024 ± 0.0001	0.0000
$[260, 310]$	0.053 ± 0.047	0.020 ± 0.0001	0.0000
$[310, 500]$	0.009 ± 0.004	0.018 ± 0.0002	0.0000

Table 4.2: Resolution obtained after taking into account SR effect, size of the Imbalance correction, and systematic due to the change of $\Delta\phi$ cut.

Finally Figure 4.11 shows the jet fractional transverse momentum resolution for the bin $|y| < 0.8$, after all the corrections. In most of the bins, the MC and data are in agreement within errors. However it is also clear that resolution of jets measured in the data seems higher than the one predicted on MC. The absolute difference is measured around 5%. Up to now no clear explanation were found to explain this shift, however studies are still ongoing.

Two jets in different resolution bins

In the case where the two jets do not belongs to the same resolution bin, Equation (4.4) becomes

$$\frac{\sigma_{p_T}}{p_T}_{\text{probe}} = \sqrt{4\sigma^2(A_{\text{tag,probe}}) - \frac{\sigma^2_{p_T}}{p^2_T}_{\text{tag}}} = \sqrt{4\sigma^2(A_{\text{tag,probe}}) - 2\sigma^2(A_{\text{tag}})} \tag{4.8}$$

The procedure described in the last two subsections is applied. The resolution is estimated here using a tag jet in the rapidity bin $|y| < 0.8$ and a probe jet in the rapidity bin $1.2 < |y| < 2.1$. The resolution in the two rapidity bin is expected to be different since each bins corresponds to a different geometrical area in the detector. The rapidity bin $1.2 < |y| < 2.1$ covers for example an area containing the EM barrel, tile barrel, extended tile barrel, EMEC and HEC calorimeters, while in the rapidity bin $|y| < 0.8$ only the EM barrel and tile barrel calorimeters are present. The impact of the transition area on the jet reconstruction is therefore expected to be different. Figure 4.12 shows the result. The data are in black and the MC is in blue.

Due to the lower statistics, the error bars are larger than in the case of the two jets in the bin $|y| < 0.8$. The differences between data and Monte Carlo is within errors in most of the bins. However the resolution measured in the data is higher than the one expected in the Monte Carlo, the absolute difference is about 2%.

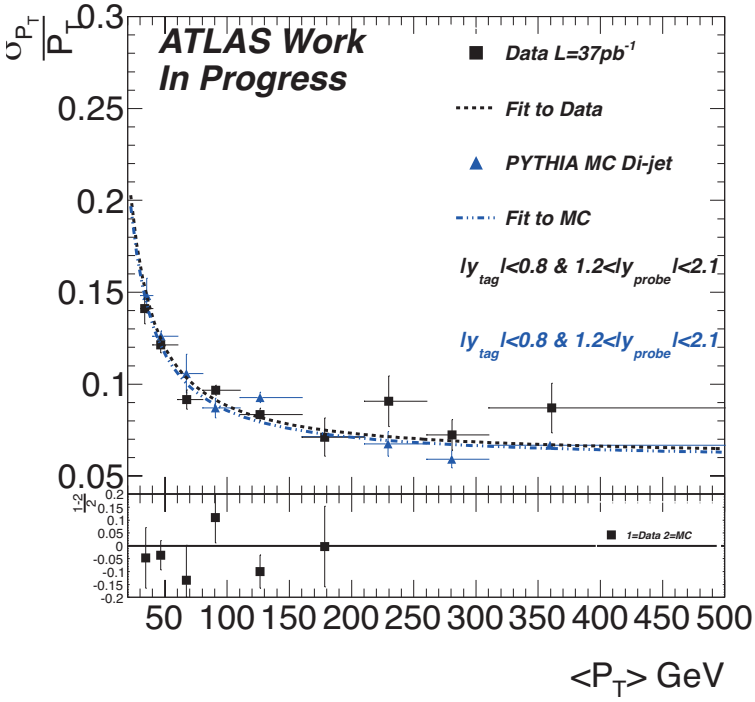

Figure 4.12: Jet fractional transverse momentum resolution for jets belonging in the $1.2 < |y| < 2.1$ bin. The distribution was obtained using a tag jet in the bin $|y| < 0.8$ and a probe jet in the bin $1.2 < |y| < 2.1$. Data are in black and MC is in blue. The residual are also shown.

However to confirm this last result, the study was also conducted using two jets in the bin $1.2 < |y| < 2.1$. The results can be found in Figure 4.13. The absolute resolution difference measured between Data and MC in this case is about 5%.

The soft radiation correction distributions obtained at the reconstructed level are given in Appendix A.3.2, for the tag and probe technique, and in Appendix A.3.2, for the two jets belonging in the same resolution bin.

Finally to compare the two methods, Figure 4.14 compares the resolutions obtained in the Monte Carlo using the tag and probe method, the two jets belonging to the same resolution bin, and the truth resolution.The truth resolution was obtained from Monte Carlo using a Gaussian fit of the distribution $\frac{p_T(reco)-p_T(truth)}{p_T(truth)}$. The results between the tag and probe technique and the two jets in

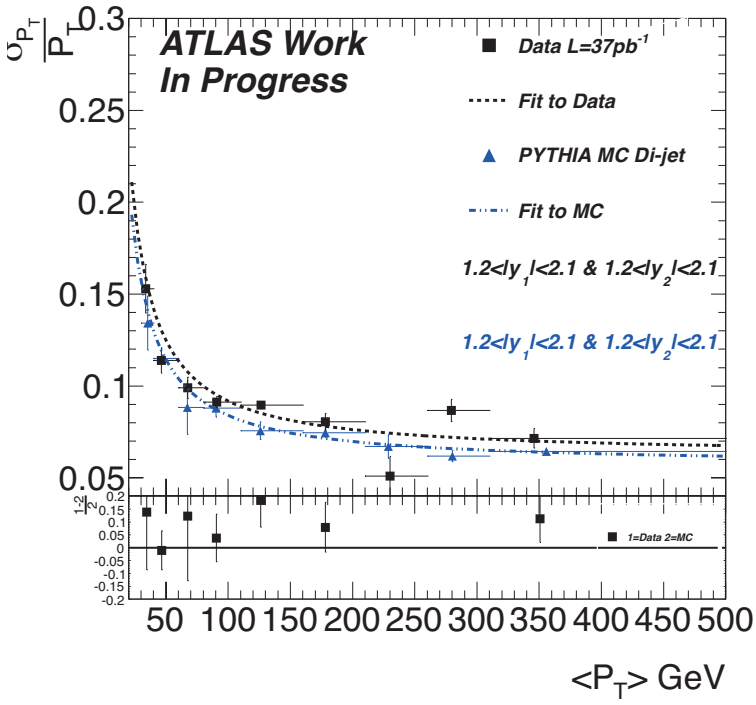

Figure 4.13: Jet fractional transverse momentum resolution for jets belonging in the $1.2 < |y| < 2.1$ bin. The distribution was obtain with two jets in the bin $1.2 < |y| < 2.1$. Data are in black and MC is in blue. The residual are also shown.

the same resolution are in fair agreement with each other. In most of the bins, the relative differences is less than 20%, and within errors. It is also interesting to noticed that the truth resolution can be recovered in most of the bins within 10%, the worse results being abound 15%.

This last result shows that it is possible to test the resolution of a probe region knowing the resolution in another one.

Source of systematic uncertainties

The systematic uncertainties are evaluated from three sources:

- The difference between the intercept recovered using the first order polynomial and the second order polynomial function for the soft radiation effect.
- The difference between the intercept recovered using the first order polynomial and the second order polynomial function for the imbalance correction.
- The study was redone varying the cut on $\Delta\phi_{12}$ from ± 0.1. The differences on the resolution are considered as a systematic.

All the systematic uncertainties are added in quadrature. The total effect can be found on Figure 4.15. The relative systematic uncertainties for the di-jet balance method are found to vary from 9% at low $\langle p_T \rangle$ down to about 1% at high $\langle p_T \rangle$. Most of these systematic uncertainties are coming from the differences on the shape for the soft radiation correction. The $\Delta\phi_{12}$ cuts bring a systematic on the order of 1‰. The systematic uncertainties are strongly dependent on the Monte Carlo statistics errors. Due to the way the Monte Carlo was generated some $\langle p_T \rangle$ bins like $[60, 80]$ or $[260, 310]$ have a lower statistics than the others. That is the reason why the systematic uncertainty distribution has this shape.

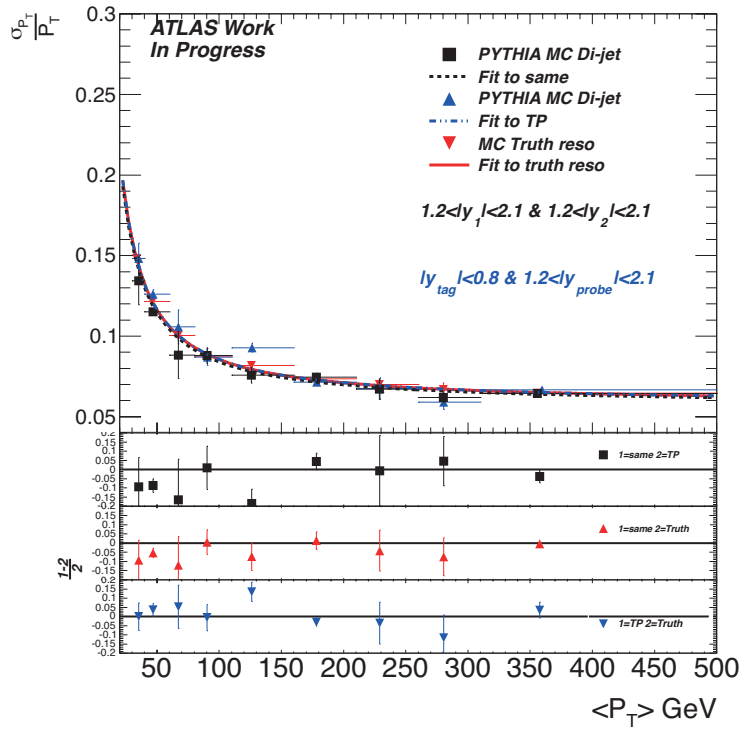

Figure 4.14: Jet fractional transverse momentum resolution for jets belonging in the $1.2 < |y| < 2.1$ bin. The graph is comparing MC obtained using the tag and probe method (black), the two jets in the same bin (blue), and the truth resolution (red).

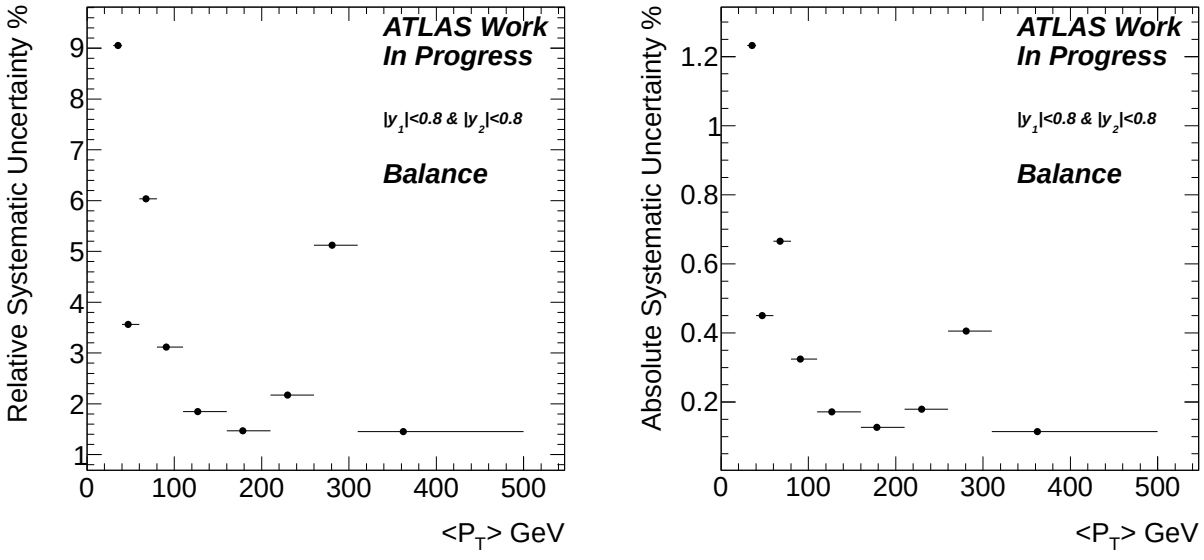

(a) Relative.

(b) Absolute.

Figure 4.15: Size of the systematic uncertainties for the di-jet balance method.

4.2.4 Bisector technique

Principle of the technique

The bi-sector method relies on the introduction of a transverse vector $\vec{p_T}$ define as the vector sum of the two leading jets momentum in the event. As shown in Figure 4.16, the imbalance vector $\vec{p_T}$ is projected along an orthogonal coordinate system in the transverse plane, (ψ, η), where η bisects $\Delta\phi_{12}$.

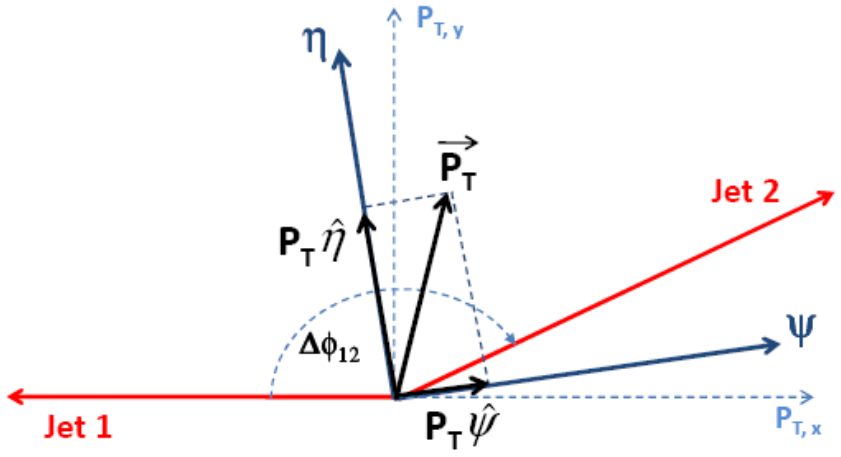

Figure 4.16: Bisector coordinate system sketch [79].

This new coordinate system is defined by

$$\begin{cases} p_T(\eta) = (p_T(1) + p_T(2)) \cos\Delta\phi_{12} \\ p_T(\psi) = (p_T(1) - p_T(2)) \sin\Delta\phi_{12} \end{cases} \tag{4.9}$$

Where $\Delta\phi_{12}$, is the angular separation between the two jets, and $p_T(1)$, $p_T(2)$ the transverse momentum of the two leading jets. As for the di-jet balance method, the choice of which jets is the first one and the second one is made randomly.

If the event selected were perfectly balanced di-jet events, then the imbalance vector would be null *ie* $\vec{p_T} = \vec{0}$. However many phenomena, such as FSR, ISR, *etc*, can lead to a non zero value of $\vec{p_T}$. This means that the variance of the $\vec{p_T}$ projection in ψ and η will be non zero. The variances are assimilated as the width of the two distribution $p_T(\eta)$ and $p_T(\psi)$: $\sigma^2_\psi \equiv \mathrm{Var}(p_T(\psi))$ and $\sigma^2_\eta \equiv \mathrm{Var}(p_T(\eta))$.

If the two jets belong to the same rapidity region, so that their energy resolution are equivalent, it can be shown that [79]

$$\frac{\sigma^{\mathrm{calo}}_{p_T}}{p_T} = \frac{\sqrt{\sigma^{2\ \mathrm{calo}}_\psi - \sigma^{2\ \mathrm{calo}}_\eta}}{\sqrt{2} p_T \sqrt{|\cos\Delta\phi_{12}|}} \tag{4.10}$$

In this equation, $\Delta\phi_{12}$ is taken as the mean value of the angular distribution between the two jets, p_T as the mean value of the jet p_T in the bin considered. The σ^{calo} represents the quantities at the reconstructed level. The resolution is expressed in terms of calorimeter observables only.

As for the di-jet balance method, the bisector measurement is affected by the imbalance at the particle level. The variance of the distribution are decomposed as

$$\begin{cases} \sigma^{2\ \mathrm{calo}}_\psi = \sigma^{2\ \mathrm{part}}_\psi + \sigma^{2\ \mathrm{reso}}_\psi \\ \sigma^{2\ \mathrm{calo}}_\eta = \sigma^{2\ \mathrm{part}}_\eta + \sigma^{2\ \mathrm{reso}}_\eta \end{cases} \tag{4.11}$$

Where the $\sigma^{2\ \mathrm{part}}$, represents the variance at the particle level, and the $\sigma^{2\ \mathrm{reso}}$, the part responsible for the resolution of the jet. The imbalance vector receives most of the contributions due to ISR and FSR. The effect of ISR is expected to be isotropic in the (ψ, η) plane. This assumption is *a priori* not true for the FSR, but the effect of FSR is expected to be less important than ISR. So one expects to have

$$\sigma_{\psi}^{2\ part} = \sigma_{\eta}^{2\ part} \tag{4.12}$$

It is also expected that $\sigma_{\psi}^{2\ \mathrm{reso}} > \sigma_{\eta}^{2\ \mathrm{reso}}$ since $p_T(\psi)$ is obtained by subtracting two large components, while $p_T(\eta)$ is the sum of two small components. The quadratic difference of the two is sensitive to $\sigma^{2\ \mathrm{reso}}$. So all the soft radiation effects are removed by subtracting in quadrature σ_η from σ_ψ at the calorimeter level.

Given all this, Equation 4.10 becomes

$$\frac{\sigma_{p_T}^{\mathrm{reso}}}{p_T} = \frac{\sqrt{\sigma_{\psi}^{2\ \mathrm{calo}} - \sigma_{\eta}^{2\ \mathrm{calo}}}}{\sqrt{2} p_T \sqrt{|\cos \Delta\phi_{12}|}} \tag{4.13}$$

Which allows an *in-situ* estimation of the jet energy resolution using calorimeter variables.

The bisector method can be biased if a too stringent cut is applied on the angular distribution separating the two jets, for this reason no cut is applied. The variances σ_η and σ_ψ are estimated by conducting a double Gaussian fit of the distributions $p_T(\psi)$ and $p_T(\eta)$. The fit functions used are the ones described in Equation (4.6). As for the di-jet balance the $p_T(\eta)$ and $p_T(\psi)$ distributions are fitted only if they contains more than 50 events.

Data and results

Figure 4.17 (a) and (b) shows the distributions of $p_T(\eta)$ (a) and $p_T(\psi)$ (b) in the case where $|y| < 0.8$ and $110 < \langle p_T \rangle < 160$ GeV. A cut of 10 GeV at the EM-scale is applied on the third leading jet. The data are found to be in good agreement with the Monte Carlo in this $\langle p_T \rangle$ bin. The double Gaussian functions are also drawn. The distributions of $p_T(\eta)$ and $p_T(\psi)$, for all the $\langle p_T \rangle$ bins are given in Appendix A.4.

To check the validity of Equation (4.12), Figure 4.18 (a) and (b) shows, at the truth level the variance of the double Gaussian fit performed on the $p_T^{\mathrm{part}}(\psi)$ and $p_T^{\mathrm{part}}(\eta)$ distributions as a function of the cut on the third jet $p_T(3)$, for the bins $60 < \langle p_T \rangle < 80$ GeV (a) and $110 < \langle p_T \rangle < 160$ GeV (b).

As expected the variances increase if the cut on the third jet is relaxed, because of the soft FSR contamination. However the difference between the two distributions is rather close to zero. The non zero difference between the two is taken into account as a systematic uncertainty. The absolute error given by this uncertainty is less than 0.9% in the worse case, and generally closer to 0.5%.

In order to investigate the effect of the soft radiation on the $p_T^{\mathrm{reco}}(\psi)$ and $p_T^{\mathrm{reco}}(\eta)$ distributions, the variance of these two distributions are drawn as a function of the cut on the third leading jet $p_T(3)^{\mathrm{EM}}$.

Figure 4.19 (a) and (b) shows these distributions for data and MC at the reconstructed level, and their difference in quadrature, as a function of the cut on the third leading jet transverse momentum, for the cases where $30 < \langle p_T \rangle < 40$ GeV (a) and $80 < \langle p_T \rangle < 110$ GeV (b), the two jets belongs to $|y| < 0.8$.

On Figure 4.19 (a), for the lowest $\langle p_T \rangle$ bin used in this study, the two variances at the reconstructed level increase when the third jet cut is relaxed. If one looks at the quadratic difference of σ_η and σ_ψ, for data (in red) and for MC (in green), between 3 GeV and 9 GeV, this difference is flat. However after 10 GeV, the same curve starts to drop. This is showing the limit on the soft radiation assumption. As said on previous section $\sigma_{\psi}^{2\ \mathrm{reso}} > \sigma_{\eta}^{2\ \mathrm{reso}}$ since $p_T(\psi)$ is obtain by subtracting two large components, while $p_T(\eta)$ is the sum of two small component. This means that $p_T(\eta)$ will be more sensitive to soft contamination than $p_T(\psi)$. When the quadratic difference is not flat anymore this means that the contamination is too large, and the isotropy assumption is not respected anymore, the bisector method won't give a correct estimation of the jet momentum resolution.

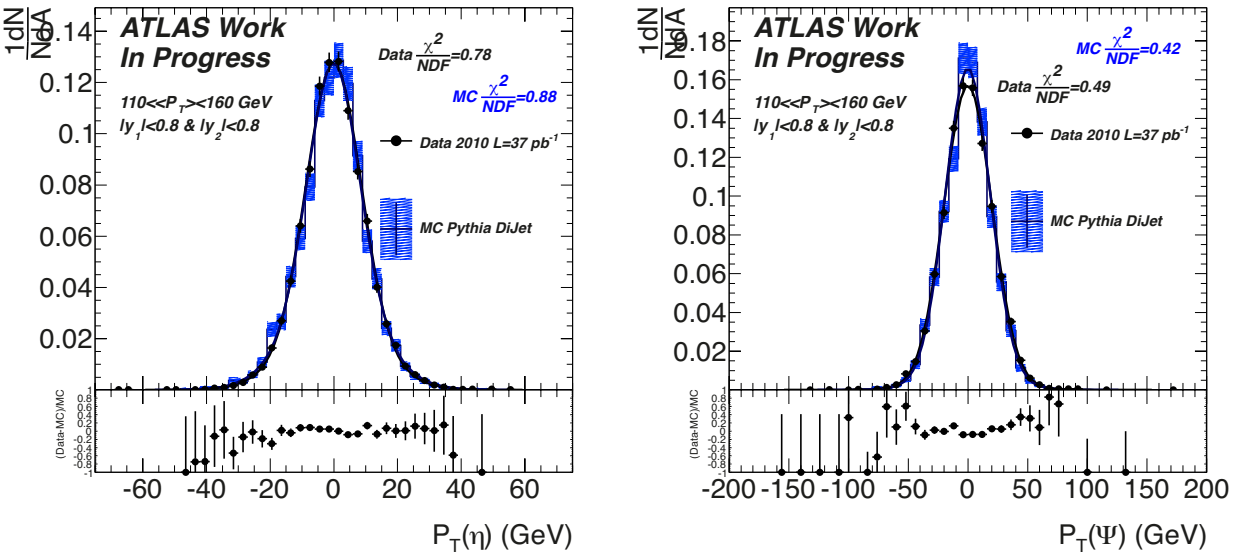

(a) $p_T(\eta)$. (b) $p_T(\psi)$.

Figure 4.17: Distribution of $p_T(\eta)$ and $p_T(\psi)$ for the Monte Carlo PYTHIA Di-jet in blue, and for the data in black. The double Gaussian fits of MC and data are also drawn. The distributions are normalized to their area.

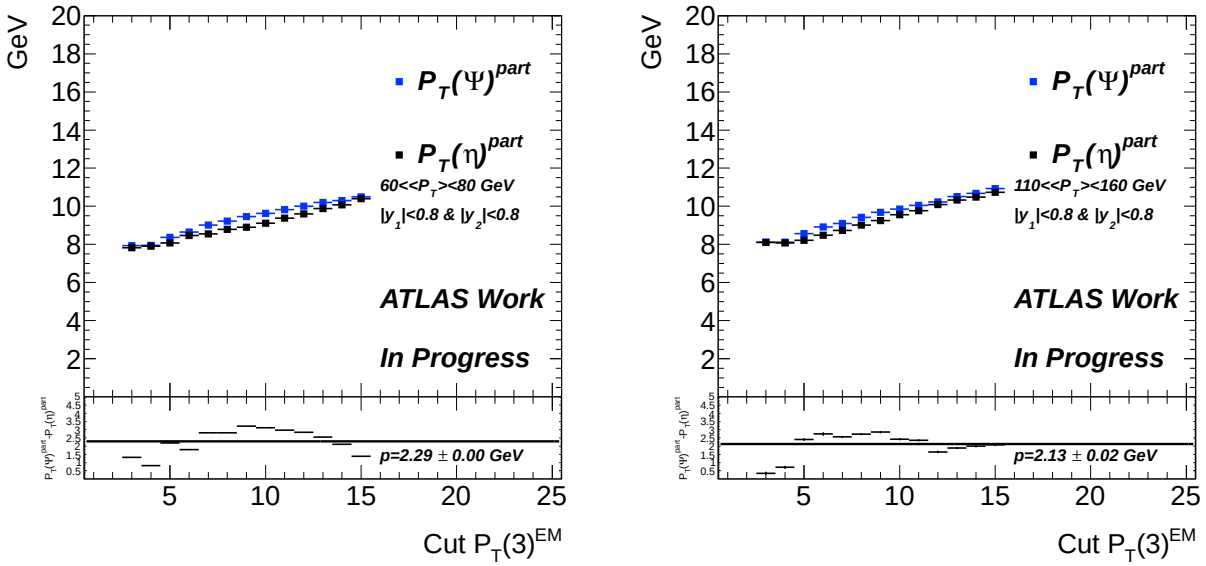

(a) $60 < \langle p_T \rangle < 80$ GeV. (b) $110 < \langle p_T \rangle < 160$ GeV.

Figure 4.18: Distribution of the variances of $p_T(\psi)$ and $p_T(\eta)$, at the particle or truth level, as a function of the third jet p_T cut. The quadratic difference between the two is also showed.

On Figure 4.19 (b), the quadratic difference is flat all over the range studied, meaning that the soft radiation assumption is valid in this case.

This result allows an *in-situ* validation of the soft radiation assumption. In the rest of this study, the cut on the third leading jet p_T, will be fixed at $p_T(3)^{\mathrm{EM}} < 8$ GeV for the first bin $30 < p_T < 40$ GeV, and $p_T(3)^{\mathrm{EM}} < 10$ GeV for all the other bins.

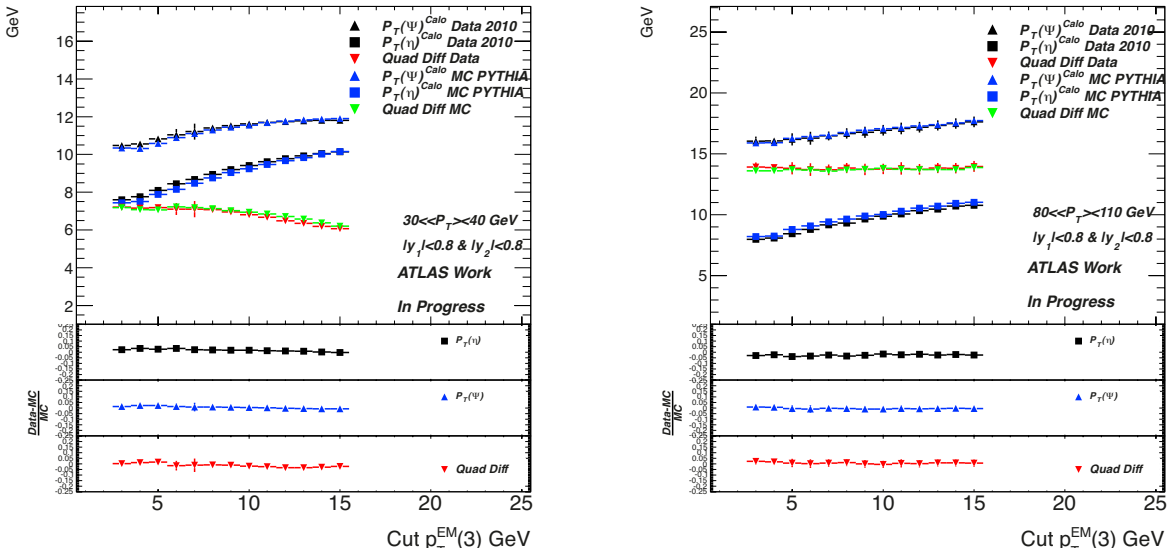

(a) $30 < \langle p_T \rangle < 40$ GeV.

(b) $80 < \langle p_T \rangle < 110$ GeV.

Figure 4.19: Distribution of the variances of $p_T(\psi)$ and $p_T(\eta)$, at the reconstructed level, as a function of the third jet p_T cut. The quadratic difference between the two is also showed.

Using this selection, one need to check the behavior of the σ_η and σ_ψ distributions versus $\langle p_T \rangle$. Figure 4.20, shows for data and MC these distributions. The agreement between data and MC is fair, and within uncertainties in most of the bins. As expected, σ_η stays almost flat in the whole $\langle p_T \rangle$ range, while σ_ψ increases.

Finally Figure 4.21 shows the jet fractional transverse momentum resolution as a function of $\langle p_T \rangle$, computed using Equation 4.13. Data and MC are visible, the error bars include both statistical and systematical uncertainties. Data and MC appeared to be in a fair agreement in most of the bins, they agree within uncertainties. However and as for the di-jet balance method, the fit using Equation 4.2 reveal an absolute systematical shift about 7 % between data and MC resolutions.

All the distributions showed in this section are given for each $\langle p_T \rangle$ bins in Appendix A.4.

Two jets in different Resolution bins

If the two jets belongs to two different resolution bins, Equation (4.10) becomes

$$\frac{\sigma_{p_T}}{p_T}\Big|_{\mathrm{probe}} = \sqrt{\frac{\sigma_\psi^{2\ calo} - \sigma_\eta^{2\ calo}}{p_T^2 |\cos\Delta\phi_{12}|}\Big|_{\mathrm{tag,probe}} - \frac{\sigma_{p_T}^2}{p_T^2}\Big|_{\mathrm{tag}}} \tag{4.14}$$

It is possible to evaluate the resolution of a jet from a probe bin, using a tag jet which belongs to a bin where the resolution is well known.

The bisector technique is used to estimate the resolution in the bin $1.2 < |y| < 2.1$ using a tag jet in the bin $|y| < 0.8$. Figure 4.22 shows the result. The data are in black, and the MC is in blue.

The absolute difference between data and MC is measured around 5%.

In order to study the validity of the Tag and probe technique, the resolution is drawn for two jets in the bin $1.2 < |y| < 2.1$. Figure 4.23 shows it. In this case the absolute difference between data and MC is measured at 6%.

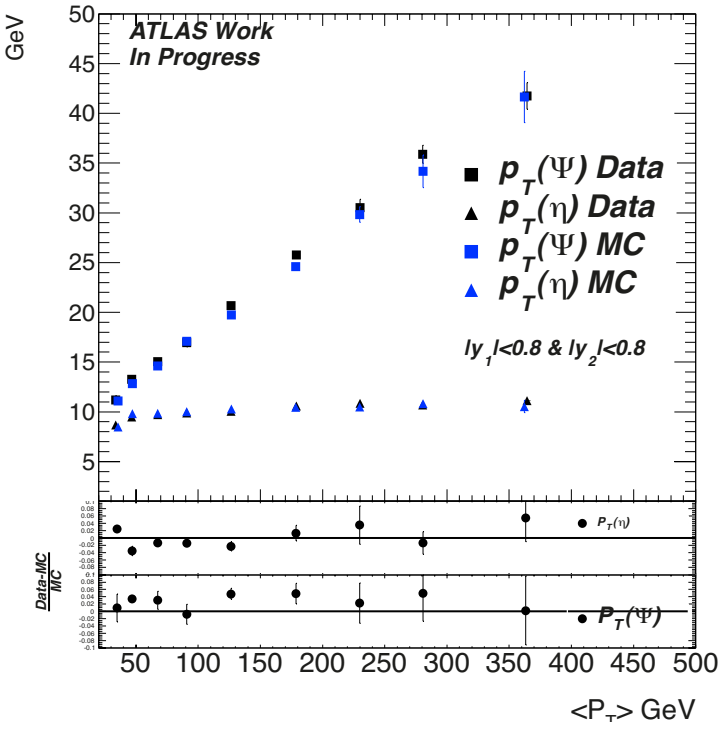

Figure 4.20: Distribution of the variances of $p_T(\psi)$ and $p_T(\eta)$, at the reconstructed level, as a function of the $\langle p_T \rangle$ value, for data and MC.

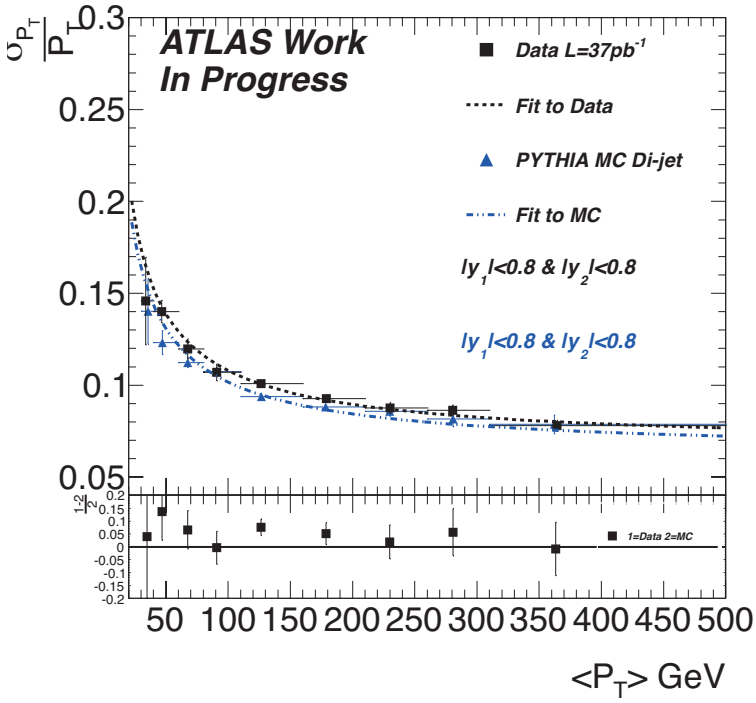

Figure 4.21: Jet fractional transverse momentum resolution for jets belonging in the $|y| < 0.8$ bin. The graph show results for the bisector method. Data are in black, and MC is in blue.

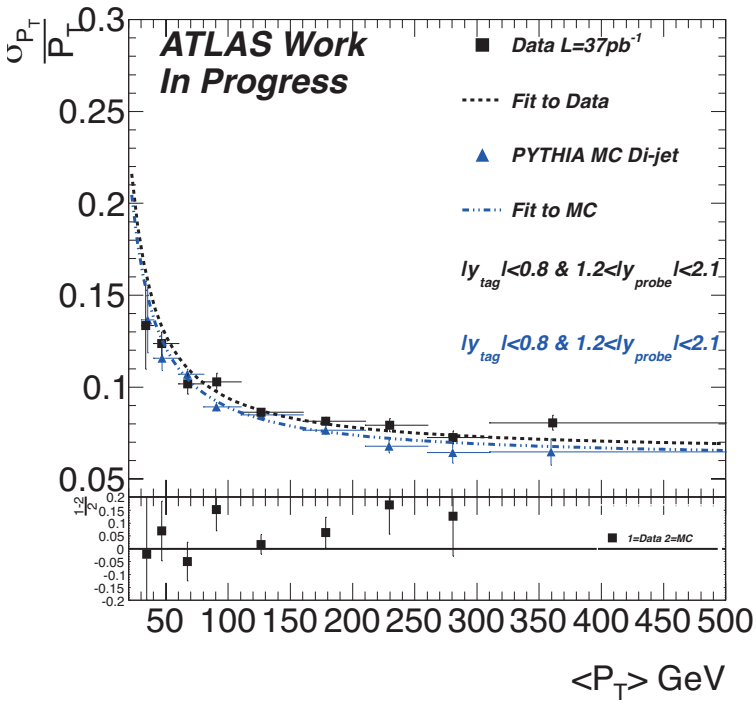

Figure 4.22: Jet fractional transverse momentum resolution for jets belonging in the $1.2 < |y| < 2.1$ bin. The distribution was obtained using a tag jet in the bin $|y| < 0.8$ and a probe jet in the bin $1.2 < |y| < 2.1$. Data are in black and MC is in blue. The residual are also shown.

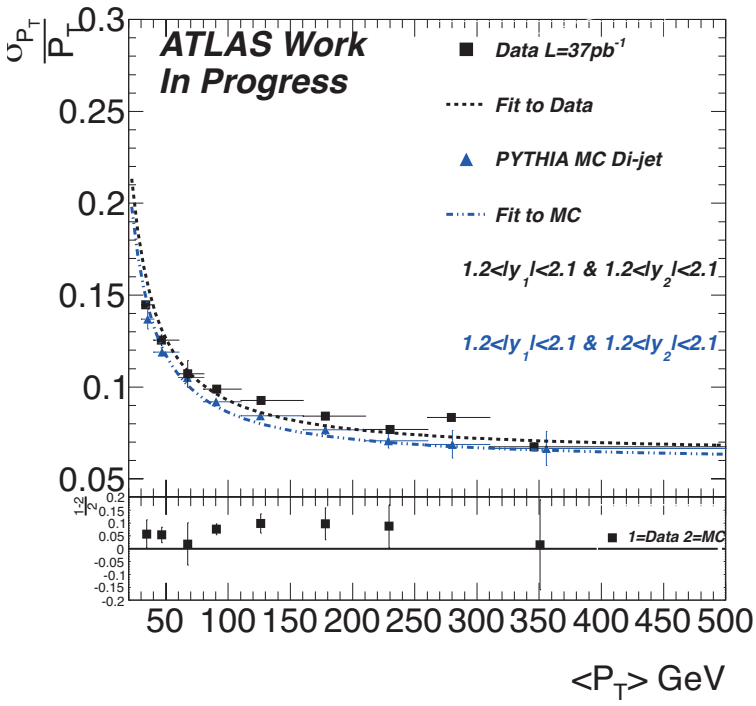

Figure 4.23: Jet fractional transverse momentum resolution for jets belonging in the $1.2 < |y| < 2.1$ bin. The distribution was obtain with two jets in the bin $1.2 < |y| < 2.1$. Data are in black and MC is in blue. The residual are also shown.

Finally, Figure 4.24 compares the tag and probe technique, and the two jet falling in the same resolution bin for the MC. The relative difference between the two is always better than 5%, and within errors. The truth resolution is recovered within 5% relative difference.

This last results shown that it is possible to evaluate the resolution of a probe jet using a tag jet in a known resolution bin. The results of the bisector techniques and of the di-jet balance can be used as a cross-check.

The soft radiation validation distributions for this section are given in Appendix A.4.1.

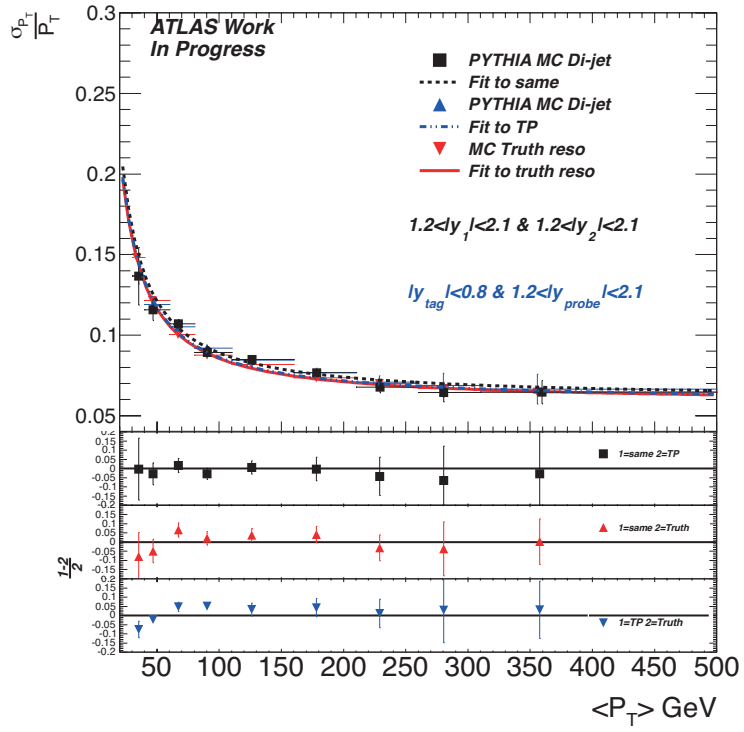

Figure 4.24: Jet fractional transverse momentum resolution for jets belonging in the $1.2 < |y| < 2.1$ bin. The graph is comparing MC obtained using the tag and probe method (black), the two jets in the same bin (blue), and the truth resolution (red).

Source of systematic uncertainties

The systematic uncertainties are evaluated from two sources:

- The effect of the imbalance of the two jets at the truth level is evaluated from MC.
- The effect of the cut on the third jet $p_T(3)^{\mathrm{EM}}$, is estimated by computing the resolution varying the cut of ± 1 GeV.

The contribution of each uncertainties sources are given in Table 4.3

All the systematic uncertainties are added in quadrature. The total effect can be found on Figure 4.25 (a) for the relative uncertainties and on Figure 4.25 (b) for the absolute uncertainties. The relative systematic uncertainties for the bisector technique are found to vary from 14% at low $\langle p_T \rangle$ down to about 2% at high $\langle p_T \rangle$.

4.2.5 Results and differences between the two techniques

One can check what are the differences between the two techniques and how well they allow to recover the truth resolution.

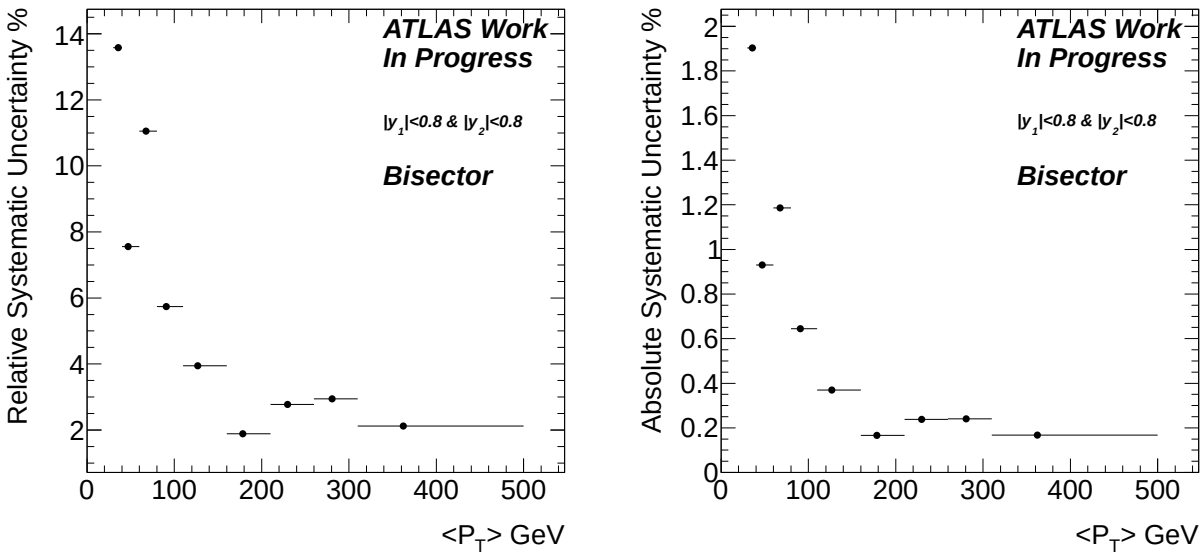

(a) Relative.

(b) Absolute.

Figure 4.25: Relative size of the systematic uncertainties for the bisector technique.

$\langle p_T \rangle$ bin	Truth systematic	varying cut ± 1 GeV
$[30, 40]$	0.007	0.018
$[40, 60]$	0.007	0.006
$[60, 80]$	0.012	0.003
$[80, 110]$	0.006	0.002
$[110, 160]$	0.004	0.001
$[160, 210]$	0.001	0.001
$[210, 260]$	0.002	0.001
$[260, 310]$	0.002	0.001
$[310, 500]$	0.002	0.001

Table 4.3: Contribution of each uncertainties source taken into account for the bisector method.

Figure 4.26, shows the jet fractional transverse momentum resolution for jets belonging in the $|y| < 0.8$ bin, for the Monte Carlo, obtained using the bisector and the di-jet balance methods.

The first noticeable element, is that the agreement between the di-jet balance and the bisector method is very good, and always within uncertainties. In most of the $\langle p_T \rangle$ bins, the relative agreement is better than 3%, the worse case being less than 5%. *The second remarkable point is that the two methods allows to recover the truth jet energy resolution with a relative agreement which is always less than* 10%*!*

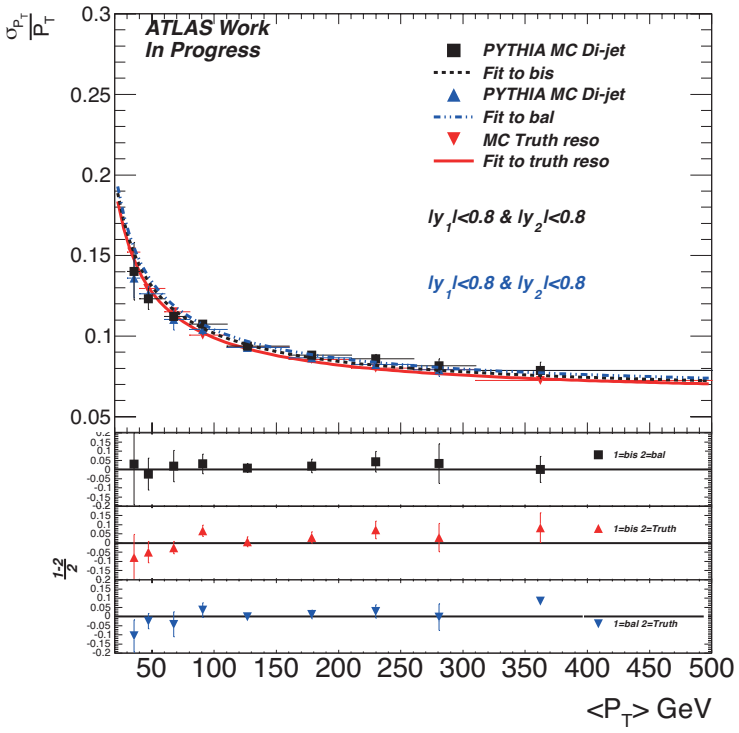

Figure 4.26: Jet fractional transverse momentum resolution for jets belonging in the $|y| < 0.8$ bin. The graph show results for the bisector, and the di-jet balance method for the MC. The balance method result is in black, the bisector method is in blue, and the truth resolution is in red.

Figure 4.27 shows the relative agreement of the bisector and the di-jet balance on data. The results of the two methods are in good agreement, and always within uncertainties. However as said earlier, a relative systematical shift about 10% is observed from the resolution expected in the Monte Carlo, to the one found in the Data.

The bisector methods gives an estimation of the jet transverse momentum fractional resolution with a relative systematic uncertainty better than 13% in the worse case, the mean result being around 4%. The di-jet balance method gives an estimation of the jet transverse momenta fractional resolution, with a relative systematic uncertainty better than 2% while the worse case is about 10% . One can also noticed that the errors in the case where the two jets belongs to $|y| < 0.8$ are dominated by the systematic uncertainties, due to high statistics available.

The results showed in this section demonstrate that it is possible to use *in-situ* techniques to evaluate the jet energy resolution.

4.3 Effect of reduced LAr HV area on jet reconstruction

The techniques to determine the jet energy resolution described in the previous Section are used to estimate the impact of non nominal calorimetric region on the jet reconstruction.

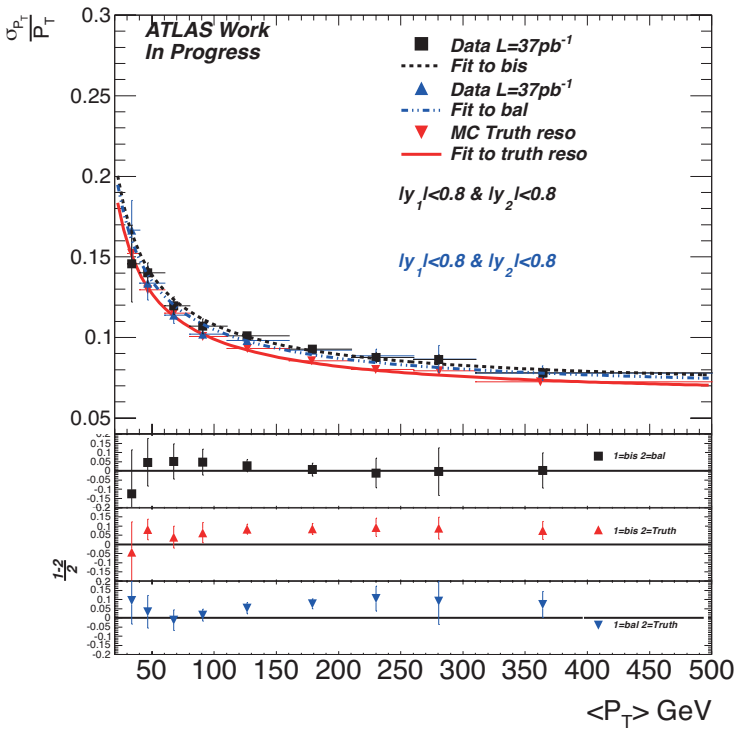

Figure 4.27: Jet fractional transverse momentum resolution for jets belonging in the $|y| < 0.8$ bin. The graph show results for the bisector, and the di-jet balance method for the Data. The balance method result is in black, the bisector method is in blue, and the truth resolution is in red.

4.3.1 Reduced LAr HV area

The goal of this study is to check the impact of the non nominal LAr HV area on the jet energy resolution. It is limited to the barrel region as explained in Section 4.2.1. As said in Chapter 3, in the barrel calorimeter the High Voltage Power Supply are typically feeding sectors of $\Delta\eta \times \Delta\phi = 0.2 \times 0.2$. Each electrodes is fed independently by two HV lines to ensure the redundancy of the system.

Two different cases will be investigated in this section.

The first one is the effect of the non nominal areas that are permanent. Some regions of the calorimeter are fed with a lower HV than the nominal one. In the case of the pre-sampler for example, the HV was reduced, to try to decrease the sporadic noise that was seen during the data taking.

The second case that will be investigated are the HV trips[11], and their impact on the jet energy resolution.

In any case, the effect of the non nominal HV area is not simulated in the Monte Carlo. The only solution to check their impact is to use data driven techniques to evaluate its impact on the jet energy resolution.

4.3.2 Effect on the energy reconstruction

A study [115] conducted on the 2010 data-set has concluded that the effect of non nominal LAr HV on the electron energy scale is less than 0.1%. This study was conducted using the electrons coming from Z boson decays. The energy scale uncertainty measured *in-situ* with electrons being much better than the one achievable using the jets, made this measurement non applicable to the JES.

[11] *ie* An High Voltage Power Supply stopping to feed the electrodes.

4.3.3 The case of the Pre-Sampler

Evaluation of the effect

In August 2010, the pre-sampler HV value was reduced from its nominal value at 2 kV to 1.6 kV at the end of the summer.

As explained in Chapter 3 Section 3.3.5, when the nominal HV is not applied to the electrode a correction factor is computed. The correction factor for the PS, to go from 2 kV to 1.6kV, is approximately 1.08. In Figure 4.28, the electronic cell noise values for the different calorimeter layers are given. For the PS this value is $\sigma_{PS} \approx 50$ MeV per cell. So applying the correction factor, the cell noise value increases to $\sigma_{PS} \approx 54$ MeV.

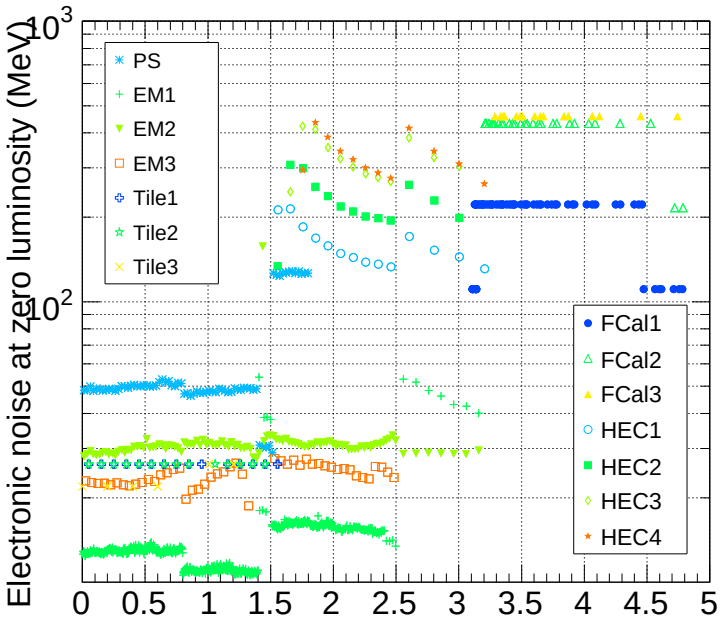

Figure 4.28: Electronic cell noise values for the different layers of the calorimeter.

The noise contribution of the cells in a layer are given by

$$\text{Noise Per Layer} = \text{Noise} \times \sqrt{N_{\text{cells (layer)}}} \tag{4.15}$$

The electronic noise value in a jet is obtained, by summing in quadrature, the contribution of each layer. Using the number of cells in the pre-sampler in 2010 jets, their transverse momentum, and the correction factor given above, it is possible to estimate what will be the energy resolution increase, due to the pre-sampler HV reduction. In the lowest $\langle p_T \rangle$ bin the effect of the HV reduction is found to be less than 0.1% in absolute. This effect decreases with rising p_T.

Even if the effect expected is rather small, even smaller than the systematic errors that were found on the two *in-situ* techniques, it is interesting to verify this in the data.

The 2010 sample is split into two samples, the one before the HV reduction, and the one after. The resolution techniques that have been described in section 4.2.1 are applied.

Check using the *in-situ* techniques

Figure 4.29 shows the results obtained using the bisector technique. The data after the reduction on the PS HV are in black and in blue for the period before it. The results of the two periods are found to be in good agreement in the low $\langle p_T \rangle$ bins, where the resolution effect was expected to be the larger, the relative agreement between the two is less than 5%, and anyway within the errors. The agreement is worse in the last $\langle p_T \rangle$ bins. No systematic shift, is observed between the two periods.

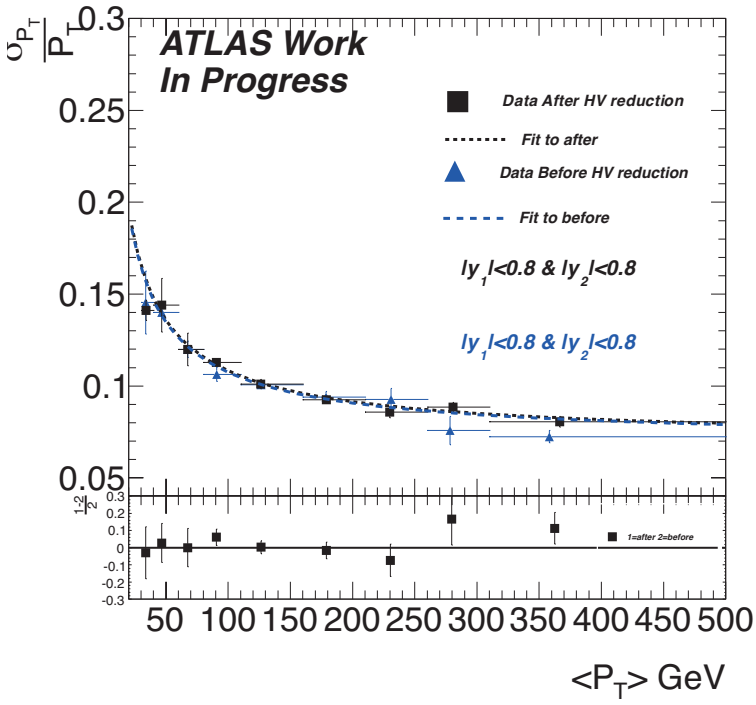

Figure 4.29: Jet fractional transverse momentum resolution for jets belonging in the $|y| < 0.8$ bin. The graph show the differences for the period before the PS HV was reduced and after. The results are shown for the bisector method. Data after the reduction are in black and data before the reduction are in blue.

Figure 4.30 shows the same results obtained using the di-jet balance method. The results showed using the di-jet balance are in worse agreement that they were for the bisector method. In the high $\langle p_T \rangle$ bins, the relative difference goes up to 30%. In the low $\langle p_T \rangle$ bins the relative difference is better than 10%. The results are anyway always within errors for the two periods.

The soft radiation effects distributions for the bisector and di-jet balance techniques are given respectively in Appendix A.4.2 and in Appendix A.3.3.

As expected, no dramatic effect is observed on the low energetic jets, where the differences were expected. The effect of the energy resolution increase does not seems to be sizable enough to be measured using these techniques.

4.3.4 Evaluation of the HV trips impacts

In order to set an upper limit on the effect we are looking at, one considers a mass-less jet produced at $|\eta| = 0$. Consider that this jet is squared with a side $S = 0.6$, since the jets studied are anti-K_T jets with $R = 0.6$. One can compute the number of cells contained in each layer of the LAr calorimeter

In Chapter 3, the size of the different calorimeter cells was given,

- PS: $\Delta\eta \times \Delta\phi = 0.1 \times 0.025$ so these jets will have 144 PS cells.
- First Layer: $\Delta\eta \times \Delta\phi = 0.1 \times 0.0031$, so about 1162 EM1 cells.
- Second Layer: $\Delta\eta \times \Delta\phi = 0.025 \times 0.025$, so about 576 EM2 cells.
- Third Layer it is $\Delta\eta \times \Delta\phi = 0.05 \times 0.025$, so about 288 EM3 cells.

Using Figure 4.28 and Equation (4.15), the electronic noise contribution of such jets is evaluated to be 1.1 GeV.

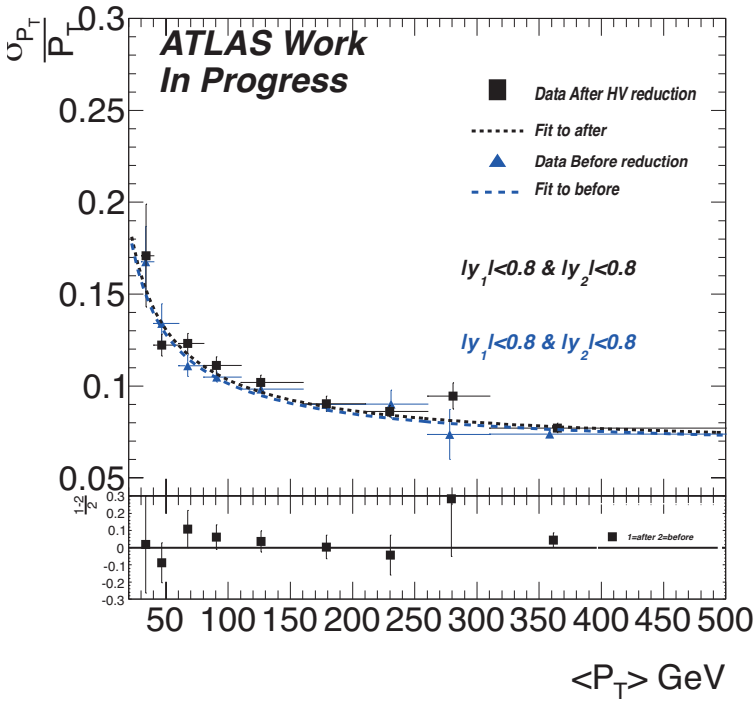

Figure 4.30: Jet fractional transverse momentum resolution for jets belonging in the $|y| < 0.8$ bin. The graph show the differences for the period before the PS HV was reduced and after. The results are shown for the di-jet balance method. Data after the reduction are in black and data before the reduction are in blue.

If this jet is located in an area where all the cells have lost the HV supply for one electrode side, then the increase of noise will be a factor 2 [98], giving an electronic noise contribution about 2.2 GeV. In this case it would mean that 9 HV (3×3 HV sector of size 0.02×0.02) sectors stopped working at the same time, which is quite unlikely.

If only one HV sector is not feeding its electrodes then the electronic noise value would be 1.3 GeV. It is also evident that if the HV is not nominal, but non zero in one sector, the impact will be smaller.

In the case of a 30 GeV mass-less jet produced at $\eta = 0$, the contribution of the electronic noise on the energy will be for the nominal case $\frac{\sigma_E}{E} \approx 3.6\%$, in the case where the 9 HV lines stopped feeding the electrodes $\frac{\sigma_E}{E} \approx 7.3\%$, and in the case of the loss of one HV sector $\frac{\sigma_E}{E} \approx 4.3\%$.

For a 300 GeV mass-less jet produced at $\eta = 0$, the same numbers are reduced to about 0.5%.

So it is interesting to notice that the loss of a couple of HV sectors could have a sizable effect on the jet energy resolution, the absolute order being about 1% or 2% for low energy jets.

In order to evaluate the impact of the non nominal HV area, one variable was introduced in the jet reconstruction

$$\mathrm{HV}_{\mathrm{Ratio}} = \frac{\sum_{\text{HV prob. cells}}}{\sum_{\text{Alls cells}}} \tag{4.16}$$

This variable counts the number of cells in a non nominal HV area and normalizes it to the total number of cells in the jets. So it can take any values from 0 to 1. To check only the impact of the HV trips on the energy resolution, only the data set before the lowering of the PS HV will be taken into account. This data-sets corresponds to an integrated luminosity[12] about 3 pb^{-1}. The low energetic bins are more populated than the energetic one due to the trigger configuration.

[12]The data set taken after the HV reduction corresponds to an integrated luminosity [116] about 34 pb^{-1}. The trigger threshold for the jets was increase when the instantaneous luminosity was raised, reasons why the low energetic $\langle p_T \rangle$ bins are more populated in the first 3 pb^{-1}.

The impact of the non nominal HV area will be evaluated by applying the di-jet balance and bisector technique analysis, on tree bins of this moment. If the HV has a sizable effect on the energy resolution, then one expect to observe an increase of the energy resolution for high HV ratio values.

In order to keep the statistic as high as possible in each bin, the binning is used:

- 0%, jet in a good area.
- $]0\%, 10\%]$, jet in medium affected area.
- $[10\%, 100\%]$, jet is in an affected area.

Due to the statistic available, the study was conducted only from the bin $30 < \langle p_T \rangle < 40$ GeV to the bin $110 < \langle p_T \rangle < 160$ GeV. The last four bins are merged in a single one $160 < \langle p_T \rangle < 500$ GeV.

Di-jet balance

Figures 4.31 (a) to (f) shows the jet fractional transverse momentum resolution versus the HV Ratio variable defined above, obtained with the jet balance method.

In all the $\langle p_T \rangle$ bins the energy resolution measured for each HV ratio bins are systematically in agreement within their errors.

The absolute difference between the two maximal central values is always less than 3%. In this study the statistical errors dominates the systematic uncertainties.

The soft radiation effect distributions for this section are given in Appendix A.3.4

Bisector Technique

Figure 4.32 (a) to (f) shows the fractional transverse momentum resolution of the jets versus HV Ratio obtained with the jet bisector technique.

In most of the $\langle p_T \rangle$ bins, the energy resolution measured in each HV ratio bin is compatible within uncertainty, except in the second $\langle p_T \rangle$ bin. It's also interesting to noticed that the energy resolution measured in each HV ratio bins are in agreement with the results found using the balance method. In the bisector study the most divergent central values are always less than 5% absolute difference.

The soft radiation validation distributions for this section are given in Appendix A.4.3.

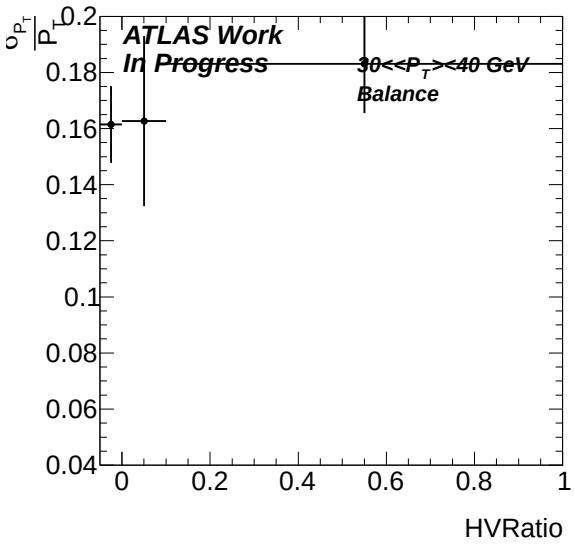

(a) $30 < \langle p_T \rangle < 40$ GeV

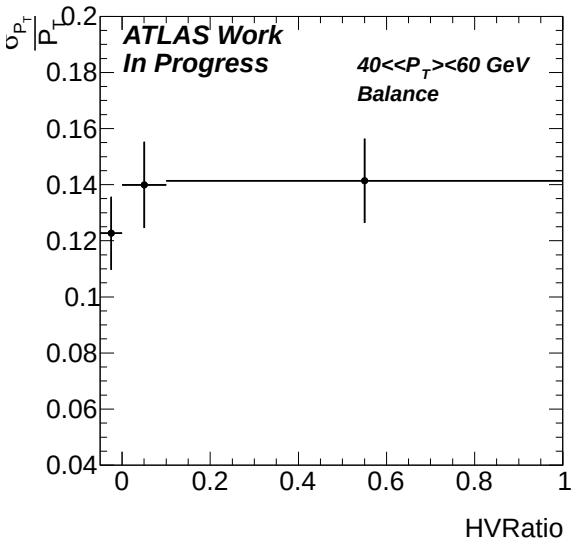

(b) $40 < \langle p_T \rangle < 60$ GeV

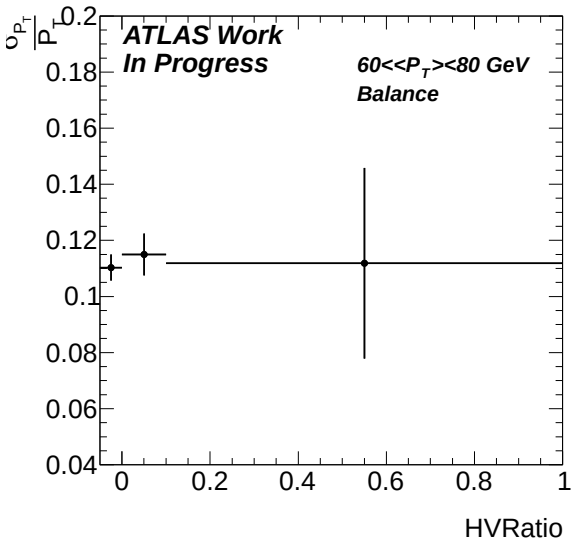

(c) $60 < \langle p_T \rangle < 80$ GeV

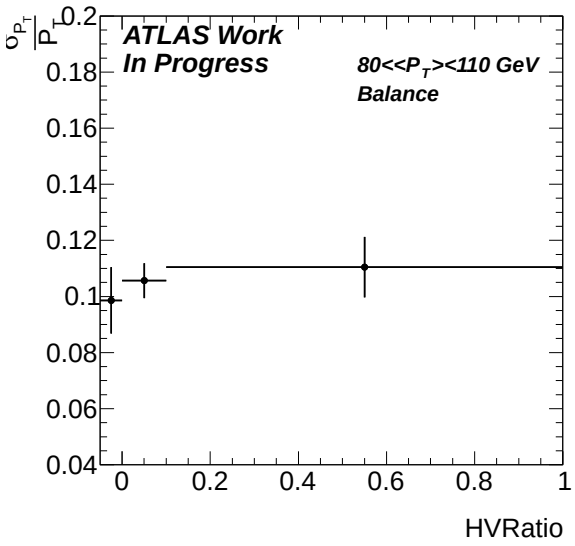

(d) $80 < \langle p_T \rangle < 110$ GeV

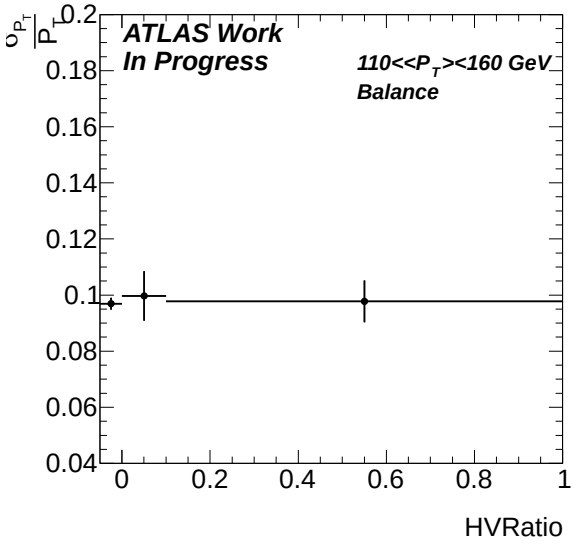

(e) $110 < \langle p_T \rangle < 160$ GeV

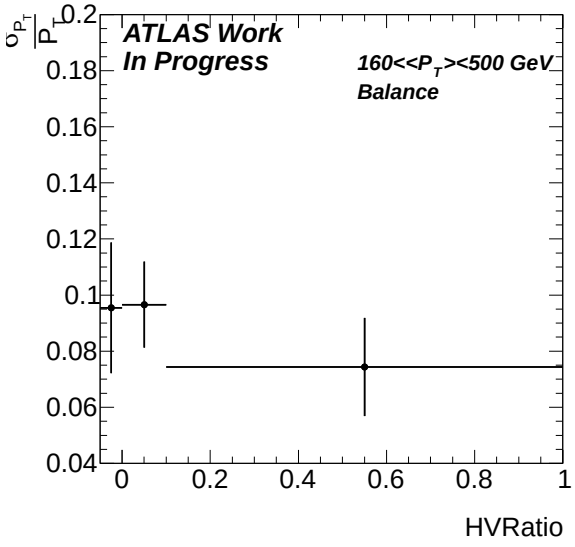

(f) $160 < \langle p_T \rangle < 500$ GeV

Figure 4.31: Jet fractional transverse momentum resolution measured vs the variable HV Ratio, for different $\langle p_T \rangle$ bins. Results obtained using the balance method.

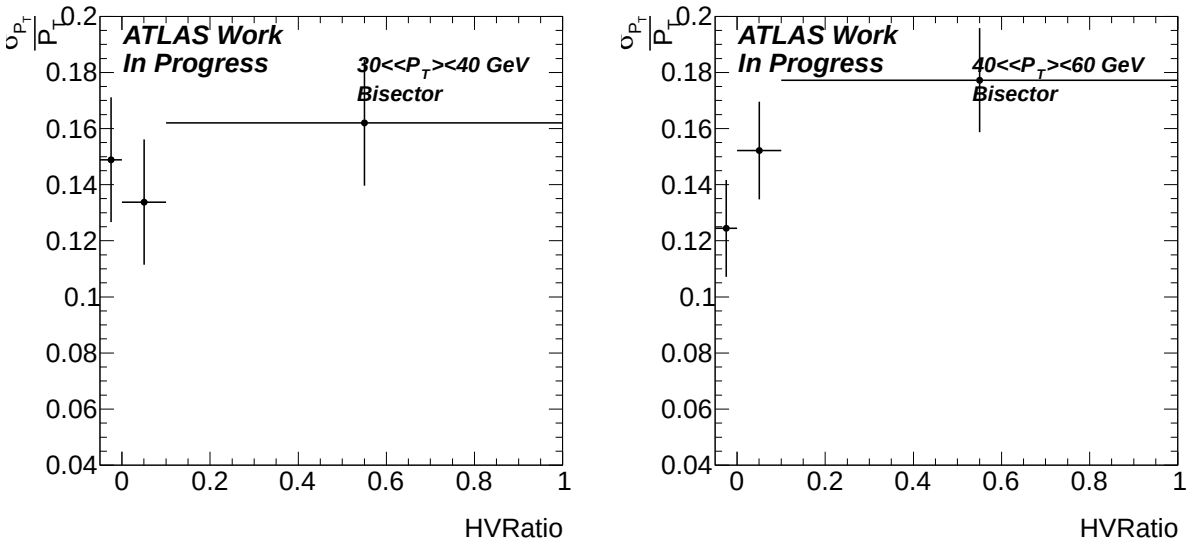

(a) $30 < \langle p_T \rangle < 40$ GeV

(b) $40 < \langle p_T \rangle < 60$ GeV

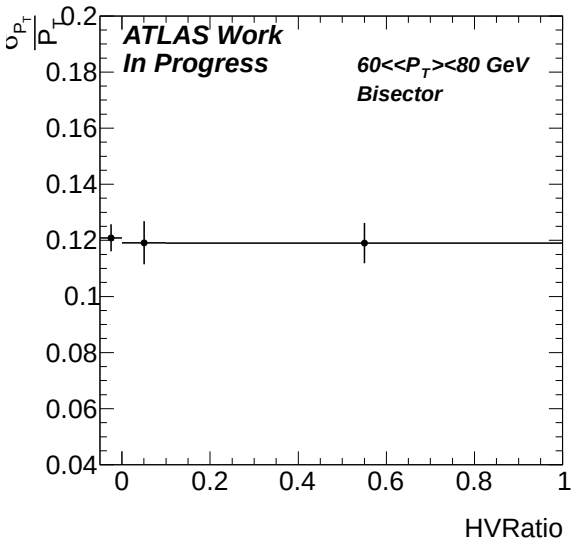

(c) $60 < \langle p_T \rangle < 80$ GeV

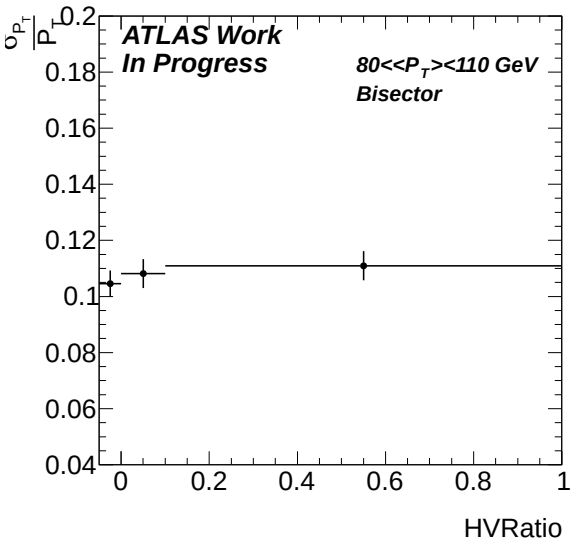

(d) $80 < \langle p_T \rangle < 110$ GeV

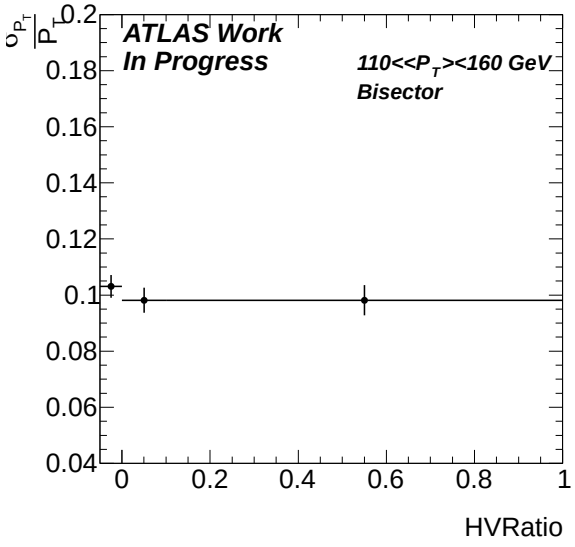

(e) $110 < \langle p_T \rangle < 160$ GeV

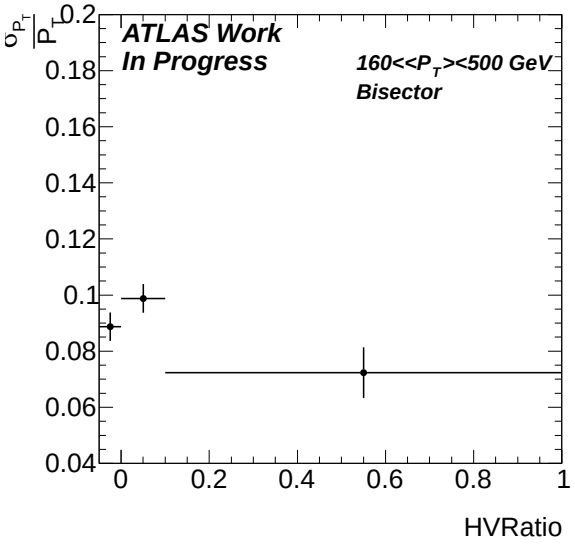

(f) $160 < \langle p_T \rangle < 500$ GeV

Figure 4.32: Jet fractional transverse momentum resolution measured vs the variable HV Ratio, for different $\langle p_T \rangle$ bins. Results obtained using the bisector technique.

Results and discussion

In order to investigate a systematic effect due to the HV, Figure 4.33 (a) and (b), shows the absolute difference between the first bin, the two jets in a nominal region, and the most divergent bin, for the di-jet balance method (a) and the bisector technique (b).

In Equation 4.2, it is expected that the contribution of the noise term to the energy resolution follows a $\frac{N}{p_T}$ shape. The two distributions in Figure 4.33 (a) and (b) are fitted using this function, to estimate the increase due the reduced HV. A single variable ΔN is introduced corresponding to the increase of the energy resolution due to the non nominal HV sectors.

For the di-jet balance method, the results gives $\Delta N \approx 0.6 \pm 0.4$ GeV, while it gives $\Delta N \approx 0.7 \pm 0.3$ GeV for the bisector technique. So it is interesting to noticed that the results obtained by the two techniques are rather similar. The systematic uncertainties of the di-jet balance and bisector techniques are on the order of 2% in absolute for the first $\langle p_T \rangle$ bins and drops to about 0.5% at $\langle p_T \rangle$.

In this study each $\langle p_T \rangle$ bins is re-divided in HV Ratio bins, so the measurements are dominated by the statistical uncertainties. It is also noticeable that for each points the systematic uncertainties contributes to a non negligible fraction of the errors. Using these data-driven techniques, the effect of the non nominal HV area on the jet energy resolution does not seems to be sizable enough to be measured.

One can however set a limit $\Delta N \lesssim 1$ GeV, which means that the effect of the non nominal HV area on the jet energy resolution is less than 3% at $p_T \approx 30$ GeV, falls at less than 1% around $p_T \approx 100$ GeV, and on the order of 0.1% at $p_T \approx 500$ GeV.

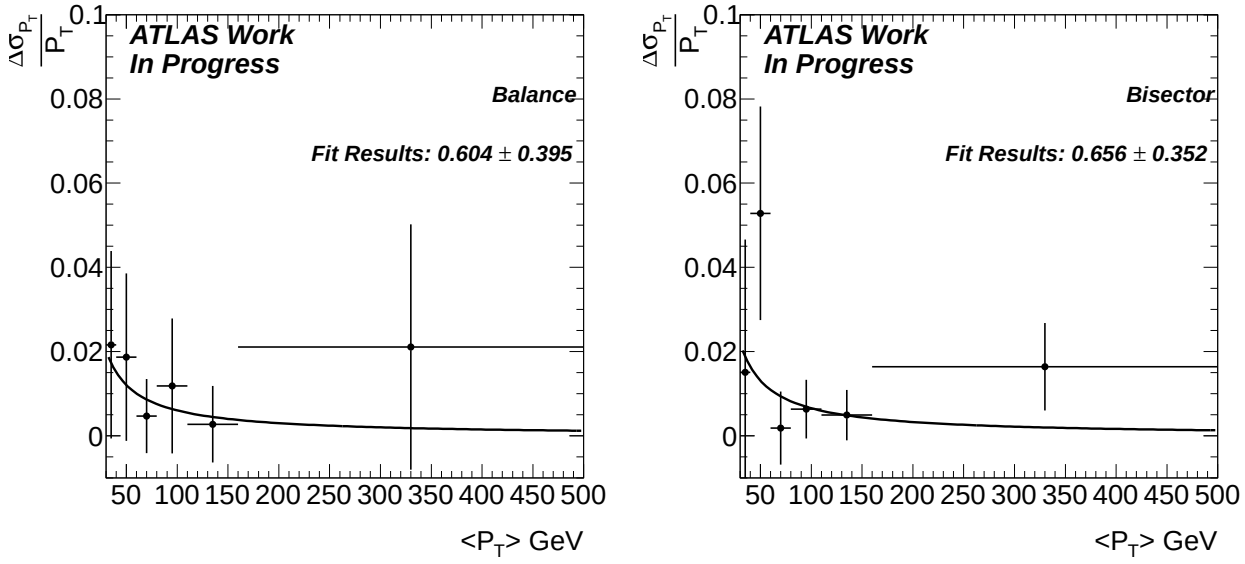

(a) Di-jet Balance.

(b) Bisector techniques.

Figure 4.33: Resolution absolute difference between the first HV Ratio bin and the most divergent one as a function of $\langle p_T \rangle$.

Conclusion

In this chapter, it was shown that it is possible to evaluate the resolution of the jets using *in-situ* techniques. It was in particular explained that when the statistics available are high enough, the truth jet energy resolution on MC is recovered with a relative difference less than 10%, and with an absolute systematic error about 2% in the first $\langle p_T \rangle$ bin for the bisector technique, and less than 2% in the first $\langle p_T \rangle$ bin for the di-jet balance method.

The jet energy resolution was also estimated on MC and on Data, a systematic shift about 10% was found in the resolution measured in the data compared to the resolution measured on MC. This result was previously found in the ATLAS collaboration, but no satisfactory answers have been discovered yet. Investigations are still ongoing.

A study was conducted to evaluate an effect on the jet energy resolution of the non nominal high voltage area in the LAr calorimeter.

The impact of the reduction of the PS HV value from its nominal value of 2 kV to 1.6 kV, was measured to be within the errors of the two *in-situ* techniques used. No degradation was found.

Using a rough approximation, the impact of the reduced high voltage area in the LAr calorimeter on the jet energy resolution, was estimated to be on the order of 1% in the firsts $\langle p_T \rangle$ bins. This effects should drops rapidly when the transverse momentum of the jet increases. This effect is *a priori* on the order of the level of precision reachable by the two data driven techniques introduced in this chapter.

A new variable was introduced in the reconstruction in order to check that the reduced HV region effect on the jet energy resolution is not larger than this estimation. The study of this variable on the data did not allow to detect a major degradation of the jet energy resolution. The measurements are subject both to the statistical and systematic uncertainties. The effect of reduced HV regions on the jet energy resolution is not sizable enough to be measured using 2010 data-sets.

A limit can be set on the increase of the Noise term: $\Delta N \lesssim 1$ GeV, meaning that the effect of the non nominal HV area at 1 σ on the jet energy resolution is less than 3% at $p_T \approx 30$ GeV, and on the order of 0.1% at $p_T \approx 500$ GeV.

This measurement can be improved by different approaches:

- Having a more important Monte Carlo data-sets could allow to have a better understanding of the systematic errors related to the di-jet and bisector techniques.

- The statistics of the 2011 data-set could be used to extend this study. However due to the increase of the instantaneous luminosity the trigger threshold for jets was raised up, meaning that the low $\langle p_T \rangle$ bins, which are *a priori* the one that will be most affected by the HV are not populated. Also the pile-up conditions are about five time larger in 2011 (15 pile-up events) than they were in 2010 (3 pile-up events), meaning that the HV impact could be drown in the pile-up noise.

- Due to the worse intrinsic energy resolution of jets, the most promising solution to study the reduced HV effect, is to change the final state from di-jet events to gamma jets or Z+jets events, the energy resolution on the photons and electrons coming from the Z bosons decay, being much better than the one of jets.

The evaluation of detector effects on performances is essential in order to provide good physics results. In the case of the reduced HV area of the LAr calorimeter, it was demonstrated that their impact on the reconstruction is not sizable enough to have a strong impact on physics.

Chapter 5

Search for Technicolor particles decaying in $W\gamma$

"Attendre et espérer !"
Alexandre Dumas, *Le comte de Monte-Cristo.*

Personal contribution
The determination of the Standard Model processes described in this Chapter follows the analysis described in Reference [117]. The analysis was redone in order to develop the analysis framework, and I added the template fit approach to cross check the results found with the 2D side band method. The optimization of the search follows an old analysis I performed during my thesis described in Reference [118]. The fits and statistical analysis on MC and data follows the analysis described in Reference [119], but was redesigned for the search in the $W\gamma$ final state.

Introduction

In the $W\gamma$ final state, no search for narrow resonances have been conducted at the LHC. This chapter describes such search, where the W boson decays into a neutrino and an electron. The muon final state is not considered in ATLAS for now but it will be done in the future.

As presented in the first Chapter, the Low Scale TechniColor (LSTC) model predicts the existence of several new resonances, in particular in the $W\gamma$ final state, two particles are foreseen: ρ_T and a_T, with close to degenerated masses. The latest constraint that have been set on the LSTC models were obtained by the ATLAS collaboration in the dilepton final state. Looking at Figures 1.12, one can see that the allowed LSTC phase space is severely constrained, under certain restrictive hypothesis, the production of the ρ_T being excluded up to to almost $M(\rho_T) = 450$ GeV [46]. This limit is not within reach in the $W\gamma$ mode with the dataset currently available. However as no study have been conducted on this final state, the LSTC model is used as a benchmark model to search for resonances in the $W\gamma$ final state.

This Chapter is organized as follows: the first Section describes the dataset and Monte Carlo samples used, the second Section makes a brief overview of the object reconstruction, the third and fourth Sections explained the study conducted to understand the SM backgrounds. The discriminating variable and optimization cuts for the search are given in the fifth Section, the fit functions, statistical and systematic errors are explained in the sixth, seventh, and eighth Sections respectively. Finally, the results obtained on the data are given in the last Section.

5.1 Data and Monte Carlo samples

5.1.1 Data

The search for technipions decaying into $W \rightarrow e\nu$ and a photon is conducted using pp data at $\sqrt{s} = 7$ TeV collected by ATLAS from March to the end of August 2011. After applying Data Quality criteria to the data, the integrated luminosity is $\mathcal{L} = 2.04$ fb^{-1}. The integrated luminosity uncertainty is 3.7% [120]. Table 5.1 summarizes the data taking periods with their corresponding integrated luminosity and the trigger selection applied.

Data Period	Run Range	Integrated Luminosity [pb^{-1}]	Electron Trigger
B	178044 → 178109	11.4	EF_e20_Medium
D	179710 → 180481	154.2	EF_e20_Medium
E	180614 → 180776	42.5	EF_e20_Medium
F	182013 → 182519	122.7	EF_e20_Medium
G	182726 → 183462	464.2	EF_e20_Medium
H	183544 → 184169	240.2	EF_e20_Medium
I	185353 → 186493	304.5	EF_e20_Medium
J	186516 → 186755	209.4	EF_e20_Medium
K	186873 → 187815	492.3	EF_e22_Medium
Total	179710 → 187815	2041.6	EF_e20_Medium or EF_e22_Medium

Table 5.1: The luminosity and trigger items for each data sample used in this analysis.

5.1.2 Monte Carlo samples

Low Scale TechniColor signals

In total 7 LSTC samples were generated with different resonance masses. The production cross section times branching ratio for each sample as well as the most important generation parameters are given on Table 5.2. Using these parameters most of the rate for each processes comes from the decay of the $a_T$mesons, the contribution the ρ_T being less important. For all these samples the ρ_T and ω_T have the

same mass. The vector and axial coupling parameters[1] are set to the mass of the ρ_T. The fourth point T290 of this study was motivated by an excess observed by CDF [49] which can be interpreted on a potential signal in the context of LSTC [51]. The parameters corresponds to those tuned to explain this excess, and are different from those used at other points. The cross sections were obtained with PYTHIA using the MRST2007 LO* [121] PDF.

Mode	π_TMass (GeV)	ρ_TMass (GeV)	a_TMass (GeV)	$\sigma\times$ BR (fb)	filter efficiency
T200	125	200	220	208.1	0.77
T225	150	225	250	131.6	0.79
T250	175	250	275	93.3	0.80
T290	160	290	320	31.0	0.82
T300	200	300	330	39.1	0.82
T350	225	350	375	21.7	0.80
T400	275	400	440	13.4	0.84

Table 5.2: Parameters, cross sections and filter efficiencies for the signal points considered in this analysis. No K-factor are used for the signal.

The LSTC samples were generated with PYTHIA, using three generator filter:

- $M_{\rho_T} - 25$ GeV $< \sqrt{s} < M_{a_T} + 25$ GeV. This filter allows to restrain the generation of the events in a range around the peak position. This is done to avoid the simulation of events, that will not be useful for a discovery.
- The events must contain one electron with $p_T(e) > 15$ GeV and $|\eta_e| < 3$.
- The events must contain one photon with $p_T(\gamma) > 15$ GeV and $|\eta_\gamma| < 3$.

The last two filters allows to simulate only events that are generated in the precision region of the detector.

The samples were simulated using the full ATLAS Geant 4 [100] simulation, and reconstructed in the same way as the data.

Standard Model backgrounds

The Standard Model backgrounds used in this analysis are given in Appendix. The main processes are summarized in Table 5.3. The cross sections quoted are the NNLO or NLO ones[2].

The inclusive single gauge bosons decaying to leptons were generated with AlpGen [122] interfaced with Herwig [123, 124] for the parton shower and Jimmy for the underlying event. Their cross sections are normalized to the Next to Next Leading Order value [61] (NNLO), using a k-factor. The production cross-sections times branching ratio, k-factor and filter efficiencies are given in Table B.1 of Appendix.

The single top and $t\bar{t}$ processes were obtained using MC@NLO [125, 126, 127] interfaced with Herwig and Jimmy. Finally the di-boson events were generated using AlpGen interfaced with Herwig and Jimmy. A $W\gamma$ sample produced with the Sherpa [128] generator is also used for cross-checks. Even if it contains more statistics than the AlpGen sample, it was however not chosen because some distributions such as number of jets describes poorly the data. They are summarized in Table B.2 of Appendix.

The inclusive W sample contains events were a photon was produced by ISR and FSR. To avoid double counting of these events between the inclusive W sample and the $W\gamma$ sample, a special treatment is applied. The events containing a photon produced by ISR or FSR are removed from the inclusive W sample. This is done, at truth level, by requiring that the mother of the photon is not

[1] see Chapter 1 for details on the quantities and the LSTC parameters.

[2] The SM $W\gamma$ cross section quoted in Table B.2 in Appendix for the AlpGen sample contains the muon final state, reason why the cross section is about twice the one quoted in Table 5.3.

Main process	Cross Section	Generator
$Z \to ee$	969 pb (NNLO)	AlpGen
$W \to e\nu$	10147 pb (NNLO)	AlpGen
$W \to \tau\nu$	10147 pb (NNLO)	AlpGen
$t\bar{t}$	165 pb (NLO)	MC@NLO
$W\gamma$	215 pb (NLO)	AlpGen

Table 5.3: Approximate cross-sections for the main Standard Model backgrounds contributing in the $W\gamma$ search.

a quark, gluon or coming from the gauge boson decay chain. The only events that are left in the inclusive W samples are those where a jet will fake a photon.

The W+jet background is estimated from data using two different data driven techniques. The QCD multi-jet background is also evaluated from the data. This is detailed in Section 5.4.

In all the following distributions, the Monte Carlo is weighted to the measured luminosity $\mathcal{L} = 2.04$ fb^{-1}; the MC uncertainties are statistical only; the first bin of the histograms also contains the underflow events, and the last bin of the histogram also contains the overflow events, except stated otherwise.

Pile-up reweighing

The Monte Carlo samples used in this analysis were produced with overlaid minimum bias, beam halo, and beam gas events to simulate the bunch train pileup and cavern background that occurred in 2011 data. The number of pile-up events follows a Poisson distribution with a mean equal to 8.6. The pile-up characteristics are *a priori* different in the data, due to the evolution of the LHC conditions in 2011. The simulated samples are therefore reweighed on an event-by-event basis to account for deviations from data in the number of average interactions per bunch crossing : $\langle\mu\rangle$.

Figures 5.1 shows the number of reconstructed vertices, with and without this correction, for the events selected at the end of the selection given in Section 5.3. The Monte Carlo distribution after correction is in good agreement with the data.

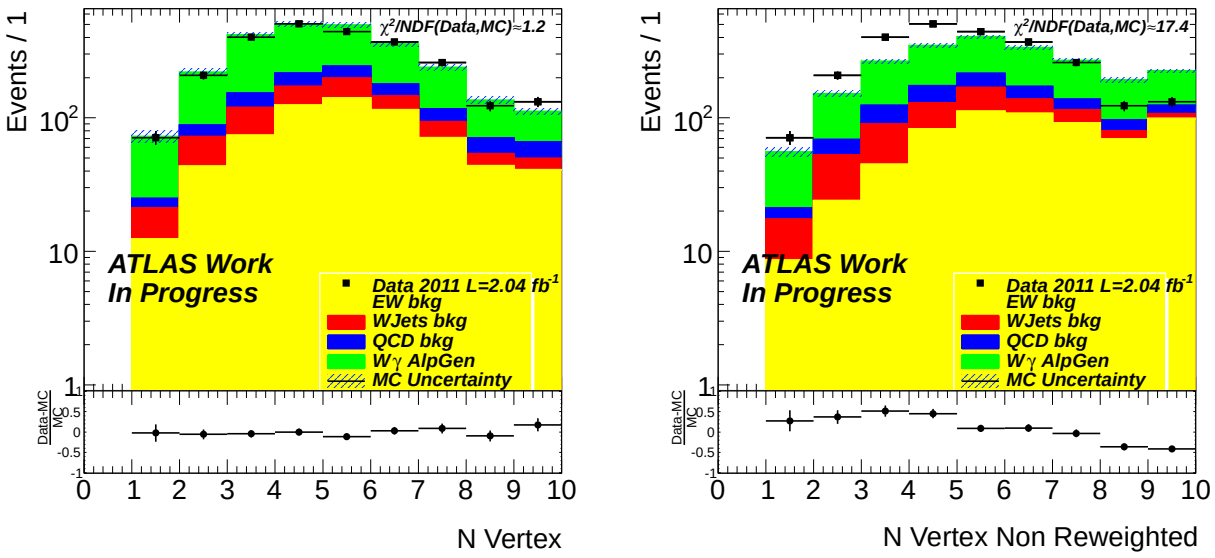

(a) With pile-up correction.

(b) Without pile-up correction.

Figure 5.1: Number of reconstructed vertices with (a) and without (b) the Pile-Up reweighing correction.

5.2 Object definitions

5.2.1 Electrons

Reconstruction

The reconstruction of electrons and photons in ATLAS starts from the calorimeter with an algorithm called "Sliding Window" [129, 130]. This algorithm allows to obtain objects with a fixed cluster size, and thus allows a very precise calibration of the cell energy.

The calorimeter is divided into a map of cell granularity corresponding to the second EM layer $\Delta\eta \times \Delta\phi = 0.025 \times 0.025$ up to $|\eta| < 2.5$.

The window is constituted from $\Delta\eta \times \Delta\phi = 5 \times 5$ cells and slides on the map, until a local maximum with an energy $E_{\text{Window}} > 3$ GeV is found. When such a maximum is found, the energies of all the cells in a rectangle around this seed are added.

The dimensions of the reconstructed electrons in terms of cells are $\Delta\eta \times \Delta\phi = 3 \times 7$ in the barrel and $\Delta\eta \times \Delta\phi = 5 \times 5$ in the end caps.

The reconstruction algorithm then loops over the tracks reconstructed using the ID. If a track with a $p_{\text{T}} > 500$ MeV is associated to the cluster, then the cluster+track object is classified as an electron.

The energy calibration of electrons is obtained using single particles in Monte Carlo simulations. This allows to determine calibration constants for each layer of the EM calorimeter. The electron cluster energy is reconstructed adding the energy of the different EM calorimeter layers weighed by the correction factor determined from MC. A global energy scale factor is set as a function of η using the Z boson masses [76].

The energy surrounding the electron cluster in a given cone of size ΔR excluding the energy of the cluster itself is called the isolation energy of the electron. It is corrected to account for the pile-up effect, using the vertex multiplicity.

Identification

In order to get a consistent definition of electrons for the different physics analyses, three sets of cuts have been introduced. The main characteristics of these sets for electron with $p_{\text{T}} > 20$ GeV produced in the central region [129] are summarized as:

- a Loose selection based on calorimeter variables only. It allows to identify electrons with an efficiency of 94%. The rejection factor between electron and jets is 614 ± 2.
- a Medium selection based on calorimeter and tracking variables. It allows to identify electrons with an efficiency of 89%. The jet rejection factor is 4435 ± 30.
- a Tight selection based on the full identification potential of the ATLAS detector. In particular identification cuts using both the calorimeter and inner detector are applied. The identification efficiency is 72% with a jet rejection factor of $(4.9 \pm 0.1) \times 10^4$. The tight selection is the one that is used in this Chapter.

The electron identification efficiencies depend on p_{T} and η, as shown on Figures 5.2.

MC Corrections

In Monte Carlo samples, electrons are corrected as follows:

- Electrons in MC simulated events do not fully reproduce the reconstruction efficiency measured in data. A correction factor (commonly called a scale factor) is applied to each electron in MC events. This factor is defined as the ratio of reconstruction efficiencies for data and MC events as measured using $Z \to ee$ events. Correction factors for Medium and Tight electrons are determined in bins of η and ϕ, with typical values of approximately 0.97.

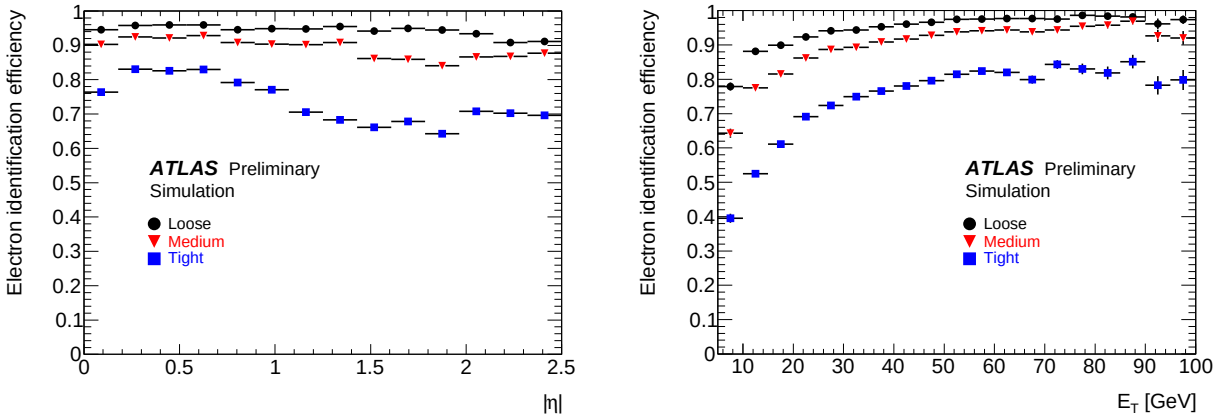

Figure 5.2: Identification of the electrons obtained on $Z \to ee$ Monte Carlo samples, for the three default set of cuts, Loose, Medium and Tight. As a function of $|\eta|$ (left) and E_T (right) [129].

- The energy of MC electrons is also smeared to reproduce the resolution measured in data using $J/\psi \to ee$ (low p_{T}) and $Z \to ee$ (high p_{T}) events.
- The Monte Carlo samples were simulated using the conditions of the detector at the beginning of 2011 run. The conditions have evolved with time, leading to non-nominal regions appearing and disappearing from one run to another one. Electrons are vetoed in the Monte Carlo, using a luminosity-weighed map of these regions.

5.2.2 Photons

Reconstruction

The "sliding window" algorithm is also used for the reconstruction of photons. The dimensions of the reconstructed cluster are different for photons. They are $\Delta\eta \times \Delta\phi = 3 \times 5$ for unconverted photons in the barrel, $\Delta\eta \times \Delta\phi = 3 \times 7$ for converted photons in the barrel and $\Delta\eta \times \Delta\phi = 5 \times 5$ for both categories in the end-caps.

If no tracks are matched to the cluster, the object is defined as an unconverted photon. If a track is matched to the cluster and points to a conversion vertex, the object is defined as a converted photon.

The photons energy is calibrated using single particles in Monte Carlo simulations. The weight are however different from that of the electrons. The global energy scale is recalibrated using the same in-situ measurement as for the electrons.

Identification

Similarly to electrons, two different baseline cut-based selections optimized for identification efficiency and background rejection are defined [130]. Their characteristics are summarized as follows:

- a Loose selection. It allows to reconstruct a $p_{\mathrm{T}}(\gamma) > 25$ GeV photon with an efficiency of 93%, with a jet rejection factor of 1030 ± 6.
- a Tight selection, allowing to reconstruct a $p_{\mathrm{T}}(\gamma) > 25$ GeV photon with an efficiency of 87% and a jet rejection factor of 5290 ± 70. The tight selection is the one used in the rest of this study.

These identification efficiencies were found using MC simulations. The full list of the variables used are given in [130]. They are p_{T} and η dependent as shown in Figure 5.3.

Five identification cuts included in the Tight set are introduced because they will be used later on. This cuts are based on the first LAr calorimeter layer:

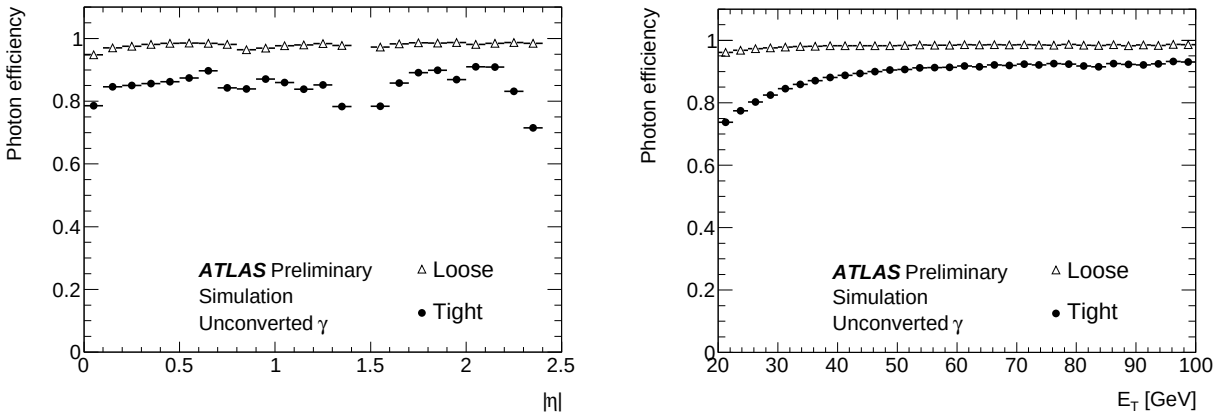

Figure 5.3: Identification of the photons obtain on MC for the two default set of cuts, Loose and Tight. As a function of $|\eta|$ (left) and E_T (right). [130]

- w_{s3}: electromagnetic shower width for three strips around the maximum strip.
- w_{stot}: total lateral shower width.
- F_{side}: fraction of energy outside a core of 3 central strips, and within 7 strips.
- ΔE: Difference between the energy associated with the second maximum in the strip layer, and the energy reconstructed in the strip with the minimal value found between the first and second maxima.
- E_{Ratio}: Ratio of the energy difference associated with the largest and second largest energy deposits over the sum of these energies.

The photon identification is also based on an isolation criterion. More precisely it is based on the measurement of the calorimetric isolation energy, defined as the total calorimetric energy deposited in a cone of radius $\Delta R = 0.3$ and outside a core of $\Delta\eta \times \Delta\phi = 0.125 \times 0.175$. This variable is called $E_T^{\text{cone(30)}}$. The isolation cone variable is corrected to take into account the pile-up effect, using the energy density in the event. A small correction is also applied to take into account the dependency of the photon p_{T}.

MC corrections

The photons Monte Carlo treatment follows most of the steps used for the electrons.

- The energy of the photon is smeared to reproduced the resolution measured in the data.
- The differences observed between data and MC in the identification efficiencies are coming from differences of the discriminating variables measuring the photon shower shape distributions. These differences are parameterized as simple shifts. These shifts are called scale factors. They are computed as the difference between the mean of a given variable in data and MC. The scale factors are then applied to the photon discriminating variables in the MC to obtain the corrected efficiency.
- The non-nominal regions of the detector are vetoed based on a luminosity weighed map depending of the actual detector conditions.

5.2.3 Jets and missing transverse energy

Jets

The jet reconstruction was described in Chapter 4. The jet definition used in this study is anti$-K_T$ topocluster jets with $R = 0.4$ calibrated at the EM+JES scale. Jets used in the analysis are required to satisfy the following criteria:

- $p_{\mathrm{T}} > 30$ GeV and $|\eta| < 4.4$.
- The distance of the jets to a photon or an electron is $\Delta R > 0.6$.
- A set of cleaning cuts has been defined to flag jets which may be coming from beam background, cosmic rays or instrumental events. Events with at least one jet flagged by these cuts are rejected.

Only the jet multiplicity variable is looked at in this study.

Missing Transverse Energy

In this analysis the missing transverse energy ($E_{\mathrm{T}}^{\mathrm{miss}}$) is determined from the energy measured in the electromagnetic and hadronic calorimeters. The $E_{\mathrm{T}}^{\mathrm{miss}}$ attributed to the calorimeter is defined as minus the vector sum of the transverse energies of the calibrated topological clusters.

Corrections

At the end of April, a malfunctioning crate controller caused a portion of the LAr detector to fail in the range ($0 < \eta < 1.4$ and $-0.8 < \phi < -0.6$). The signal was lost in the second and third layers of the EM barrel on this range. The situation was partially recovered on beginning of July by retrieving the output from the EM barrel second layer. Since approximately 42% of the 2.04 fb^{-1} of data used in this analysis were collected with this failure, the effect needs to be propagated to the MC. Events in data and MC that contain at least one jet with $p_{\mathrm{T}} > 20$ GeV in the region $-0.1 < \eta < 1.5$ and $-0.9 < \phi < -0.5$ are vetoed if they are part of the run affected on data, and based on a luminosity weighted random generator on Monte Carlo.

This failure is referred to as "*LAr hole*" in the following.

5.3 Selection

5.3.1 Pre selection

In order to optimize the analysis time, the full data set and Monte Carlo samples were skimmed. They are preselected in the analysis if they pass this set of cut:

- Pass the trigger selection EF_e20_Medium or EF_e22_Medium.
- The events must contain one Loose electron with $|\eta| < 2.5$ and $p_{\mathrm{T}} > 15$ GeV.
- The events must contain one EM object reconstructed as a photon with $|\eta| < 2.5$ and $p_{\mathrm{T}} > 10$ GeV, and $\Delta R(e, \gamma) > 0.1$.
- The events must have at least $E_{\mathrm{T}}^{\mathrm{miss}} > 10$ GeV.

5.3.2 Selection

Once the data and Monte Carlo are pre-selected, the analysis selection is applied on both to obtain a $W + \gamma$ sample as pure as possible. The selection follows that of the Standard Model $W\gamma$ analysis [117] and is made as follows:

- On the data the event must pass a good run selection, allowing to remove the data where the conditions were not sufficiently good to be added in physics analysis. This selection is suppress on Monte Carlo.
- The events must contain a Primary vertex with at least three tracks with $p_{\mathrm{T}} > 150$ MeV, and within 200 mm of the beam spot position along z.
- The trigger selection is applied. The events must pass the trigger item EF_e20_Medium for data up to period K and EF_e22_Medium for this last period. On Monte Carlo the trigger item is chosen according to the luminosity of each period. These trigger items are the lowest un-prescaled electron trigger item.
- The events must contain a Tight electron with $p_{\mathrm{T}} > 25$ GeV and $|\eta| < 2.47$. The tight selection is used in order to get an higher electron purity sample. The cut $p_{\mathrm{T}} > 25$ GeV is made such that the electron reconstruction efficiency is not biased by the trigger selection. If the events contain a second Medium electron (with $|\eta| < 2.47$ and $p_{\mathrm{T}} > 25$ GeV) the events are vetoed. This cut suppresses the backgrounds coming from Z boson decays.
- The Missing transverse energy in the event must be $E_{\mathrm{T}}^{\mathrm{miss}} > 25$ GeV.
- The transverse mass of the event is defined using the electron and the $E_{\mathrm{T}}^{\mathrm{miss}}$ as

$$M_T = \sqrt{2p_{\mathrm{T}}(e)E_{\mathrm{T}}^{\mathrm{miss}}[1 - \cos(\phi(e) - \phi^{\mathrm{miss}})]} \tag{5.1}$$

  This quantity has a Jacobian shape peaking at the mass of the W for the events containing a W boson. The transverse mass is required to be $M_T > 40$ GeV. The $E_{\mathrm{T}}^{\mathrm{miss}}$ and M_T cuts are designed such as the contamination of QCD multi-jet events is suppressed.
- The events must contain one Tight photon with $p_{\mathrm{T}} > 25$ GeV, and $|\eta| < 2.37$, with a distance $\Delta R(e, \gamma) > 0.7$. This latter cut is done such that the contamination from FSR is reduced.
- The energy surrounding the photon in a cone of $\Delta R = 0.3$, is required to be $E_T^{\mathrm{cone(30)}}(\gamma) < 6$ GeV. This selection is made so that the W+jets background, where a jet is faking a photon is suppressed.
- The invariant mass of the photon and the electron is required to be $|M(e, \gamma) - M_Z| > 10$ GeV[3]. This cut is also designed to suppress even further the background coming from the Z boson decay.
- The events where a photon, electron or jet is reconstructed in the *LAr hole*, as defined in Section 5.2.3, are rejected, in order to avoid mis-measurement of the $E_{\mathrm{T}}^{\mathrm{miss}}$.

This first selection allows to study the SM backgrounds and in particular the QCD and W+jets backgrounds that are estimated from the data, as it is explained in the next section.

5.4 Standard Model backgrounds

The Tight electron and Tight photon selections are used to remove most of QCD multi-jets and W+jets backgrounds. However as said in Section 5.2.1 and Section 5.2.2 the estimated jet-rejection factors for Tight electrons and Tight photons are respectively about 50000 and 5000. The processes leading to a fake electron or a fake photon are not well described by the full simulation and the Monte Carlo statistics available to study them is generally not sufficient. Even if the analysis selection is such that these events are highly suppressed, their contamination needs to be evaluated.

In this section, the contamination of the multi-jet and W+jets processes faking the $W + \gamma$ final state, is evaluated using data-driven techniques. In order to get a cross check, two different methods are used to retrieve the normalization of these background.

[3]The mass of the Z is taken as the value given in the PDG, $M_Z = 91.1876$ GeV [13].

5.4.1 Multi-jet contamination

Figure 5.4 (a) shows the $E_{\mathrm{T}}^{\mathrm{miss}}$ distribution of the selected events without the $E_{\mathrm{T}}^{\mathrm{miss}} > 25$ GeV cut, for the data in black and for the Monte Carlo samples. The lower part of the $E_{\mathrm{T}}^{\mathrm{miss}}$ spectrum is in disagreement with the Monte Carlo. In this region, the data shows an excess with respect to the MC. The core and the tail of the distribution especially above $E_{\mathrm{T}}^{\mathrm{miss}} > 25$ GeV are in better agreement.

Figure 5.4 (b) shows the isolation variable of the electron $E_T^{\mathrm{cone(30)}}$(e), for data and Monte Carlo, after all the selection are made. The core of the Data distribution is in agreement with the Monte Carlo one, but the tail of this distribution shows more events in the data, than what is expected in the MC.

In these two figures, the Monte Carlo samples are separated in two. The green samples corresponds to the Monte Carlo samples containing real missing transverse energy, while the yellow samples does not contain real missing transverse energy.

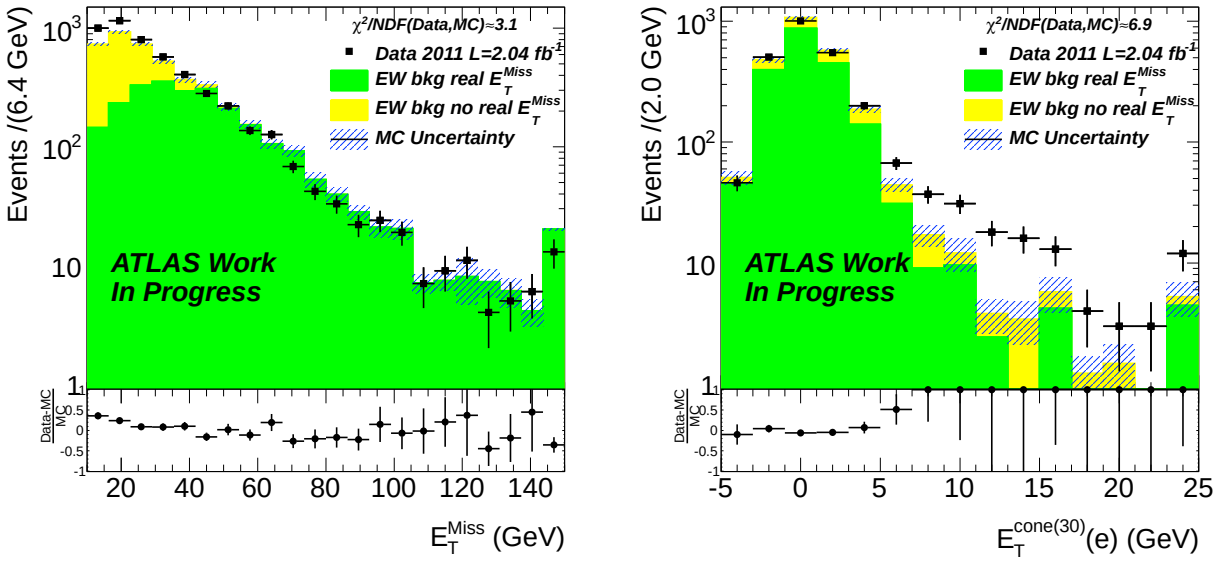

(a) $E_{\mathrm{T}}^{\mathrm{miss}} > 10$ GeV

(b) Isolation of the electrons, with $E_{\mathrm{T}}^{\mathrm{miss}} > 25$ GeV.

Figure 5.4: Monte Carlo versus data after the selection is applied for the $E_{\mathrm{T}}^{\mathrm{miss}}$ distribution (a) and for the electron isolation (b).

These two distributions show the impact of the QCD background. As this background is difficult to be estimated from MC, two independent data driven techniques are presented in the rest of this section, in order to cross check the results obtained. Multi-jet and gamma-jet Monte Carlo events were tested, but due to the limited statistics available almost no events pass the final selection.

Template fit method

The first method that can be used to estimate the QCD background contamination is a template fit approach. This method consists in fitting simultaneously the $E_{\mathrm{T}}^{\mathrm{miss}}$ spectrum in the signal and in a control region. As one can see on Figure 5.4 (a) the QCD contamination in the $E_{\mathrm{T}}^{\mathrm{miss}}$ spectrum is enhanced below 25 GeV. For this reason in this study, the missing energy cut is reduced to $E_{\mathrm{T}}^{\mathrm{miss}} > 10$ GeV.

The control region is defined as the regular event selection, except for the $E_{\mathrm{T}}^{\mathrm{miss}} > 10$ GeV cut, and the electrons are required to pass the Medium selection criteria and fail the Tight selection criteria.

The template fit approach assumes that the $E_{\mathrm{T}}^{\mathrm{miss}}$ distribution for the QCD sample does not depend on the identification of the electrons, and that the Monte Carlo used for the other background are properly describing the distribution shapes.

In order to simplify the notation, the Monte Carlo events are classified in two datasets.

- One containing "*real*" missing energy, is called "*W+X*". This MC-set is made with the following MC samples: $t\bar{t}$, single top, τ, W.
- One containing "*no real*" missing energy and called "*Z+X*". This MC-set is made of the remaining Monte Carlo samples.

One need to find an appropriate Probability Density Function (*pdf*) for the samples *W+X*, *Z+X*. Each of this distribution is fitted using a Novosibirsk function, define in Appendix B.3.

Figures 5.5 shows the template distributions and fits for the *W+X* sample Tight (a), for the *W+X* sample anti-Tight (b) for the *Z+X* sample Tight (c) and for the *Z+X* sample anti-Tight (d). The fit function model properly the distributions.

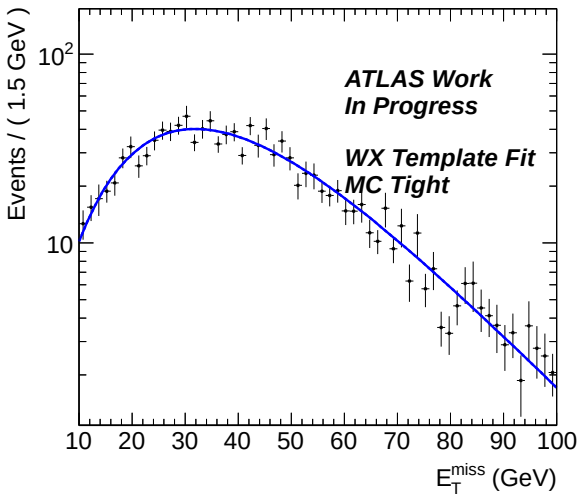

(a) *W+X* template.

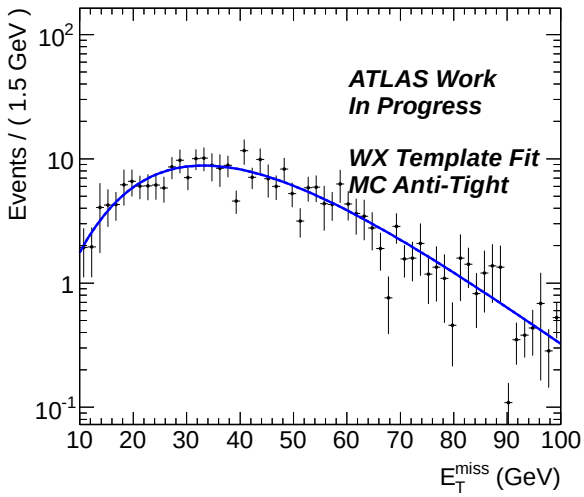

(b) *W+X* template Anti-Tight.

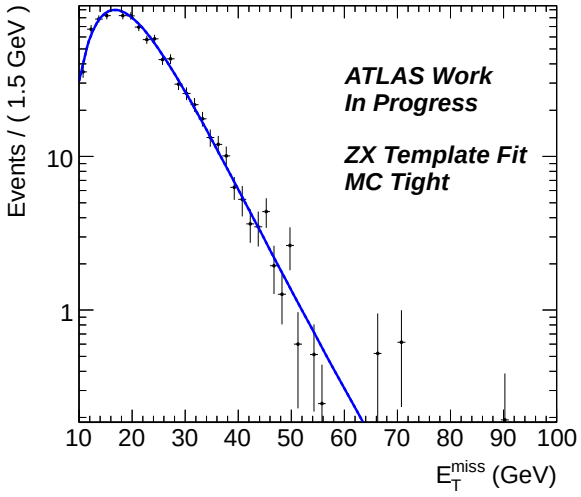

(c) *Z+X* template.

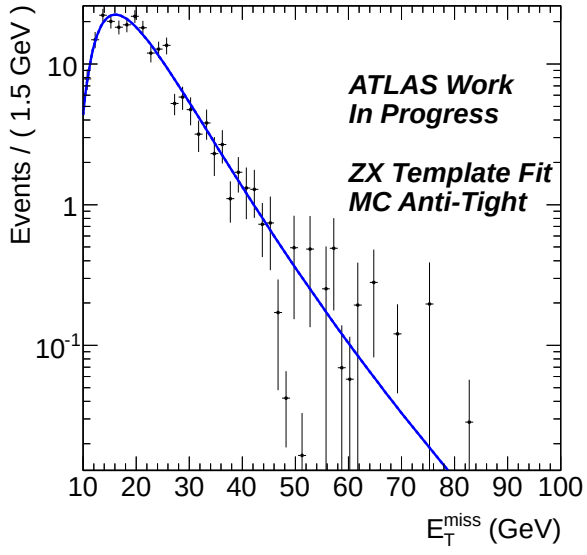

(d) *Z+X* template Anti-Tight.

Figure 5.5: Template fit distributions of $E_{\mathrm{T}}^{\mathrm{miss}}$ for Monte Carlo in the Tight and anti-Tight samples.

In order to determine an appropriate fit function for the QCD multi-jet background, the Monte Carlo samples are subtracted to the data in the Tight and anti-Tight. This is shown on Figure5.6 (a)

for the Tight sample and (b) for the anti-Tight sample. These functions are also fitted using a Novosibirsk function.

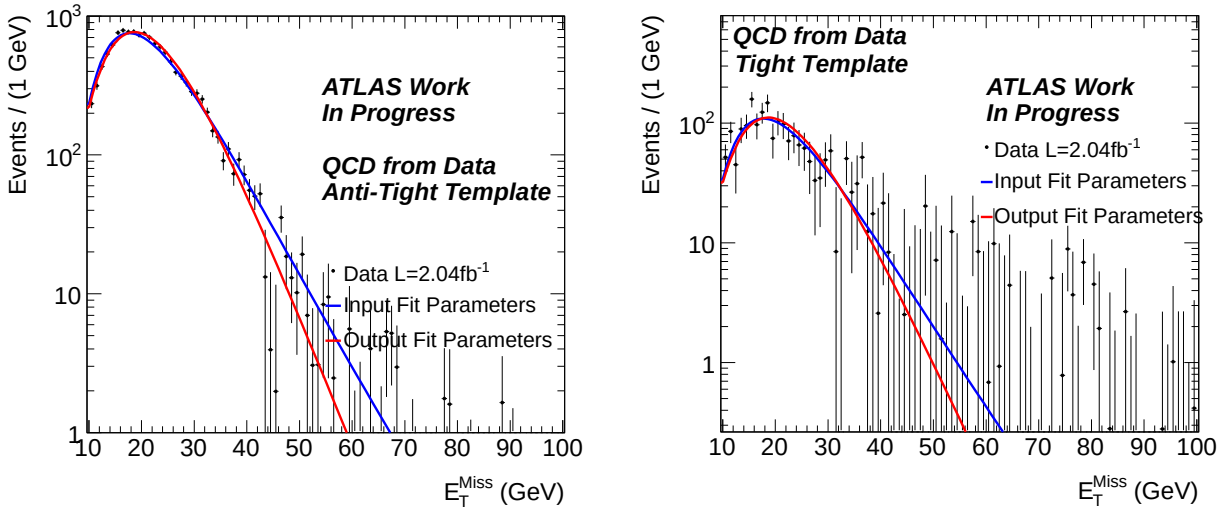

(a) Anti-Tight template.

(b) Tight template.

Figure 5.6: $E_{\mathrm{T}}^{\mathrm{miss}}$ distributions of data Monte Carlo subtracted in the tight and anti-tight samples. The blue line corresponds to the fit of the Novosibirsk function performed on this distribution. The red line corresponds to the output of the total simultaneous fit.

One creates a total *pdf* which is the sum of the three Novosibirsk functions. The total *pdf* is fitted simultaneously to the data in the Tight and anti-Tight samples. The fit is an un-binned maximum log likelihood fit, where 5 parameters are free: The three parameters of the QCD Novosibirsk function, the normalization of the QCD background and the normalization of the W+X sample. The normalization of the Z+X samples is fixed since its template shape is very close to that of the QCD component. The input parameters of the fit for the QCD background are the one found after the fit performed on Figure 5.6 (a) and (b) in blue. But once again these fit parameters are free to vary during the simultaneous fit. The output of the simultaneous fit are also shown on Figure 5.6 (a) and (b) in red.

The results of the total *pdf* fit on $E_{\mathrm{T}}^{\mathrm{miss}}$ distributions is shown on Figure 5.7 (a) for the anti-Tight sample, and on Figure 5.7 (b) for the Tight sample. One can see that the total *pdf* models correctly the data in both cases, with a χ^2/NDF close to unity. Table 5.4 recapitulates the parameters found after the fit.

Fit Parameter	Value
μ_{W+X}	0.86 ± 0.02
N QCD Anti Tight sample	5711 ± 82
N QCD Tight sample	790 ± 71
λ_{QCD}	0.36 ± 0.02
μ_{QCD} (MeV)	17679 ± 176
σ_{QCD} (MeV)	6744 ± 153

Table 5.4: Fit parameters obtained after the template fit.

This fit procedure allows to get the number of QCD background events in the signal[4] region, which is evaluated to $N_{\mathrm{QCD}}^{\mathrm{sig}} = 230 \pm 25^{\mathrm{stat}}$. The scale factor of the W+X sample, is found to

[4]Tight electron and $E_{\mathrm{T}}^{\mathrm{miss}} > 25$ GeV.

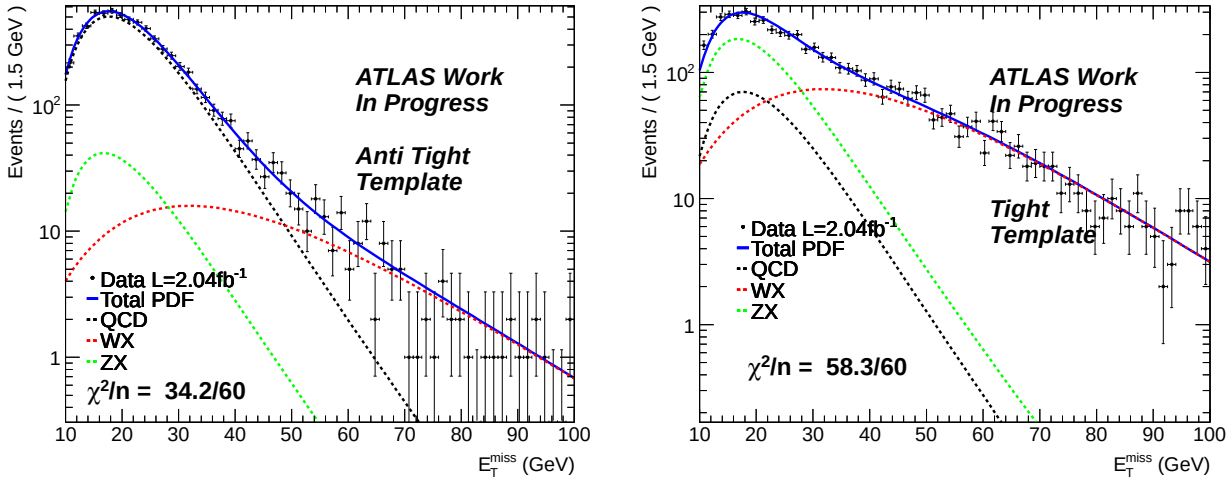

(a) Anti-Tight sample

(b) Tight sample.

Figure 5.7: Results of the simultaneous fit conducted on the $E_{\mathrm{T}}^{\mathrm{miss}}$ distributions on Data. The blue plain line is the total *pdf*, the black dashed line the QCD *pdf*, the red dashed line the *W+X pdf* and the green line is the *Z+X pdf*.

be $\mu_{W+X} = 0.86 \pm 0.03$. The Monte Carlo expectation for the contribution of this background is therefore probably too high. These two numbers are correlated with a factor of 0.48.

Systematic uncertainties

Four different sources of systematic errors were investigated. The fit procedure is re-conducted using different cuts. The systematic uncertainties and their impact are listed below:

- The identification criteria of the anti Tight sample was varied. The electrons are asked to pass the Medium selection and fail a modified Tight selection where the cut on the $\frac{E}{p}$ variable[e] is removed. This uncertainty is evaluated around 1%.
- The cut on the $E_{\mathrm{T}}^{\mathrm{miss}}$, was varied to 15 GeV, leading to an uncertainty of 11%.
- The normalization of the *W+X* sample is fixed and not floated in the fit. This leads to an uncertainty of about 24%.
- A bias on the total *pdf* function was investigated, by re conducting the fit on 1000 pseudo-experiments. The number of QCD events obtained at the end of this procedure is distributed according to a Gaussian with a width of 22 events. This number is taken as a systematic on the fit function and leads to an uncertainty about 10%.

All the systematic uncertainties are added in quadrature, giving a correction of total systematic uncertainty of 61 events, or 28%. The QCD background contamination in the signal region is evaluated with the template fit method to:

$N_{\mathrm{QCD}}^{\mathrm{sig}} = 230 \pm (25)^{\mathrm{stat}} \pm (65)^{\mathrm{sys}}$

Table 5.5 summarizes the number of QCD events found investigating each systematic uncertainty and the relative disagreement.

[e]This variable discriminates electrons from hadrons. For an electron this quantity should be close to 1 while it goes to high values for jets.

cut varied	Number of QCD events measured	relative difference
Identification	232 ± 25	0.9%
Fix the normalization of W+X	176 ± 20	23.5%
variation of the $E_{\mathrm{T}}^{\mathrm{miss}}$ cut to 15 GeV	204 ± 25	11.3%
Systematic on the fit	230	9.56%

Table 5.5: Number of QCD events measured and relative disagreement by varying some of the template fit cuts.

2D sideband method

The second method used to evaluate the QCD yield is a 2D sideband method. The main idea of this method is to measure the number of events containing real electrons, and deduce from that the number of QCD events contaminating the selection. Figure 5.8 shows a sketch of the principle of this method. The data are separated in four regions depending on the isolation and "Tightness" of the electron. One region is enhanced in events containing electrons, the other control regions contains mostly QCD events.

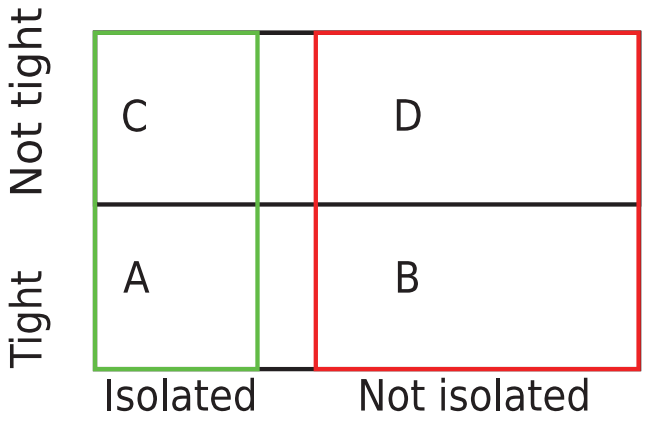

Figure 5.8: Sketch of the 2D sideband method principle.

In order to simplify the notation, the Monte Carlo events are classified in two different datasets, that are different from the one used in the template fit approach:

- The W+jets and W+γ one, called *W*.
- All the other remaining backgrounds are classified together, and are called *SMEW*.

The regions are divided as:

- Region A (Enhanced signal region): Tight and Isolated electron, the candidates pass the Tight selection criteria and are isolated: $E_T^{\mathrm{cone(30)}}(e) < 5$ GeV.
- Region B (Control region): Tight and non Isolated electron, the candidates pass the Tight selection, and are not isolated: $E_T^{\mathrm{cone(30)}}(e) < 7$ GeV.
- Region C (Control region): Anti-Tight and Isolated electron, the candidates fail the Tight selection criteria and are isolated: $E_T^{\mathrm{cone(30)}}(e) < 5$ GeV.
- Region D (Control region): Anti-Tight and non Isolated electron, the candidates fail the Tight selection, and are not isolated: $E_T^{\mathrm{cone(30)}}(e) > 7$ GeV.

The Anti-Tight electron samples are obtained as in the template fit method, by requiring that the selected electrons pass the Medium selection criteria and fail the Tight selection criteria.

The 2D sideband method is based the following assumptions:

- The presence of W events in the three control region (B, C and D) is small, and can be obtained from MC. One consider that all the reconstructed electrons falling in these regions are coming from backgrounds. The part of them coming from *SMEW* backgrounds is assumed to be known (*cf* Table 5.6) from Monte Carlo and subtracted:

$$N_B = N_B^{QCD} + N_B^{SMEW} + N_B^W \tag{5.2}$$
$$N_C = N_C^{QCD} + N_C^{SMEW} + N_C^W \tag{5.3}$$
$$N_D = N_D^{QCD} + N_D^{SMEW} + N_D^W \tag{5.4}$$
$$\tag{5.5}$$

- The ratio of isolated to not-isolated background candidates from jet fake in the anti-Tight bin ($\frac{N_D^{QCD}}{N_C^{QCD}}$) is equal to the same ratio in the Tight bin ($\frac{N_B^{QCD}}{N_A^{QCD}}$). This means that the shape of the isolation distribution is expected to be independent of the electron identification criteria.

- $R^{QCD} = \frac{N_B^{QCD} N_C^{QCD}}{N_A^{QCD} N_D^{QCD}}$, is defined to account for the bias on the isolation due to reverse-cuts procedure. This factor characterizes differences in the shape of the QCD background depending on the isolation of the electron. As no Monte Carlo sample describing the QCD samples are available, it is fixed at one. It will however be varied to evaluate a systematic uncertainty.

- $C_X = \frac{N_X^W}{N_A^W}$, X=(B,C,D) are defined to account for W leakage into control regions B, C, D. These factor C_X are estimated using the Monte Carlo.

The yield of W events in region A can be calculated as following:

$$N_A^{corr} = (N_A - N_A^{SMEW}) - \frac{1}{R^{QCD}} \frac{(N_B - N_B^{SMEW} - c_B N_A^W)(N_C - N_C^{SMEW} - c_C N_A^W)}{N_D - N_D^{SMEW} - c_D N_A^W} \tag{5.6}$$

The number of QCD events in region A is obtained by subtracting from the data the number of *SMEW* events in region A to the number found using Equation (5.6).

$$N_A^{QCD} = (N_A - N_A^{SMEW} - N_A^{corr}) \tag{5.7}$$

In the final event selection, no cut is applied on the isolation of the electron variable: $E_T^{\text{cone}(30)}(e)$. The shape of this background is obtained by taking the Anti-Tight shape. This is described in Section 5.4.1. The total number of QCD events is retrieved by normalizing this shape to the number of QCD events found in region A.

Table 5.6 summarizes the different parameter found using the 2D sideband method.

region	Number of Data event	N *SMEW*	C_X
A	2355	473.4 ± 15.0	1.
B	128	17.4 ± 2.9	0.01 ± 0.003
C	1383	95.3 ± 6.4	0.20 ± 0.01
D	509	6.1 ± 1.7	0.01 ± 0.002

Table 5.6: Parameters obtained with the 2D sideband method.

- The number of W events in region A is measured to be $N_A^{corr} = 1719 \pm 66^{\text{stat}}$, the expected number W events in region A based on Monte Carlo was $N_A^{MC} = 1772 \pm 43^{\text{stat}}$.
- The number of QCD events in region A is measured to be $N_{\text{QCD}}^{\text{A}} = 163 \pm 17^{\text{stat}}$.
- The total number of QCD events in the final selection is measured to be $N_{\text{QCD}}^{\text{sig}} = 247 \pm 15^{\text{stat}}$.

Systematic uncertainties

Four sources of systematic errors were studied for the 2D sideband method:

- R^{QCD} is unknown since no Monte Carlo is available to study its impact. However the shape of the isolation is expected to be largely independent of the identification cuts. This parameter was varied from 0.8 to 1.2 to check its impact. This leads to a mean uncertainty of about 30%.
- The cut applied on the isolation of the electron is varied from 7 GeV to 5 GeV. The median deviation was observed to be about 5%.
- The identification of the Anti-Tight background is changed to Medium-not-Tight removing the $\frac{E}{p}$ cut, this leads to an uncertainty of about 2%.
- Finally in top of the nominal selection, the $E_{\text{T}}^{\text{miss}}$ cut was inverted to obtain a sample even more contaminated in QCD events, leading to an uncertainty of 13%.

All the systematic uncertainties are added in quadrature, giving a correction of total systematic uncertainty of 81 events, or 32.9%. The QCD background is evaluated with the template fit method to:

$N_{\text{QCD}}^{\text{sig}} = 247 \pm 15^{\text{stat}} \pm 81^{\text{stat}}$

Table 5.7 summarizes the number of event found investigating on each systematic, and the relative disagreement found.

cut varied	Number of QCD events measured	relative difference
$R^{QCD} = 0.8$	309 ± 18	25%
$R^{QCD} = 1.2$	206 ± 15	16%
Identification	250 ± 15	1.2%
Identification isol<6 GeV	255 ± 16	3.2%
isol<6 GeV	252 ± 15	2.%
isol<7 GeV	258 ± 16	4.4%
$E_{\text{T}}^{\text{miss}} < 25$ GeV	279 ± 16	13%

Table 5.7: Number of QCD events measured and relative disagreement by varying some of the template fit cuts.

Extraction of the QCD shape

Now that the number of QCD events have been determined, one needs to find a way to estimate the shape of this background.

Figures 5.9 (a) and (b) show the isolation distribution shape for the electron, for the Anti-Tight selection, for the modified ID Anti-Tight selection, and in two control regions. The first control region is defined to be $E_{\text{T}}^{\text{miss}} < 25$ GeV region which is enriched in QCD background. The second control zone is obtained by reverting the photon p_{T} cut $p_{\text{T}}(\gamma) < 25$ GeV, which leads to an increase in W+jet background. The four curves are normalized to their integral. A χ^2 test was performed between the histograms and the distributions are found to be in good agreement, generally within errors: The

χ^2/NDF is 1.3 for the case where the $E_{\mathrm{T}}^{\mathrm{miss}} < 25$ GeV, 0.2 for the case where the electron ID is modified, and 1.5 for the case where the photon p_{T} cut is inverted. The isolation QCD background shape therefore seems to be largely independent on the selection.

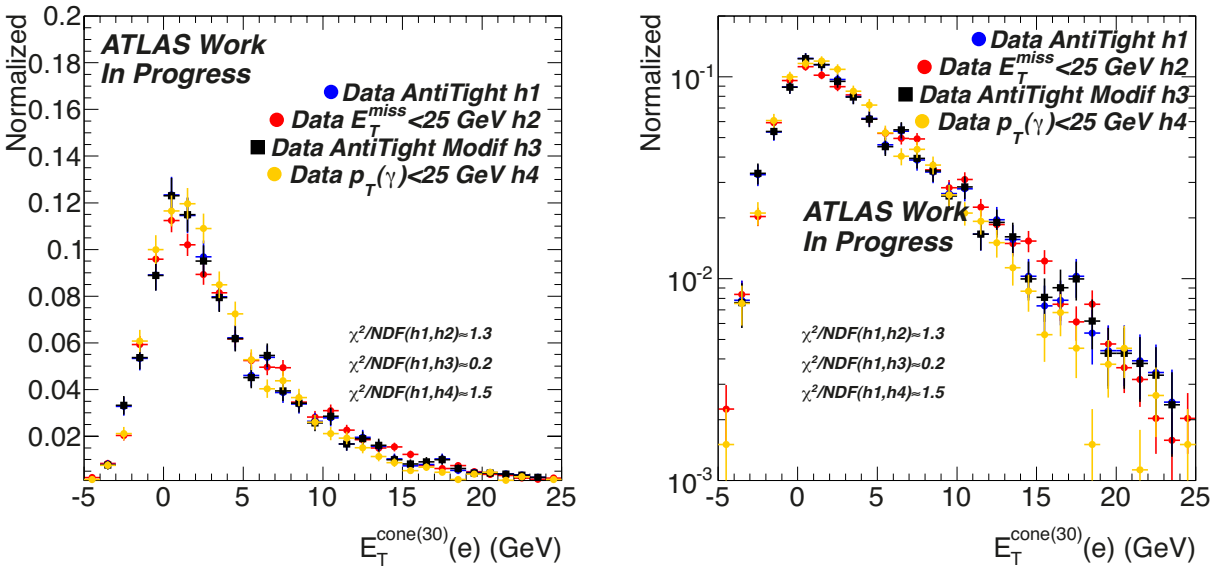

(a) linear (b) log scale

Figure 5.9: Template isolation shape for the electron.

The template selection of this background must reproduce the QCD in the signal region, for this reason its selection must be done as close as possible to the final selection. The QCD template is determined using electrons from a sample where the Tight electron selection has been inverted. However, based on Monte Carlo, about 25% of the total number of events in the Anti-Tight selection are coming from W and $SMEW$ events. This number is probably over estimated, as shown by the isolation distribution in the Anti-Tight sample, and in the Anti-Tight-$E_{\mathrm{T}}^{\mathrm{miss}}$ reverted sample, but it is decided to select the QCD template in the non isolated region $E_T^{\mathrm{cone}(30)}(e) > 5$ GeV. Applying this cut drops the number of electroweak events to about 5% in the Monte Carlo. Some template control distributions are given in Appendix B.4, to check the impact of the electroweak pollution in the QCD sample.

The QCD template is then normalized to the number of QCD event found in the signal region.

Conclusion on the QCD background

The results found using the two data driven techniques are in good agreement with each other. They are:

- For the template fit: $N_{\mathrm{QCD}}^{\mathrm{sig}} = 230 \pm (25)^{\mathrm{stat}} \pm (65)^{\mathrm{sys}}$.
- For the 2D side band method: $N_{\mathrm{QCD}}^{\mathrm{sig}} = 247 \pm (15)^{\mathrm{stat}} \pm (81)^{\mathrm{sys}}$.

Figure 5.10 (a), shows the $E_{\mathrm{T}}^{\mathrm{miss}}$ distribution for the electroweak backgrounds and the QCD background. Compared to Figure 5.4 (a), the data is now in good agreement with the Monte Carlo, even at the low edge of the distribution. A χ^2 test between the histograms of data and that of the Monte Carlo is performed, its results is now close to unity.

It is also interesting to check other distributions such as p_{T}(e) as shown on Figure 5.11 (a), p_{T}(w) on Figure 5.11 (b), or $M_T(W)$ on Figure 5.12 (a). All these distributions show a good agreement between data and Monte Carlo, as shown by the χ^2 values close to unity.

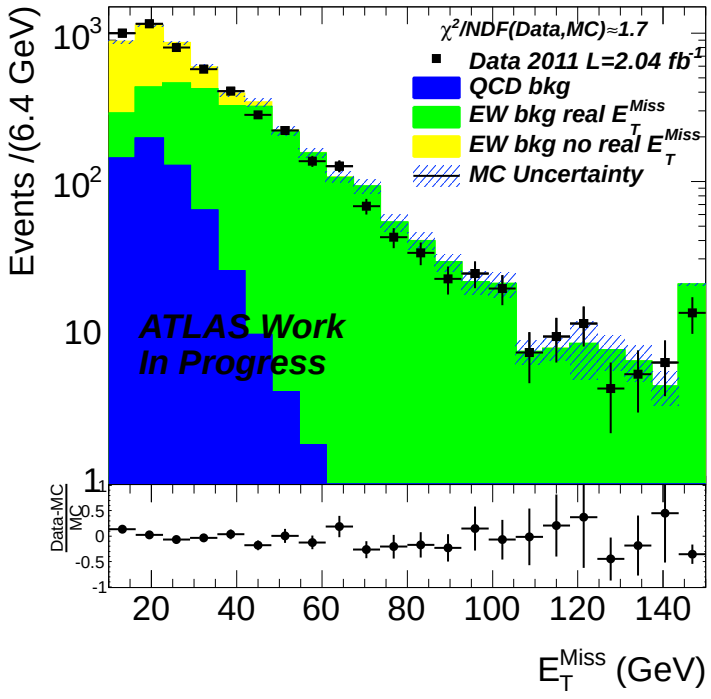

Figure 5.10: $E_{\mathrm{T}}^{\mathrm{miss}}$ distribution obtained adding the QCD background template.

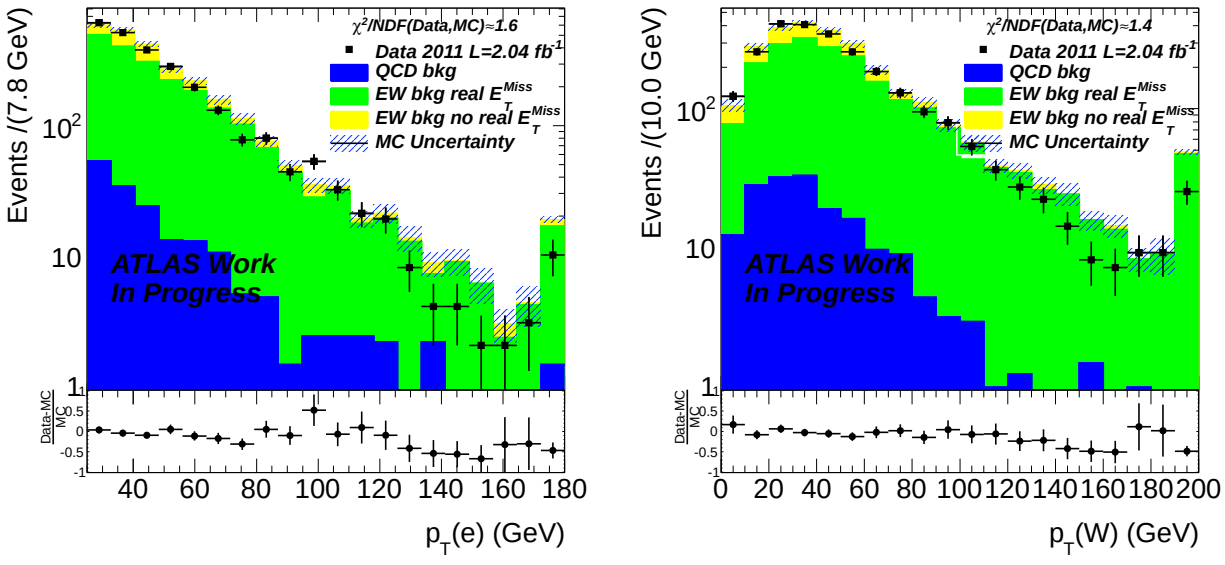

(a) $p_{\mathrm{T}}(e)$ (b) $p_{\mathrm{T}}(W)$

Figure 5.11: Control distributions obtained adding the QCD background template, for p_{T}(e) (left) and p_{T}(W) (right).

Figure 5.12 (b) shows the distribution of the photon isolation. This distribution shows the poorer agreement between data and MC, as attested by the χ^2 test value. The photon isolation distribution should be peaked around zero for isolated photon, whereas it should goes to higher values for jets faking photon background. As this distribution is in relatively bad agreement between data and Monte Carlo, this means that the jet faking photon background is not fully understood at this point.

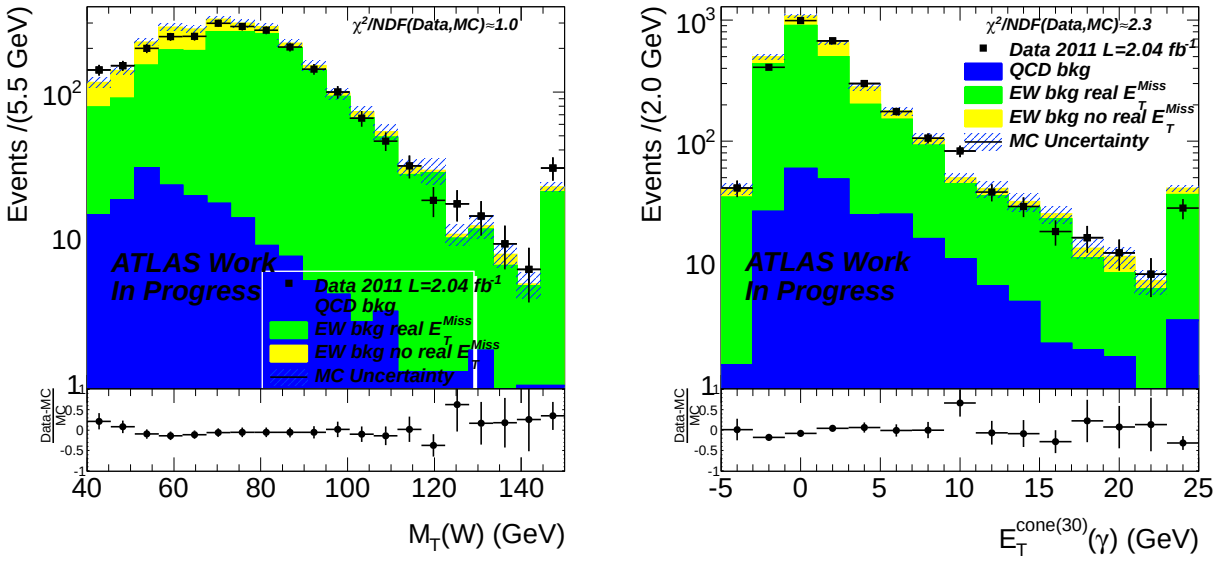

(a) $M_T(W)$

(b) Isolation of the photons.

Figure 5.12: Control distributions obtained adding the QCD background template, for $M_T(W)$ (left) and $E_T^{\text{cone}(30)}(\gamma)$ (right).

This leads us to the second background that needs to be evaluated from data driven techniques: W+jets.

5.4.2 W+jets

For this study, the Standard Model backgrounds are split in four components: the SM $W\gamma$, the W+jets, the QCD background, and all the others[6] that are collectively called *SMEW*. In this section, the determination of the W+jet background using the same two data driven techniques is developed. This time one is interested by the normalization of the SM $W\gamma$ and that of the W+jets.

Template fit

The template fit approach was already explained for the QCD background yeld estimation. It is now used to evaluate the number of $W + \gamma$ and W+jets events that pass the selection.

The template fit is conducted in the photon isolation energy distribution. The signal region, also referred to as Tight sample in the following, is obtained by applying all the selection cuts except the $E_T^{\text{cone}(30)}(\gamma)$ which is relaxed.

The Anti-Tight sample is defined by removing four photon identification cuts based on the first LAr calorimeter layer introduced in Section 5.2.2: w_{s3}, F_{side}, ΔE and E_{Ratio}. These variables were found to be uncorrelated with isolation [24, 117].

The $W + \gamma$ sample, as well as the QCD background obtained in the previous section and the *SMEW* backgrounds, are fitted using a crystal ball function, which is defined in Appendix B.2.

The selection for these 3 backgrounds as well as the fits performed in the Tight and anti-Tight samples are shown in Figures 5.13.

[6] $Z \to ee$,$t\bar{t}$, single top, di-bosons, $Z \to \tau\tau$ and $W \to \tau\nu$.

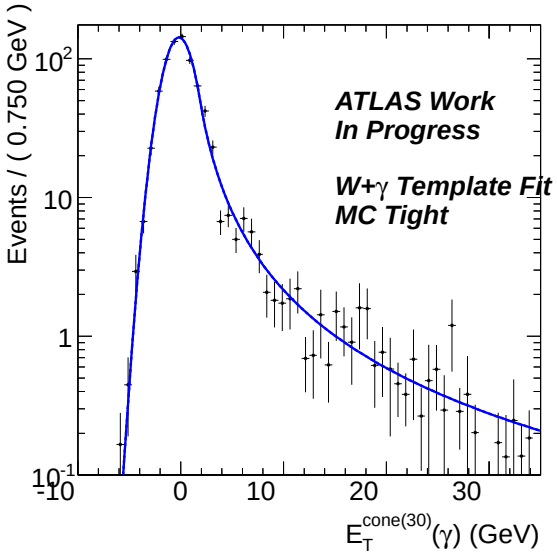

(a) $W\gamma$ Tight template.

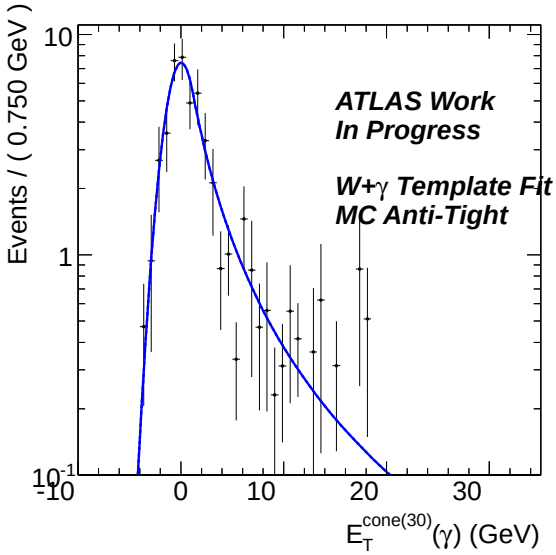

(b) $W\gamma$ anti-Tight template.

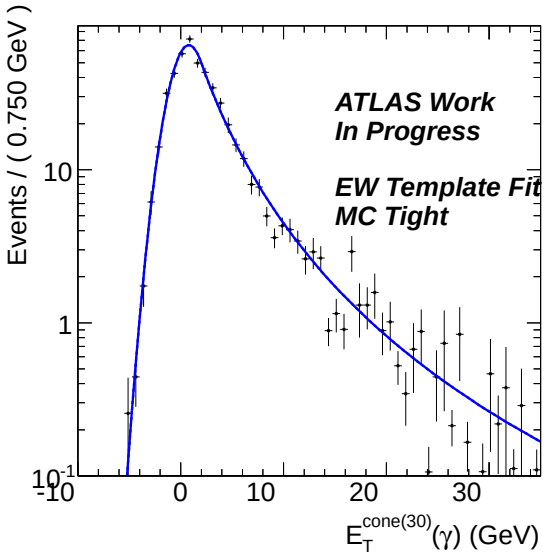

(c) EW Tight template

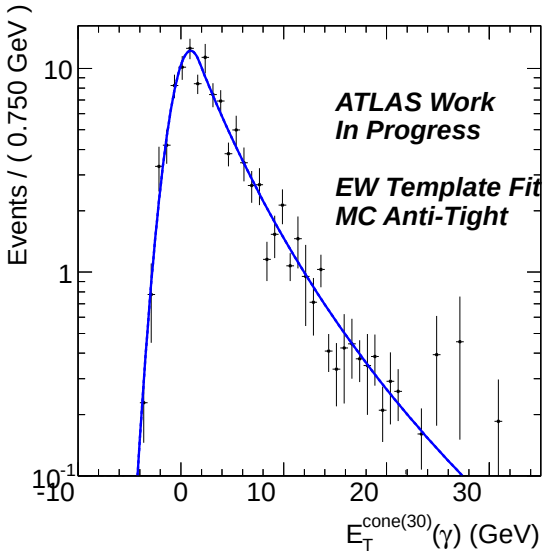

(d) EW anti-Tight template

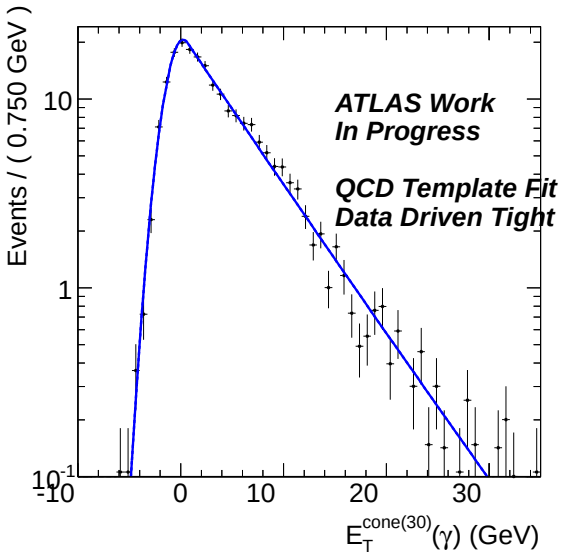

(e) QCD template

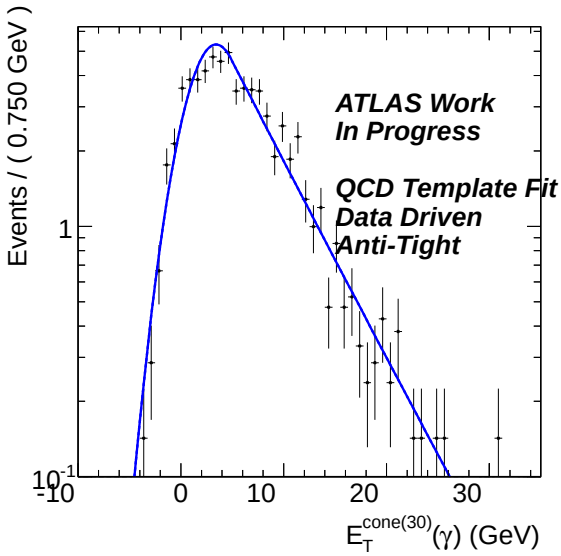

(f) QCD anti-Tight template

Figure 5.13: Photon isolation template fit distributions for the $W + \gamma$, QCD background and the *SMEW* backgrounds.

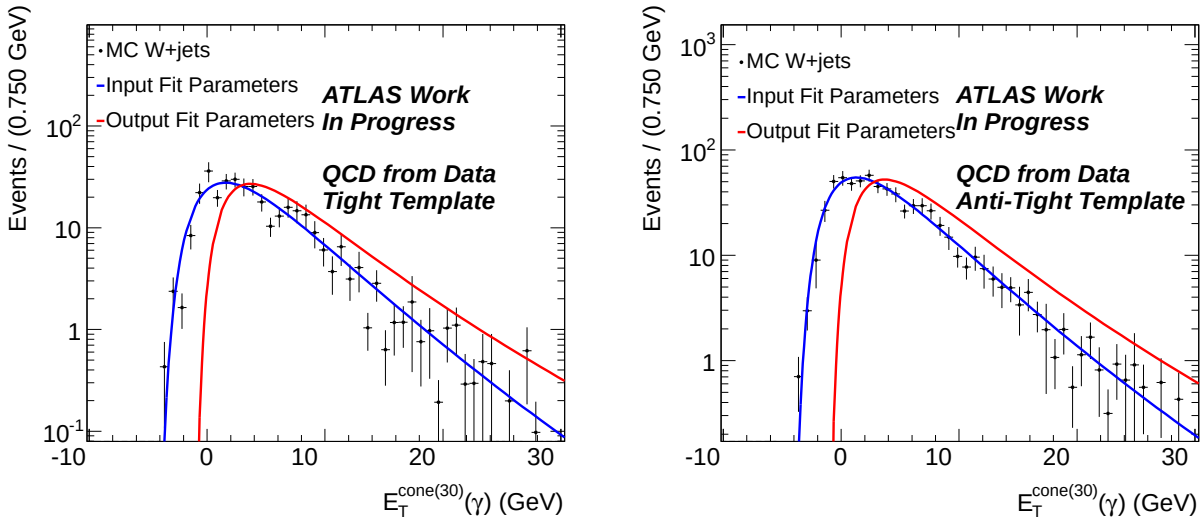

(a) W+jets from MC Tight

(b) W+jets from MC anti-Tight

Figure 5.14: Photon isolation template fit distributions for the W+jets background. The shape of this background is taken from Monte Carlo. The distribution are fitted using a Novosibirsk function. The results of the fit performed on Monte Carlo is shown in blue, it serves as the input parameters of the global fit performed later on, but with all these parameters free to vary. The results of the global fit performed on data are also shown in red.

The W+jets shape is investigated in the Monte Carlo, as shown on Figure 5.14. The photon isolation distribution is fitted using a Novosibirsk function, the fit performed on Monte Carlo is shown in blue in these distributions. The function fitted after the simultaneous fit on data on the Tight and anti-Tight sample is shown in red. A discrepancy between data and Monte Carlo is observed.

The total *pdf* is the sum of the 3 Crystal-Ball and the Novosibirsk functions. An un-binned maximum log-likelihood fit is performed on the Tight and anti-Tight sample simultaneously. The fit is performed with all the normalization and *pdf* parameters coming from the QCD and EW background fixed. The normalization of the $W + \gamma$ template is free, as well as all the parameters of the W+jets background. The input parameters for the fit are the ones determined on MC. The QCD normalization was retrieved using the 2D side band method, for the Tight and anti-Tight samples with $E_T^{\text{cone}(30)}(\gamma)$ relaxed. These parameters are given in Appendix B.4.

Figures 5.15 (a) shows the fits result for the anti-Tight selection and for the Tight selection in Figure 5.15 (b). The *pdf* describes correctly both distribution as shown by the χ^2 close to unity.

Fit Parameter	Value
$\mu_{W\gamma}$	1.04 ± 0.03
$\mu_{W+\text{jets A-T}}$	1.19 ± 0.05
$\mu_{W+\text{jets T}}$	0.58 ± 0.06
$\lambda_{W+\text{jets}}$	0.61 ± 0.06
$\mu_{W+\text{jets}}$ (MeV)	3680 ± 254
$\sigma_{W+\text{jets}}$ (MeV)	3359 ± 253

Table 5.8: Fit parameter obtained after the template fit.

Table 5.8 summarizes the fit parameters found. The fit leads to:

- $N_{W\gamma}^{\text{sig}} = 1432 \pm (38)^{\text{stat}}$

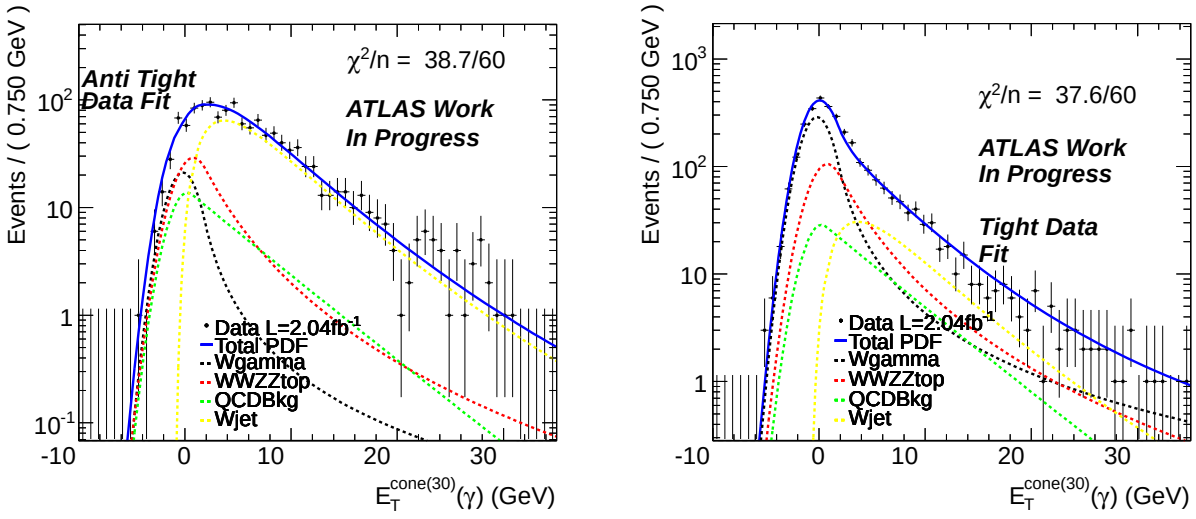

(a) Anti Tight selection

(b) Tight selection.

Figure 5.15: Results of the simultaneous fit on the Tight and anti Tight sample, for the W+jets background. The blue line is the total *pdf*, the black line the $W\gamma$ *pdf*, the red line the EW *pdf*, the green line the QCD background *pdf* and the yellow line the W+jets *pdf*.

- $N^{\text{sig}}_{W+jet} = 292 \pm (22)^{\text{stat}}$

Evaluation of the systematic uncertainties

Three different sources of systematic errors were investigated. They are listed below:

- The identification of the anti Tight sample, was varied by reverting some cuts in the selection. One uses 2 sample where 5[g] and 3[h] identification cuts were inverted. This uncertainty is evaluated to be 3.6% for the number of W+jets events and 5.8% for the number of $W + \gamma$ events.
- The mean of the $W + \gamma$ distribution is let free in the fit, to evaluate a systematic shift of this distribution. The fit finds a shift of the mean value of $\Delta\text{Mean}(W\gamma) = 227 \pm 95$ MeV. Allowing this parameter to float in the fit leads to a 10% change in the number of W+jets events and 5% for the number of $W + \gamma$.
- A bias on the total *pdf* function was investigated, by re conducting the fit on 1000 pseudo-experiments. The number of W+jets and $W\gamma$ events obtained at the end of this procedure are distributed according to Gaussians with a width of respectively 22 and 48 events. This number are taken as a systematic on the fit function and leads to an uncertainty about 8% for the number of W+jets and 3% on the number of $W\gamma$ events.

All the systematic uncertainties are added in quadrature, giving a correction of total systematic uncertainty of 39 events for the W+jets background or 13.3%. The W+γ systematic uncertainty is evaluated to 119 events or 8.3%. The W+jets background is evaluated with the template fit method to:

- $N^{\text{sig}}_{W\gamma} = 1432 \pm (38)^{\text{stat}} \pm (119)^{\text{sys}}$
- $N^{\text{sig}}_{W+jets} = 292 \pm (22)^{\text{stat}} \pm (39)^{\text{sys}}$

Table 5.9 summarizes the number of events found investigating on each systematic, and the relative disagreement.

[g] All Tight cuts except for those on w_{s3}, F_{side}, ΔE, w_{stot} and E_{Ratio}.
[h] All Tight cuts except for those on w_{s3}, F_{side}, ΔE.

cut varied	W+jets	rel. diff. W+jets	W+γ	rel. diff. W+γ
Identification 5 cuts	295 ± 22	1.%	1499 ± 39	4.7%
Identification 3 cuts	302 ± 25	3.4%	1385 ± 38	3.3%
Mean of Wγ not fixed	262 ± 21	10.3%	1504 ± 40	4.9%
Systematic on the fit	292	7.53%	1432	3.35%

Table 5.9: Number of W+jets and Wγ events measured and relative disagreement by varying some of the template fit cuts.

2D sideband method

The second method used to evaluate the W+jets yield is a 2D sideband method using the isolation and the identification of the photon. As this as been explained in the previous section the data are separated in four regions depending on the isolation and "Tightness" of the photon.

- Region A (Signal region): Tight and Isolated photon, the candidates pass the Tight selection criteria and are isolated: $E_T^{\text{cone30}}(\gamma) < 6$ GeV.
- Region B (Control region): Tight and non Isolated photon, the candidates pass the Tight selection, and are not isolated: $E_T^{\text{cone30}}(\gamma) > 8$ GeV.
- Region C (Control region): Anti-Tight and Isolated photon, the candidates fail the Tight selection criteria and are isolated: $E_T^{\text{cone30}}(\gamma) < 6$ GeV.
- Region D (Control region): Anti-Tight and non Isolated photon, the candidates fail the Tight selection, and are not isolated: $E_T^{\text{cone30}}(\gamma) > 8$ GeV.

The Anti-Tight photon sample is obtained by inverting the same photon identification cuts as in the template fit approach. In order to simplify things, the QCD events are counted with the EW backgrounds.

In this procedure R^{W+jets} is again fixed at one, meaning that the photon isolation is independent on the photon identification, but it is varied to evaluate a systematic effect.

Table 5.10 summarizes the parameters found.

region	Number of Data event	N EW + QCD bkg	C_X
A	2564	913.2 ± 21.6	1
B	326	115.5 ± 6.6	0.04 ± 0.004
C	768	250.8 ± 10.4	0.06 ± 0.006
D	399	84.7 ± 4.6	0.01 ± 0.002

Table 5.10: Parameters obtained with the 2D sideband method.

The numbers of W+jets and W+γ events are measured to be:

- $N_{W\gamma}^{\text{sig}} = 1421 \pm (40)^{\text{stat}}$
- $N_{W+jet}^{\text{sig}} = 231 \pm (46)^{\text{stat}}$

Systematic uncertainties

The systematic errors studied in the 2D sideband method are as follows:

- The identification of the photon is varied as in the template fit approach, by removing 5 and 3 identification cuts of the tight criteria. This leads to an uncertainty about 3.8% for the number of $W\gamma$, and about 24% on the estimation of the number of W+jets events.

- The factor R^{W+jets} was fixed to one, but it can be estimated from the Monte Carlo W+jets sample. This parameter is evaluated for each Anti-Tight selection described above:
  - Inversion of 4 Identification cuts: $R^{W+jets} = 0.8 \pm 0.3$
  - Inversion of 3 Identification cuts: $R^{W+jets} = 0.9 \pm 0.4$
  - Inversion of 5 Identification cuts: $R^{W+jets} = 0.7 \pm 0.3$

  As one can see, the parameter is indeed close to 1 for each set of cuts, and anyway compatible with unity within errors. On the nominal sample, it was moved to 0.8, leading to an uncertainty of 21% for the number of W+jets events, and about 3.5% on the number of $W + \gamma$ events.

- The cut applied on the isolation of the photon is varied from 7 GeV to 5 GeV. Leading to an uncertainty about 0.4% on the number of $W\gamma$ event and about 2.7% for the number of W+jets events.

- The $W\gamma$ isolation distribution seems shifted by a few hundred MeV, with respect to the data. This was confirmed in the template fit approach by letting this parameter free in the fit procedure. The shift was estimated to be about 230 MeV. The Monte Carlo distribution $W\gamma$ is shifted by this value to check the impact. This leads to an uncertainty about 0.5% for the number of $W\gamma$ events, and about 3.5% for the number of W+jets event.

All the systematic uncertainties are added in quadrature, giving a correction of total systematic uncertainty of 74 events for the number of $W\gamma$ events, or 5.2%, and 73 events for the number of W+jets events, or 31%. One finally obtained:

- $N^{\text{sig}}_{W\gamma} = 1421 \pm (42)^{\text{stat}} \pm (74)^{\text{sys}}$
- $N^{\text{sig}}_{W+jets} = 231 \pm (47)^{\text{stat}} \pm (73)^{\text{sys}}$

Table 5.11 summarizes the number of events found investigating on each systematic, and the relative disagreement found.

cut varied	W+jets	rel. diff. W+jets	W+γ	rel. diff. W+γ
Identification 5 cuts	198 ± 46	14.2%	1452 ± 40	2.2%
Identification 3 cuts	273 ± 45	18.4%	1377 ± 39	3.1%
Isolation < 7 GeV	225 ± 45	2.3%	1425 ± 40	0.3%
Isolation < 5 GeV	234 ± 45	1.4%	1416 ± 40	0.3%
R^{W+jets}	279 ± 45	21.1%	1371 ± 40	3.5%
Mean of Wγ shifted	222 ± 45	3.5%	1427 ± 40	0.5%

Table 5.11: Number of W+jets and $W\gamma$ events measured and relative disagreement by varying some of the template fit cuts.

Determination of the W+jets shape

Figures 5.16 (a) and (b) show the isolation distribution shape for the photon, for each Anti-Tight selection, and for the Monte Carlo. All these control regions are enriched in backgrounds, since the identification requires that they pass the Loose selection but fail the Tight one. All curves are normalized to their integrals and a χ^2 test is performed between the histograms. The four distributions coming from data are in good agreement as shown by the different χ^2/NDF test performed and quoted on the figures. The Monte Carlo seems however different and gives the worst χ^2/NDF test results.

The W+jets template background is taken from data in the Anti-Tight selection. In this case the pollution of non W+jets processes is important and estimated around 25%. The EW, QCD and $W+\gamma$

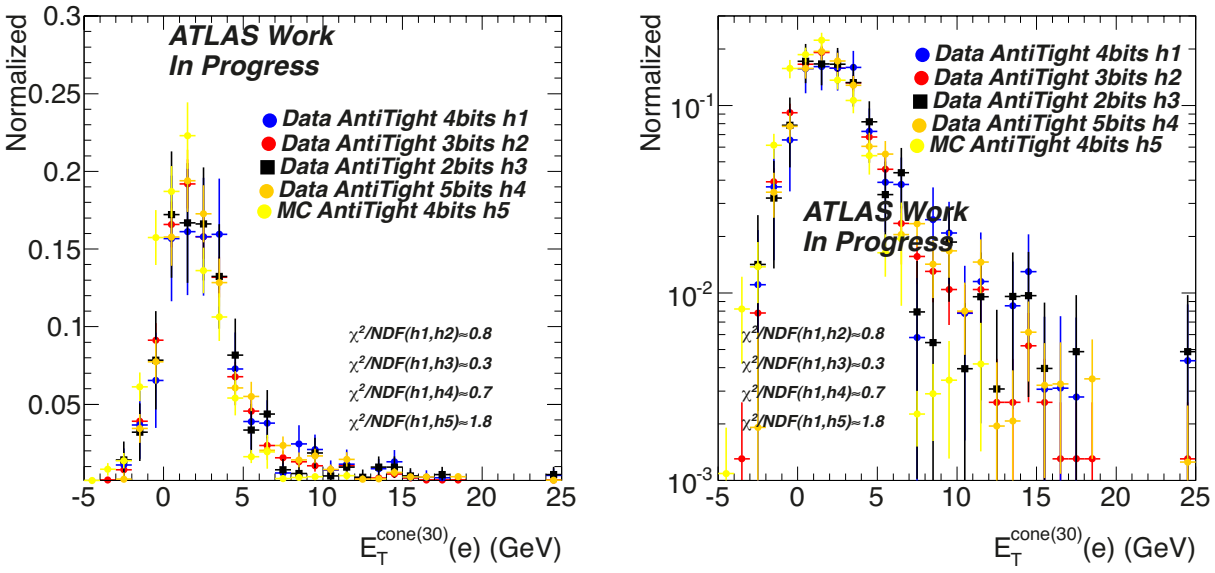

(a) linear (b) log scale

Figure 5.16: Template isolation shape for the photon.

samples are subtracted from the data in this side band to obtain the new shape that is used in the rest of this study. The anti-Tight data set without MC subtraction is also kept to study a systematic effect on the distributions later on. The shape of the data subtracted MC is shown for a few kinematic quantities in Appendix B.5.

5.4.3 Conclusion on the background estimation

In summary for this section, two data driven techniques were used to determine the normalization of the QCD, W+jets and $W\gamma$ backgrounds. The 2D side band method, is the method preferred in most of the cases, the template fit approach is implemented to cross checks the results. A global fit could also have been performed on the photon isolation to retrieve independently the three normalization, but the photon isolation distributions for the QCD and $W\gamma$ shapes are too close to get meaningful results. The shapes of the QCD and W+jets backgrounds are taken from data. The shape of the $W\gamma$ sample is taken from Monte Carlo. The shape and normalization of the electroweak backgrounds are taken from Monte Carlo since good agreement with data is expected.

The number of QCD background events was estimated using these techniques to:

- For the template fit: $N_{\mathrm{QCD}}^{\mathrm{sig}} = 230 \pm (25)^{\mathrm{stat}} \pm (65)^{\mathrm{sys}}$.
- For the 2D side band method: $N_{\mathrm{QCD}}^{\mathrm{sig}} = 247 \pm (15)^{\mathrm{stat}} \pm (81)^{\mathrm{sys}}$.

The number of W+jets events was estimated to:

- For the template fit: $N_{W+jets}^{\mathrm{sig}} = 292 \pm (22)^{\mathrm{stat}} \pm (39)^{\mathrm{sys}}$
- For the 2D side band method: $N_{W+jets}^{\mathrm{sig}} = 231 \pm (47)^{\mathrm{stat}} \pm (73)^{\mathrm{sys}}$

And the number of $W\gamma$ events was estimated to:

- For the template fit: $N_{W\gamma}^{\mathrm{sig}} = 1432 \pm (38)^{\mathrm{stat}} \pm (119)^{\mathrm{sys}}$
- For the 2D side band method: $N_{W\gamma}^{\mathrm{sig}} = 1421 \pm (42)^{\mathrm{stat}} \pm (74)^{\mathrm{sys}}$

All these results are in good agreement, always within statistical error. In what follows, the average of the template fit and the 2D side band methods is used. The highest systematic error is kept, to be conservative.

The electroweak backgrounds contribute $N_{EW}^{\text{sig}} = 683 \pm (17)^{\text{stat}}$ events. Table 5.12 gives the number of observed events, and the expected contribution from each component.

Sample	Number of Events
QCD	$239 \pm (15)^{\text{stat}} \pm (81)^{\text{sys}}$
W+jets	$262 \pm (16)^{\text{stat}} \pm (73)^{\text{sys}}$
$W\gamma$	$1426 \pm (38)^{\text{stat}} \pm (119)^{\text{sys}}$
total Data Driven	$1927 \pm (44)^{\text{stat}} \pm (273)^{\text{sys}}$
WW/WZ/ZZ	$17 \pm (1)^{\text{stat}}$
$t\bar{t}$	$122 \pm (3)^{\text{stat}}$
single top	$20 \pm (2)^{\text{stat}}$
$W \to \tau\nu$	$18 \pm (5)^{\text{stat}}$
$Z \to ee$	$490 \pm (15)^{\text{stat}}$
$Z \to \tau\tau$	$16 \pm (3)^{\text{stat}}$
Total EW	$683 \pm (17)^{\text{stat}}$
Total bkg	$2610 \pm (47)^{\text{stat}}$
Data	2564 ± 51

Table 5.12: Number of events measured and predicted.

All the samples are stacked together and compared to data in Figures 5.17 and 5.18.

Figure 5.17 (a) shows the number of jets in the event, Figure 5.17 (b) the number of reconstructed vertices, Figure 5.17 (c) the transverse momentum of the photon and Figure 5.17 (d) the photon isolation variable $E_T^{\text{cone}(30)}(\gamma)$. All Monte Carlo distributions are in good agreement with the data as shown by the χ^2/NDF close to unity, except the isolation distribution which is in worse agreement and have a $\chi^2/NDF \approx 1.9$. If one shifts the $W + \gamma$ mean by 270 MeV, as found in Section 5.4.2, the difference between the two distributions decreases to $\chi^2/NDF \approx 1.7$.

5.5 $W\gamma$ invariant mass

5.5.1 Reconstruction

The goal of this study is to look at narrow resonances decaying into $W\gamma$. In order to differentiate the Standard Model background from the signal coming from new physics, one needs a discriminating variable. The most intuitive one to use is the invariant mass between the photon and the W. However as one looks at the decay of the W in an electron and a neutrino, reconstructing its four-momentum is difficult since the neutrino is not reconstructed in the detector. One can however assign the $E_{\text{T}}^{\text{miss}}$ to the neutrino transverse momentum. The longitudinal momentum $p_z(\nu)$ of the neutrino can then be obtained by requiring that the invariant mass of the electron and the neutrino match the PDG value of the W mass, $M(W) = 80.403$ GeV [13].

This constraint yields a second-order equation in $p_z(\nu)$, which allows two solutions

$$p_z^{\pm} = \frac{p_z(e)\left[M^2(W) + 2\mathbf{E}_T^{\text{miss}} \cdot \mathbf{p}_T(e)\right] \mp E(e)\sqrt{\left[M^2(W) + 2\mathbf{E}_T^{\text{miss}} \cdot \mathbf{p}_T(e)\right]^2 - p_z^2(e)\left(E_T^{\text{miss}}\right)^2}}{2p_T^2(e)}. \tag{5.8}$$

Various algorithms were tested to select the solution giving the best reconstruction of the W four-momentum: selecting the solution minimizing or maximizing the angle between the electron and the reconstructed neutrino (MinAngle and MaxAngle respectively), and the solution minimizing or

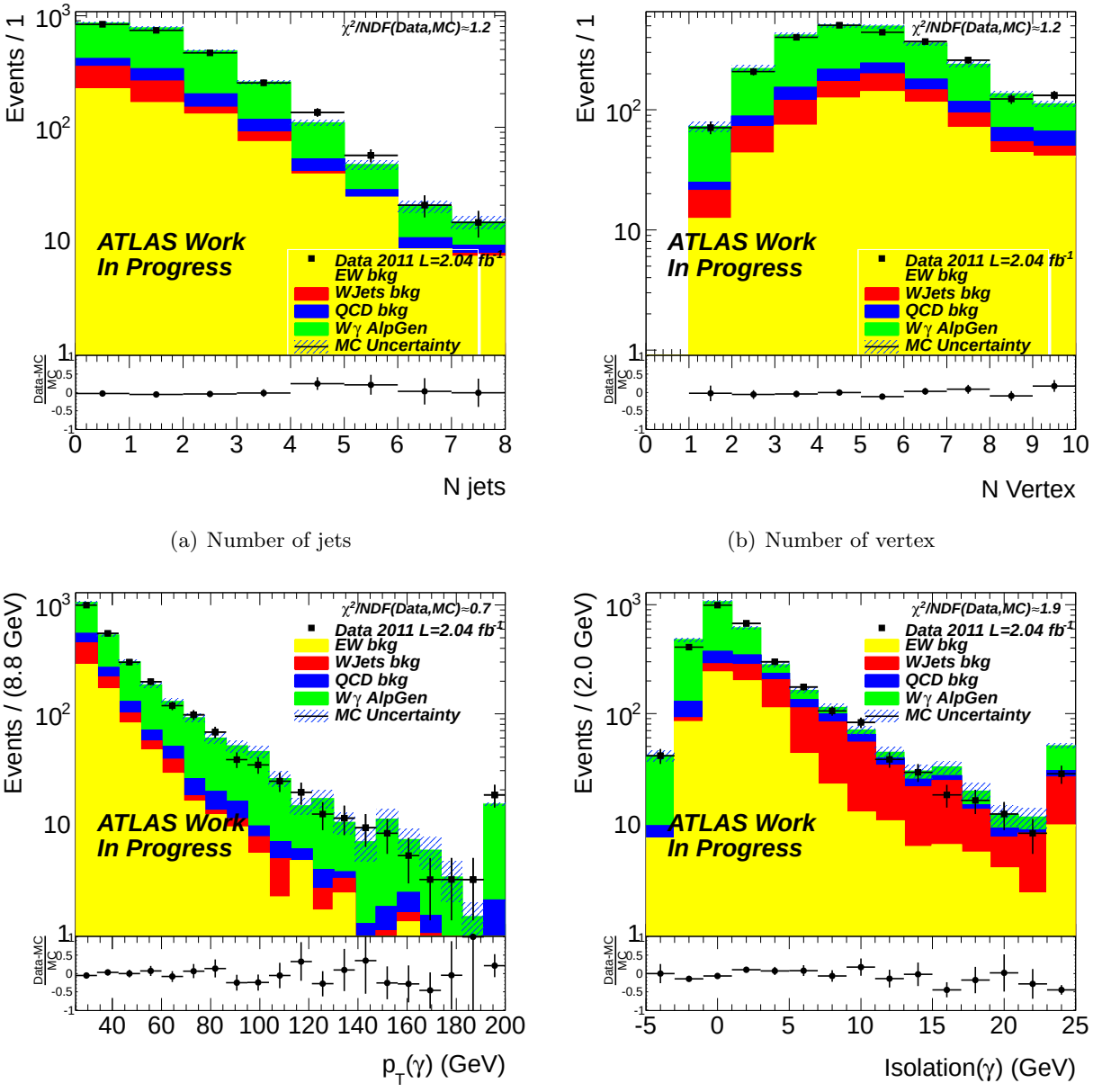

(a) Number of jets

(b) Number of vertex

(c) $p_{\mathrm{T}}(\gamma)$

(d) $E_T^{\mathrm{cone}(30)}(\gamma)$

Figure 5.17: Control distributions after adding all the SM processes.

Figure 5.18 (a) shows the $E_{\mathrm{T}}^{\mathrm{miss}}$ distribution, Figure 5.18 (b) the electron transverse momentum distribution, Figure 5.18 (c) the transverse mass distribution and Figure 5.18 (d) the transverse momentum of the W bosons distribution. Again all the Monte Carlo distributions shows a good agreement with data as proven by the χ^2/NDF close to unity.

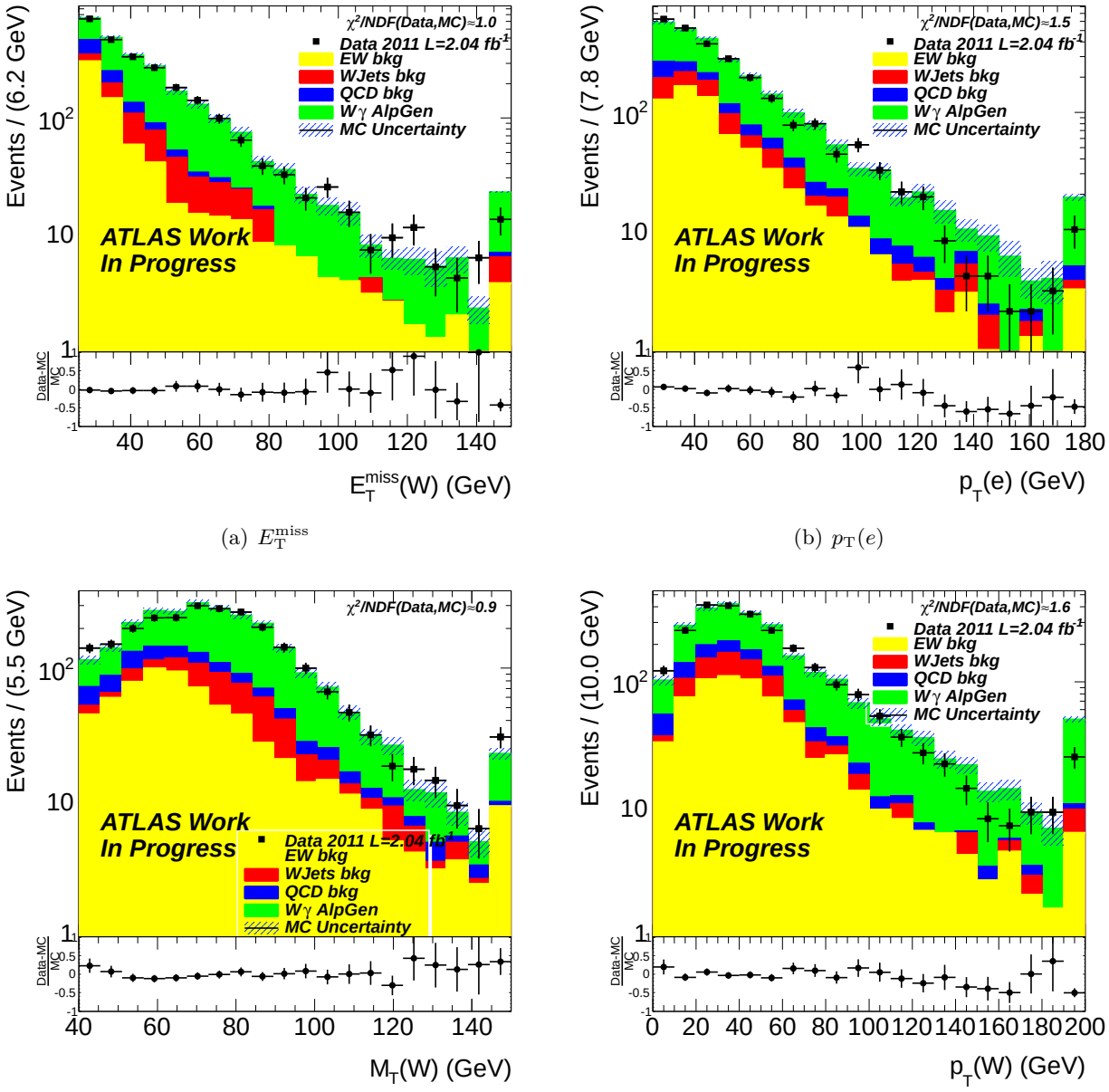

(a) $E_{\mathrm{T}}^{\mathrm{miss}}$ (b) $p_{\mathrm{T}}(e)$

(c) $M_T(W)$ (d) $p_{\mathrm{T}}(W)$

Figure 5.18: Control distributions after adding all the SM processes.

Solution	Efficiency of the selection (%)
p_z^+	50.98
p_z^-	50.02
Min Angle	67.40
Max Angle	32.60
Min p_z	67.42
Max p_z	32.58

Table 5.13: Efficiency of various algorithms to select the neutrino p_z, using MC truth information.

maximizing the longitudinal momentum of the neutrino (MinPz, MaxPz). Figure 5.19 shows the difference between the longitudinal momentum of the reconstructed neutrino and its truth value for various methods.

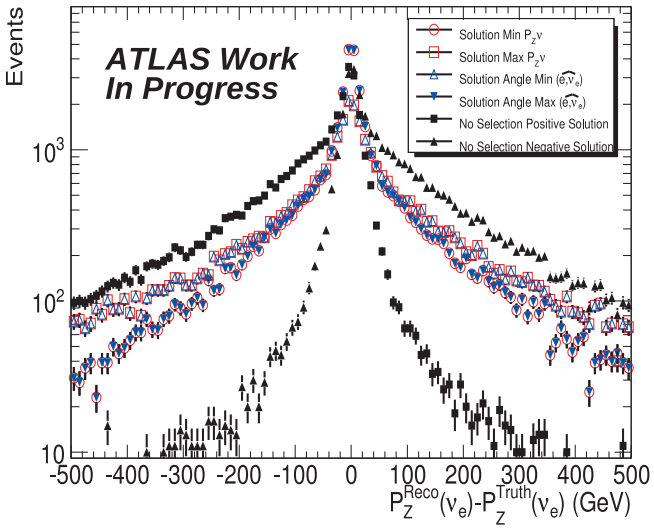

Figure 5.19: Resolution distributions for the reconstruction of the neutrino p_z according to the algorithms presented in the text.

In order to choose the best method, we apply each algorithm in turn on MC truth, using the true neutrino p_{T} and electron four-momentum as inputs to Eq. 5.8. Table 5.13, gives the efficiency for the different algorithms at the MC truth level. The efficiency for each solution of the algorithms is defined by the ratio of events matching the truth solution on the total number of events. The solution minimizing the longitudinal momenta (MinPz) is used in the rest of this study, as it gives the best efficiency (by a small margin). It is however important to noticed that if the two solution are far apart then in most of the cases the solution minimizing the longitudinal momenta return almost always the correct solution, while if the two solution are quite close, the kinematic of the event is not changed by taking one or the other solution.

Equation 5.8 may give imaginary solutions. In this case, the imaginary part of the equation is neglected. Figure 5.20 (a) shows the reconstructed mass of the W for the LSTC sample mode T250. As expected, about 60% of the events have the mass set to the W PDG value, $M(W) = 80.403$ GeV, but the tails of this distribution extend up to 1 TeV. It is also important to noticed that less than 10% of the events are reconstructed with a mass bigger than 100 GeV.

Figure 5.20 (b) shows the reconstructed $E_{\mathrm{T}}^{\mathrm{miss}}$ versus the truth $E_{\mathrm{T}}^{\mathrm{miss}}$ for the events where $M(W) < 200$ GeV, while Figure 5.20 (c) shows the same distribution for the events where $M(W) > 200$ GeV. Both distributions were fitted using a first order polynomial. The results of the slope shows that the $E_{\mathrm{T}}^{\mathrm{miss}}$ has too large value at the reconstructed level with respect to the truth value, when $M(W) >$

200 GeV. The events reconstructed with $M(W) > 200$ GeV are therefore vetoed in the rest of this analysis. The effect of this cut on the signal is low: for a luminosity of $\mathcal{L} = 2.04$ fb^{-1}, 0.1 events are lost.

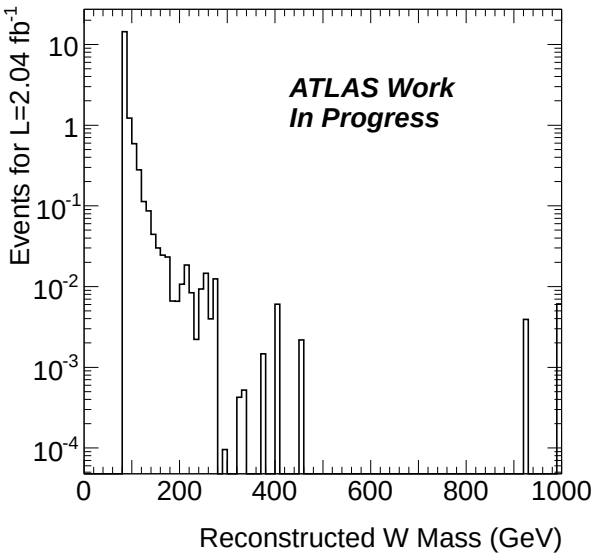

(a) Reconstructed $M(W)$.

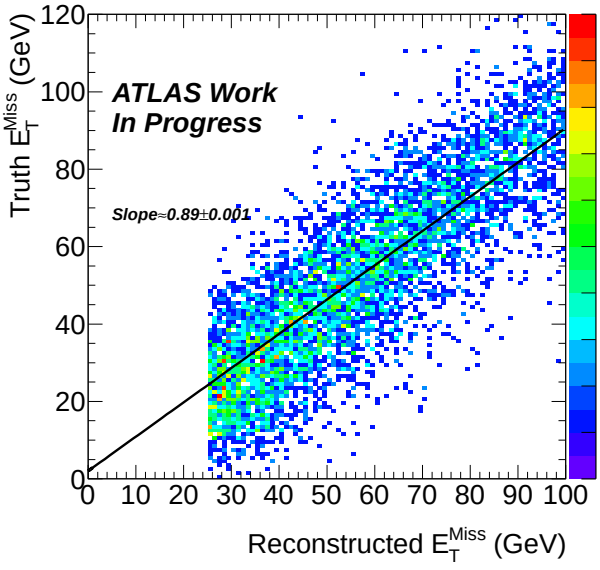

(b) Reconstructed $E_{\mathrm{T}}^{\mathrm{miss}}$ vs truth $E_{\mathrm{T}}^{\mathrm{miss}}$ for $M(W) < 200$ GeV.

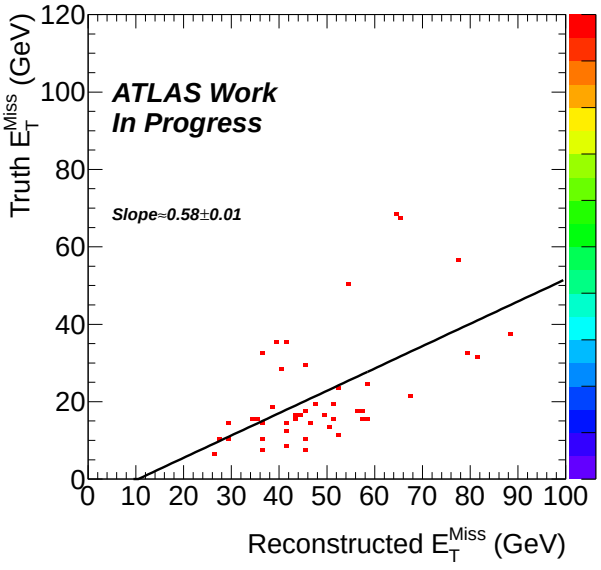

(c) Reconstructed $E_{\mathrm{T}}^{\mathrm{miss}}$ vs truth $E_{\mathrm{T}}^{\mathrm{miss}}$ for $M(W) > 200$ GeV.

Figure 5.20: (a) Reconstructed W mass for the LSTC sample mode T250. Reconstructed versus truth $E_{\mathrm{T}}^{\mathrm{miss}}$ distributions for events where $M(W) < 200$ GeV (b) and $M(W) > 200$ GeV (c).

The four momentum of the $W\gamma$ system is then obtained by summing the W and γ 4 momentum. The corresponding invariant mass will be used as the "*discovery*" variable. The analysis is conducted blindly with respect to it in the data. One needs to find a way, to verify that the Monte Carlo distributions model correctly the data but without having a look at it. This is done by searching control zone, where the signal is *a priori* not present, and by looking at the data MC agreement in these controls zone.

5.5.2 Signal invariant mass

Generator level

As said in the introduction, two particles participate to the $W\gamma$ final states: ρ_T and a_T, which are nearly degenerate. Figure 5.21 (a) shows the invariant mass of the $W\gamma$ system for the $\rho_T \to W\gamma$ and $a_T \to W\gamma$ in the LSTC sample mode T200, at generator level. Fitting this distribution to a double Breit-Wigner shape gives two peak positions at 200.60±0.01 GeV and 220.689±0.002 GeV. The width of the resonances is small, in both cases less than 200 MeV. The hypothesis used for the generation of this point does not fit completely the requirements of the LSTC model, indeed in this case the ρ_T and a_T have a similar contribution to the $W\gamma$ final state since the $\rho_T \to W\pi_T$ is closed, therefore the ρ_T decays also mostly in $W\gamma$. A more realistic point, with respect to the LSTC assumptions, can be observed in Figure 5.21 (b) corresponding to the LSTC sample mode T290. The fit of the double Breit-Wigner distribution gives the peak positions at 290.70 ± 0.07 GeV and 320.910 ± 0.007 GeV, in this case most of the $W\gamma$ is due to the a_T as expected.

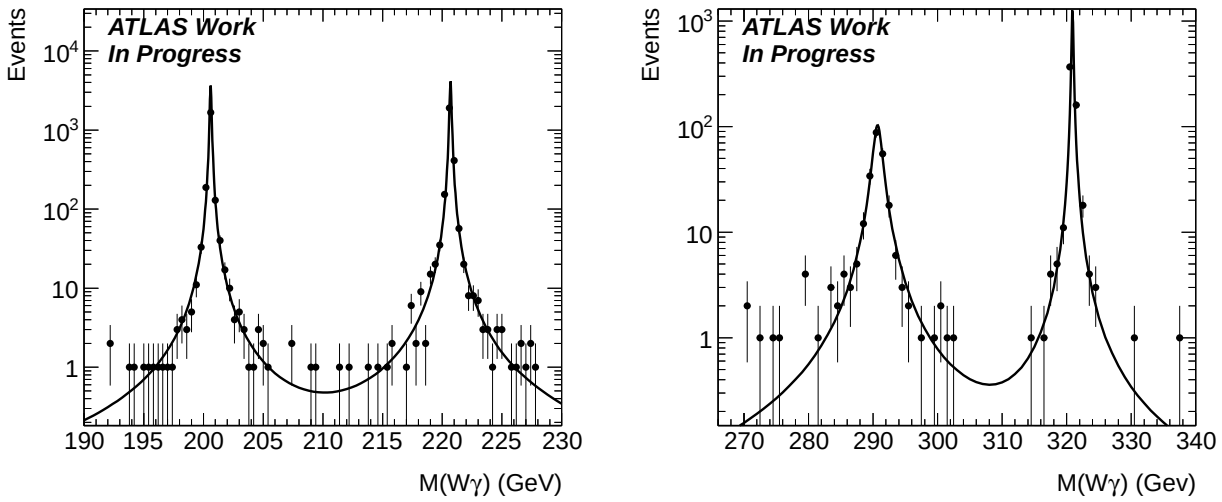

(a) LSTC sample mode T200.

(b) LSTC sample mode T290.

Figure 5.21: Generator-level $W\gamma$ invariant mass distribution. The distributions are fitted using a double Breit-Wigner function.

Reconstructed level

Figure 5.22 shows the invariant mass of the $W\gamma$ system generated at $M(\rho_T) = 200$ GeV and $M(a_T) = 220$ GeV, at reconstructed level. Due to the resolution effects of the detector, only a single peak is observed. For this reason the resonances are fitted using a single function, which is the sum of a Gaussian and a Crystal-Ball. In this case, the fit function is in good agreement with the Monte Carlo, giving $\chi^2/NDF \approx 1.0$.

The assumption that only a single peak is observed is however not completely true: between 200 and 230 GeV, a structure can be observed near the top of the peak. This structure is dependent on the production ratio ρ_T versus a_T and of their mass splitting. In the LSTC sample mode T250, the most important discrepancy is observed, leading to the worse χ^2 results: $\chi^2/NDF \approx 2.1$. The distributions for all the samples are given in Figures B.4 Appendix.

5.5.3 Control regions

One wants to check the data Monte Carlo agreement for the invariant mass distribution in control regions close to that of the signal, but without having a chance to see it.

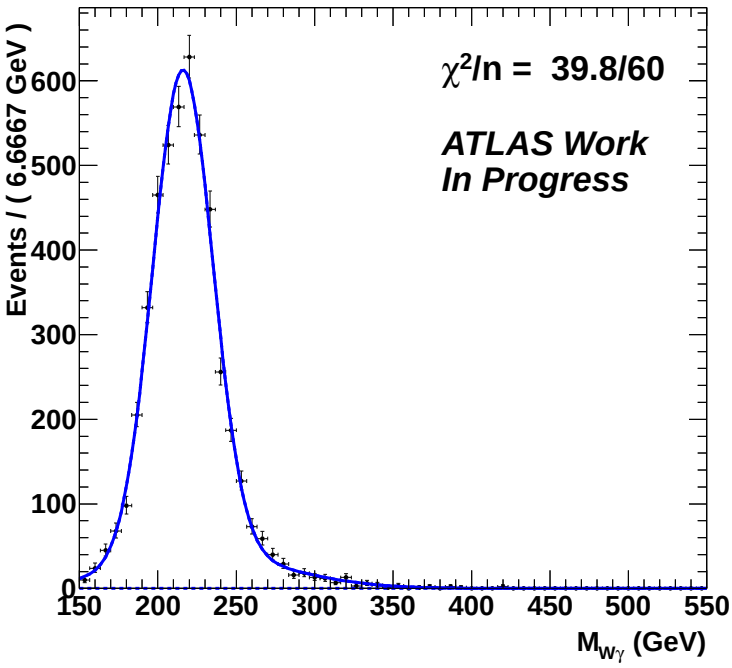

Figure 5.22: Reconstructed-level $W\gamma$ invariant mass distribution for the LSTC sample mode T200. The distribution is fitted using the sum of a Gaussian and a Crystal-Ball function.

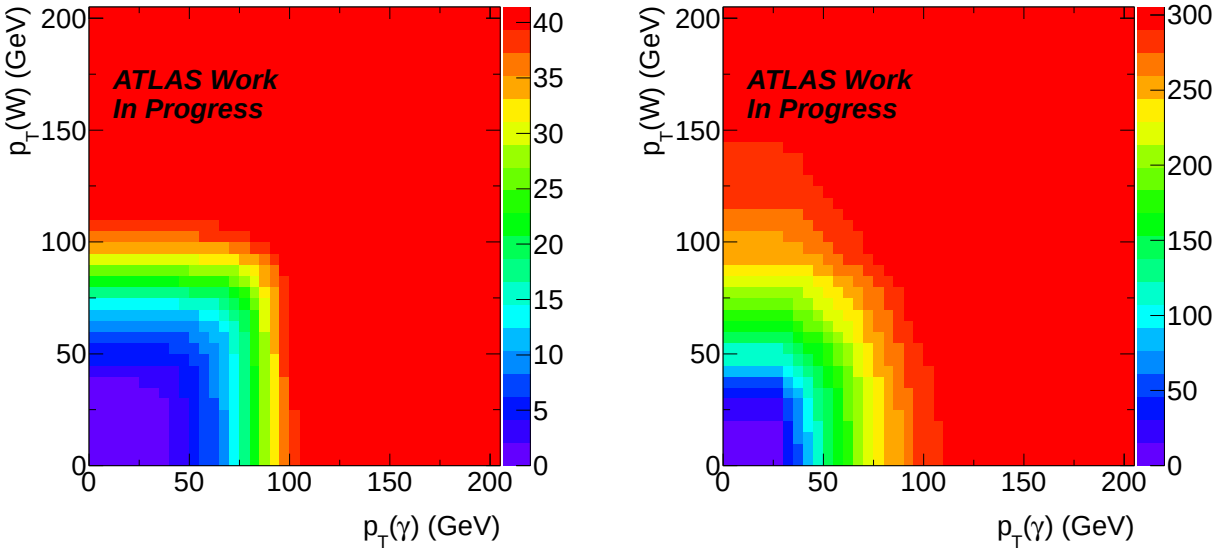

(a) LSTC

(b) SM backgrounds

Figure 5.23: Number of events in a window $200 < \sqrt{s} < 230$ GeV passing a cut less than $p_{\mathrm{T}}(W)$ or $p_{\mathrm{T}}(\gamma)$, for the LSTC sample mode T200 (a), and the Standard Model Backgrounds (b).

Figure 5.23 (a) shows, for the LSTC sample mode T200, a map of the number of LSTC events having $p_{\mathrm{T}}(W) < x$ or $p_{\mathrm{T}}(\gamma) < y$. One can see that if the photon or the W boson are requested to have $p_{\mathrm{T}} < 60$ GeV, there is about 12 events. Figure 5.23 (b) shows the same map for the Standard Model backgrounds, in a window $200 < \sqrt{s} < 230$ GeV. One can see that in the same conditions the number of SM events is evaluated about 200 events. This means that if one requires $p_{\mathrm{T}}(W) < 60$ GeV or $p_{\mathrm{T}}(\gamma) < 60$ GeV, if a resonance is present in the data one will not see it. This is the first control zone one can looked at to check the $W\gamma$ mass spectrum, data MC agreement.

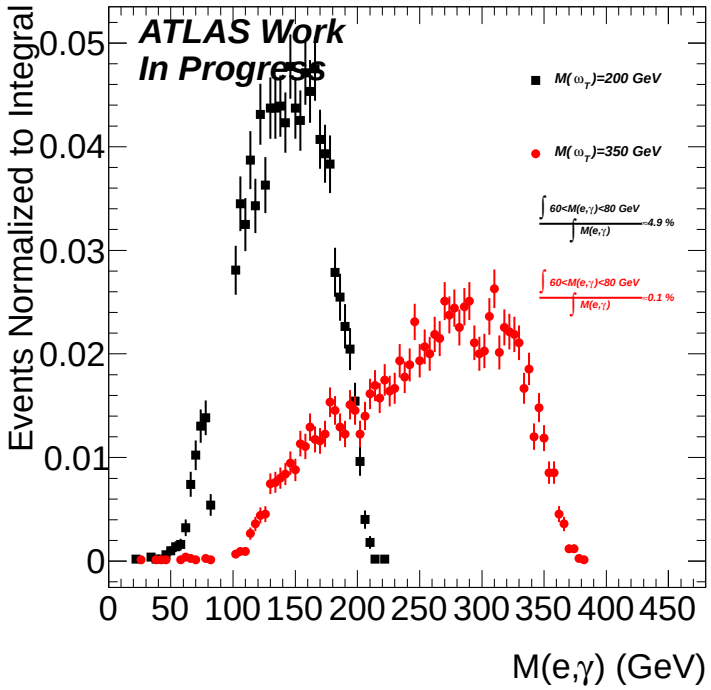

Figure 5.24: Invariant mass between photon and electron, for the LSTC sample mode T200 (black) and T350 (red).

Looking at Table 5.12, there is about 20% of $Z \to ee$ events in this selection. As this background is taken from Monte Carlo, one needs to find an enriched region in such events, to check the data Monte Carlo agreement. There is a cut on the invariant mass of the electron-photon system at the Z mass to reduced the $Z \to ee$ events, however the $60 < M(e,\gamma) < 80\ GeV$ region is *a priori* enriched in Drell-Yan events. One still needs to verify that the LSTC signal is not present in this region.

Figure 5.24 shows the invariant mass between the photon and the electron for the LSTC sample modes T200 and T350. For the first sample, there is less than 5% of the events that have their mass reconstructed in the range $60 < M(e,\gamma) < 80\ GeV$, for the second sample it is about 0.1% of the events. This region is taken as the second control region.

First control region, $p_{\mathrm{T}}(W) < 60$ GeV or $p_{\mathrm{T}}(\gamma) < 60$ GeV

Figures 5.25 were obtained by requiring $p_{\mathrm{T}}(\gamma) < 60$ GeV or $p_{\mathrm{T}}(W) < 60$ GeV. Figure 5.25 (a) shows the W transverse momentum, Figure 5.25 (b) the photon transverse momentum, and finally Figure 5.25 (c) the $W\gamma$ mass distribution. In this control region, the data is in good agreement with the Monte Carlo model, all the χ^2 tests return values close to unity.

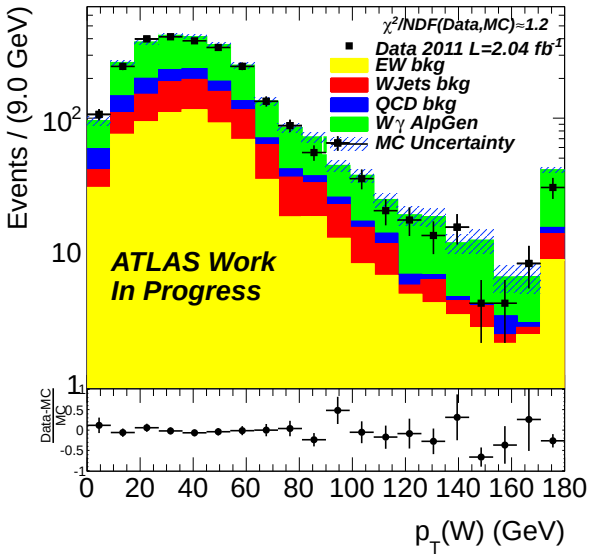

(a) $p_{\mathrm{T}}(W)$

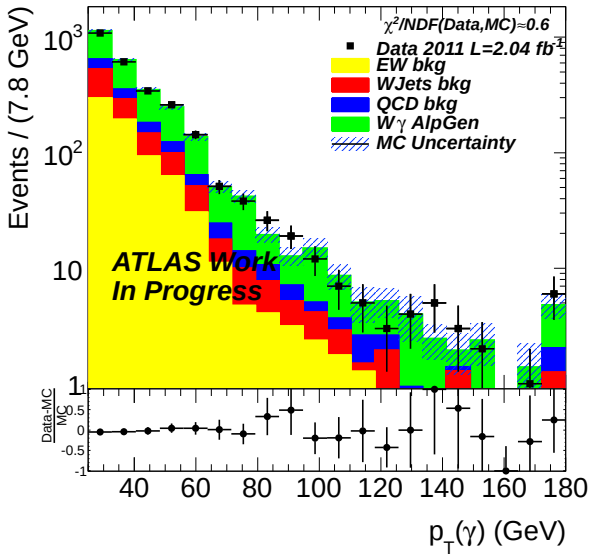

(b) $p_{\mathrm{T}}(\gamma)$

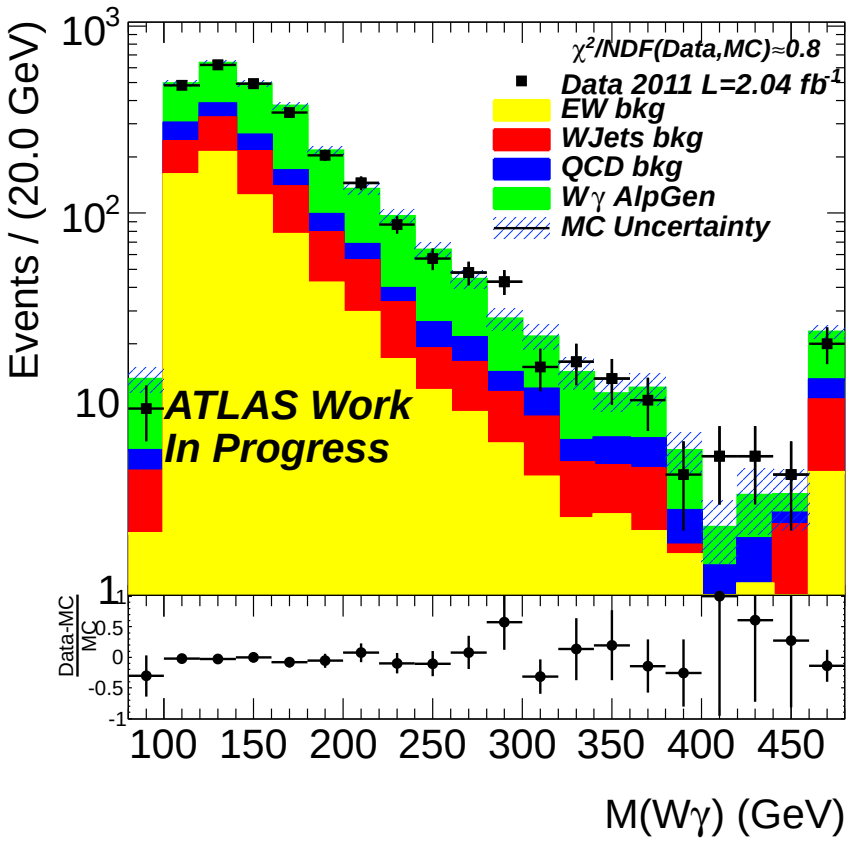

(c) $M(W\gamma)$

Figure 5.25: Distribution of $p_{\mathrm{T}}(W)$ (a), $p_{\mathrm{T}}(\gamma)$ (b) and $M(W\gamma)$ (c) in the control region $p_{\mathrm{T}}(\gamma) < 60$ GeV or $p_{\mathrm{T}}(W) < 60$ GeV.

Second control region, $60 < M(e,\gamma) < 80\ GeV$

The second control zone is defined by requiring that the selected photon and the electron have an invariant mass between 60 and 80 GeV. Figures 5.26 show in this control region, the W boson transverse momentum on Figure 5.26 (a), the photon transverse momentum on Figure 5.26 (b) and the $W\gamma$ invariant mass distribution on Figure 5.26 (c). Once again the distributions show a good agreement between data and Monte Carlo. The worse χ^2 test is obtained in the $p_{\mathrm{T}}(W)$ distribution and is $\chi^2/NDF \approx 1.2$.

Shape of the Standard Model backgrounds

In the control regions the agreement between data and Monte Carlo is good which validates the Monte Carlo model. The photon and W transverse momenta were also in good agreement between data and MC in the control zone and in the selection as shown by Figures 5.17 (c) and 5.18 (d).

Figure 5.27 shows the $W\gamma$ invariant mass distribution obtained in Monte Carlo for different cuts on $p_{\mathrm{T}}(\gamma)$ and $p_{\mathrm{T}}(W)$.

The distribution is decomposed in two parts: The low mass region which exhibits a turn-on behavior and the tail of the distribution that follows an exponential law.

Raising the p_{T} cut has a strong impact on the turn-on position, while the effect on the slope of the tail is small.

5.5.4 Selection optimization

Introduction

The analysis is optimized, by applying different cuts on the transverse momentum of the photon and the W boson. The selection is optimized using a variable called observation significance:

If a signal region, expected to contain N_{bkg}^{exp} background events in the absence of signal, is found to actually contain $N = N_{sig} + N_{bkg}^{exp}$, events, we define p_{obs} to be the probability that the measured signal originates from a statistical fluctuation within the no-signal hypothesis. Assuming $\delta(N - N_{bkg}^{exp}) = \delta N = \sqrt{N}$, the corresponding statistical significance is:

$$Z_{obs} = \frac{N_{sig}}{\sqrt{N_{sig} + N_{bkg}^{exp}}}, \tag{5.9}$$

Selection

Figure 5.28 shows the observation significance for $p_{\mathrm{T}}(\gamma) > y$ and $p_{\mathrm{T}}(W) > x$, for the LSTC sample mode T200. One can see that this distribution shows its maximum when $p_{\mathrm{T}}(\gamma) > 60$ GeV and $p_{\mathrm{T}}(W) > 60$ GeV cuts are applied. In this case $Z_{obs} \approx 2.8$. Looking to Figure 5.22, one can see that the LSTC signal peaks between 200 and 240 GeV. On Figure 5.27, one can see that for the Standard Model background, with these cuts applied, the turn on of the curve is located just at this place. This is not satisfactory since if a new physics signal is discovered, one want to have a striking proof that this signal exists, which is better observed on a relatively flat background shape.

Applying $p_{\mathrm{T}}(\gamma) > 50$ GeV and $p_{\mathrm{T}}(W) > 30$ GeV cuts, decrease the observation significance only to $Z_{obs} \approx 2.6$, but looking at Figure 5.27, it places the kinematical turn-on of the background away from the expected peak. The turn-on peaks in that case near $M(W\gamma) = 160$ GeV. For this reason, it is decided in the rest of this analysis, that the photon and W transverse momentum are required to be $p_{\mathrm{T}}(\gamma) > 50$ GeV and $p_{\mathrm{T}}(W) > 30$ GeV.

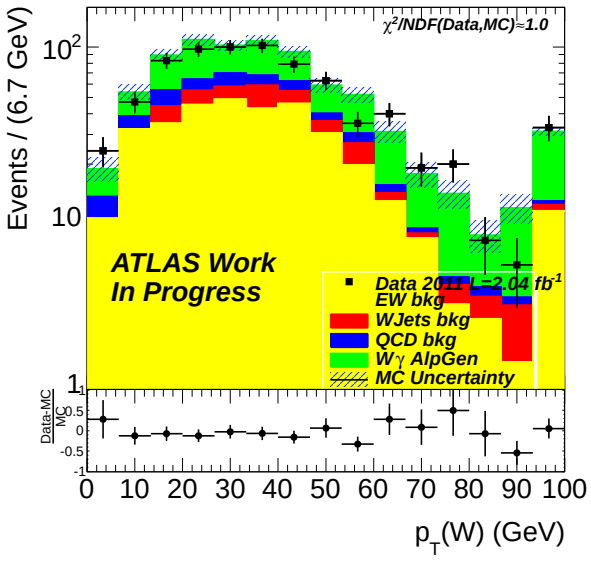

(a) $p_{\mathrm{T}}(W)$

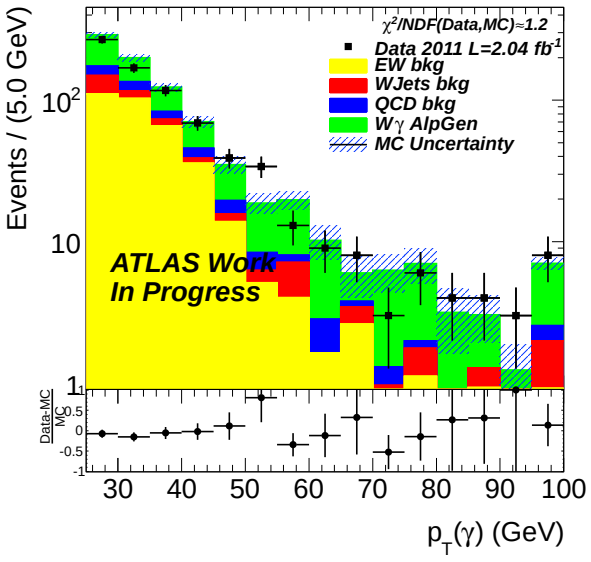

(b) $p_{\mathrm{T}}(\gamma)$

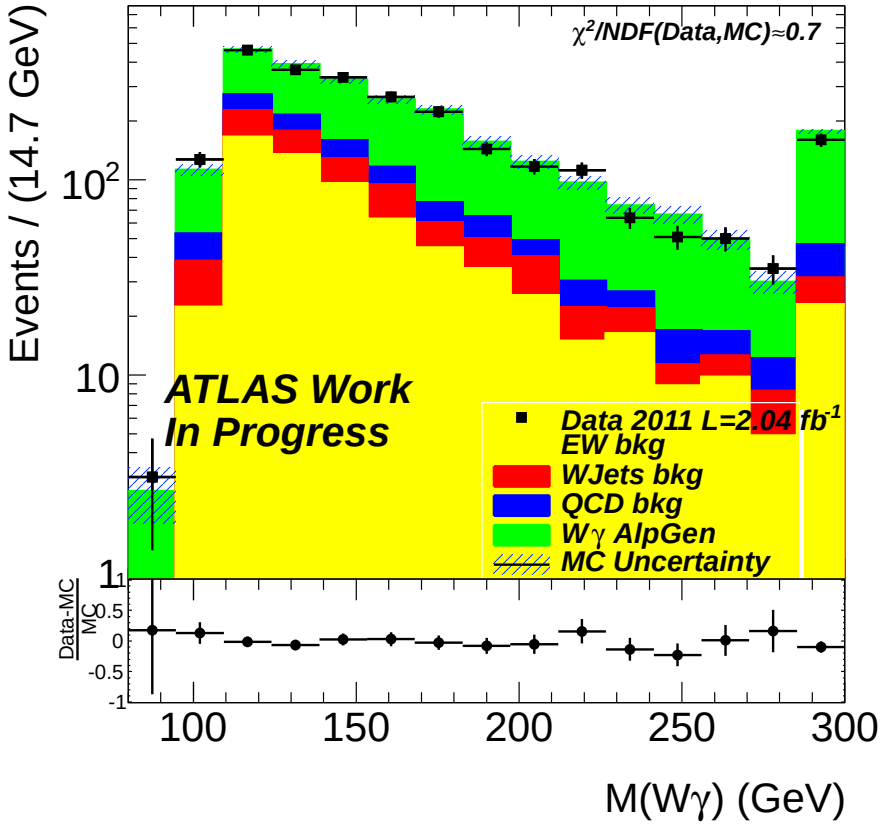

(c) $M(W\gamma)$

Figure 5.26: Distribution of $p_{\mathrm{T}}(W)$ (a), $p_{\mathrm{T}}(\gamma)$ (b) and $M(W\gamma)$ (c) in the control region $60 < M(e,\gamma) < 80\ GeV$.

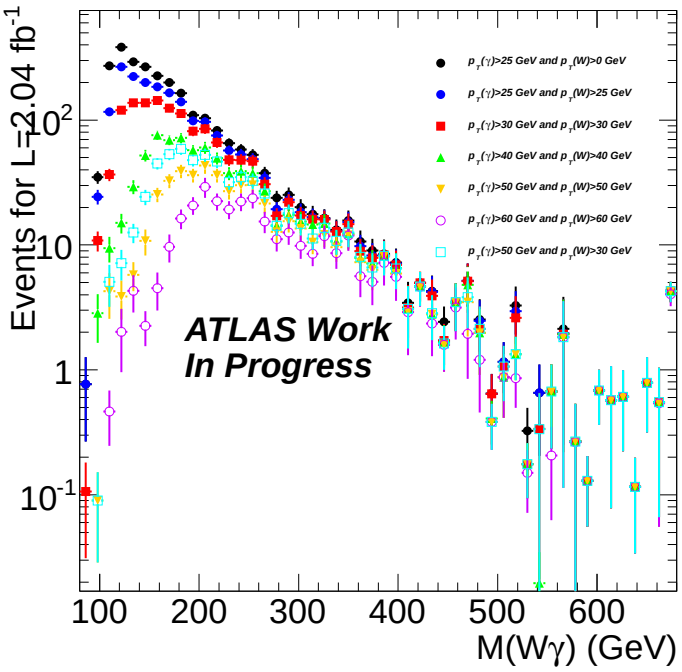

Figure 5.27: Invariant Mass distribution for the background obtained in MC, using different cuts on $p_{\mathrm{T}}(\gamma)$ and $p_{\mathrm{T}}(W)$

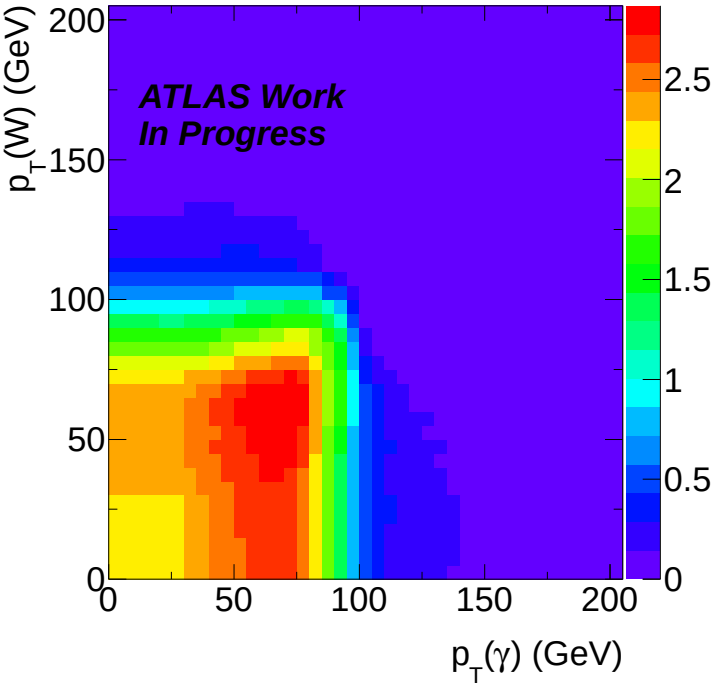

Figure 5.28: Observation significance, for different $p_{\mathrm{T}}(W)$ and $p_{\mathrm{T}}(\gamma)$ cuts. The significance is computed in a window $200 < \sqrt{s} < 230$ GeV, for the LSTC sample mode T200, and for the Standard Model Backgrounds.

Parameter	T200
μ_{CB}	215.5 ± 0.4 GeV
σ_{CB}	7.1 ± 0.12 GeV
α_{CB}	10 ± 2
n_{CB} (fixed)	100 ± 0
β	0.85 ± 0.02
μ_G	229 ± 4 GeV
σ_G	51 ± 2 GeV

Table 5.14: Fit parameter found for the T200 samples mode.

5.6 Fit

5.6.1 Signal

As said in Section 5.5.2, the signal is fitted using a function which is the sum of a Gaussian and a Crystal-Ball:

$$pdf_{\text{sig}} = (\beta) \times f_{CB}(m, \mu_{CB}, \sigma_{CB}, \alpha_{CB}, n_{CB}) + (1-\beta) \times f_{Gaus}(m, \mu_G, \sigma_G) \tag{5.10}$$

The signal is fitted on Monte Carlo, on each sample. Figure 5.22 shows the fit obtained for the sample mode T200. Table 5.14 gives the parameters obtained at the end of the fit on this nominal sample. The fit distributions for all the TC sample mode as well as their fit parameters are given in Figures B.4 and Table B.7 in Appendix.

5.6.2 Standard Model backgrounds

As said in Section 5.5.3, the Standard Model background shape has a turn-on behavior in the low mass region and an exponential tail. Two functions were investigated to fit this shape:

- One describing the turn on of the curve using a Fermi function. It is shown in Figure 5.29 (a).

$$F_{\text{bkg}}^{\text{Fermi}} = \frac{\exp^{\frac{-m}{\mu}}}{(1+\exp^{\frac{-(m-m_0)}{\sigma_{bkg}}})} \tag{5.11}$$

  In this function, μ is the parameter of the exponential, m_0 the position of the turn on, and σ_{bkg} a parameter describing the turn on width. All these parameters are free in the fit.

- One describing the turn on of the curve using a power law. It is shown in Figure 5.29 (b).

$$F_{\text{bkg}}^{\text{Power}} = \exp^{\frac{-m}{\mu}} \times (1 - \frac{m_0}{m})^{\alpha_{bkg}} \tag{5.12}$$

  In this function, μ is the parameter of the exponential, m_0 the position of the turn on, and α_{bkg} a parameter describing the turn on. All these parameters are free in the fit.

The fit function was tested against various Monte Carlo sample hypotheses:

The relative normalization of the $W\gamma$, QCD, W+jets and electroweak background is varied in the positive and negative direction of their systematic uncertainties. Different samples were also used to models the W+jets and $W\gamma$ shapes.

Figure 5.30 (a) shows the residual of the fits function versus $M(W\gamma)$, for the nominal Monte Carlo sample. The residual shows a disagreement in the 2σ band in the range $[280, 310]$ GeV. This artifact is in fact due to a statistical fluctuation of the Monte Carlo distribution in this range, as shown on Figures 5.29 (a) and (b). The statistics of the AlpGen $W\gamma$ sample are indeed low in this region.

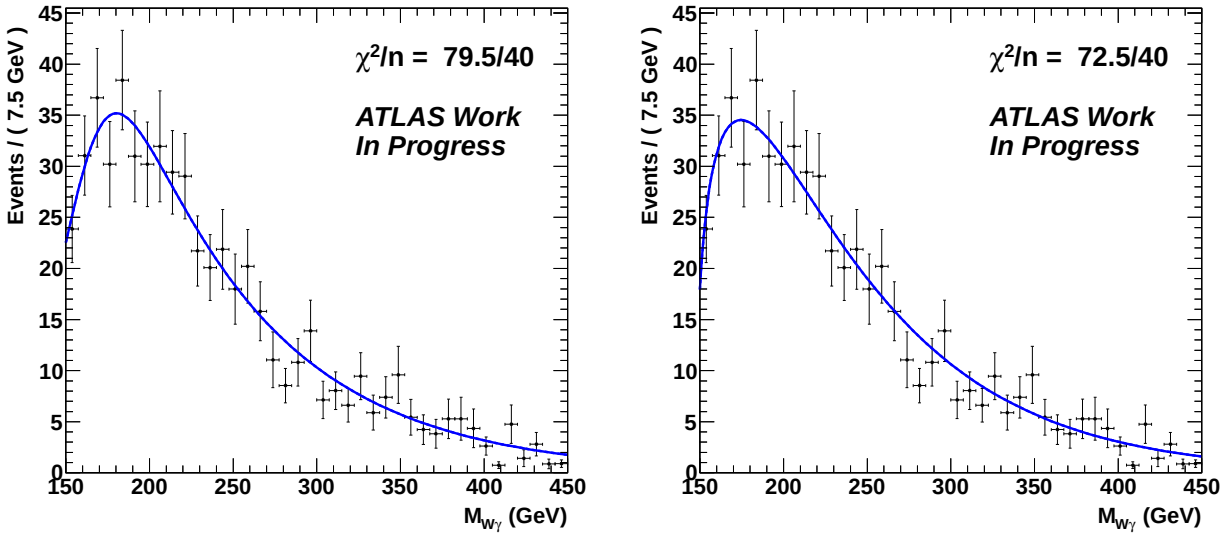

(a) Fit function using the Fermi turn on description.

(b) Fit function using the Power Law turn on Description

Figure 5.29: Distribution of the Standard Model background fit, obtained on Monte Carlo sample.

Parameter	value
μ_{bkg}	65 ± 4 GeV
$m(0)_{bkg}$	146 ± 3 GeV
α_{bkg} (fixed)	0.5

Table 5.15: Fit parameter found for the Standard Model background fit.

Figure 5.30 (b) shows the same distribution using the Sherpa sample introduced at the beginning of this Chapter, that contains more events. The fit is in that case in better agreement over the whole range. The Sherpa sample was however not describing properly some distributions such as the number of jets in the event, or $E_{\mathrm{T}}^{\mathrm{miss}}$; this is the reason why it was not used in this study. These two distributions are given in Figure B.3 in Appendix.

The Power Law fit function seems to model the background with a better accuracy than the Fermi function, for this reason it is used to model the background in the rest of this study. However it shows an instability when several fits are performed on the same dataset. This is due to the 99% correlation between the parameters m_0 and α_{bkg}, the correlation between the parameters is strong enough so that the fit find several minimums of the likelihood. As these two parameters characterize the turn position and shape, that are due to kinematic effects properly described by the Monte Carlo, it is decided to fix the α_{bkg} value in the fits. Since the best-fit value in the nominal MC sample is $\alpha_{bkg} = 0.46 \pm 0.2$, $\alpha_{bkg} = 0.5$ is chosen as the fixed value. Fixing the α_{bkg} parameters completely cancels the instability of the fit.

Figures 5.29 (c) and (d) shows the residual distributions in the case were α_{bkg} is fixed, the distributions are almost identical as Figures 5.29 (a) and (b).

The same distributions for all the tested hypothesis are given in Figures B.6 and Figures B.5 in Appendix. In all cases, the residuals are within error bands and show no significant deviations. This shows that the fit model can describe the range of Monte Carlo distribution that was determined in previous Section, and can thus be used to fit the data.

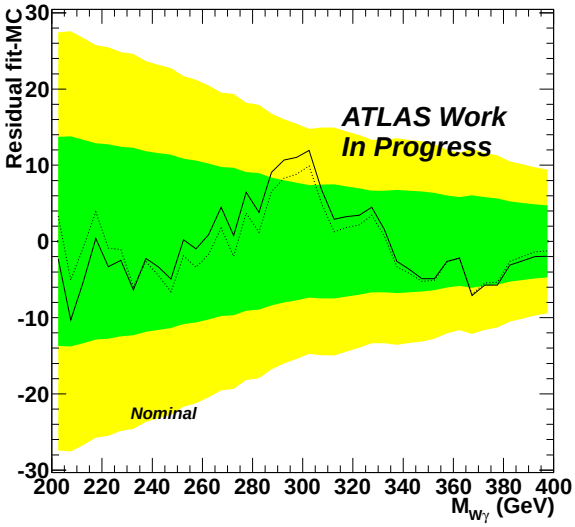

(a) AlpGen.

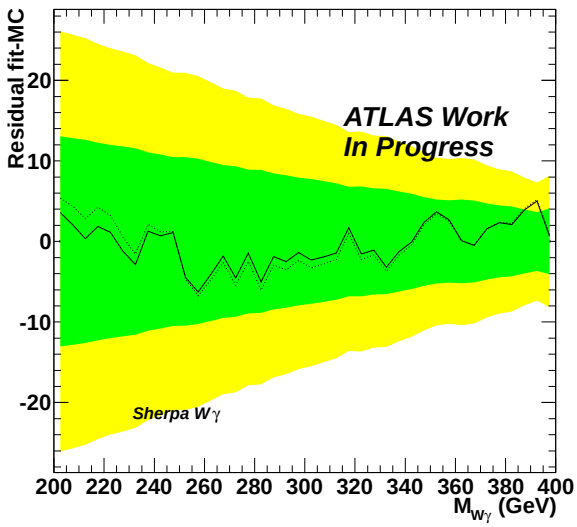

(b) Sherpa.

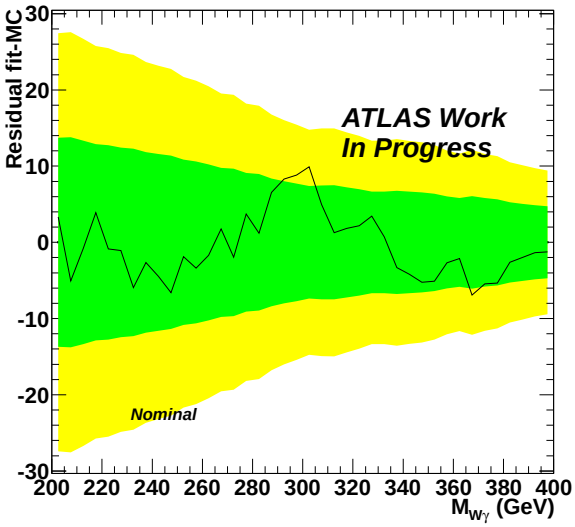

(c) AlpGen, α_{bkg} fixed.

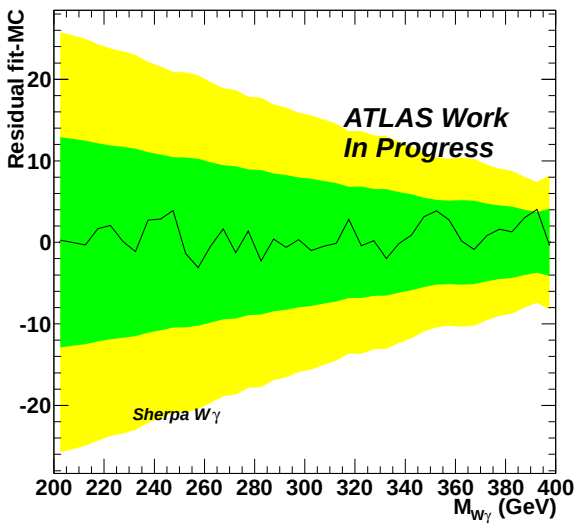

(d) Sherpa, α_{bkg} fixed.

Figure 5.30: Residual of the SM background fit for the nominal case using the AlpGen sample (a) and the Sherpa sample (b) with all the fit parameters free and with α_{bkg} fixed on (c) and (d) for the SM $W\gamma$. The plain line is the residual distribution of the fit using the Fermi function, while the dashed line is that of the Power Law function, the yellow and green bands are respectively the Monte Carlo uncertainty at 1 and 2σ.

TC sample	Fiducial cross section (fb)	Total cross section (fb)	Reconstruction Efficiency
T200	$53.1 \pm (^{1.12}_{0.73})^{sys}$	26.6	0.501
T225	$37.8 \pm (^{1.10}_{1.05})^{sys}$	19.3	0.511
T250	$29.2 \pm (^{0.80}_{0.86})^{sys}$	15.7	0.538
T290	$10.8 \pm (^{0.23}_{0.22})^{sys}$	6.1	0.561
T300	$13.9 \pm (^{0.42}_{0.63})^{sys}$	7.8	0.563
T350	$8.3 \pm (^{0.37}_{0.39})^{sys}$	4.7	0.569
T400	$5.5 \pm (^{0.20}_{0.12})^{sys}$	3.1	0.554

Table 5.16: Fiducial cross section and systematic errors evaluated from the PDF, total cross section, and reconstruction efficiency, for the seven LSTC sample modes.

5.6.3 Fit procedure

On the data and pseudo-data experiments, the fit is conducted to measure the number of Standard Model backgrounds events and TC signal events. It is an un-binned maximum log likelihood fit.

For the standard model background, the parameters of the fit function that are free to vary are: the normalization, μ and m_0; α_{bkg} is fixed.

For the LSTC signal, the parameters from the Crystal Ball and the Gaussian are fixed to their nominal values. Two nuisance terms are introduced in the signal fit, to account for systematic uncertainties, one for the signal rate and the other for the signal resolution. These terms are distributed according to asymmetric Gaussian distributions, constrained by the systematic uncertainties determined in the next Section. The signal shape nuisance parameter is added to the σ_G and σ_{CB} of the signal *pdf*. Its effect is to increase the width of the signal peak.

For the signal part of the fit, 3 parameters are free, the normalization, and the two nuisance parameters.

The normalization of the signal is fitted according to the following equation

$$N_S = \sigma_{\text{Fid}} \times \epsilon_{\text{Reco}} \times L \tag{5.13}$$

In this equation:

- σ_{Fid} is the fiducial cross-section. It is the TC sample cross-section obtained applying the acceptance cuts at the generator level. This is the parameter of interest in the study.
- ϵ_{Rec} is the signal reconstruction efficiency, defined as the ratio of the signal cross-section after all analysis cuts are applied to the fiducial cross-section.
- L is the luminosity.

Table 5.16 gives the fiducial cross section, total cross section[9] and reconstruction efficiency for all the TC samples. The way the PDF errors were derived is described below in Section 5.7.1.

5.7 Systematic uncertainties

5.7.1 Parton Distribution Function systematic uncertainties

The central value of the production cross section is calculated with the PYTHIA generator, using the MRST2007 LO* PDF and the corresponding ATLAS MC10 tune.

The systematic uncertainties on the cross section due to the limited knowledge of the proton PDFs comes from the error matrices of the MSTW08LO [131, 132] PDF set for which the eigen-vectors of the Hessian matrix are known. This set consists of 41 PDFs, one with nominal parameter eigen-values, and each of the others having an eigen-value increased or decreased by one standard deviation.

[9]The total cross section is the fiducial cross section times reconstruction efficiency.

The cross section for the signal is then evaluated for each of these PDFs. Since the eigen-vectors form an orthonormal basis, the deviations from the central value from sets which lead to an increase (decrease) in the cross section are added in quadrature and taken to be the size of the uncertainty in the cross section in the positive (negative) direction [133].

5.7.2 Systematic on the event rate and peak position

The following form of systematic uncertainty were considered for the signal.

- The jet energy scale.
- The electron energy scale.
- The electron trigger and reconstruction scale factor.
- The photon energy scale, identification, and isolation.
- The *LAr Hole*.
- The luminosity.

For the background, they are not considered since they are either negligible, or already accounted for in the degrees of freedom of the background *pdf*. The effect of the systematic uncertainties can be parameterized on the following parameters:

- an uncertainty on the signal rate.
- and uncertainty on the position of the signal peak which translates into an uncertainty on the peak resolution.

The effect of the various forms of systematic and how they are quantified is described below.

Jet Energy Scale

The jet transverse momentum is shifted by the uncertainty affecting the Jet Energy Scale, in the positive and negative directions. The $E_{\mathrm{T}}^{\mathrm{miss}}$ is then recomputed to account for this shift. The magnitude of the shift varies as a function of p_T and η, ranging from approximately 4% for jets with $p_{\mathrm{T}} = 30$ GeV to approximately 2.5% for jets with $p_{\mathrm{T}} > 60$ GeV.

For the LSTC sample mode T200, the shift of the Jet Energy Scale gives an uncertainty of about 2%, for the event yield and about 1 GeV on the peak position reconstruction.

Electron and Photon Energy Scale

The electron and photon energies are shifted by 1σ of the energy scale correction applied on the Monte Carlo, in the positive and negative direction. This shift depends on the transverse momentum of the object and on its position.

For the LSTC sample T200, the shift of the electron energy scale gives an uncertainty of about 0.4% on the signal event yield and shifts the position of the peak position by less than 0.1 GeV. The situation is similar for photons, with and uncertainty on the number of events and on the peak position of, respectively 0.2% and less than 0.1 GeV.

Electron Identification, Trigger and Reconstruction Scale Factor Uncertainties

For electrons, trigger, identification, and reconstruction efficiency corrections are applied to MC. The scale factors and their corresponding uncertainties are provided by the e/γ combined performance group. The uncertainties on these scale factors are added in quadrature on an event by event basis. The scale factor is modified by adding or subtracting these uncertainties to the nominal value.

For the T200 sample, the scale factor gives an uncertainty about 1.5% on the signal yield, and about 0.1 GeV for the peak position reconstruction.

Photon Identification and Isolation Uncertainties

The photon identification uncertainty was estimated to be 5% [134] in 2011. To estimate its effects, on the peak position, one imposes a scale factors per events of 1.05 to evaluate the positive direction effect and 0.95 for the negative direction. No impact is found on the peak position reconstruction.

The photon isolation was also varied from ±500 MeV from its nominal value, corresponding to about twice the shift that was observed between data and Monte Carlo. This adds an uncertainty of about 0.2% on the number of reconstructed signal event rate and about 0.1 GeV in the peak position reconstruction, for the sample mode T200.

LAr Hole Event Cleaning Uncertainty

In order to estimate the impact of the *LAr Hole* veto procedure, the cut on the jets is varied from $p_{\mathrm{T}} > 20$ GeV to $p_{\mathrm{T}} > 16$ GeV and $p_{\mathrm{T}} > 24$ GeV. The impact is found to be small in the T200 sample mode, 0.3% on the signal event yield and no effect on the peak position reconstruction.

Luminosity Uncertainty

The uncertainty on the luminosity is measured to be 3.7% [135]. This uncertainty affects only the signal event rate.

5.7.3 Summary

All these uncertainties are added in quadrature. For the T200 sample mode, one obtains $N_{ev} = 54. \pm \binom{4}{3}^{sys}$ and the peak position Peak= $211.15 \pm \binom{0.89}{0.93}^{sys}$ GeV.

The systematic uncertainties for all the LSTC samples are given in Appendix B.9.

5.8 Statistical methods

5.8.1 Introduction

This section introduced the statistics used to discover a signal or set a limit on the production of the LSTC signal. It is largely taken from [119].

The Modified Frequentist method (CL_s method) [136] is adopted to interpret the data, following the recommendations in the ATLAS Collaboration.

First, a "*Discovery*" hypothesis test is performed to evaluate the compatibility between data and the null hypothesis, which only assumes the existence of Standard Model background processes. If the hypothesis test shows no presence of any significant excess in data, a limit on the $W\gamma$ resonance production cross section will be set.

The compatibility between data and the null hypothesis is indicated by the p-value of a null hypothesis p_0. When an excess over the background is present in data, p_0 will be close to 0, indicating a significant discrepancy between data and the null hypothesis.

In the case of setting an exclusion limit, the hypothesis in question is a Signal+Background hypothesis. It is tested against the background only hypothesis. As one is interested to know for which level of signal the Signal+Background hypothesis is excluded, various hypotheses on the strength of the signal are tested.

In the CL_s method, the confidence level modified to take into account downward background fluctuations, and the modified p-value is quoted as CL_s. When CL_s is less than 0.05, the hypothesis in question is claimed to be excluded at 95 $\%C.L.$

In the following subsections, the details of the above procedure will be presented.

5.8.2 Test statistic

The test statistic used in this analysis is the Profile Likelihood Ratio [137], which is the ratio of two maximized likelihood functions built from Signal+Background model.

The method used to extract the signal is an un-binned maximum likelihood (ML) fitting technique. The likelihood is defined as

$$\mathcal{L}(\sigma_{Fid}, \boldsymbol{\theta}) = e^{-N_S(\sigma_{Fid})-N_B} \prod_{k=1}^{n} N_S(\sigma_{Fid}) f_S(\mathbf{x}_k; m_{TC}, \boldsymbol{\theta}_S) + N_B f_B(\mathbf{x}_k; \boldsymbol{\theta}_B) \tag{5.14}$$

In the equation above, n is the number of entries in the fitted dataset $\mathbf{x}$ and each $\mathbf{x}_k$ represents one entry. In our case, each entry contains the value of $M_{W\gamma}$ for the event considered. The quantities f_S and f_B are the probability density functions (*pdf*) for the signal and background component respectively . The number of background events is denoted N_B, and the number of signal events is expressed as $N_S(\sigma_{Fid})$ defined in equation (5.13), with the parameter of interest which is the fiducial cross sections:σ_{Fid}.

The remaining ("nuisance") parameters in the signal and background *pdf* are denoted by the vector $\boldsymbol{\theta}_S$ and $\boldsymbol{\theta}_B$ respectively.

In what follows the combined vector $\boldsymbol{\theta} = \boldsymbol{\theta}_S \cup \boldsymbol{\theta}_B$ will be used. The parameter m_{TC}, the value of the TC sample considered, is always fixed in the fits and therefore not included in the nuisance parameters. The floating parameters in the fit are σ_{Fid}, N_B and the $\boldsymbol{\theta}$.

The test statistic for a discovery is defined as:

$$t_0 = -2ln\left(\frac{\mathcal{L}(\sigma_{Fid}, \hat{\boldsymbol{\theta}})}{\mathcal{L}(\sigma_{Fid}=0, \hat{\hat{\boldsymbol{\theta}}})}\right) \tag{5.15}$$

The test statistic for exclusion is defined as:

$$\tilde{q}_{\sigma_{Fid}} = \begin{cases} -2\,ln\frac{\mathcal{L}(\sigma_{Fid};\hat{\hat{\boldsymbol{\theta}}})}{\mathcal{L}(0,\hat{\boldsymbol{\theta}})} & \sigma_{\hat{Fid}} < 0, \\ -2\,ln\frac{\mathcal{L}(\sigma_{Fid},\hat{\hat{\boldsymbol{\theta}}})}{\mathcal{L}(\sigma_{\hat{Fid}},\hat{\boldsymbol{\theta}})} & 0 \leq \sigma_{\hat{Fid}} \leq \sigma_{Fid}, \\ 0 & \sigma_{\hat{Fid}} > \sigma_{Fid} \end{cases} \tag{5.16}$$

where σ_{Fid}, the fiducial signal cross section, is the strength parameter, $\sigma_{\hat{Fid}}$ is the fit favored σ_{Fid} value, $\hat{\hat{\theta}}$ is the collective denotation of the fit favored nuisance parameters values when σ_{Fid} is constant in the fit, $\hat{\theta}$ is the collective denotation of the fit favored nuisance parameters values when σ_{Fid} is also free in the fit.

5.8.3 Generation of pseudo-data

Pseudo datasets are generated under a *pdf* corresponding to a certain hypothesis. To find the expected confidence level and extract CL_s limit, requires the generation of Background-only pseudo datasets.

When a pseudo dataset is generated, all parameters in the *pdf* are fixed to their nominal values. The expected numbers of events used to produce Poisson random number for the normalization are $N_S(\sigma_{Fid})$ and N_B^{exp} .

The treatment of nuisance parameters used for systematic uncertainties follows the "unconditional ensemble" prescription: for each pseudo dataset the central values of the constraints are drawn from their *pdf*, and these values are used in the calculations of $\mathcal{L}$ and $\tilde{q}_{\sigma_{Fid}}$.

5.8.4 Determination of p-value

After fitting a dataset (either real data or pseudo-data), values of $\tilde{q}_{\sigma_{Fid}}$ are computed for various values of σ_{Fid} where pseudo datasets are generated, denoted as σ'_{Fid}. For a given σ'_{Fid} at a chosen LSTC mass m_{TC}, calculating $\tilde{q}_{\sigma_{Fid}}$ for each pseudo dataset generated under Signal+Background hypothesis leads to a distribution of $\tilde{q}_{\sigma_{Fid}}$, $f(\tilde{q}_{\sigma_{Fid}}|\sigma_{Fid} = \sigma'_{Fid})$. A p-value for the dataset tested is defined as

Data	604 ± 24
MC	$635 \pm (20)^{stat}$
SM $W\gamma$	$440 \pm (18)^{stat}$
W+jets	$39 \pm (18)^{stat}$
QCD	$49 \pm (2)^{stat}$
EW	$120 \pm (7)^{stat}$
T200	$54 \pm ^{3}_{4}$
T225	$39 \pm ^{3}_{3}$
T250	$32 \pm ^{2}_{2}$
T290	$12 \pm ^{1}_{1}$
T300	$16 \pm ^{1}_{1}$
T350	$9 \pm ^{1}_{1}$
T400	$6 \pm ^{1}_{1}$

Table 5.17: Number of data and MC events in the final selection. Expected number of events for all LSTC hypotheses.

$$p_{\sigma'_{Fid}} = \int_{\tilde{q}_{\sigma'_{Fid},obs}}^{\infty} f(\tilde{q}_{\sigma_{Fid}}|\sigma_{Fid} = \sigma'_{Fid})\ dq_{\sigma_{Fid}} \tag{5.17}$$

where $\tilde{q}_{\sigma'_{Fid},obs}$ is the test statistic value calculated from the dataset tested. Such p-value is also quoted as p_{s+b}.

5.8.5 Definition of exclusion limit

The CL_s method is used to compute the confidence level (CL). The CL_s limit claims exclusion at $95\% C.L.$ when $CL_s = 0.05$. The CL_s is defined as [136]:

$$CL_s = \frac{p_{s+b}}{1 - p_0} \tag{5.18}$$

where p_0 is the integrated value of the Background-only distribution from 0 to $q^{obs}_{\sigma_{Fid}}$. 1-p_0 is also referred as the confidence level of Background-only hypothesis (CL_b).

5.8.6 Interpolation of Limit

When the limit setting CL_s is decided, to find its 95% exclusion limit, an iteration over values of σ_{Fid} is performed. This is usually done by scanning a predefined set of values to identify a small interval $[\sigma^{low}_{Fid}, \sigma^{high}_{Fid}]$ containing σ^{up}_{Fid} which satisfies the requirement stated in Section 5.8.5, and estimating the crossing point using a linear interpolation.

Here one uses σ_{Fid} values ranging from 0 to 200 fb, in step of 2 fb in the range $[0, 6]$ fb, 1 fb in the range $]6, 30]$ fb, 2 fb in the range $]30, 40]$ fb, 5 fb in the range $]40, 50]$ fb, and the values 75 fb, 100 fb, 150 fb and 200 fb.

5.9 Results

Once the analysis is un-blinded, the $W\gamma$ mass distributions was looked at. A comparison of data versus the SM background is shown on Figure 5.31. The Standard Model backgrounds describes properly the data, as shown by the χ^2 test close to unity. In total in this selection, the background expectation gives $635 \pm (20)^{stat}$ events, and 604 events are observed in the data.

Table 5.17 gives for the final selection the number of expected and observed events in the data. The expected number of events for $\mathcal{L} = 2.04$ fb^{-1} of data is also given for each LSTC hypothesis.

Hypothesis	T200	T225	T250	T290	T300	T350	T400
p_0	0.67	0.69	0.95	0.42	0.55	0.88	0.55

Table 5.18: p_0 values obtained for the different LSTC hypothesis.

5.9.1 Confidence level for background hypothesis

The procedure described in Section 5.8 to compute the discovery p-value p_0 is applied to the data. For each mode point, a value of p_0 is obtained, which should be close to 1 in the case of perfect agreement between data and background MC, and small in the case of a significant disagreement. The result of the fit with the signal normalization free is shown in Figure 5.32 for the T200 sample parameters. In this case $p_0 \approx 0.67$, showing no excess in the data. Testing the various LSTC mass points against the background only hypothesis does not gives any significant results as shown in Table 5.18.

The fit distributions obtained for each LSTC hypothesis are given on Figure B.9 in Appendix.

The T290 mode was added in this study to test an hypothesis corresponding to the un-explained excess seen at CDF [51]. The statistic test gives $p_0 \approx 0.42$ corresponding to a significance of 0.8σ, meaning that no deviation from the SM processes is observed.

An interpolation is performed using the six other LSTC mass points to perform a scan, by step of 1 GeV, over the M(a_T) range [220,440] GeV.

Corresponding p_0 values over this range are shown on Figure 5.33. Two excesses can be seen in this distribution, the first and most important one at $M(a_\mathrm{T}) = 329$ GeV corresponding to a significance of 0.71σ, and the another at $M(a_\mathrm{T}) = 409$ GeV corresponding to a significance of 0.70 σ. Since the range

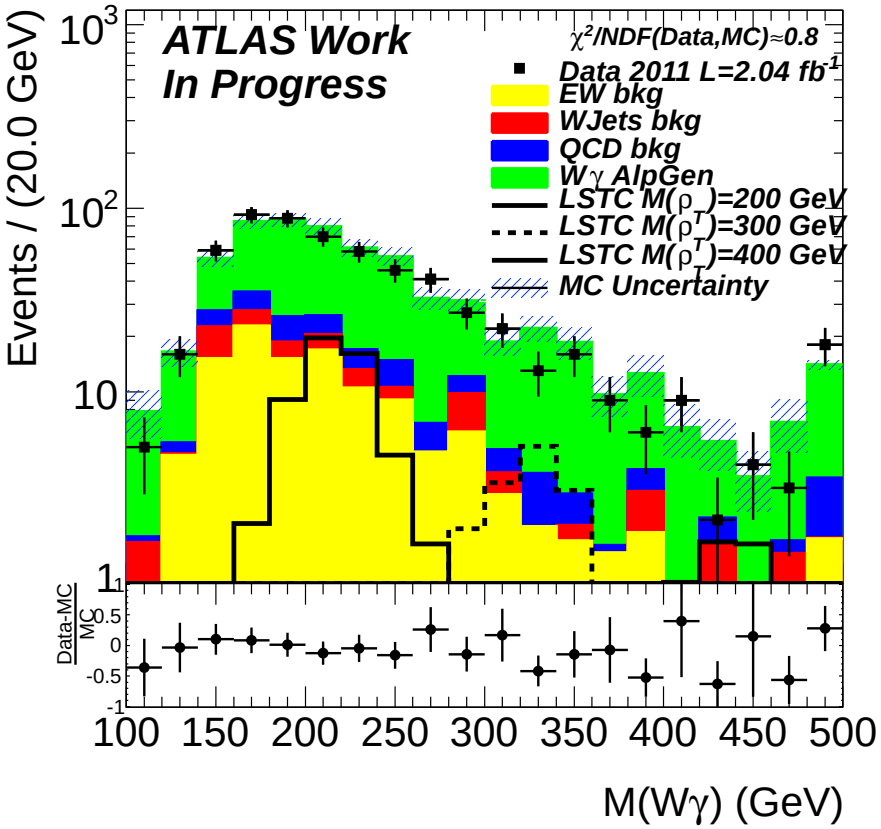

Figure 5.31: Reconstructed M($W\gamma$) distribution for the final selection for the data and Monte Carlo. Are also shown 3 LSTC signal hypothesis.

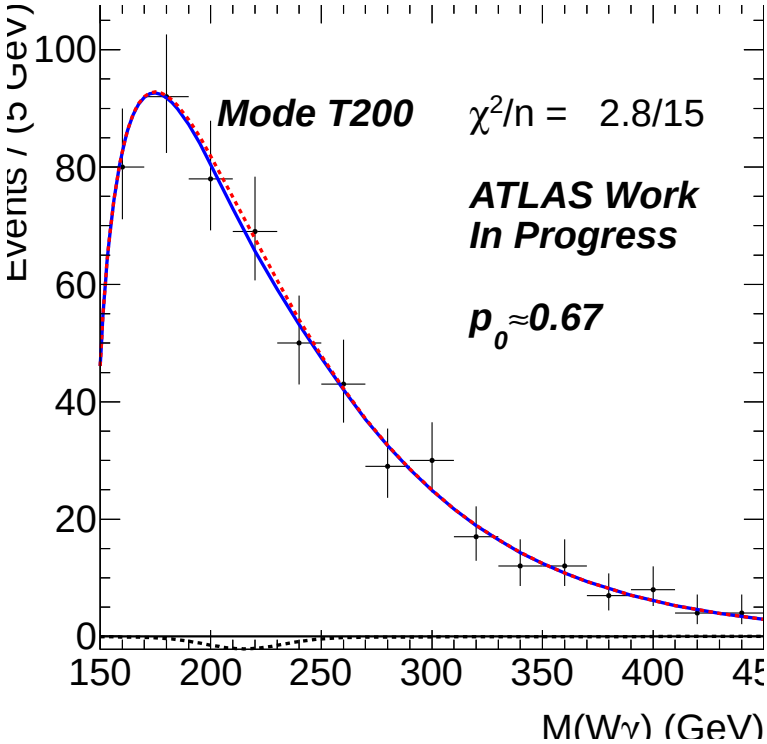

Figure 5.32: Fit of the model on the data using the T200 sample parameters. The dashed line is the background only hypothesis fit, while the plain line represents the signal+background hypothesis. In this case the signal+background fit tries to fit a negative fluctuation.

under consideration includes 5-6 independent measurements, fluctuations of this order are expected due to the Look Elsewhere Effect. One therefore conclude that no significant excess from the SM predictions is observed in the $M(W\gamma)$ spectrum, for TC masses, in the range [220,440] GeV.

5.9.2 Limits

For the expected limit, mass points ranging from 200 to 400 GeV are considered, in steps of 25 GeV. For the observed limit, the same range is used with a step size of 5 GeV.

Since the a_T resonance is the dominant production mode, we choose to parameterize the limits in term of $M(a_\mathsf{T})$. For comparison with other measurements, distributions as a function of $M(\rho_\mathsf{T})$ are also provided.

Figure 5.34 (a) and Figure 5.34 (b) show the cross section limits assuming no systematic uncertainties and full systematic uncertainties as a function of $M(a_\mathsf{T})$. The same limits as a function of $M(\rho_\mathsf{T})$ are given in Figure 5.35 (a) and Figure 5.35 (b). It can be noticed that the influences of the systematic uncertainties are marginal with respect to the total errors. The lower limit on the resonance mass is derived from the intersection of the central excluded limit line and the production cross section. With this definition the lower mass limits, one can derive are $M(a_\mathsf{T}) > 265$ GeV and $M(\rho_\mathsf{T}) > 243$ GeV.

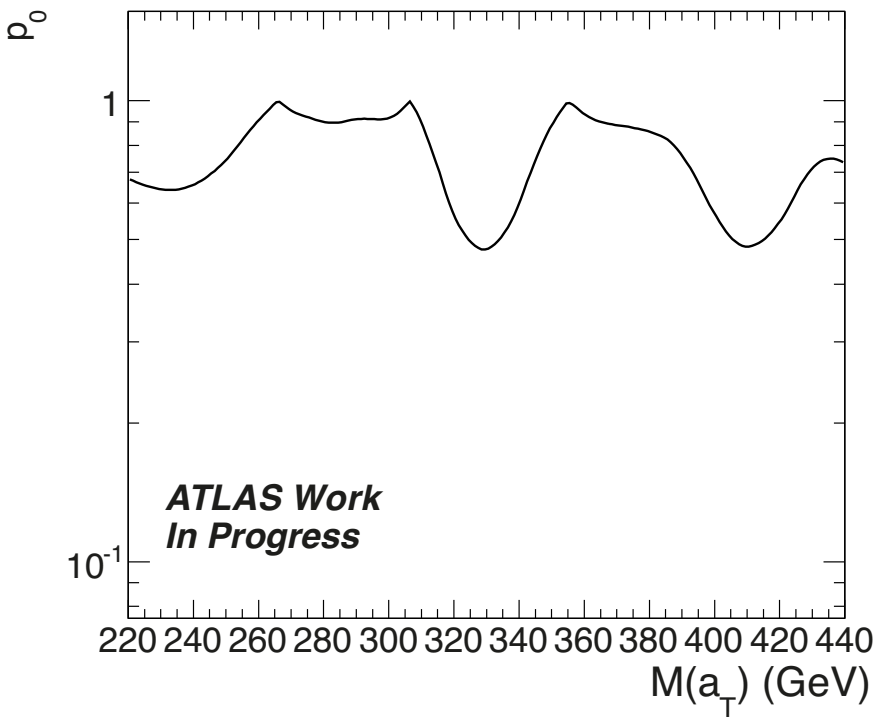

Figure 5.33: p_0 values for the scan of the M(a_T) spectrum, obtained by extrapolation of the TC samples parameters.

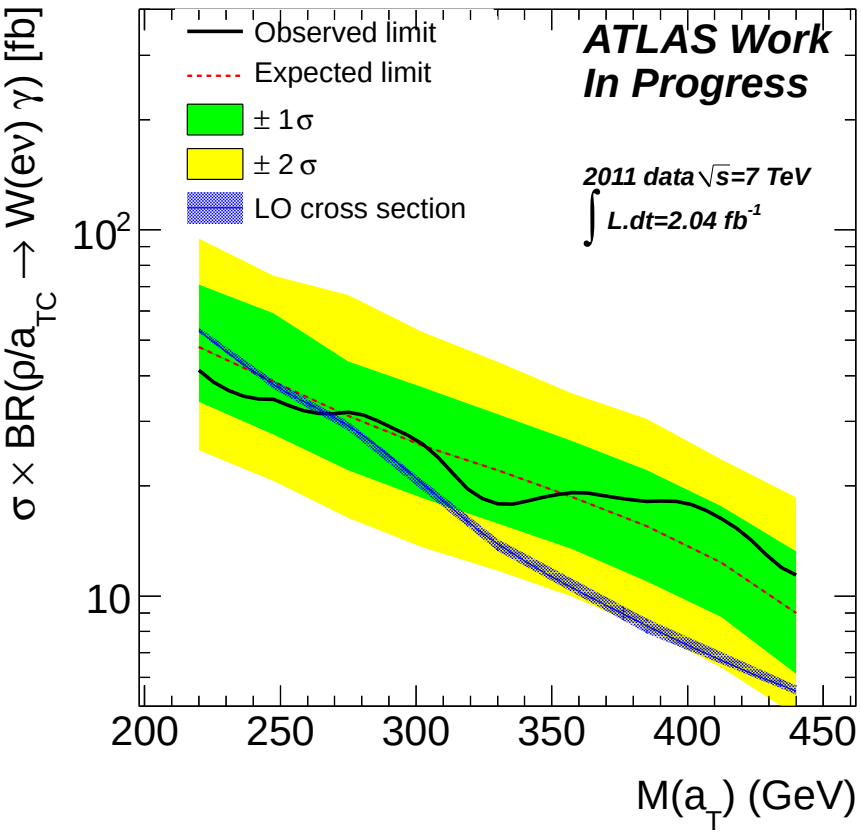

(a) Without the effect of systematic errors.

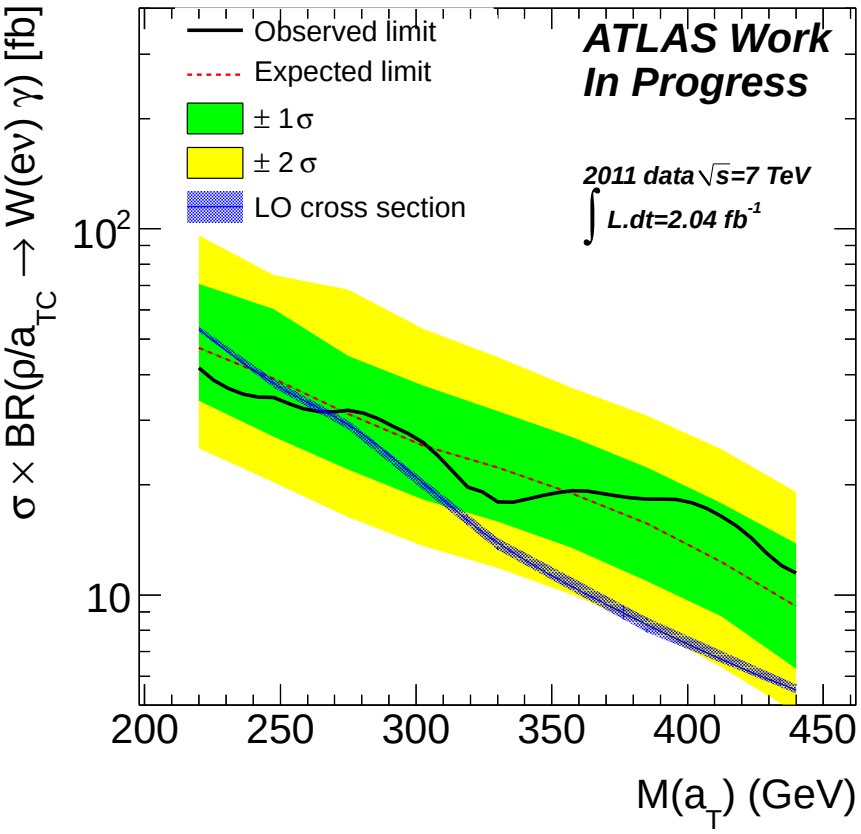

(b) With the effect of systematic errors.

Figure 5.34: Expected and excluded production cross section limit multiplied by the branching fraction for the $W\gamma$ final state assuming the $\rho_T \to W\gamma$ and $a_T \to W\gamma$ signal, as a function of the a_T mass.

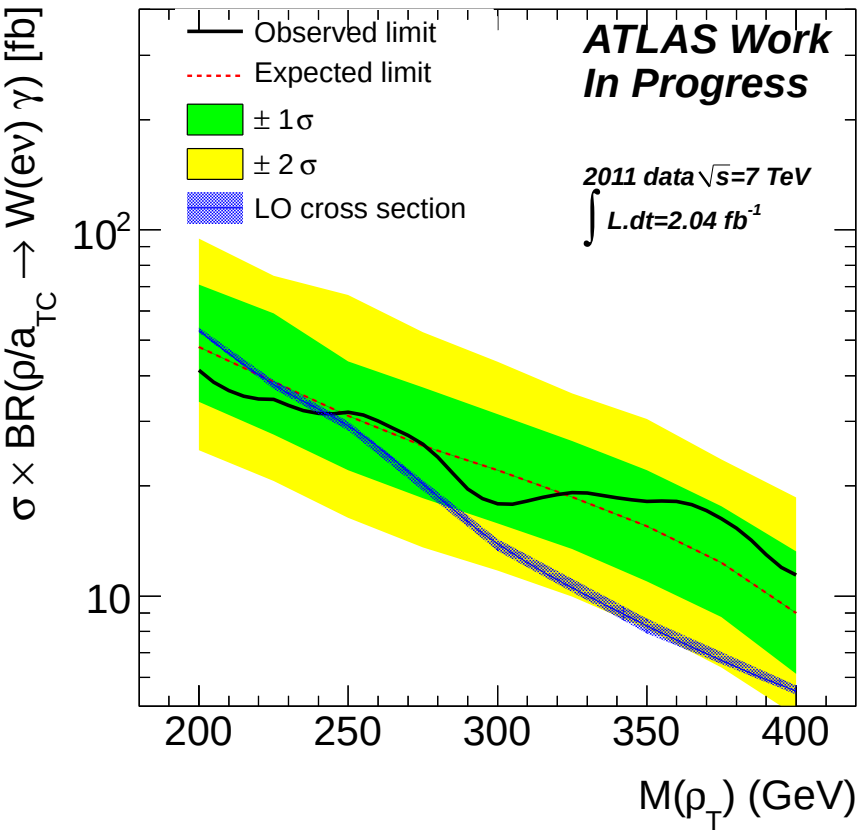

(a) Without the effect of systematic errors.

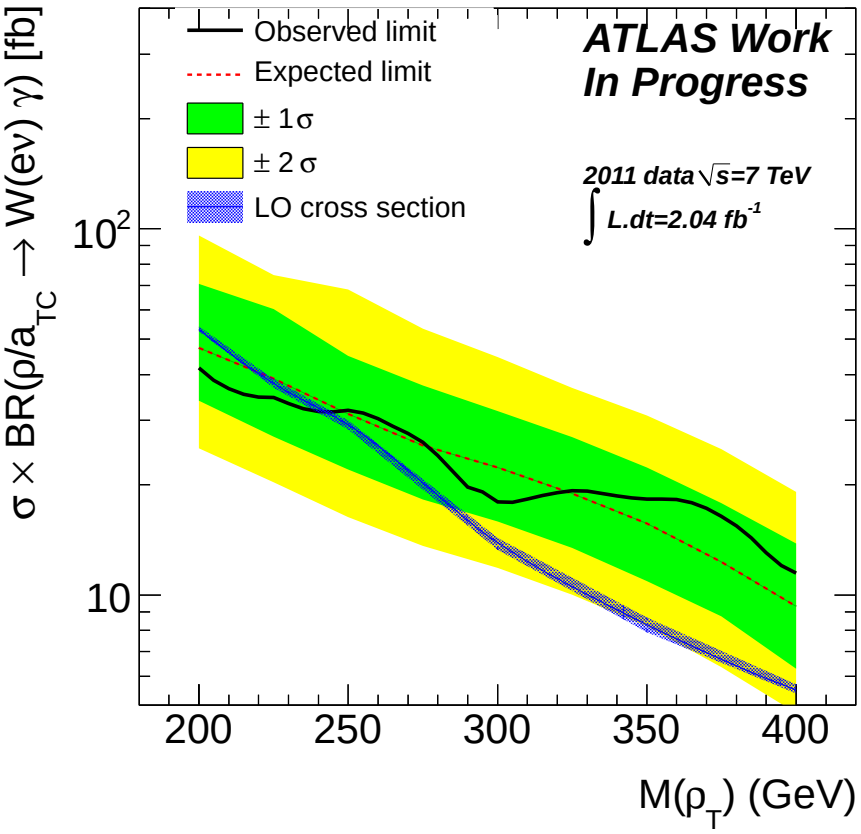

(b) With the effect of systematic errors.

Figure 5.35: Expected and excluded production cross section limit multiplied by the branching fraction for the $W\gamma$ final state assuming the $\rho_T \to W\gamma$ and $a_T \to W\gamma$ signal, as a function of the ρ_T mass.

Conclusion

In this Chapter, the W($e\nu$)γ final state was studied, using $\mathcal{L} = 2.04$ fb^{-1} of pp collisions at $\sqrt{s} = 7$ TeV.

In a first part, the backgrounds contributing to this final state were estimated. In particular, the normalization and shape of the QCD multi-jets and W+jets backgrounds were estimated using two different data driven techniques. The SM $W\gamma$ normalization was also estimated in the data. The residual electroweak backgrounds, such as $t\bar{t}$, single top, $Z \to ee$, $Z \to \tau\tau$, $W \to \tau\nu$ were estimated from the Monte Carlo. The estimated Standard Model background shape and normalization were found to give a good description of the data in the control region, and once the search was un-blinded, in the signal region.

In a second part a search for new physics in the $W\gamma$ final state was conducted. It was shown that it is possible to reconstruct the 4-momentum of the W boson, by applying a mass constraint on the electron-$E_{\mathrm{T}}^{\mathrm{miss}}$ system. The $W\gamma$ invariant mass is then reconstructed and used as a discriminating variable to search for narrow resonances. A final selection for the search was determined using LSTC MC samples and the standard model backgrounds. The selection maximizing the discovery significance while separating the kinematic threshold from the peak of the first mass point at 200 GeV was found to be $p_{\mathrm{T}}(\gamma) > 50$ GeV and $p_{\mathrm{T}}(W) > 30$ GeV.

The search was then conducted on the data. No significant excess over the Standard Model predictions was observed in the $W\gamma$ mass spectrum for TC masses in the range [220,440] GeV. The most important excess observed was seen at $M(a_{\mathsf{T}}) = 329$ GeV with a significance of 0.71σ. The hypothesis of signal at $M(\rho_{\mathsf{T}}) = 290$ GeV as suggested in Ref [51] was investigated, but no obvious deviation is observed. Finally this selection was used to set an exclusion on the production of TC particles for $M(a_{\mathsf{T}}) > 265$ GeV in this final state.

This search can be improved following different approaches. The systematic uncertainties should be studied more carefully, in particular the estimation of ISR/FSR and PDF effects can be estimated with a better accuracy by reproducing signal samples with these settings changed. Systematic uncertainties can also be investigated in the Standard Model backgrounds. However due to the small impact of systematic uncertainties on the final result, gains in this direction will be limited.

The statistics available for the SM $W\gamma$ sample should be increased in the signal region of this analysis, for a better understanding of this background. The AlpGen and Sherpa differences can also be investigated.

The final analysis optimization cuts can be obtained separately for each LSTC mass scenario in order to increase the significance, and extends the limits.

Due to the small production rate of LSTC processes, the largest improvement will come from analyzing more data. For the ATLAS experiments, moving to the full 2011 dataset should give a factor 2.5 increase in integrated luminosity, using the $W \to \mu\nu$ decay could add another factor 2. If the same search was conducted in CMS, the statistics can be also multiplied by a factor two directly. At the end of 2012, one could also expect an increase of luminosity up to $15-20$ fb^{-1}, which represents almost 3 to 4 times what was acquired in 2011. Using the 2012 datasets should allow to be sensitive to the production of technihadrons up to $M(a_{\mathsf{T}}) \approx 500$ GeV.

Conclusion

"Pour conclure, voici la conséquence
de tout ce qui vient d'être dit."
Nicolas Machiavel, *Le Prince.*

Since the restart of the LHC in 2009, the accumulated dataset has increased from 50 pb^{-1} to almost 5 fb^{-1} at the end of 2011. The LHC is performing extremely well providing lots of data used to understand the detector and to perform physics analysis.

For the experiments it is crucial that the data taken respects quality criteria, to avoid "*discovering new physics*" due to detector effects. In the third Chapter of this thesis, it was explained why it is important to have reliable monitoring that allows to identify quickly the problems and fix them. The monitoring that was developed during my thesis allows in particular to performed a few basics checks that allows to trust the energy, timing and quality factor reconstruction of the Calorimeter cells.

For the physics analysis it is crucial to have a good understanding of the impact of detector effects on physics object. In the fourth Chapter the energy resolution of the jets was estimated using two different data driven techniques, using pp collisions at $\sqrt{s} = 7$ TeV on the full 2010 dataset.

This study has shown that in 2010, the Monte Carlo was underestimating the energy resolution of the jets by a relative factor of about 10%. This discrepancy is not yet understood and still under investigation.

The method used to measure the jet energy resolution was then applied to evaluate the impact of the LAr calorimeter reduced HV regions. The impact of the reduced HV region was found to be negligible. For jets produced with a rapidity $|y| < 0.8$, the increase of energy resolution due to the HV reduction, is evaluated at less than 3% for a $p_{\text{T}} = 30$ GeV jet and less than 0.1% for $p_{\text{T}} > 500$ GeV.

Finally, a search for narrow resonances on the $W\gamma$ final state was conducted. The standard model backgrounds contributing to this final state were estimated from Monte Carlo and from data. In particular, the QCD multi-jet and W+jets backgrounds normalization and shape were estimated using data driven techniques. The SM $W\gamma$ normalization was estimated from data, its shape from Monte Carlo. The other electroweak backgrounds were estimated from Monte Carlo.

Using this modeling of the SM backgrounds, the analysis was conducted blindly with respect to the invariant mass of the $W\gamma$ system. The data Monte Carlo agreement was checked and found to be in good agreement in two different control regions, close to that of the signal. The signal selection was optimized in order to distinguish the SM background from an eventual signal peak. The optimization was found to be $p_{\text{T}}(\gamma) > 50$ GeV and $p_{\text{T}}(W) > 30$ GeV.

The $W\gamma$ invariant mass was finally un-blinded in the signal region. A good agreement between data and the SM backgrounds modeling was found. The search was then conducted on the data. No significant excess from the Standard Model predictions was observed in the $W\gamma$ mass spectrum for TechniColor masses in the range [220,440] GeV. The most important excess observed was seen at $M(a_{\text{T}}) = 329$ GeV with a significance of 0.71σ.

The hypothesis of signal at $M(\rho_{\mathsf{T}}) = 290$ GeV as suggested in Ref [51] was investigated, but no obvious deviation was observed. Finally this selection was used to set an exclusion on the production of TC particles for $M(a_{\mathsf{T}}) > 265$ GeV, in this final state. This limit can be expressed in term the ρ_{T} masses and is found to be $M(\rho_{\mathsf{T}}) > 243$ GeV, it is in good agreement with the limits sets by the ATLAS collaboration in the dilepton channel, since the production of the ρ_{T} was excluded up to to almost $M(\rho_{\mathsf{T}}) = 450$ GeV [46].

Appendix A

Appendix to the jet energy resolution

A.1 Trigger menu used

The full trigger menu used on this analysis is summarized in table A.1. It is the one used for the performances studies by the ATLAS jet group in 2010 [138].

In this table L1_MBTS, is the level one minimum bias trigger scintillator [66]. It is a trigger composed of scintillating tiles placed on the LAr end-caps cryostat, used to trigger minimum bias events. ZDC, is the Zero Degree Calorimeter, it's a forward calorimeter placed at 140 m from the ATLAS detector [139].

The L1_JXX and L1_2JXX trigger items are level one jet triggers. Finally the EF_JXX and EF_2JXX triggers items are Event Filter jet trigger items. The XX represent the threshold above which the calorimeter trigger is accepted.

For the Monte Carlo the last period selection was applied.

P_T bin	Run< 152777	Run $\geq$ 152777 - period F	Period G - Period I
(30,60)	L1_MBTS	L1_J5 OR ZDC	EF_j20 OR ZDC
(60,80)	L1_MBTS	L1_J10 OR L1_2J10	EF_j30 OR EF_2j30
		1 L1_J5 OR L1_2J5	EF_j20 OR EF_2j20
(80,110)	L1_MBTS	L1_J15 OR L1_2J15	EF_j35 OR EF_2j35
		1 L1_J10 OR L1_2J10	EF_j30 OR EF_2j30
(110,160)	L1_MBTS	L1_J30 OR L1_2J30	EF_j50 OR EF_2j50
		1 L1_J15 OR L1_2J15	EF_j35 OR EF_2j35
(160,210)	L1_MBTS	L1_J55 OR L1_2J55	EF_j75 OR EF_2j75
		L1_J30 OR L1_2J30	EF_j50 OR EF_2j50
(210,260)	L1_MBTS	L1_J55	EF_j95 OR EF_j75
(260,310)	L1_MBTS	L1_J55	L1_J95 OR L1_J75
>310	L1_MBTS	L1_J55	L1_J115

Table A.1: Calorimeter Trigger used to select the events in the jet resolution study.

A.2 Monte Carlo samples

The Monte Carlo samples were generated using PYTHIA, then events are passed in a Geant 4 simulation of the ATLAS Detector and reconstructed using the same chain as the data. The trigger selection described above is also applied.

The events are generated to obtain di-jet events, an upper and lower cut are applied on $\sqrt{s}$, to obtain a regular spectrum. The samples are merged using their production cross-sections.

Sample name	Cut on $\sqrt{s}$ (GeV)	Cross section
J1	$[17, 35]$	667 pb
J2	$[35, 70]$	41 pb
J3	$[70, 140]$	2.2 pb
J4	$[140, 280]$	87 nb
J5	$[280, 560]$	2.3 nb
J6	$[560, 1120]$	0.03 nb

Table A.2: MC samples used in the jet resolution study.

A.3 Di-jet balance resolution

A.3.1 Two jet in same resolution bin

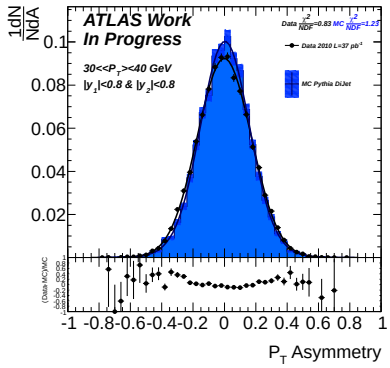

(a) $30 < \langle p_T \rangle < 40$ GeV

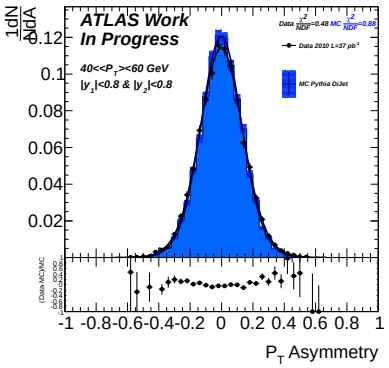

(b) $40 < \langle p_T \rangle < 60$ GeV

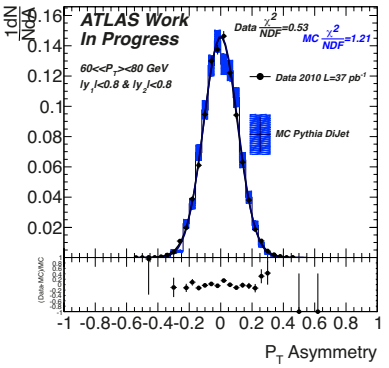

(c) $60 < \langle p_T \rangle < 80$ GeV

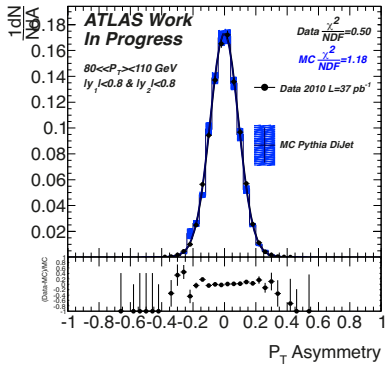

(d) $80 < \langle p_T \rangle < 110$ GeV

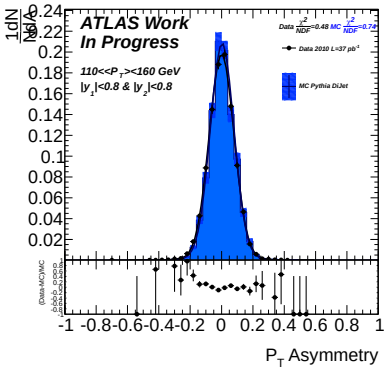

(e) $110 < \langle p_T \rangle < 160$ GeV

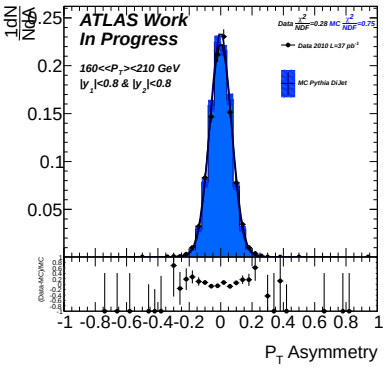

(f) $160 < \langle p_T \rangle < 210$ GeV

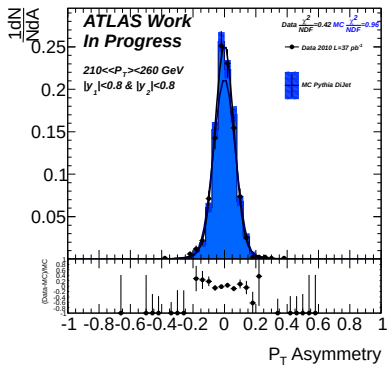

(g) $210 < \langle p_T \rangle < 260$ GeV

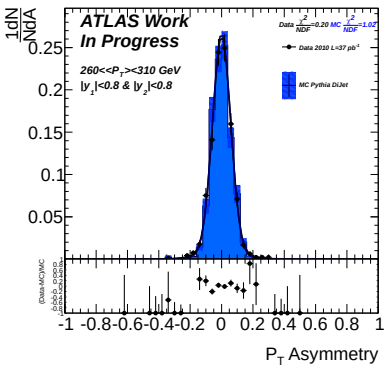

(h) $260 < \langle p_T \rangle < 310$ GeV

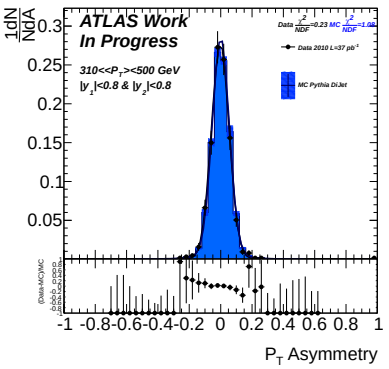

(i) $310 < \langle p_T \rangle < 500$ GeV

Figure A.1: Asymmetry distributions for the two jets in the bin $|y| < 0.8$.

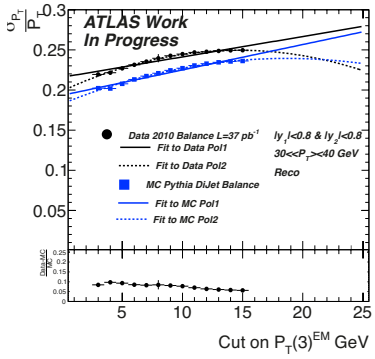

(a) $30 < \langle p_T \rangle < 40$ GeV

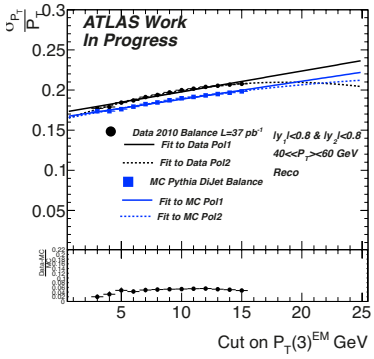

(b) $40 < \langle p_T \rangle < 60$ GeV

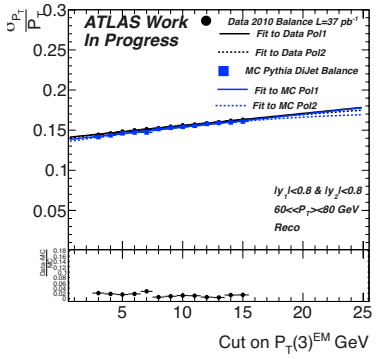

(c) $60 < \langle p_T \rangle < 80$ GeV

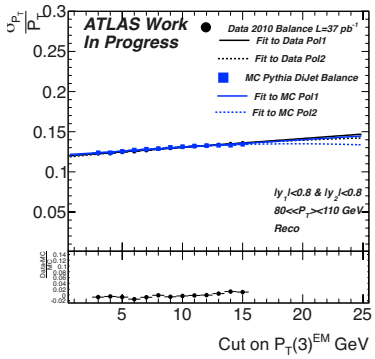

(d) $80 < \langle p_T \rangle < 110$ GeV

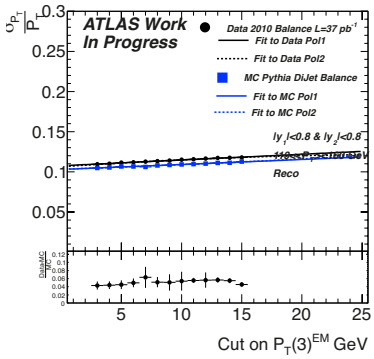

(e) $110 < \langle p_T \rangle < 160$ GeV

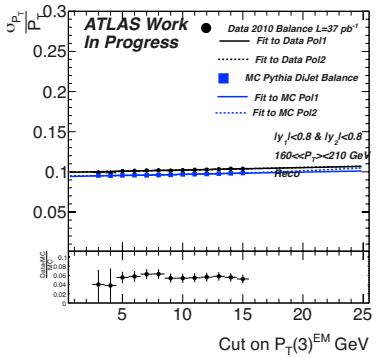

(f) $160 < \langle p_T \rangle < 210$ GeV

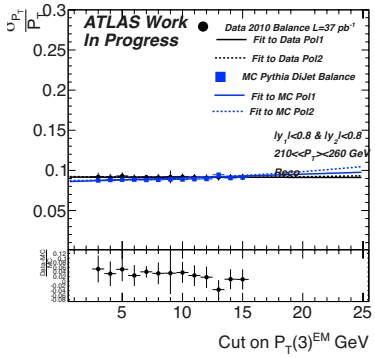

(g) $210 < \langle p_T \rangle < 260$ GeV

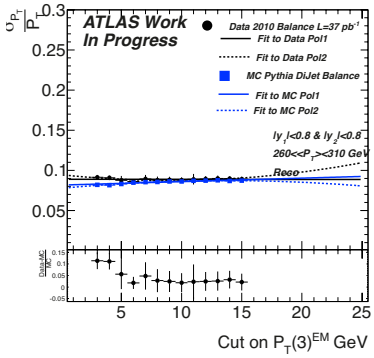

(h) $260 < \langle p_T \rangle < 310$ GeV

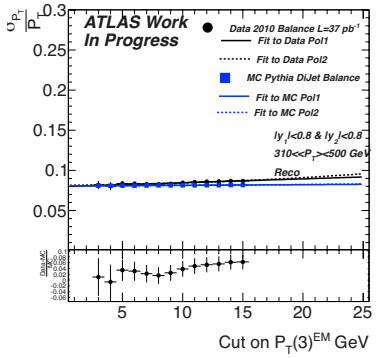

(i) $310 < \langle p_T \rangle < 500$ GeV

Figure A.2: Soft Radiation Effect for the two jets in the bin $|y| < 0.8$. Di-jet balance method.

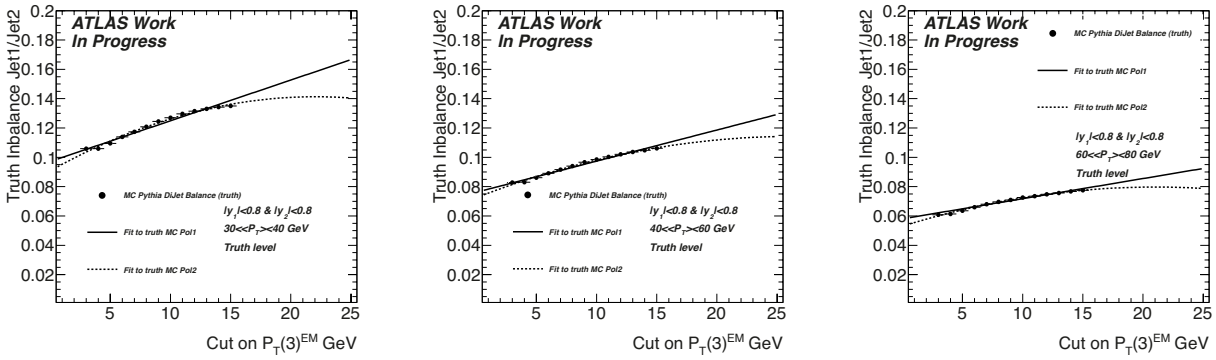

(a) $30 < \langle p_T \rangle < 40$ GeV (b) $40 < \langle p_T \rangle < 60$ GeV (c) $60 < \langle p_T \rangle < 80$ GeV

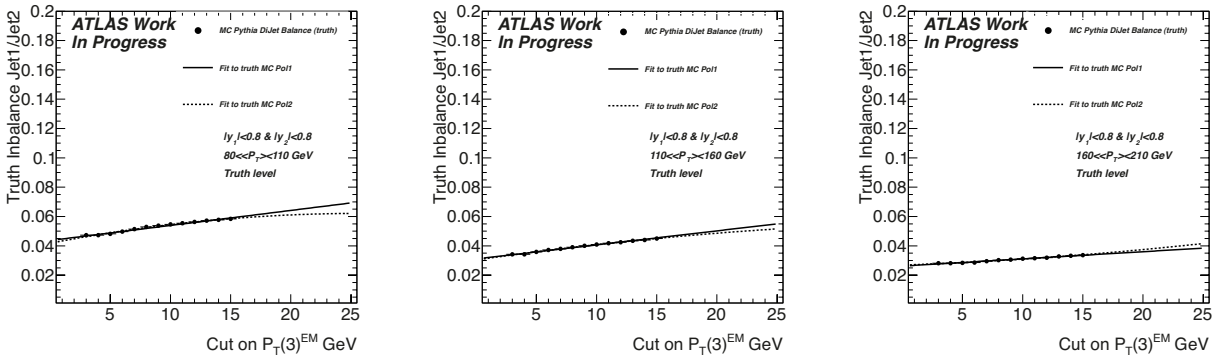

(d) $80 < \langle p_T \rangle < 110$ GeV (e) $110 < \langle p_T \rangle < 160$ GeV (f) $160 < \langle p_T \rangle < 210$ GeV

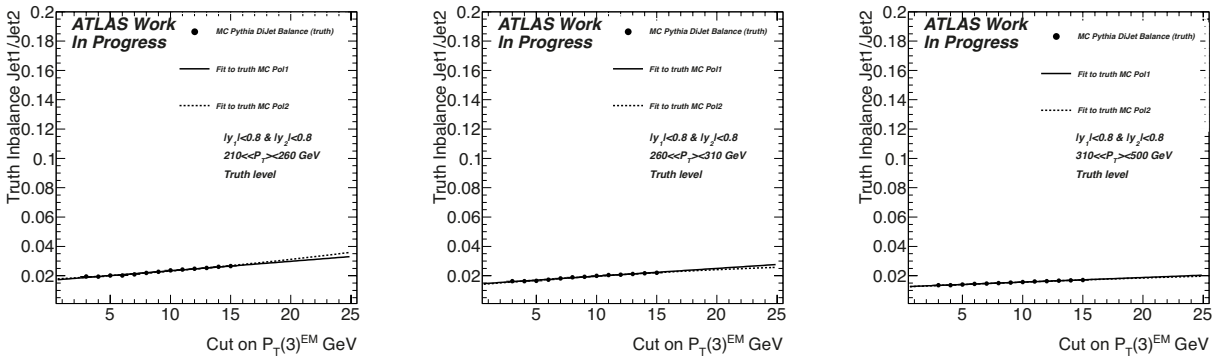

(g) $210 < \langle p_T \rangle < 260$ GeV (h) $260 < \langle p_T \rangle < 310$ GeV (i) $310 < \langle p_T \rangle < 500$ GeV

Figure A.3: Truth Soft Radiation Effect for the two jets in the bin $|y| < 0.8$. Di-jet balance method.

A.3.2 Two jet in different resolution bin

Tag and probe

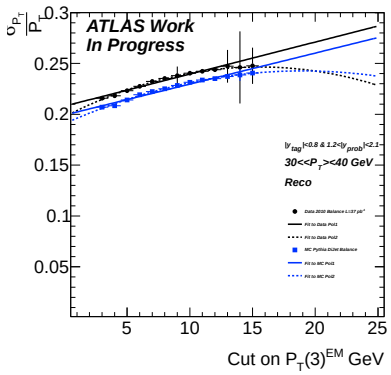

(a) $30 < \langle p_T \rangle < 40$ GeV

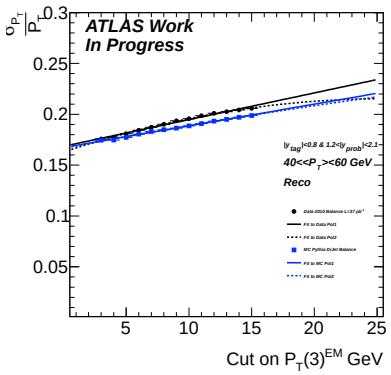

(b) $40 < \langle p_T \rangle < 60$ GeV

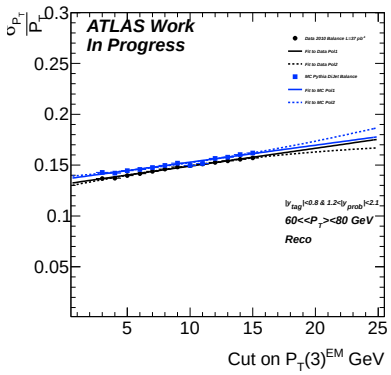

(c) $60 < \langle p_T \rangle < 80$ GeV

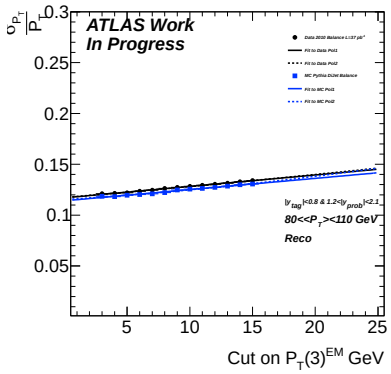

(d) $80 < \langle p_T \rangle < 110$ GeV

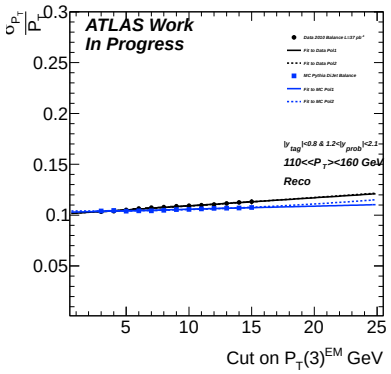

(e) $110 < \langle p_T \rangle < 160$ GeV

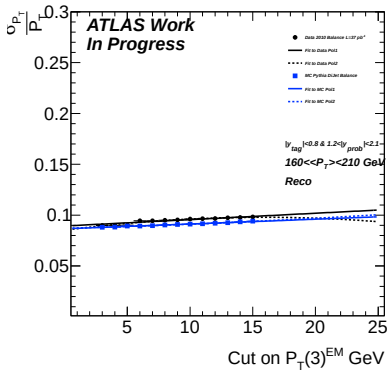

(f) $160 < \langle p_T \rangle < 210$ GeV

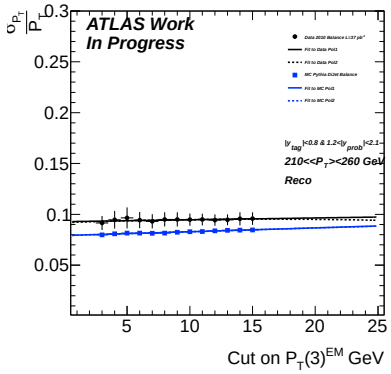

(g) $210 < \langle p_T \rangle < 260$ GeV

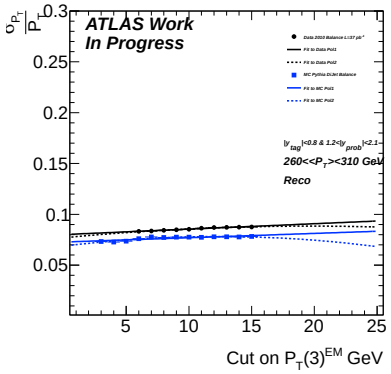

(h) $260 < \langle p_T \rangle < 310$ GeV

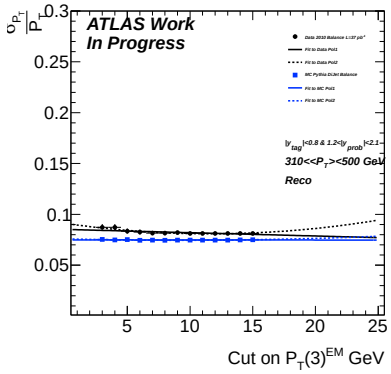

(i) $310 < \langle p_T \rangle < 500$ GeV

Figure A.4: Soft Radiation Effect for $|y_{tag}| < 0.8 \& 1.2 < |y_{probe}| < 2.1$. Di-jet balance method.

same bin

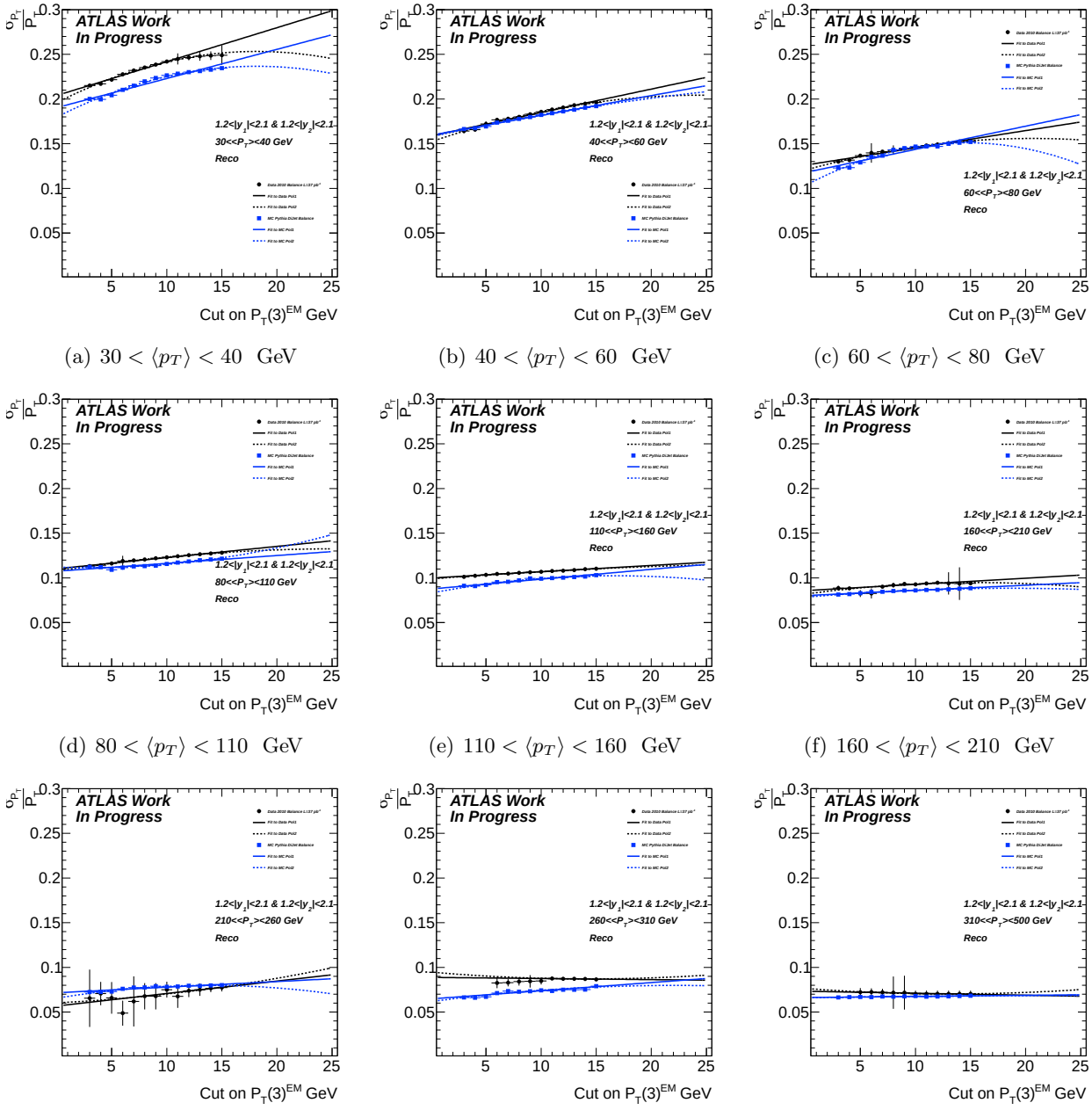

(a) $30 < \langle p_T \rangle < 40$ GeV (b) $40 < \langle p_T \rangle < 60$ GeV (c) $60 < \langle p_T \rangle < 80$ GeV

(d) $80 < \langle p_T \rangle < 110$ GeV (e) $110 < \langle p_T \rangle < 160$ GeV (f) $160 < \langle p_T \rangle < 210$ GeV

(g) $210 < \langle p_T \rangle < 260$ GeV (h) $260 < \langle p_T \rangle < 310$ GeV (i) $310 < \langle p_T \rangle < 500$ GeV

Figure A.5: Soft Radiation Effect for two jets in $1.2 < |y| < 2.1$. Di-jet balance method.

A.3.3 After-Before PS HV reduction

After

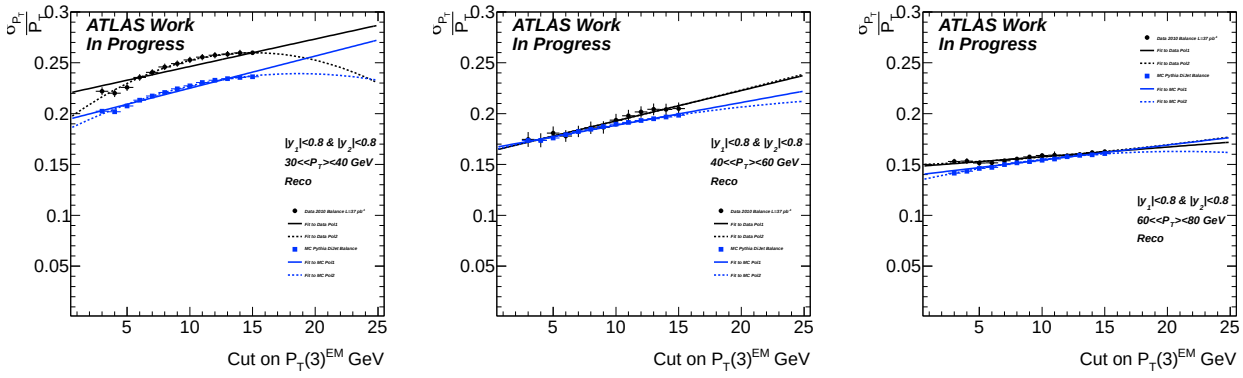

(a) $30 < \langle p_T \rangle < 40$ GeV (b) $40 < \langle p_T \rangle < 60$ GeV (c) $60 < \langle p_T \rangle < 80$ GeV

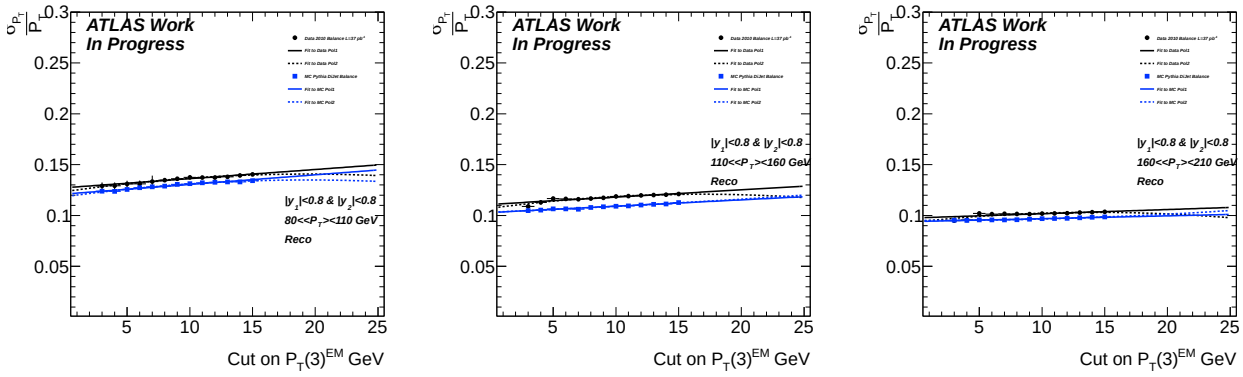

(d) $80 < \langle p_T \rangle < 110$ GeV (e) $110 < \langle p_T \rangle < 160$ GeV (f) $160 < \langle p_T \rangle < 210$ GeV

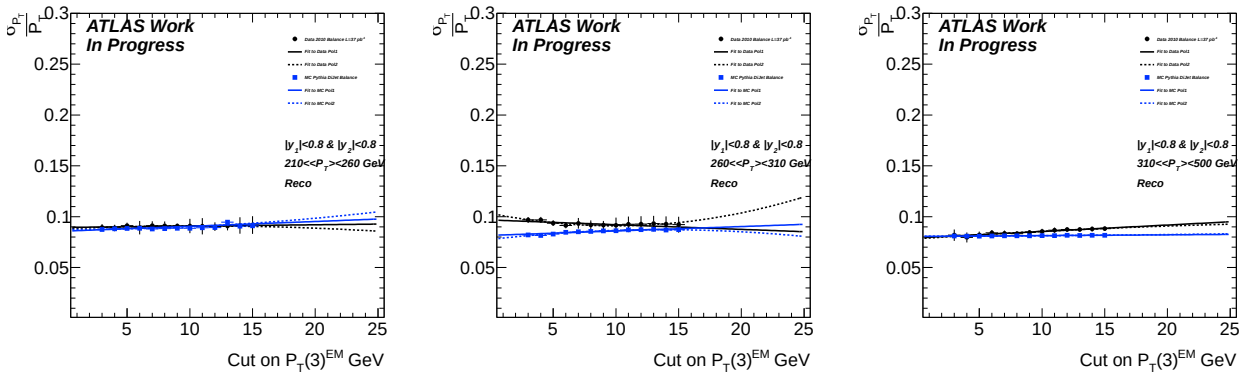

(g) $210 < \langle p_T \rangle < 260$ GeV (h) $260 < \langle p_T \rangle < 310$ GeV (i) $310 < \langle p_T \rangle < 500$ GeV

Figure A.6: Soft Radiation Effect for two jets in $|y| < 0.8$. After PS HV reduction. Di-jet balance method.

Before

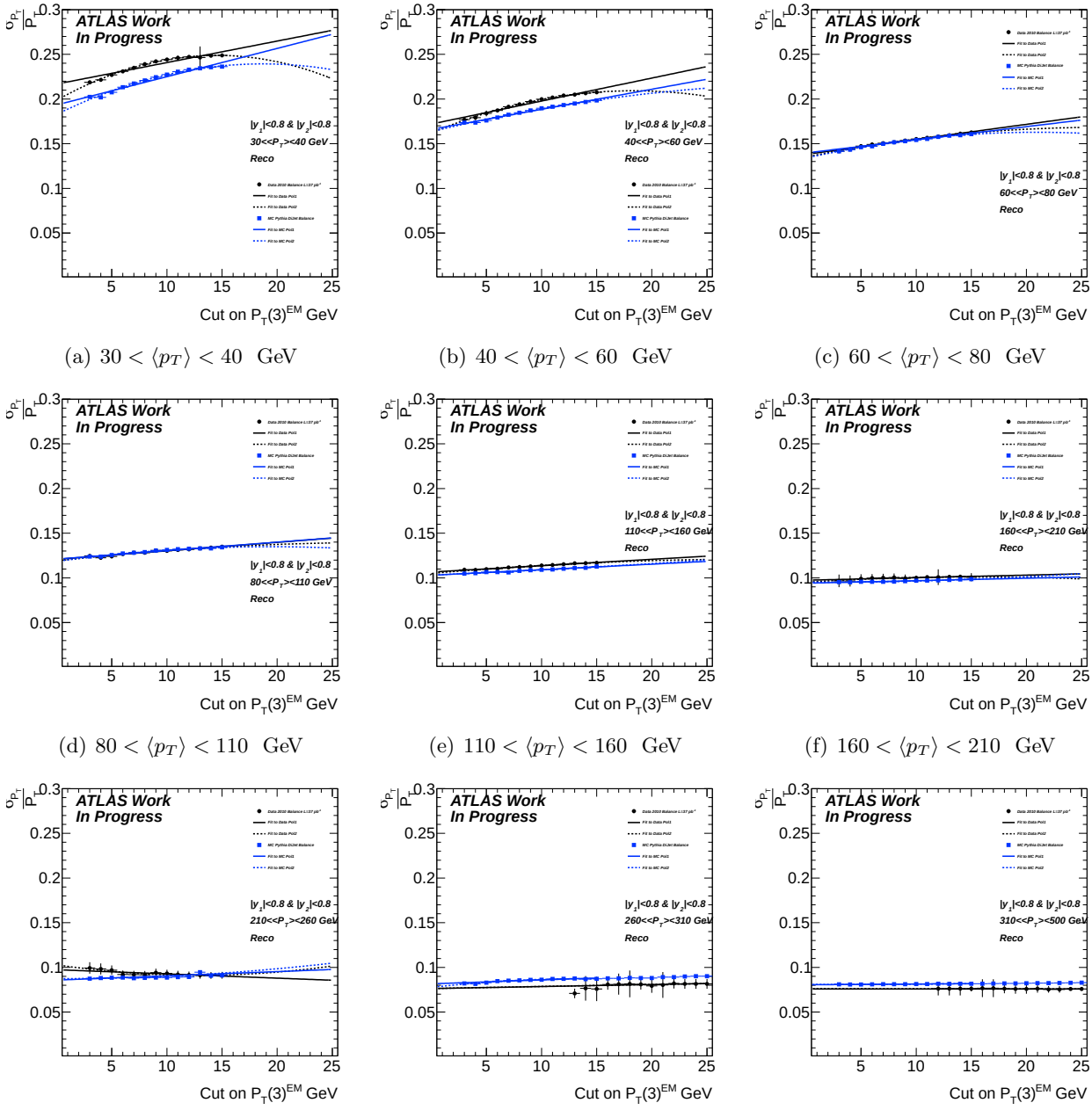

(a) $30 < \langle p_T \rangle < 40$ GeV (b) $40 < \langle p_T \rangle < 60$ GeV (c) $60 < \langle p_T \rangle < 80$ GeV

(d) $80 < \langle p_T \rangle < 110$ GeV (e) $110 < \langle p_T \rangle < 160$ GeV (f) $160 < \langle p_T \rangle < 210$ GeV

(g) $210 < \langle p_T \rangle < 260$ GeV (h) $260 < \langle p_T \rangle < 310$ GeV (i) $310 < \langle p_T \rangle < 500$ GeV

Figure A.7: Soft Radiation Effect for two jets in $|y| < 0.8$. Before PS HV reduction. Di-jet balance method.

A.3.4 HV trips

Two jets in clean areas

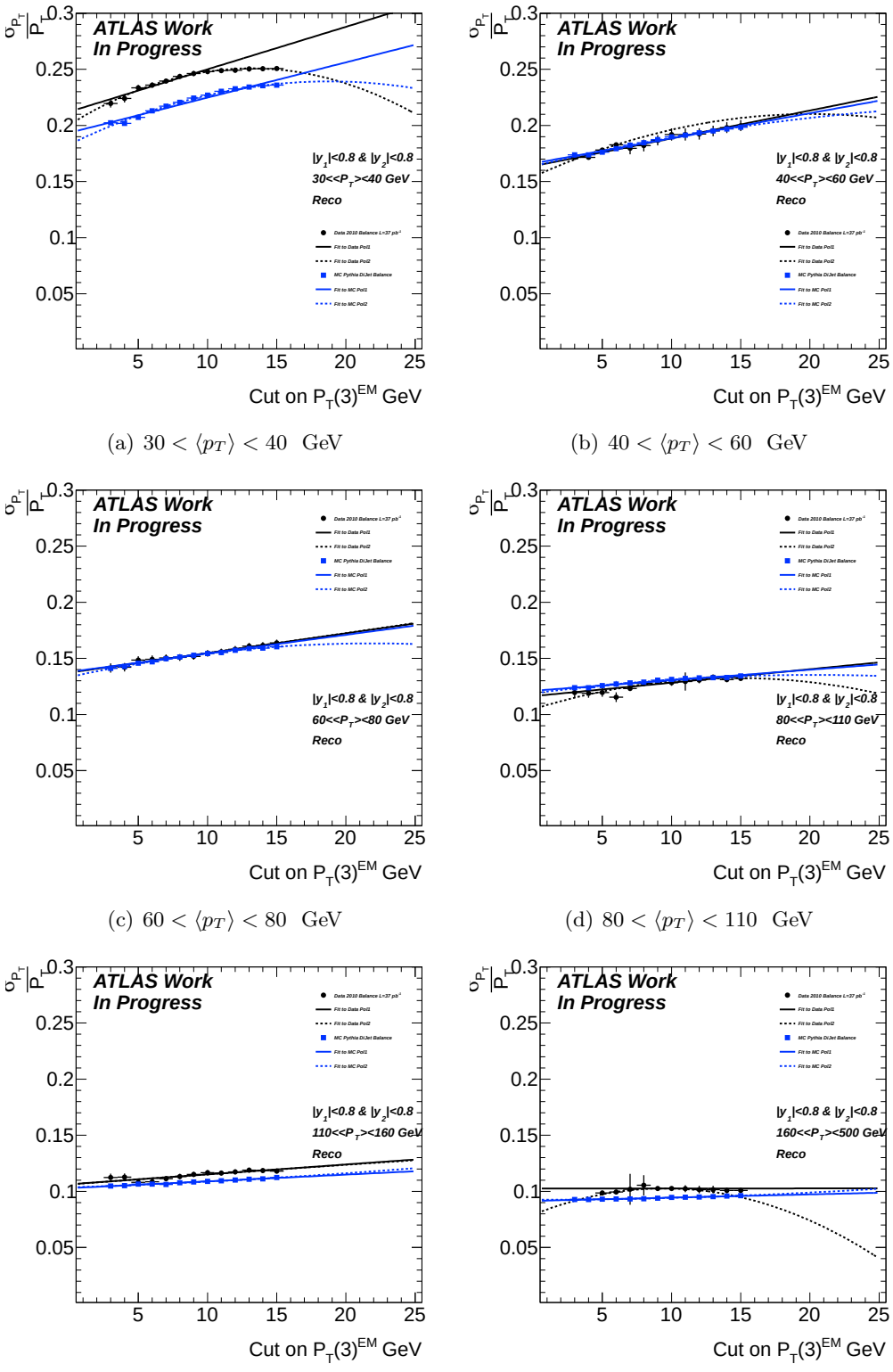

(a) $30 < \langle p_T \rangle < 40$ GeV

(b) $40 < \langle p_T \rangle < 60$ GeV

(c) $60 < \langle p_T \rangle < 80$ GeV

(d) $80 < \langle p_T \rangle < 110$ GeV

(e) $110 < \langle p_T \rangle < 160$ GeV

(f) $160 < \langle p_T \rangle < 500$ GeV

Figure A.8: Soft Radiation Effect for two jets in $|y| < 0.8$. Two jets in non affected HV area. Di-jet balance method.

Medium Affected

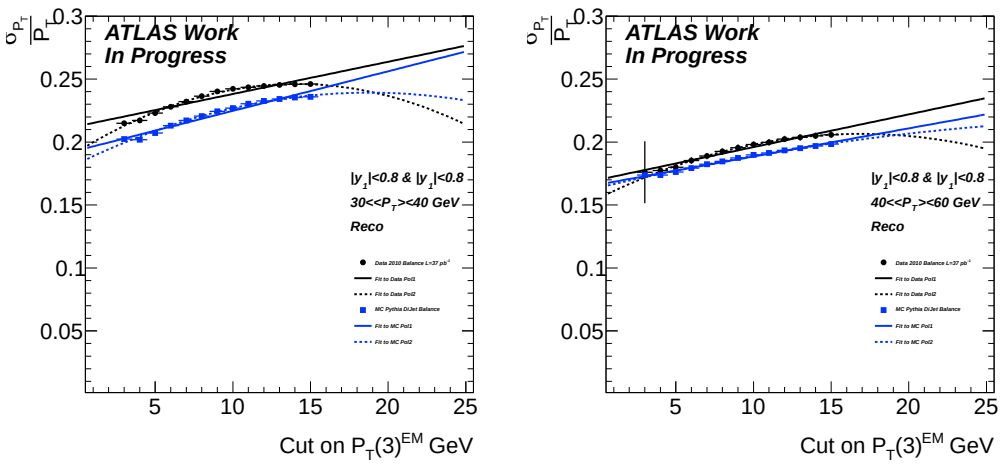

(a) $30 < \langle p_T \rangle < 40$ GeV

(b) $40 < \langle p_T \rangle < 60$ GeV

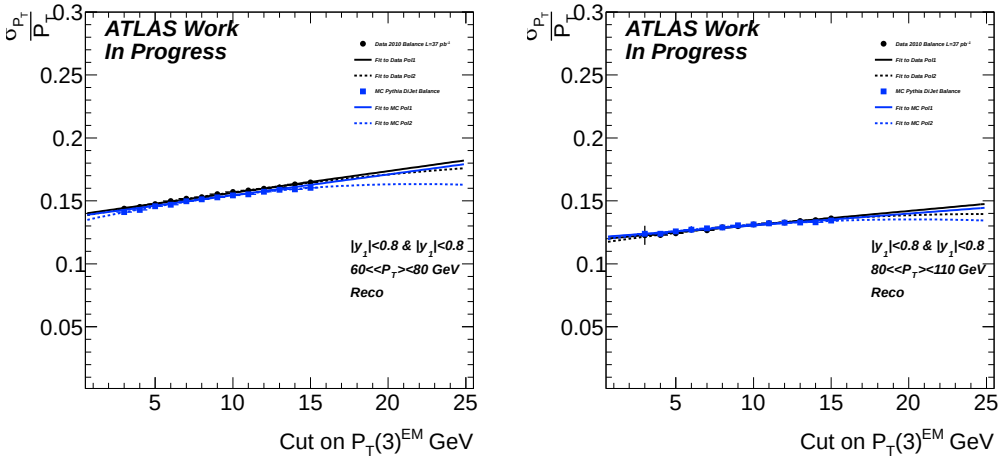

(c) $60 < \langle p_T \rangle < 80$ GeV

(d) $80 < \langle p_T \rangle < 110$ GeV

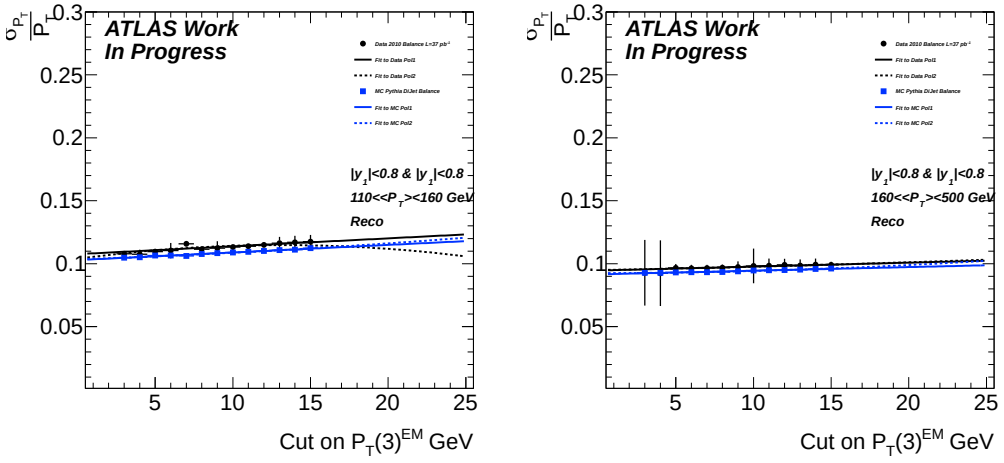

(e) $110 < \langle p_T \rangle < 160$ GeV

(f) $160 < \langle p_T \rangle < 500$ GeV

Figure A.9: Soft Radiation Effect for two jets in $|y| < 0.8$. Tag jet in non affected HV area, probe medium HV area. Di-jet balance method.

Affected

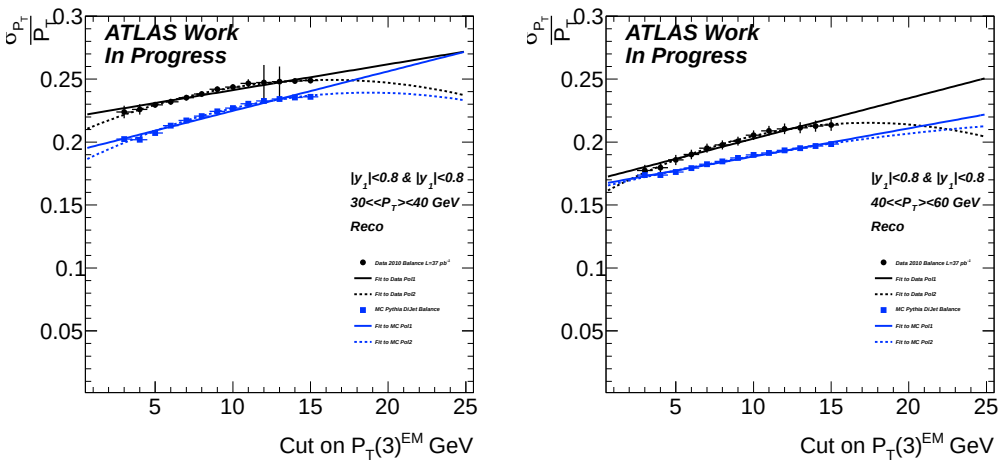

(a) $30 < \langle p_T \rangle < 40$ GeV

(b) $40 < \langle p_T \rangle < 60$ GeV

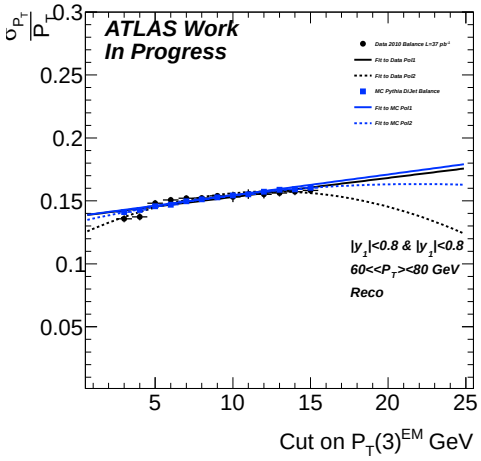

(c) $60 < \langle p_T \rangle < 80$ GeV

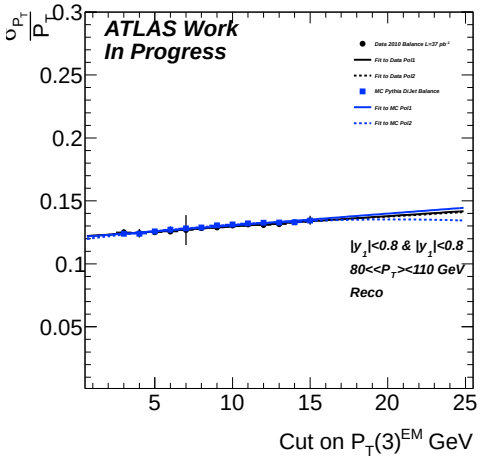

(d) $80 < \langle p_T \rangle < 110$ GeV

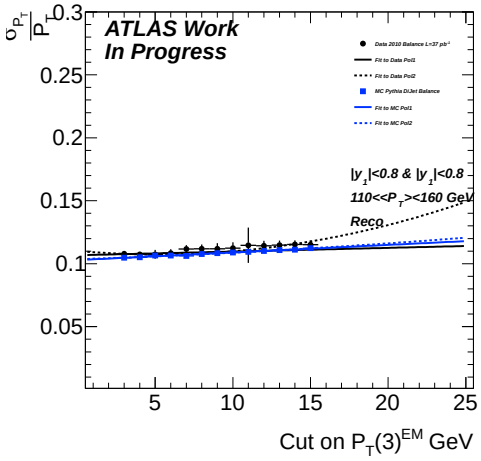

(e) $110 < \langle p_T \rangle < 160$ GeV

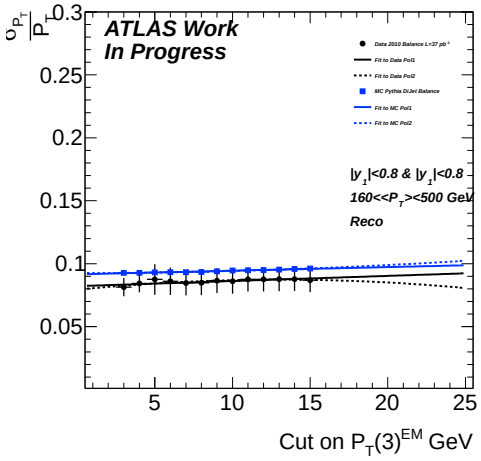

(f) $160 < \langle p_T \rangle < 500$ GeV

Figure A.10: Soft Radiation Effect for two jets in $|y| < 0.8$. Tag jet in non affected HV area, probe in HV area. Di-jet balance method.

A.4 Bisector technique resolution

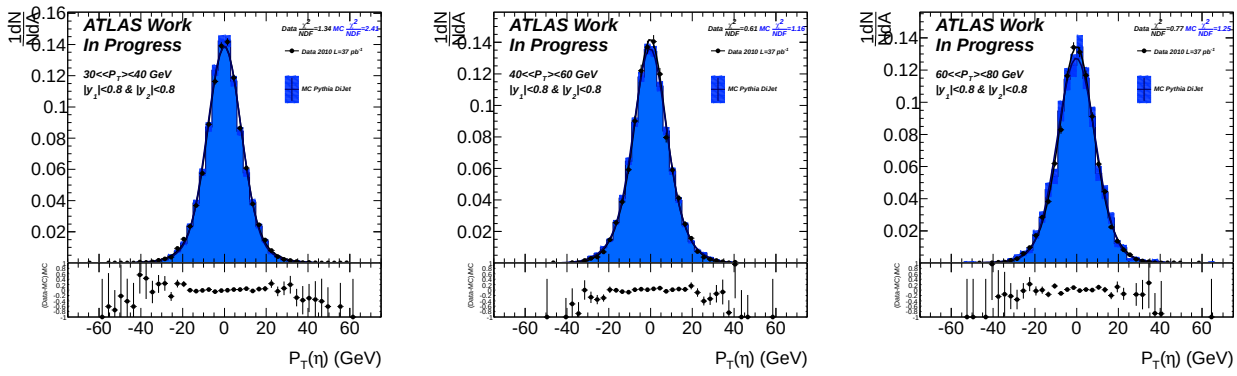

(a) $30 < \langle p_T \rangle < 40$ GeV

(b) $40 < \langle p_T \rangle < 60$ GeV

(c) $60 < \langle p_T \rangle < 80$ GeV

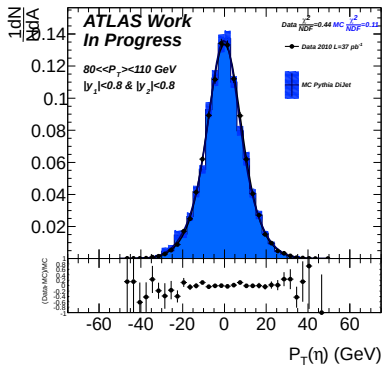

(d) $80 < \langle p_T \rangle < 110$ GeV

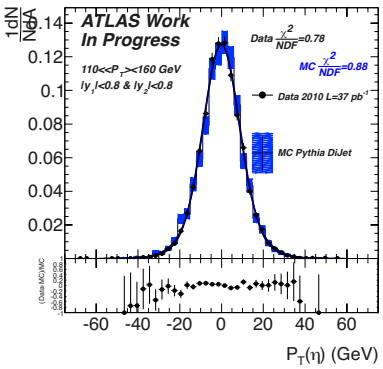

(e) $110 < \langle p_T \rangle < 160$ GeV

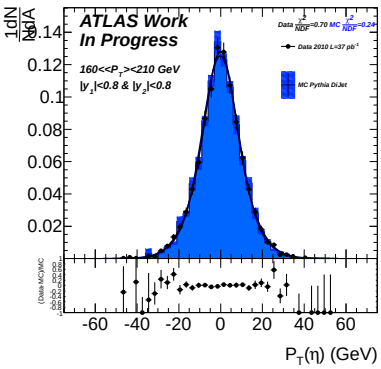

(f) $160 < \langle p_T \rangle < 210$ GeV

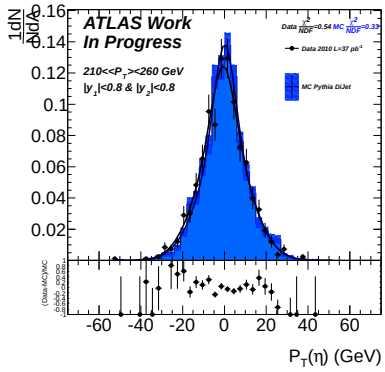

(g) $210 < \langle p_T \rangle < 260$ GeV

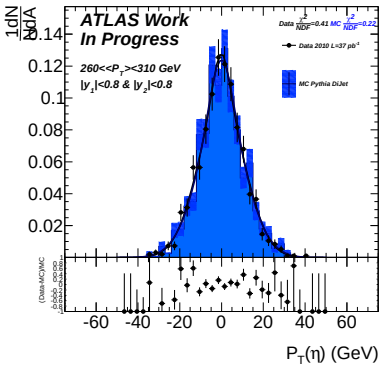

(h) $260 < \langle p_T \rangle < 310$ GeV

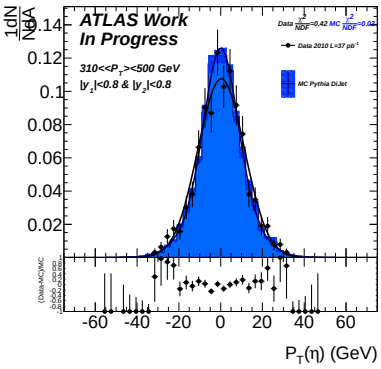

(i) $310 < \langle p_T \rangle < 500$ GeV

Figure A.11: $p_T(\eta)$ distributions for two jets in $|y| < 0.8$. Bisector Technique.

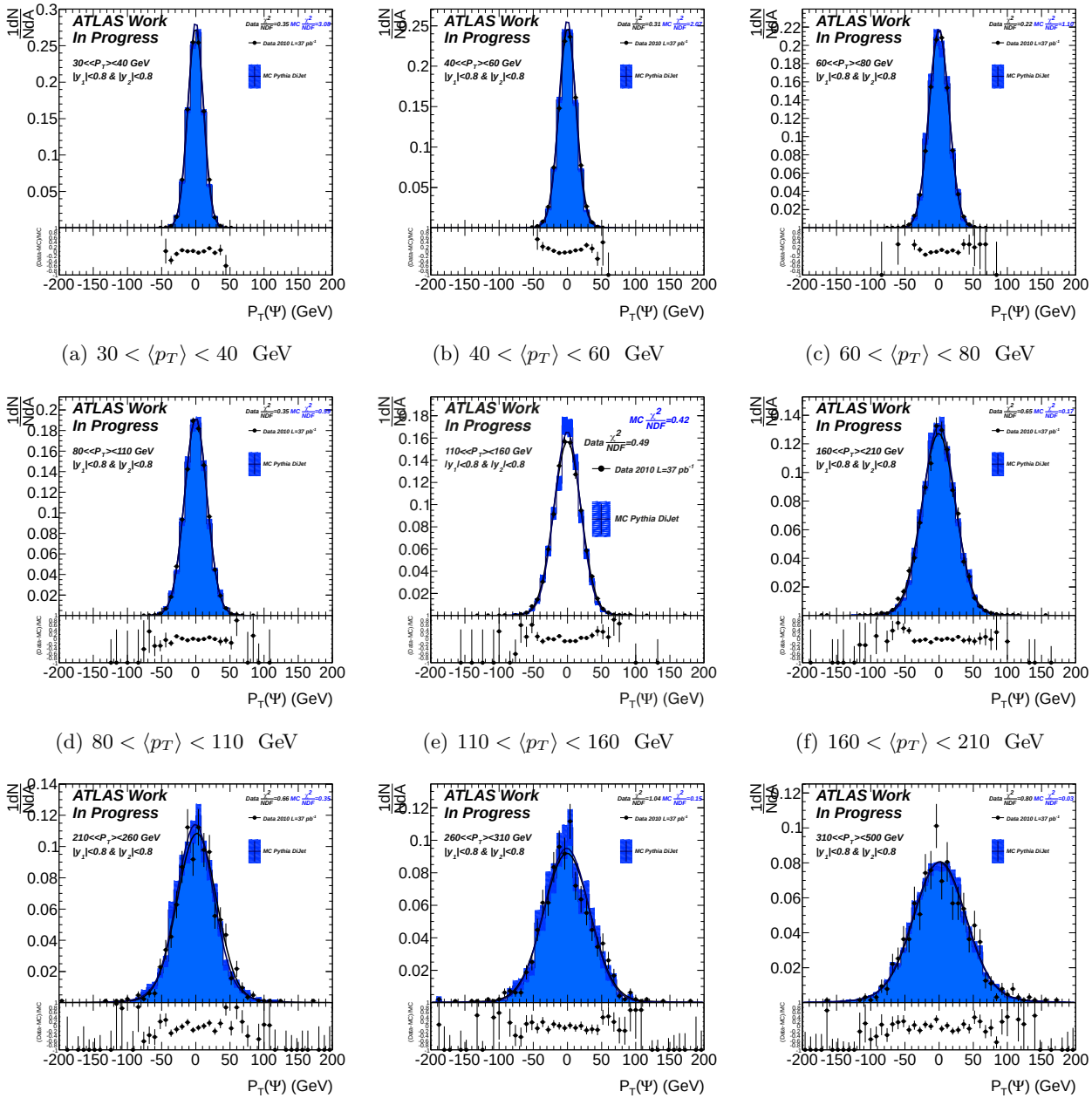

(a) $30 < \langle p_T \rangle < 40$ GeV (b) $40 < \langle p_T \rangle < 60$ GeV (c) $60 < \langle p_T \rangle < 80$ GeV

(d) $80 < \langle p_T \rangle < 110$ GeV (e) $110 < \langle p_T \rangle < 160$ GeV (f) $160 < \langle p_T \rangle < 210$ GeV

(g) $210 < \langle p_T \rangle < 260$ GeV (h) $260 < \langle p_T \rangle < 310$ GeV (i) $310 < \langle p_T \rangle < 500$ GeV

Figure A.12: $p_T(\psi)$ distributions for two jets in $|y| < 0.8$. Bisector Technique.

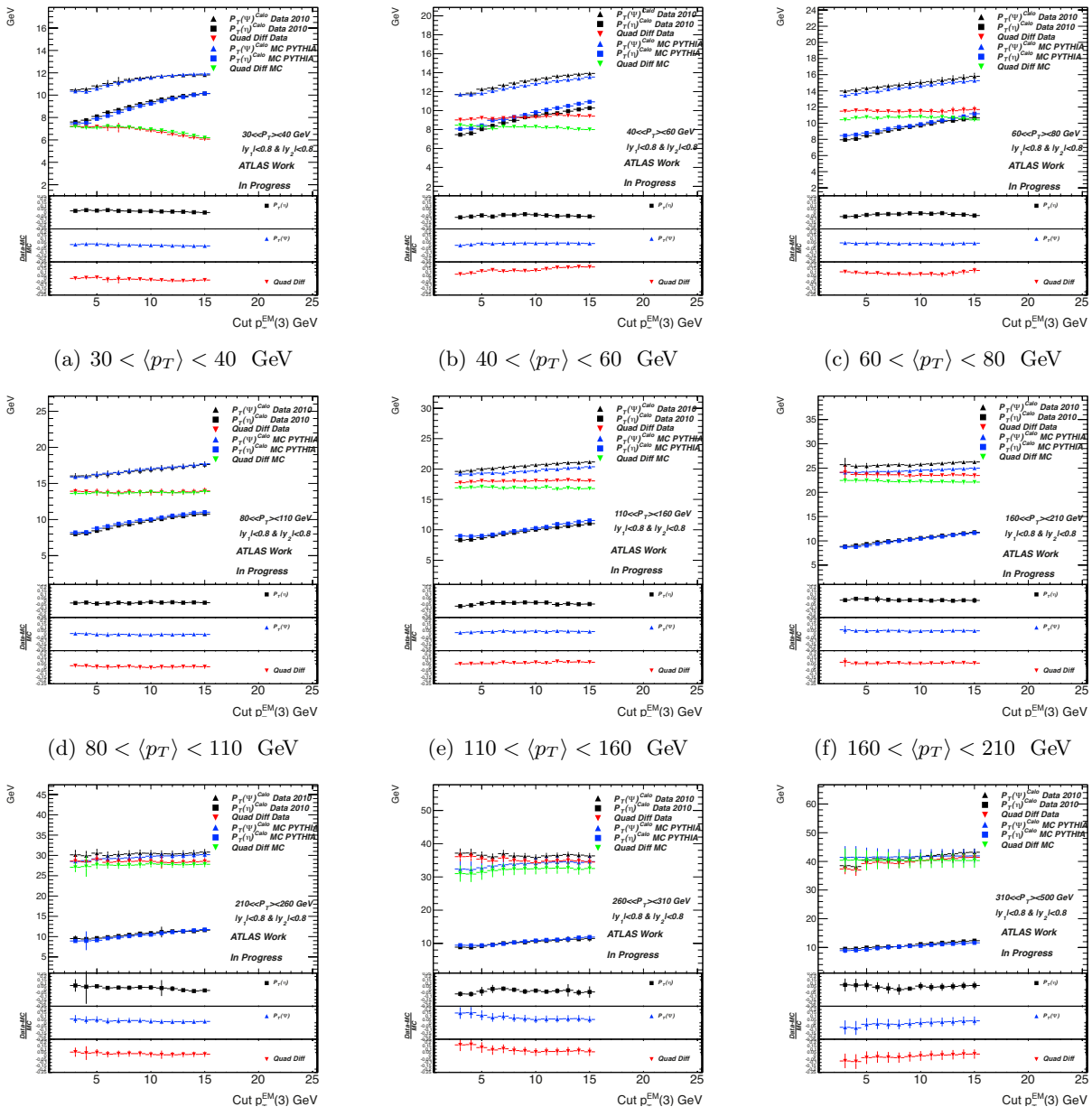

(a) $30 < \langle p_T \rangle < 40$ GeV (b) $40 < \langle p_T \rangle < 60$ GeV (c) $60 < \langle p_T \rangle < 80$ GeV

(d) $80 < \langle p_T \rangle < 110$ GeV (e) $110 < \langle p_T \rangle < 160$ GeV (f) $160 < \langle p_T \rangle < 210$ GeV

(g) $210 < \langle p_T \rangle < 260$ GeV (h) $260 < \langle p_T \rangle < 310$ GeV (i) $310 < \langle p_T \rangle < 500$ GeV

Figure A.13: Soft Radiation validation distributions for two jets in $|y| < 0.8$. Bisector Technique.

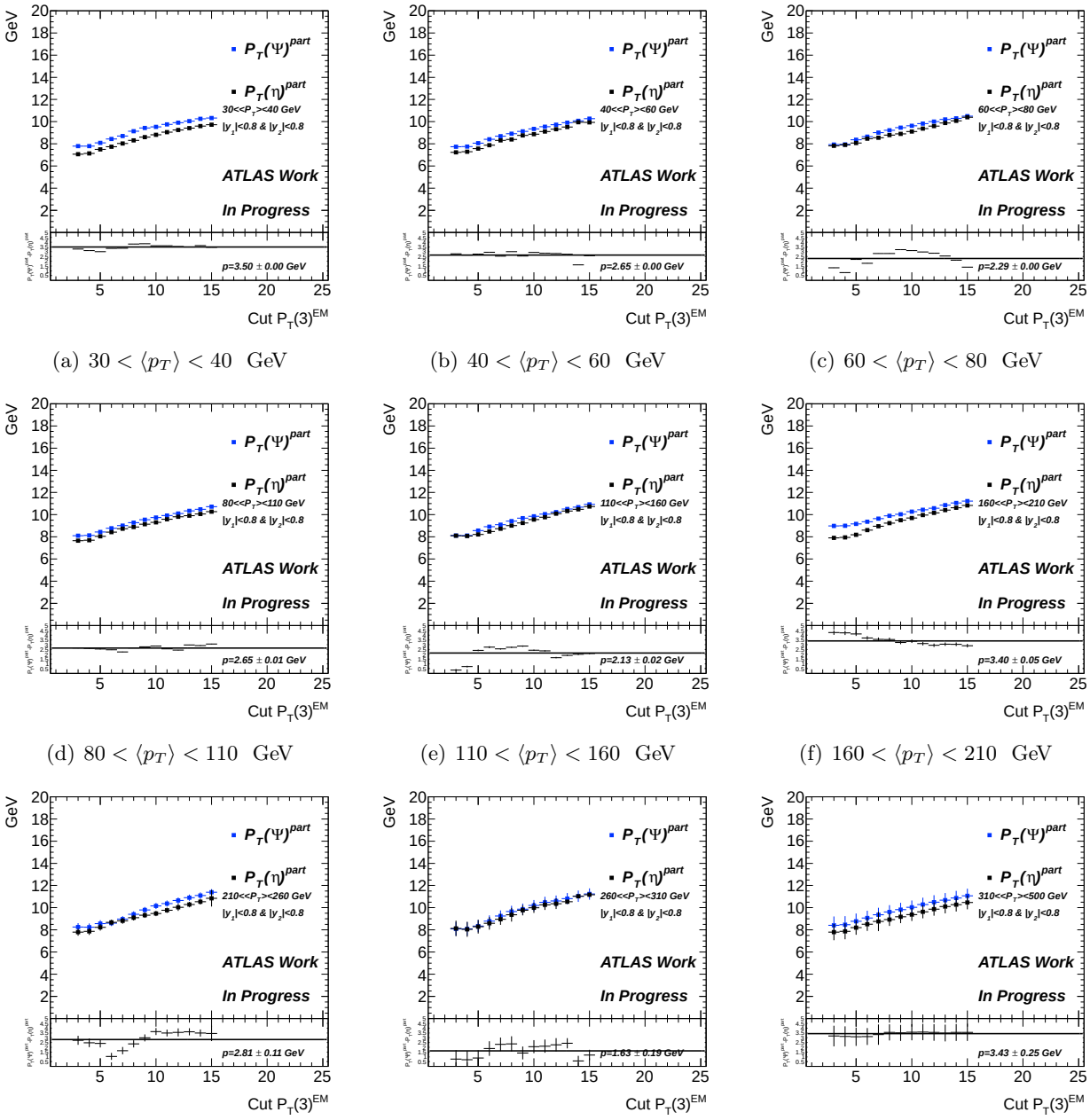

(a) $30 < \langle p_T \rangle < 40$ GeV (b) $40 < \langle p_T \rangle < 60$ GeV (c) $60 < \langle p_T \rangle < 80$ GeV

(d) $80 < \langle p_T \rangle < 110$ GeV (e) $110 < \langle p_T \rangle < 160$ GeV (f) $160 < \langle p_T \rangle < 210$ GeV

(g) $210 < \langle p_T \rangle < 260$ GeV (h) $260 < \langle p_T \rangle < 310$ GeV (i) $310 < \langle p_T \rangle < 500$ GeV

Figure A.14: Truth Soft Radiation validation distributions for two jets in $|y| < 0.8$. Bisector Technique.

A.4.1 Two jet in different resolution bin

Tag and probe

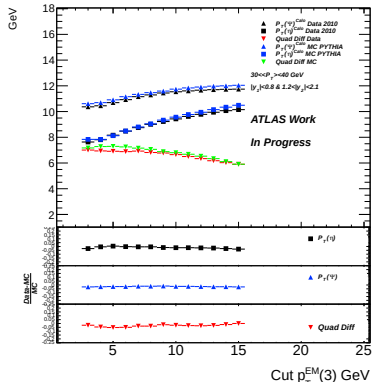

(a) $30 < \langle p_T \rangle < 40$ GeV

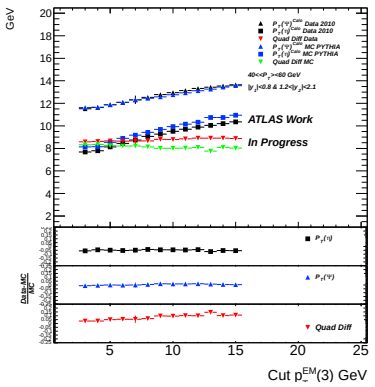

(b) $40 < \langle p_T \rangle < 60$ GeV

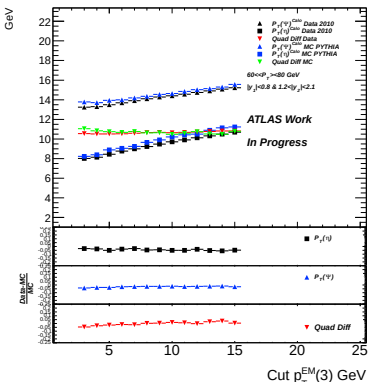

(c) $60 < \langle p_T \rangle < 80$ GeV

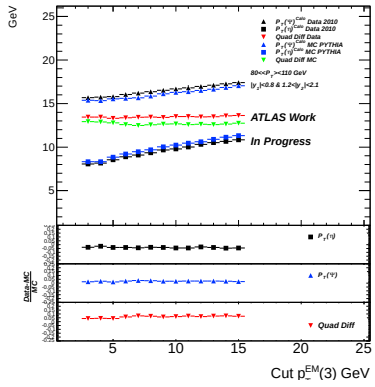

(d) $80 < \langle p_T \rangle < 110$ GeV

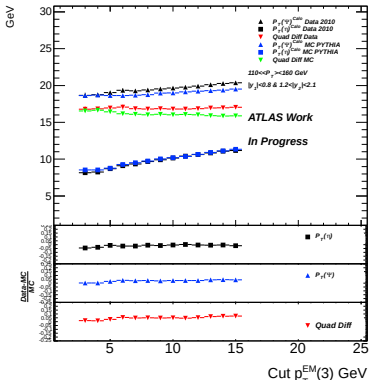

(e) $110 < \langle p_T \rangle < 160$ GeV

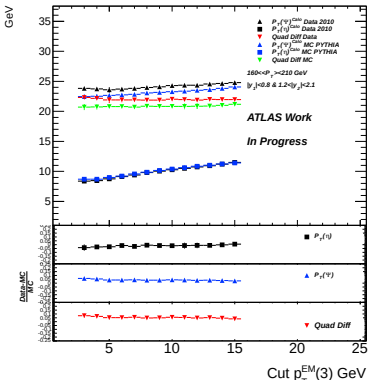

(f) $160 < \langle p_T \rangle < 210$ GeV

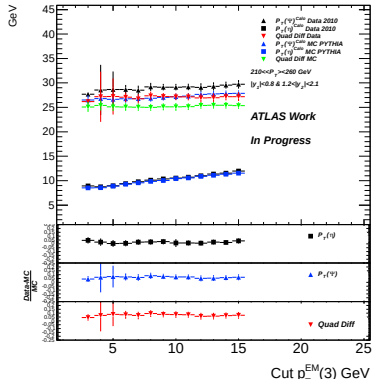

(g) $210 < \langle p_T \rangle < 260$ GeV

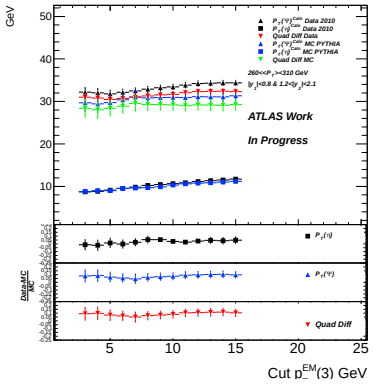

(h) $260 < \langle p_T \rangle < 310$ GeV

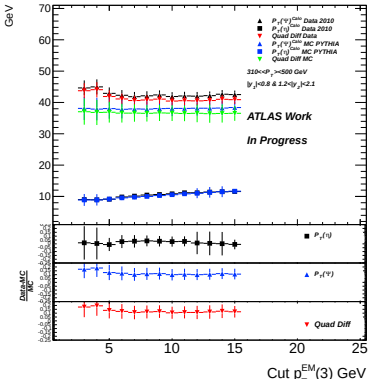

(i) $310 < \langle p_T \rangle < 500$ GeV

Figure A.15: Soft Radiation validation distributions for $|y_{tag}| < 0.8 \& 1.2 < |y_{probe}| < 2.1$. Bisector Technique.

same bin

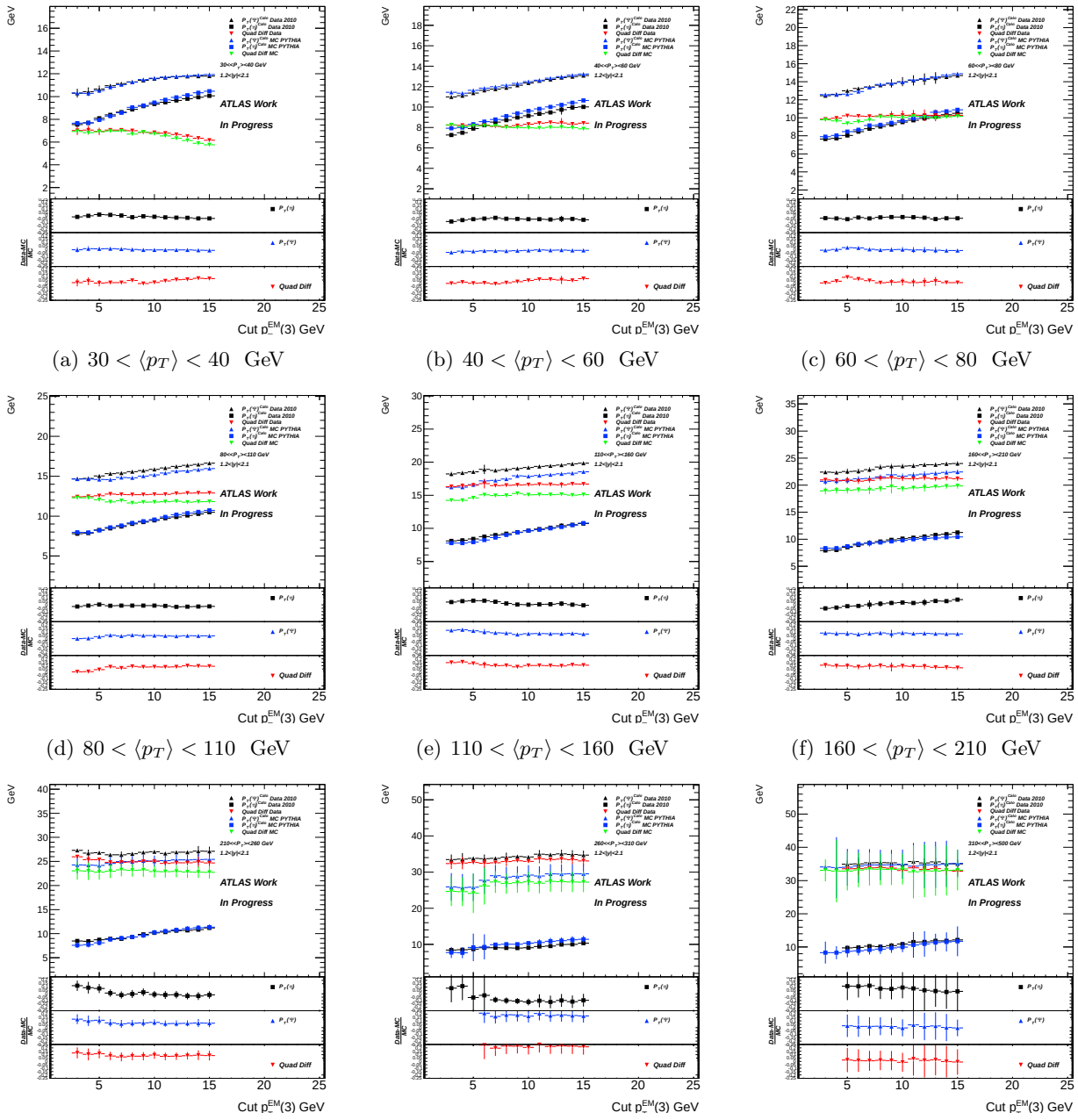

(a) $30 < \langle p_T \rangle < 40$ GeV (b) $40 < \langle p_T \rangle < 60$ GeV (c) $60 < \langle p_T \rangle < 80$ GeV

(d) $80 < \langle p_T \rangle < 110$ GeV (e) $110 < \langle p_T \rangle < 160$ GeV (f) $160 < \langle p_T \rangle < 210$ GeV

(g) $210 < \langle p_T \rangle < 260$ GeV (h) $260 < \langle p_T \rangle < 310$ GeV (i) $310 < \langle p_T \rangle < 500$ GeV

Figure A.16: Soft Radiation validation distributions for two jets in $1.2 < |y| < 2.1$. Bisector Technique.

A.4.2 After-Before PS HV reduction

After HV reduction

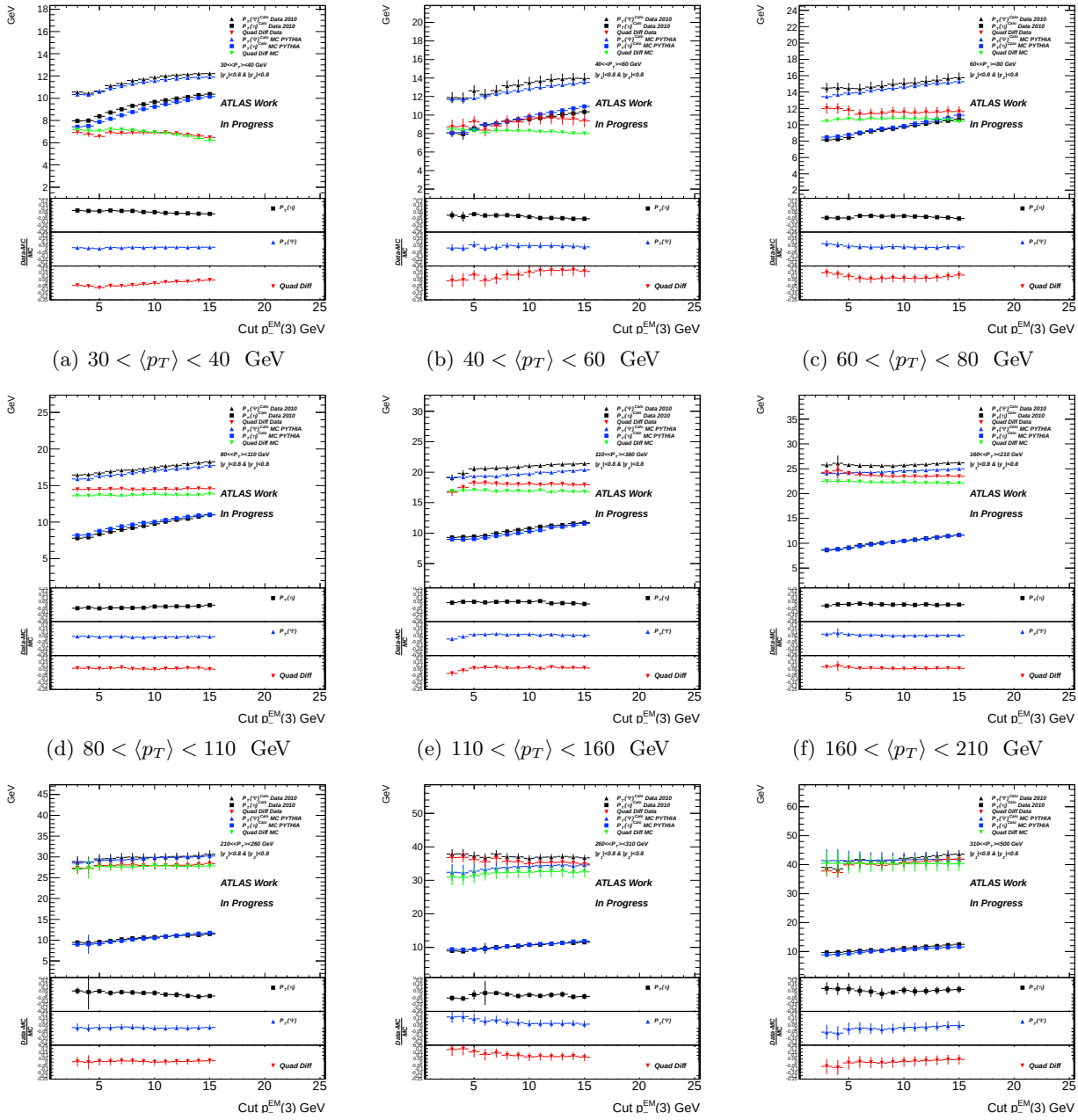

(a) $30 < \langle p_T \rangle < 40$ GeV (b) $40 < \langle p_T \rangle < 60$ GeV (c) $60 < \langle p_T \rangle < 80$ GeV

(d) $80 < \langle p_T \rangle < 110$ GeV (e) $110 < \langle p_T \rangle < 160$ GeV (f) $160 < \langle p_T \rangle < 210$ GeV

(g) $210 < \langle p_T \rangle < 260$ GeV (h) $260 < \langle p_T \rangle < 310$ GeV (i) $310 < \langle p_T \rangle < 500$ GeV

Figure A.17: Soft Radiation validation distributions for two jets in $|y| < 0.8$. After HV PS reduction. Bisector Technique.

Before HV reduction

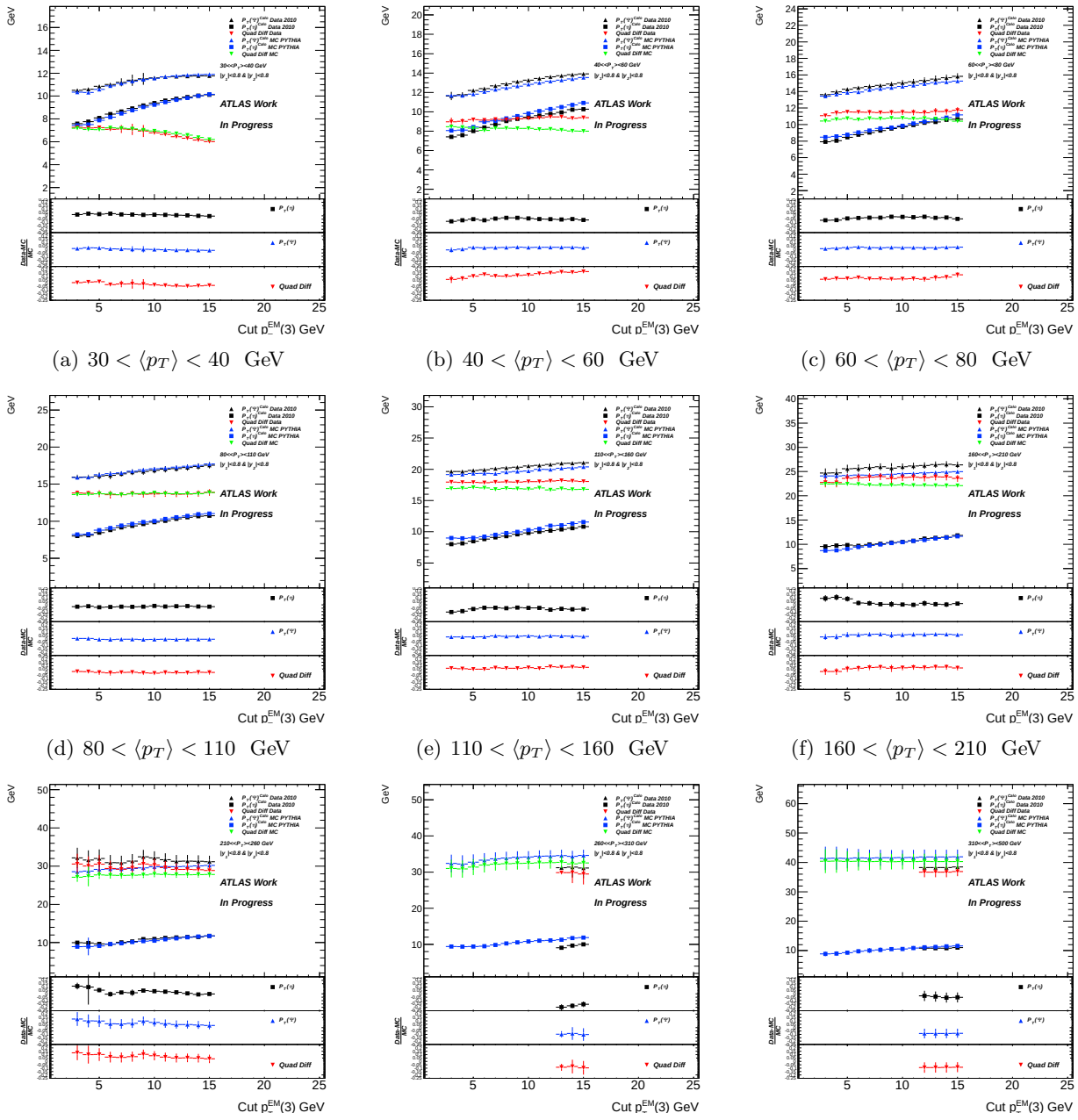

(a) $30 < \langle p_T \rangle < 40$ GeV (b) $40 < \langle p_T \rangle < 60$ GeV (c) $60 < \langle p_T \rangle < 80$ GeV

(d) $80 < \langle p_T \rangle < 110$ GeV (e) $110 < \langle p_T \rangle < 160$ GeV (f) $160 < \langle p_T \rangle < 210$ GeV

(g) $210 < \langle p_T \rangle < 260$ GeV (h) $260 < \langle p_T \rangle < 310$ GeV (i) $310 < \langle p_T \rangle < 500$ GeV

Figure A.18: Soft Radiation validation distributions for two jets in $|y| < 0.8$. Before HV PS reduction. Bisector Technique.

A.4.3 HV trips

Two jets in clean areas

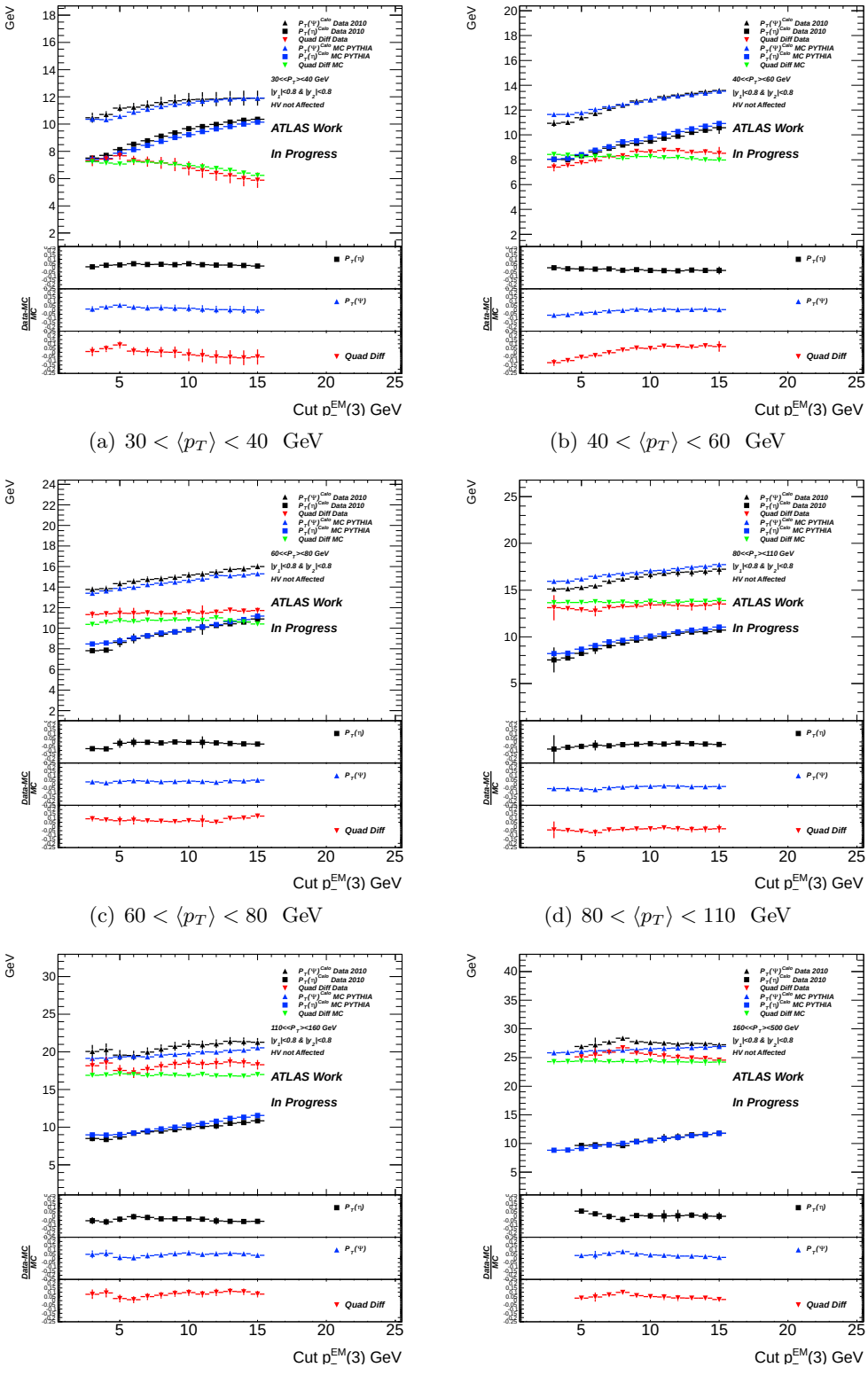

(a) $30 < \langle p_T \rangle < 40$ GeV

(b) $40 < \langle p_T \rangle < 60$ GeV

(c) $60 < \langle p_T \rangle < 80$ GeV

(d) $80 < \langle p_T \rangle < 110$ GeV

(e) $110 < \langle p_T \rangle < 160$ GeV

(f) $160 < \langle p_T \rangle < 500$ GeV

Figure A.19: Soft Radiation validation distributions for two jets in $|y| < 0.8$. Both jets in non affected area. Bisector Technique.

Medium Affected

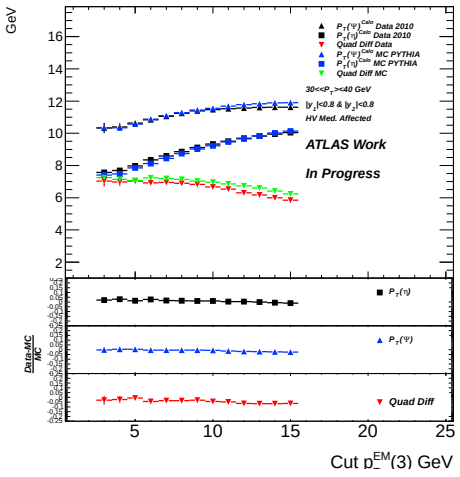

(a) $30 < \langle p_T \rangle < 40$ GeV

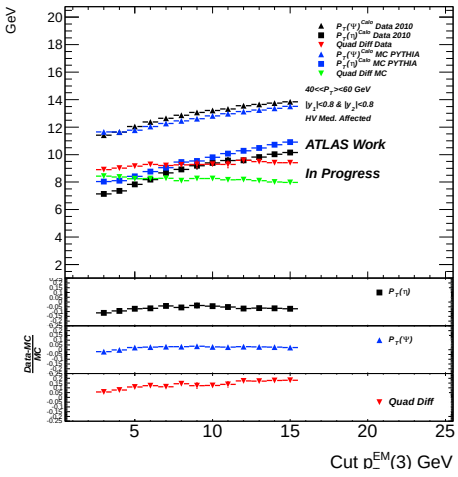

(b) $40 < \langle p_T \rangle < 60$ GeV

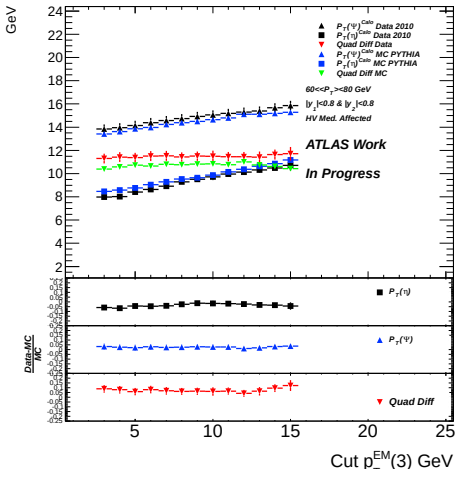

(c) $60 < \langle p_T \rangle < 80$ GeV

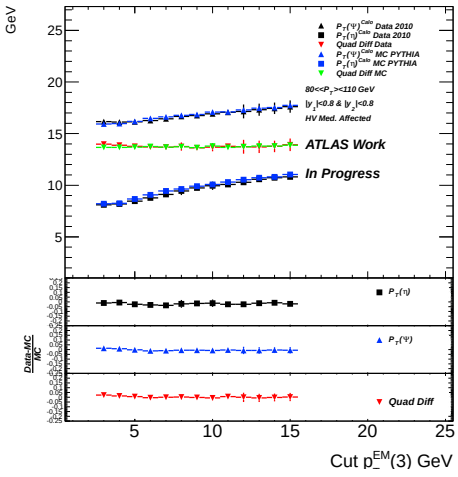

(d) $80 < \langle p_T \rangle < 110$ GeV

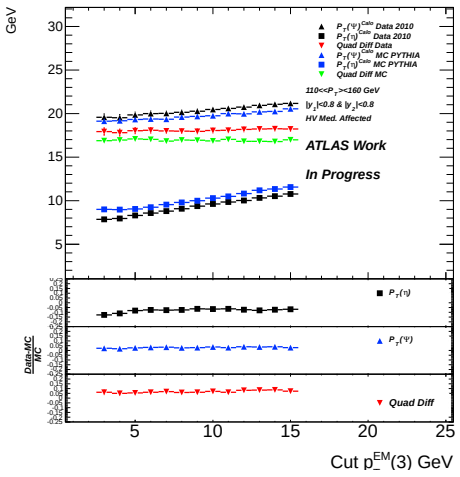

(e) $110 < \langle p_T \rangle < 160$ GeV

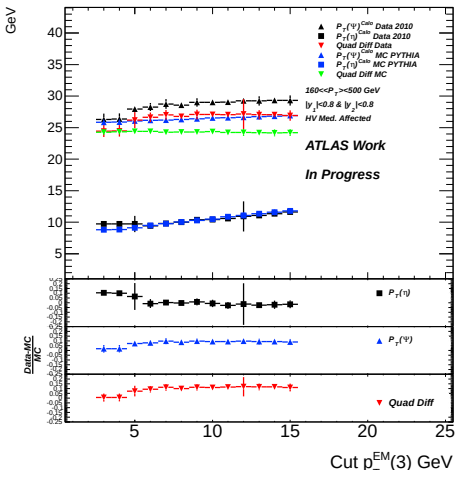

(f) $160 < \langle p_T \rangle < 500$ GeV

Figure A.20: Soft Radiation validation distributions for two jets in $|y| < 0.8$. Tag jet in non affected area, probe medium HV. Bisector Technique.

Affected

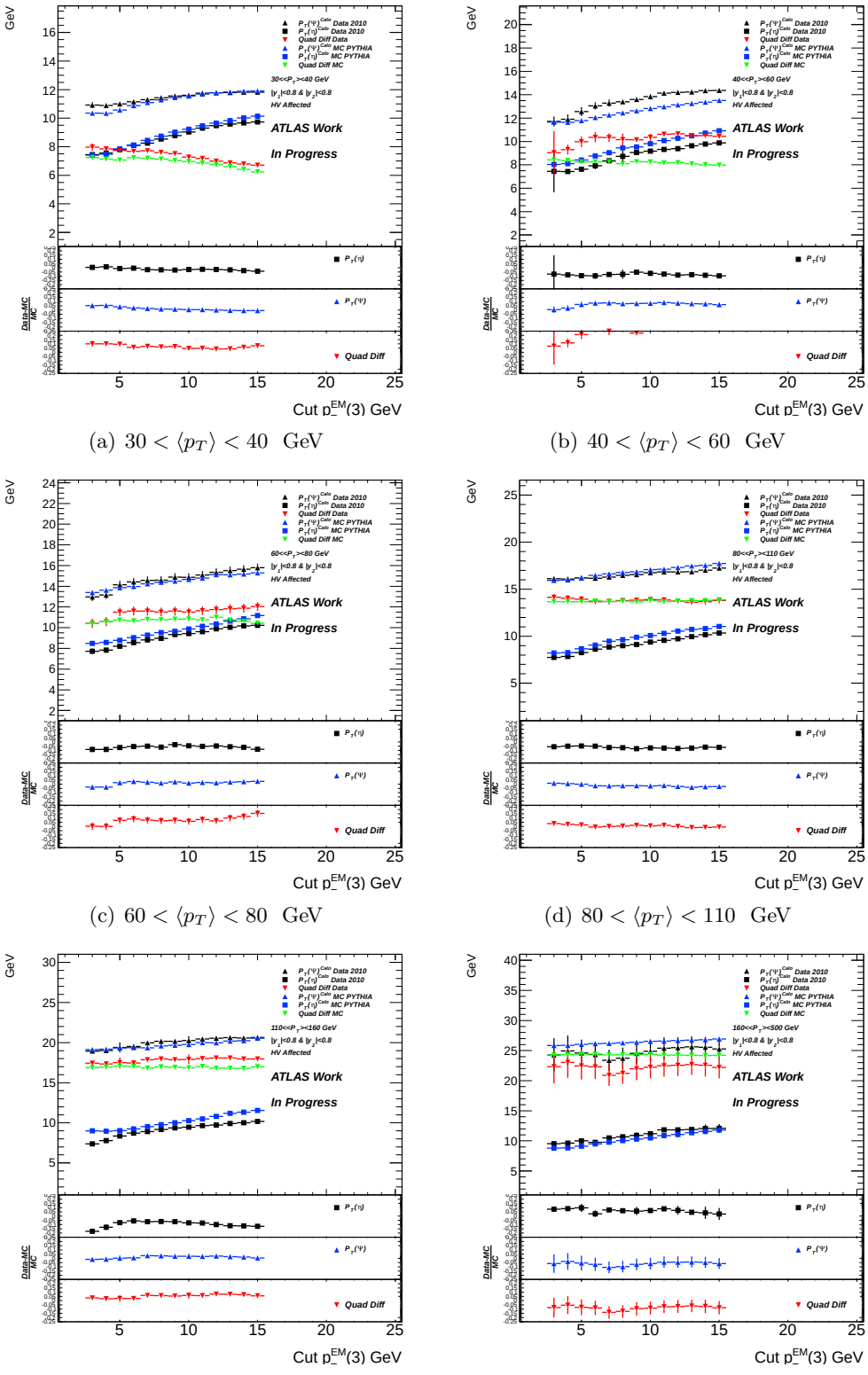

(a) $30 < \langle p_T \rangle < 40$ GeV

(b) $40 < \langle p_T \rangle < 60$ GeV

(c) $60 < \langle p_T \rangle < 80$ GeV

(d) $80 < \langle p_T \rangle < 110$ GeV

(e) $110 < \langle p_T \rangle < 160$ GeV

(f) $160 < \langle p_T \rangle < 500$ GeV

Figure A.21: Soft Radiation validation distributions for two jets in $|y| < 0.8$. Tag jet in non affected area, probe HV. Bisector Technique.

Appendix B

Appendix to the Technicolor search

B.1 Standard Model backgrounds

Process	raw xsec x BR (pb)	k-factor	filter efficiency	dataset tag
$Z \to ee$	668.32	1.25	1.0	107650.AlpgenJimmyZeeNp0_pt20
	134.36	1.25	1.0	107651.AlpgenJimmyZeeNp1_pt20
	40.54	1.25	1.0	107652.AlpgenJimmyZeeNp2_pt20
	11.16	1.25	1.0	107653.AlpgenJimmyZeeNp3_pt20
	2.88	1.25	1.0	107654.AlpgenJimmyZeeNp4_pt20
	0.83	1.25	1.0	107655.AlpgenJimmyZeeNp5_pt20
$Z \to \tau\tau$	657.4	1.22	1.0	107670.AlpgenJimmyZtautauNp0_pt20
	133.0	1.22	1.0	107671.AlpgenJimmyZtautauNp1_pt20
	40.4	1.22	1.0	107672.AlpgenJimmyZtautauNp2_pt20
	11.0	1.22	1.0	107673.AlpgenJimmyZtautauNp3_pt20
	2.9	1.22	1.0	107674.AlpgenJimmyZtautauNp4_pt20
	0.7	1.22	1.0	107675.AlpgenJimmyZtautauNp5_pt20
$W \to e\nu$	6921.60	1.2	1.0	107680.AlpgenJimmyWenuNp0_pt20
	1304.30	1.2	1.0	107681.AlpgenJimmyWenuNp1_pt20
	378.29	1.2	1.0	107682.AlpgenJimmyWenuNp2_pt20
	101.43	1.2	1.0	107683.AlpgenJimmyWenuNp3_pt20
	25.87	1.2	1.0	107684.AlpgenJimmyWenuNp4_pt20
	7.0	1.2	1.0	107685.AlpgenJimmyWenuNp5_pt20
$W \to \tau\nu$	6835.8	1.22	1.0	107700.AlpgenJimmyWtaunuNp0_pt20
	1276.8	1.22	1.0	107701.AlpgenJimmyWtaunuNp1_pt20
	376.6	1.22	1.0	107702.AlpgenJimmyWtaunuNp2_pt20
	100.8	1.22	1.0	107703.AlpgenJimmyWtaunuNp3_pt20
	25.7	1.22	1.0	107704.AlpgenJimmyWtaunuNp4_pt20
	7.0	1.22	1.0	107705.AlpgenJimmyWtaunuNp5_pt20

Table B.1: Cross section times branching ratio (times k-factor when applied), and filter efficiency for leptonic simulated background samples.

Process	raw xsec x BR (pb)	k-factor	filter efficiency	dataset tag
single top	7.1522	1.0	1.0	108340.st_tchan_enu_McAtNlo_Jimmy
	7.1522	1.0	1.0	108342.st_tchan_taunu_McAtNlo_Jimmy
	0.46856	1.0	1.0	108343.st_schan_enu_McAtNlo_Jimmy
	0.46856	1.0	1.0	108345.st_schan_taunu_McAtNlo_Jimmy
	14.581	1.0	1.0	108346.st_Wt_McAtNlo_Jimmy
$t\bar{t}$	164.57	1.0	0.5551	105200.T1_McAtNlo_Jimmy
WW (dilepton)	2.095	1.0	1.0	107100.AlpgenJimmyWWincllNp0
	0.99623	1.0	1.0	107101.AlpgenJimmyWWincllNp1
	0.4547	1.0	1.0	107102.AlpgenJimmyWWincllNp2
	0.1581	1.0	1.0	107103.AlpgenJimmyWWincllNp3
WZ (dilepton)	0.67183	1.0	1.0	107104.AlpgenJimmyWZincllNp0
	0.41376	1.0	1.0	107105.AlpgenJimmyWZincllNp1
	0.22493	1.0	1.0	107106.AlpgenJimmyWZincllNp2
	0.094977	1.0	1.0	107107.AlpgenJimmyWZincllNp3
ZZ (dilepton)	0.50861	1.0	1.0	107108.AlpgenJimmyZZincllNp0
	0.23417	1.0	1.0	107109.AlpgenJimmyZZincllNp1
	0.088623	1.0	1.0	107110.AlpgenJimmyZZincllNp2
	0.031388	1.0	1.0	107111.AlpgenJimmyZZincllNp3
$W\gamma$	213.1	1.49	1.0	117410.AlpgenJimmyWgammaNp0_pt20
	52.2	1.49	1.0	117411.AlpgenJimmyWgammaNp1_pt20
	17.3	1.49	1.0	117412.AlpgenJimmyWgammaNp2_pt20
	5.3	1.49	1.0	117413.AlpgenJimmyWgammaNp3_pt20
	1.4	1.49	1.0	117414.AlpgenJimmyWgammaNp4_pt20
	0.3	1.49	1.0	117415.AlpgenJimmyWgammaNp5_pt20
	48	1.69	1.0	126009.Sherpa_Wenugamma
	79	1.69	1.0	126013.Sherpa_Wenugamma_1jet

Table B.2: Cross section times branching ratio (times k-factor when applied), and filter efficiency for top quark and diboson simulated background samples. The AlpGen $W\gamma$ samples also contained the muon final state.

B.2 Crystal Ball function

The Crystal Ball *pdf* [140] is given by a Gaussian shape extended on the low side by a power-law tail. Its parametric form is

$$f_{CB}(m, \mu_{CB}, \sigma_{CB}, \alpha_{CB}, n_{CB}) = N \cdot \begin{cases} \exp\left(-\frac{(m-\mu_{CB})^2}{2\sigma^2}\right) & \text{for } \frac{m-\mu_{CB}}{\sigma_{CB}} > -\alpha_{CB} \\ A_{CB} \cdot (B_{CB} - \frac{m-\mu_{CB}}{\sigma_{CB}})^{-n_{CB}} & \text{for } \frac{m-\mu_{CB}}{\sigma_{CB}} < -\alpha_{CB} \end{cases} \tag{B.1}$$

with

$$A_{CB} = \left(\frac{n_{CB}}{|\alpha_{CB}|}\right)^n \cdot \exp\left(-\frac{|\alpha_{CB}|^2}{2}\right) \tag{B.2}$$

$$B_{CB} = \frac{n}{|\alpha_{CB}|} - |\alpha_{CB}| \tag{B.3}$$

chosen so that the *pdf* is $\mathcal{C}^1$ at the transistion between Gaussian and power-law behavior. The normalization parameter N is chosen so that the function integrates to 1.

B.3 Novosibirsk function

The Novosibirsk function is defined as

$$f(m_{ES}) = A_S \exp(-\frac{1}{2}(\frac{\ln^2[1 + \Lambda\tau \cdot (m_{ES} - m_0)]}{\tau^2})) \tag{B.4}$$

where,

$$\Lambda = \sinh(\tau\sqrt{\ln 4})/(\sigma\tau\sqrt{\ln 4}) \tag{B.5}$$

The peak position is m_0, the width is σ, and τ is the tail parameter. In the limit $\tau \to 0$ the distriution tends to a Gaussian shape, while a tail appear in the right side for $\tau > 0$.

B.4 QCD templates control plots

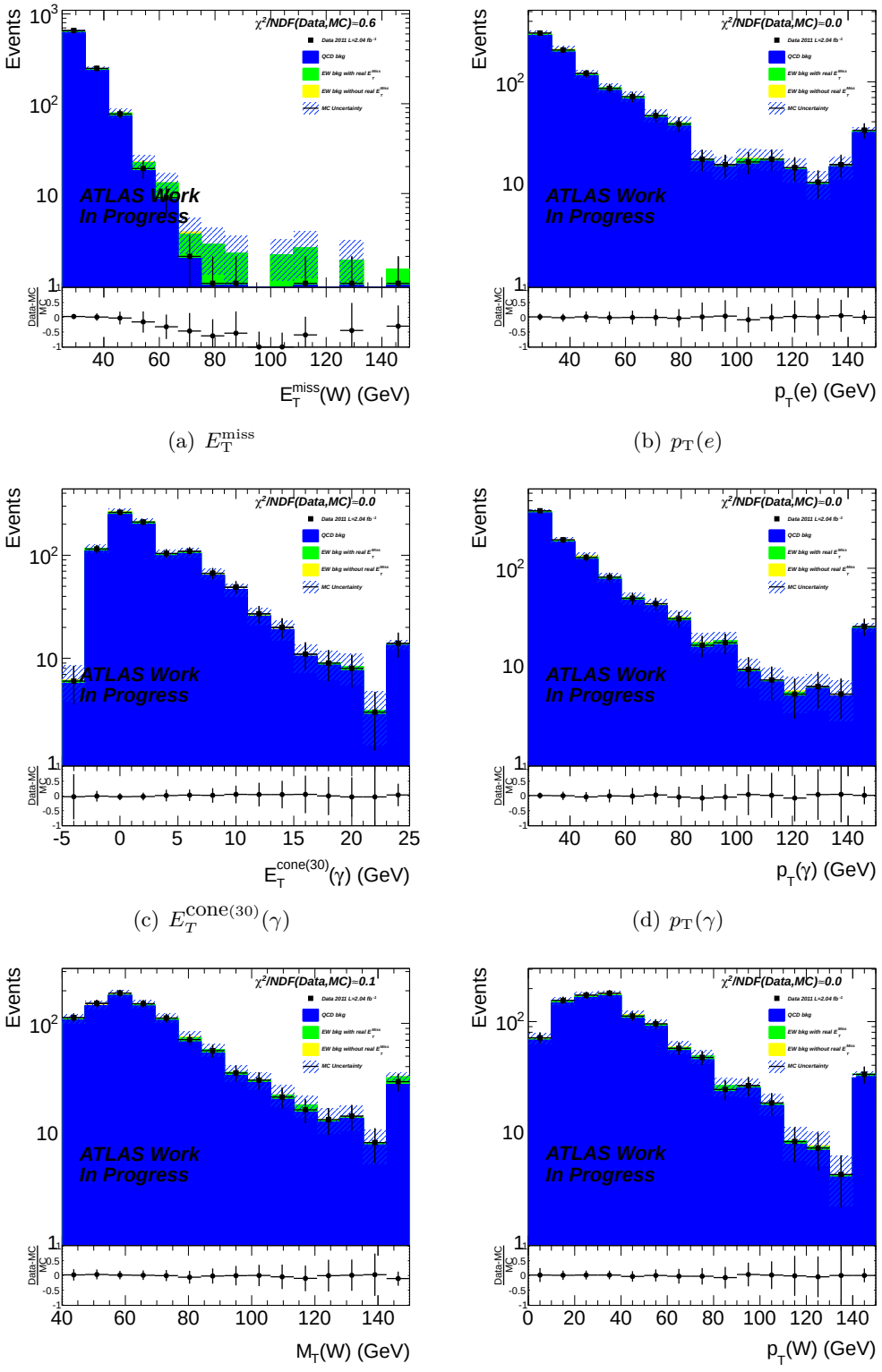

(a) $E_{\mathrm{T}}^{\mathrm{miss}}$ (b) $p_{\mathrm{T}}(e)$

(c) $E_T^{\mathrm{cone}(30)}(\gamma)$ (d) $p_{\mathrm{T}}(\gamma)$

(e) $M_T(e)$ (f) $p_{\mathrm{T}}(W)$

Figure B.1: Control plots for the template QCD selection.

region	NData	NEW	CX
A	2748	525 ± 16	$1. \pm 0.$
B	172	19 ± 3	0.02 ± 0.003
C	1629	105 ± 7	0.2 ± 0.01
D	752	8 ± 2	0.01 ± 0.002
W events	W MC events	ratio	QCD events
1910 ± 73	1920 ± 51	1.005	306 ± 18

Table B.3: Parameters of the ABCD method relaxing the $E_T^{\text{cone(30)}}(\gamma)$ cuts, number of W and QCD events found.

region	NData	NEW	CX
A	1141	100 ± 7	$1. \pm 0.$
B	83	3 ± 1	0.02 ± 0.003
C	822	35 ± 5	0.26 ± 0.03
D	461	1 ± 1	0.01 ± 0.002
W events	W MC events	ratio	QCD events
903 ± 50	920 ± 35	1.010	147 ± 12

Table B.4: Parameter of the ABCD method relaxing the $E_T^{\text{cone(30)}}(\gamma)$ cuts and asking that the photon fail the tight minus 4 photon identification cuts, number of W and QCD events found.

region	NData	NEW	CX
A	549	66 ± 6	1 ± 0
B	42	3 ± 1	0.02 ± 0.004
C	359	23 ± 3	0.26 ± 0.04
D	200	1 ± 1	0.01 ± 0.004
W events	W MC events	ratio	QCD events
415 ± 34	423 ± 21	1.02	68 ± 9

Table B.5: Parameter of the ABCD method relaxing the $E_T^{\text{cone(30)}}(\gamma)$ cuts and asking that the photon fail the tight minus 3 photon identification cuts, number of W and QCD events found.

region	NData	NEW	CX
A	1836	136.3 ± 8.0	1.00 ± 0.000
B	138	3.1 ± 1.3	0.02 ± 0.004
C	1338	41.7 ± 4.6	0.26 ± 0.022
D	781	1.9 ± 1.1	0.01 ± 0.002
W events	W MC events	ratio	QCD events
1476 ± 64	1549 ± 51	1.05	253 ± 16

Table B.6: Parameter of the ABCD method relaxing the $E_T^{\text{cone(30)}}(\gamma)$ cuts and asking that the photon fail the tight minus 5 photon identification cuts, number of W and QCD events found.

B.5 W+jets templates control plots

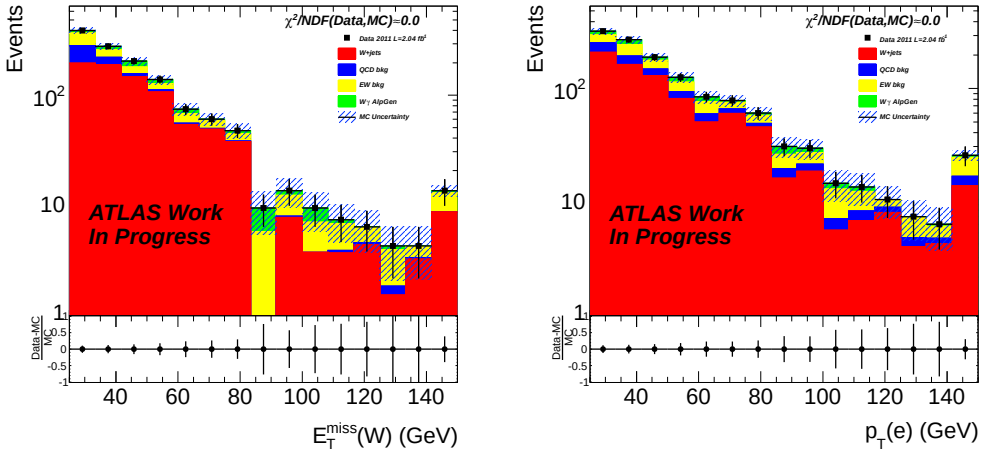

(a) $E_{\mathrm{T}}^{\mathrm{miss}}$

(b) $p_{\mathrm{T}}(e)$

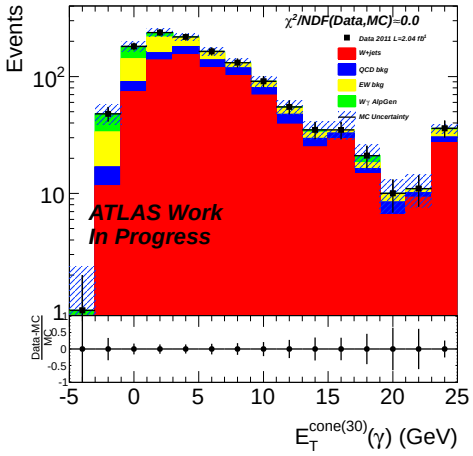

(c) $E_T^{\mathrm{cone}(30)}(\gamma)$

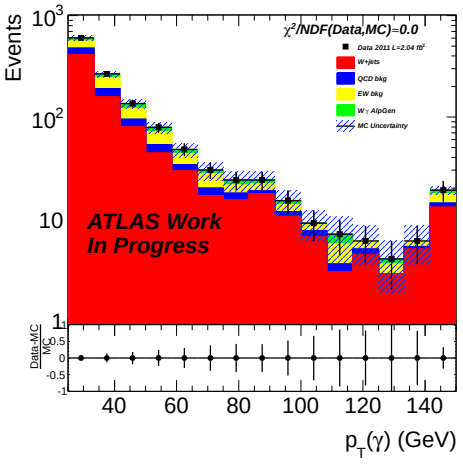

(d) $p_{\mathrm{T}}(\gamma)$

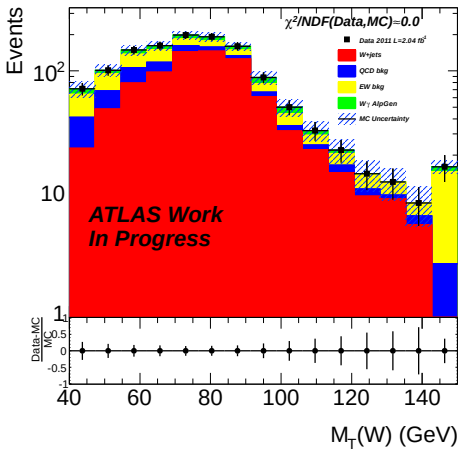

(e) $M_T(e)$

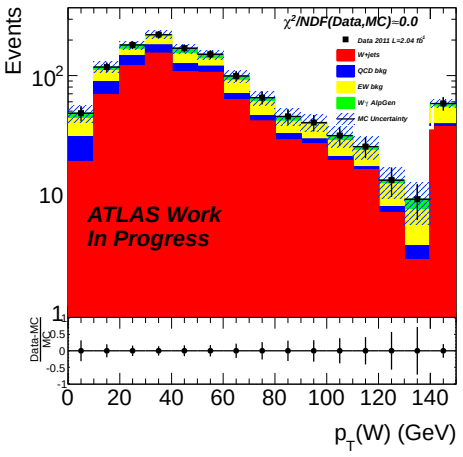

(f) $p_{\mathrm{T}}(W)$

Figure B.2: Control plots for the template W+jets selection.

B.6 Disagreement Sherpa Data

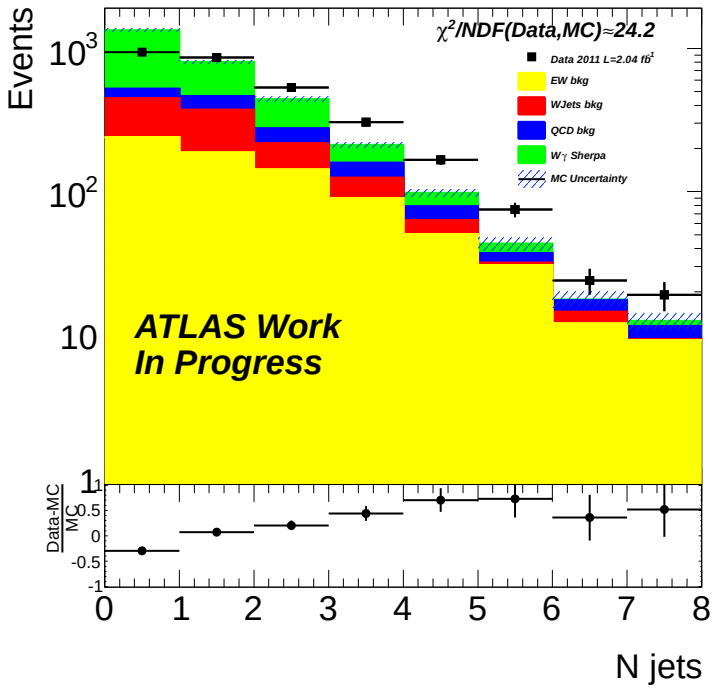

(a) N jets distribution

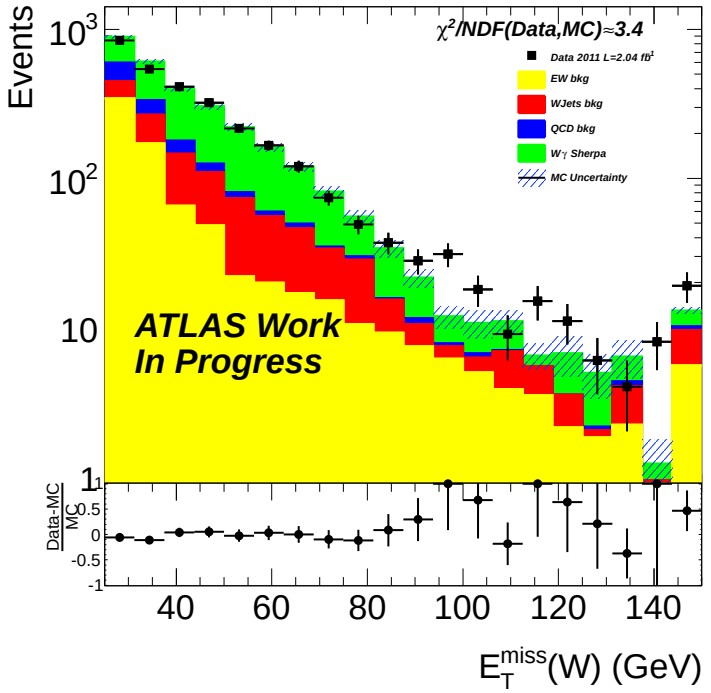

(b) $E_{\mathrm{T}}^{\mathrm{miss}}$ distribution

Figure B.3: Control distribution obtained with the Sherpa sample, after the selection given in Section 5.3.

B.7 LSTC search template fit

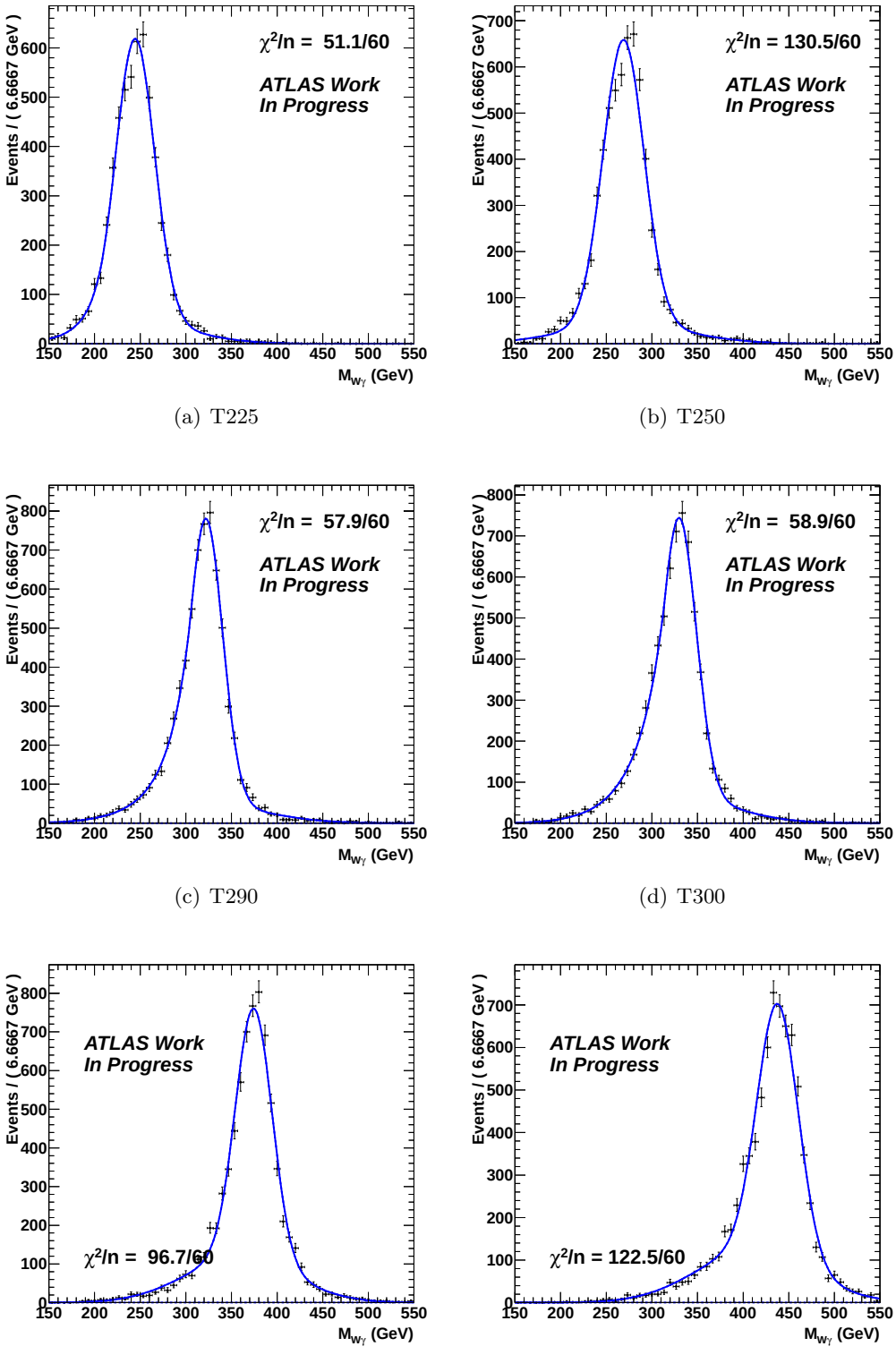

(a) T225 (b) T250

(c) T290 (d) T300

(e) T350 (f) T400

Figure B.4: Fit of all the LSTC signal point.

Parameter	T225	T250	T290	T300	T350	T400
μ_{CB}	242.8 ± 4.3 GeV	269.5 ± 6 GeV	321 ± 10 GeV	331 ± 12 GeV	375 ± 13 GeV	$440. \pm 20$ GeV
σ_{CB}	20 ± 4 GeV	20 ± 7 GeV	16 ± 11 GeV	$17. \pm 20$ GeV	19 ± 21 GeV	$19. \pm 20$ GeV
α_{CB}	1.0 ± 0.8	1.0 ± 0.7	0.93 ± 1.7	0.7 ± 1	0.9 ± 2	0.7 ± 2
n_{CB} (fixed)	100 ± 0	100 ± 0	100 ± 0	100 ± 0	100 ± 0	100 ± 0
β	0.83 ± 0.21	0.90 ± 0.2	0.7 ± 0.8	0.8 ± 0.8	0.8 ± 0.8	0.8 ± 0.9
μ_G	243 ± 30 GeV	300 ± 56 GeV	310 ± 73 GeV	328 ± 4 GeV	369 ± 82 GeV	420 ± 85 GeV
σ_G	59 ± 35 GeV	51 ± 93 GeV	51 ± 37 GeV	52 ± 47 GeV	67 ± 88 GeV	70 ± 99 GeV

Table B.7: Fit parameters found for all the nominal signal TC samples mode.

B.8 SM background fit

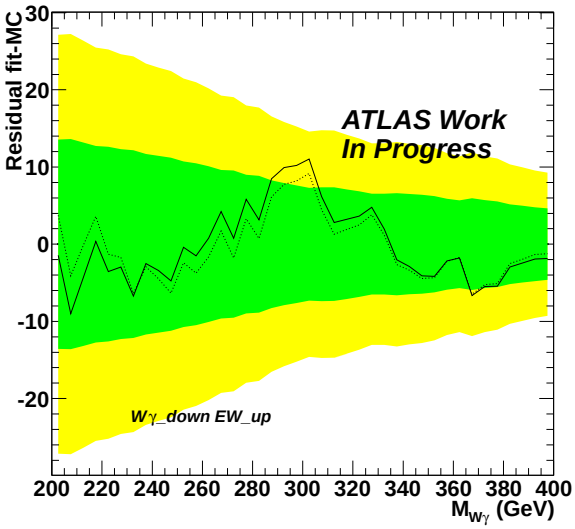

(a) $W\gamma$ reduced EW enhanced

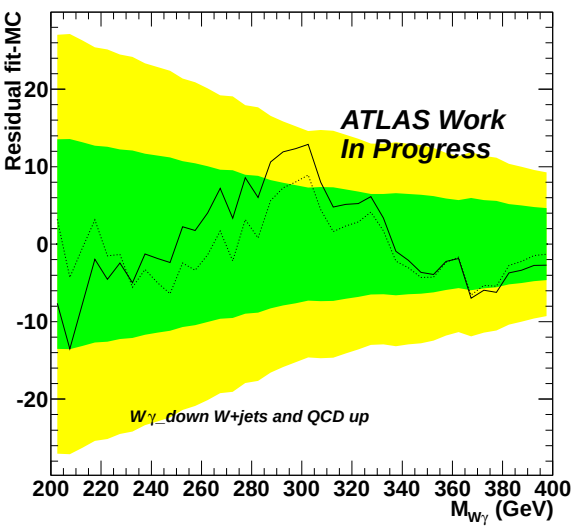

(b) $W\gamma$ reduced QCD and W+jets enhanced

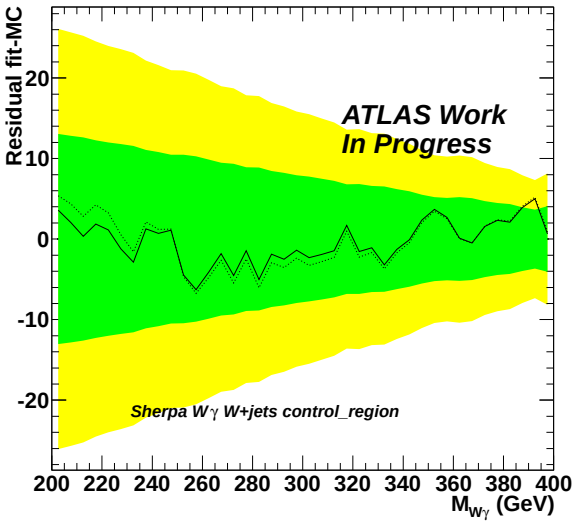

(c) $W\gamma$ sherpa W+jets from a control region

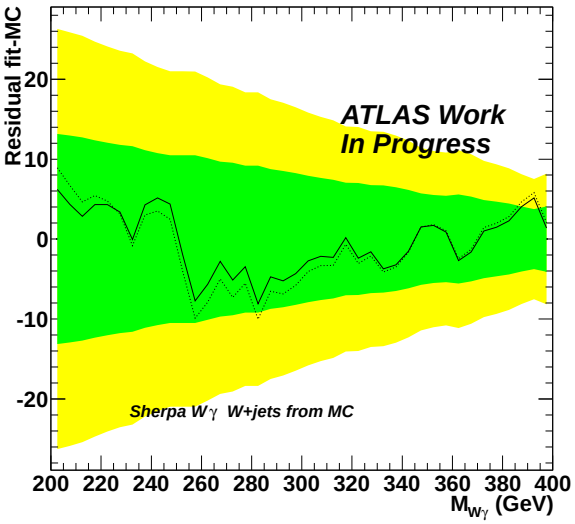

(d) $W\gamma$ sherpa W+jets from MC

Figure B.5: Residual of the SM background fit for various hypothesis.

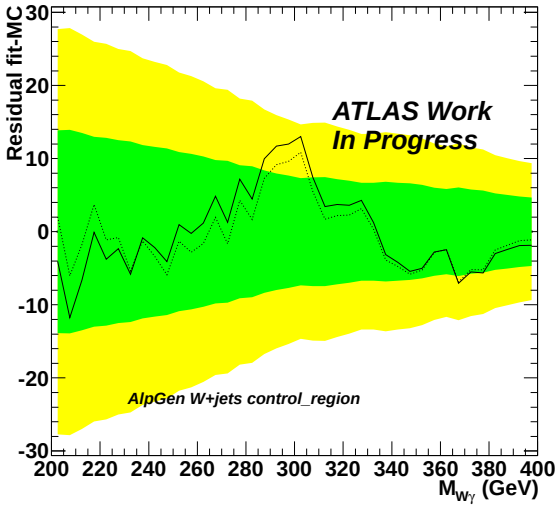

(a) Nominal W+jets from a control region

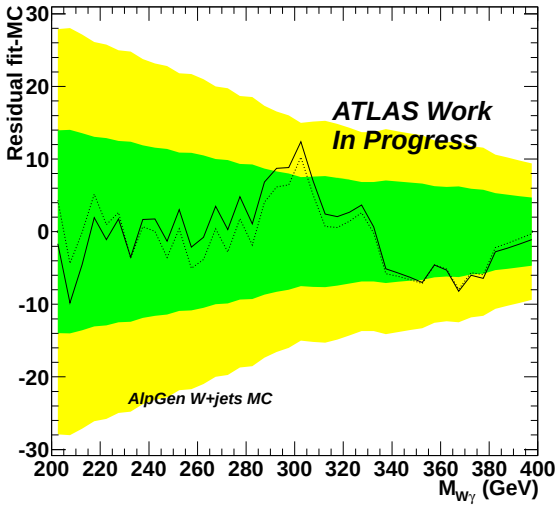

(b) Nominal W+jets from MC

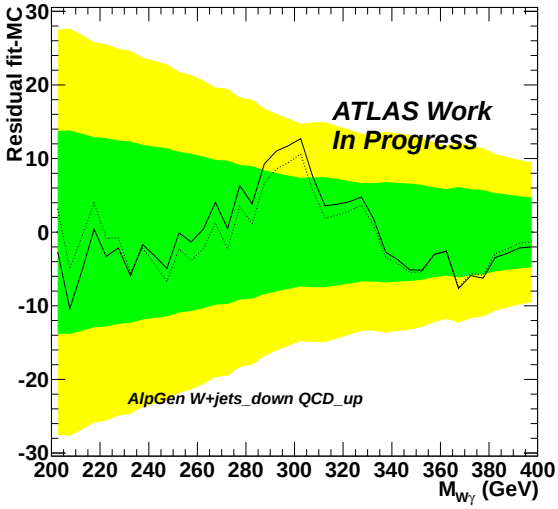

(c) W+jets reduced QCD enhanced

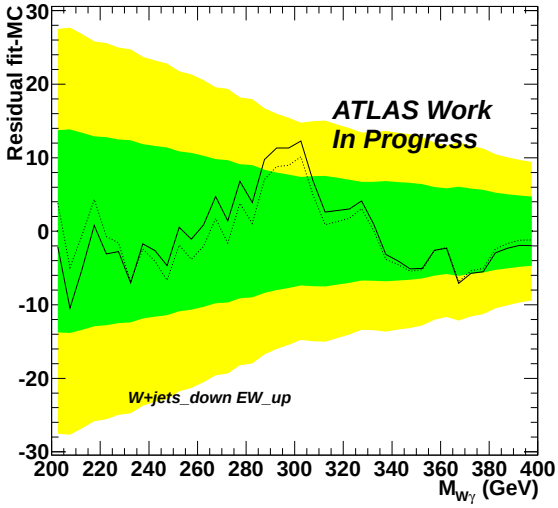

(d) W+jets reduced EW enhanced

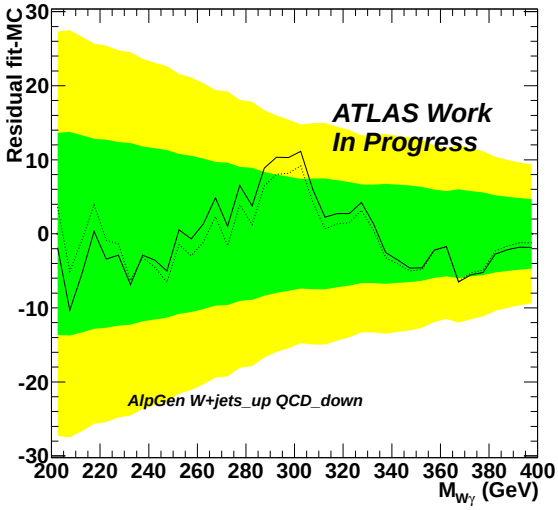

(e) W+jets enhanced QCD reduced

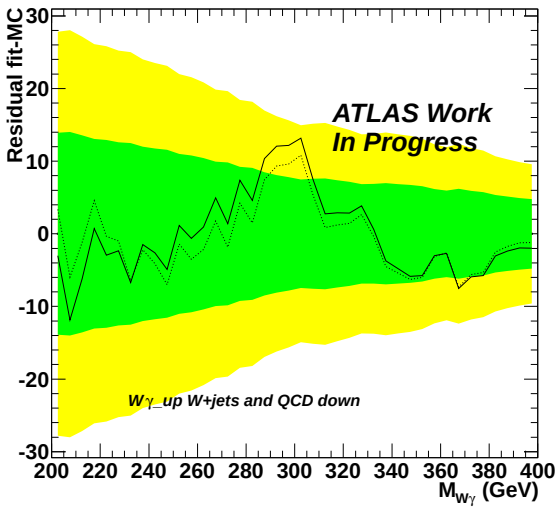

(f) $W\gamma$ enhanced QCD and W+jets reduced

Figure B.6: Residual of the SM background fit for various hypothesis.

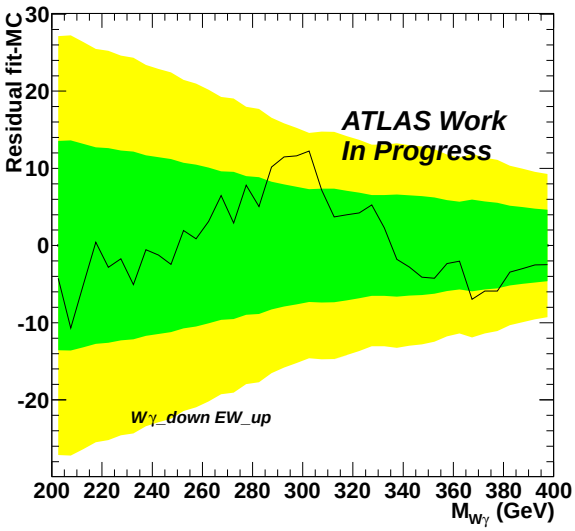

(a) $W\gamma$ reduced EW enhanced

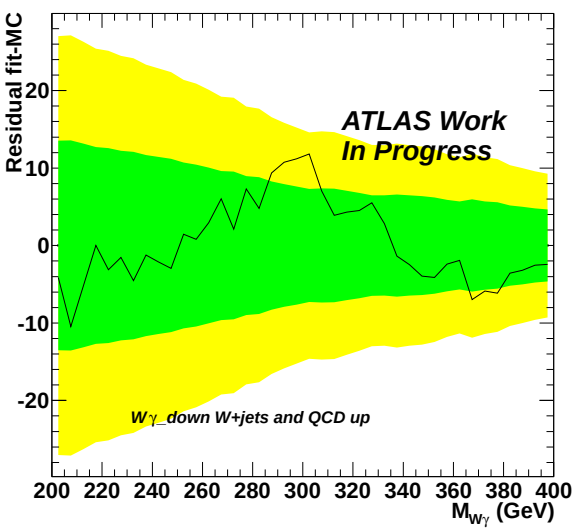

(b) $W\gamma$ reduced QCD and W+jets enhanced

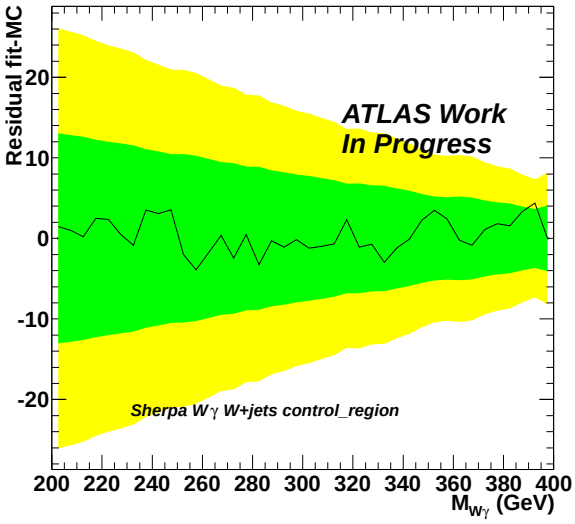

(c) $W\gamma$ sherpa W+jets from a control region

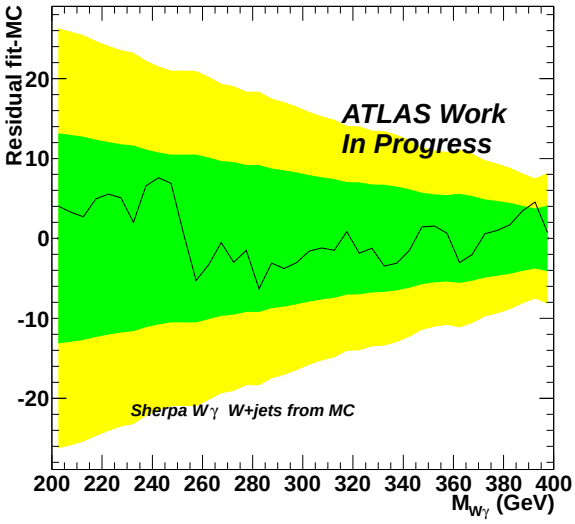

(d) $W\gamma$ sherpa W+jets from MC

Figure B.7: Residual of the SM background fit for various hypothesis, α fixed.

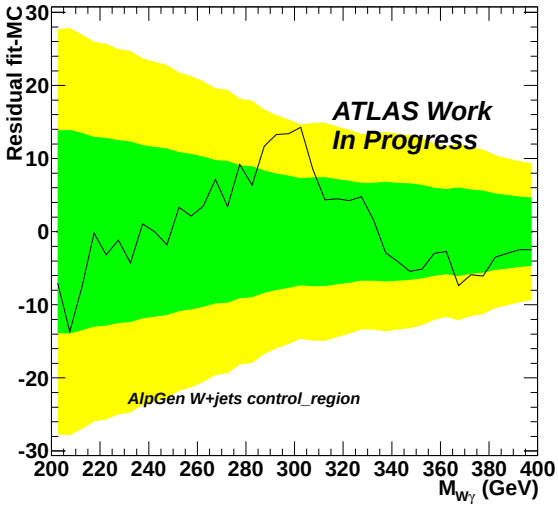

(a) Nominal W+jets from a control region

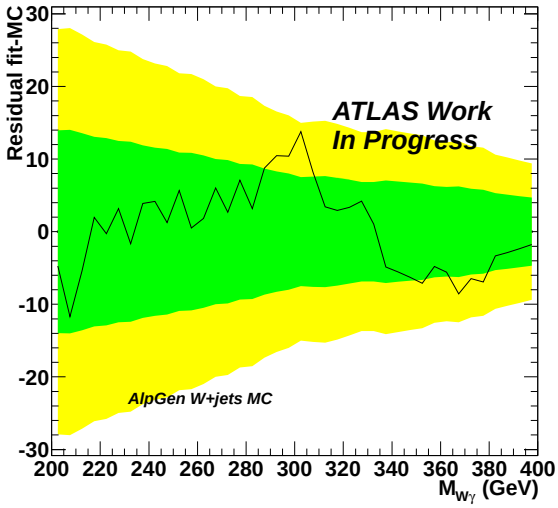

(b) Nominal W+jets from MC

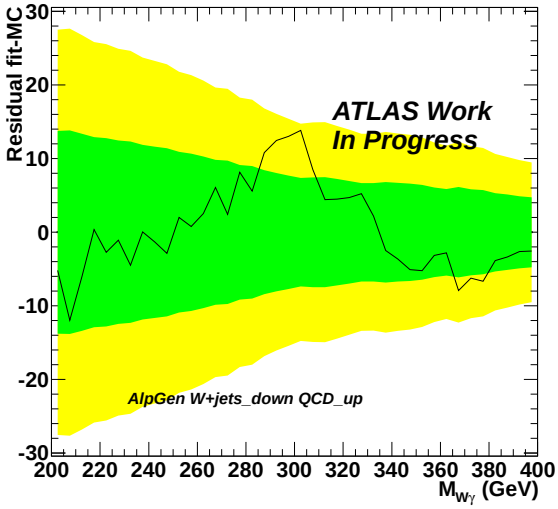

(c) W+jets reduced QCD enhanced

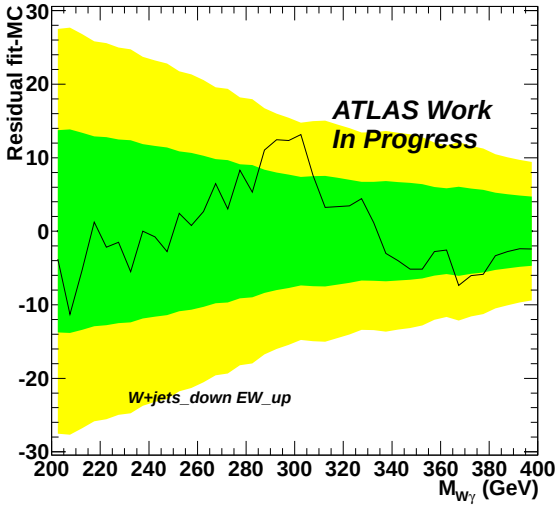

(d) W+jets reduced EW enhanced

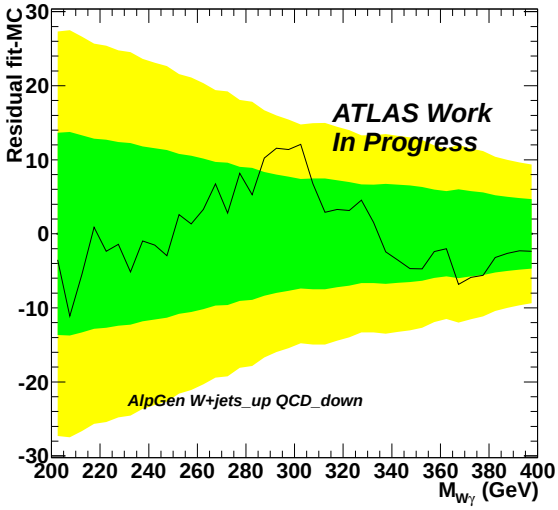

(e) W+jets enhanced QCD reduced

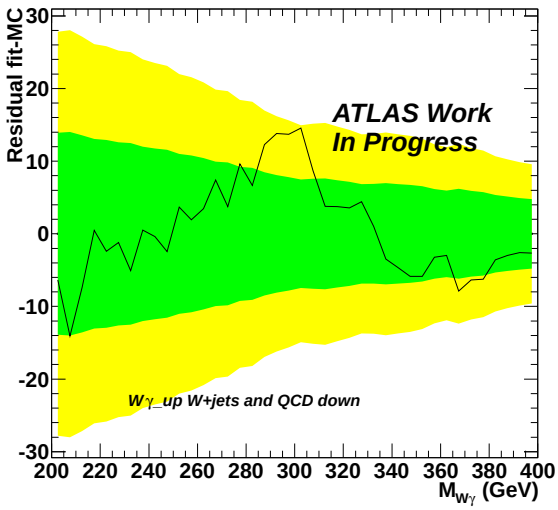

(f) $W\gamma$ enhanced QCD and W+jets reduced

Figure B.8: Residual of the SM background fit for various hypothesis, α fixed.

B.9 Systematic uncertainties

Parameter	T200 %	T225 %	T250 %	T290 %	T300 %	T350 %	T400 %
JES Down	−2.02	−2.16	−1.30	−1.80	−1.71	−0.96	−1.09
JES Up	1.76	1.27	0.68	1.14	0.69	0.54	0.42
LES Down	−0.33	−0.61	−0.53	−0.89	−0.12	−0.42	−0.22
LES Up	0.16	0.19	0.57	0.95	0.37	0.36	0.77
eID Down	−1.34	−1.41	−1.39	−1.39	−1.36	−1.31	−1.35
eID Up	1.34	1.41	1.39	1.39	1.36	1.31	1.35
PES Down	−0.22	−0.07	−0.18	−0.23	−0.19	−0.19	−0.11
PES Up	0.24	0.02	0.01	0.27	0.18	0.16	0.04
γID U-D	±5	±5	±5	±5	±5	±5	±5
OTX Down	−0.26	−0.37	−0.15	−0.09	−0.16	−0.35	−0.13
OTX Up	0.13	0.13	0.17	0.09	0.12	0.08	0.12
Lumi	±3.7	±3.7	±3.7	±3.7	±3.7	±3.7	±3.7
N signal	$54.22 \pm {}^{6.64\%}_{6.70\%}$	$39.41 \pm {}^{6.52\%}_{6.80\%}$	$32.02 \pm {}^{6.44\%}_{6.54\%}$	$12.31 \pm {}^{6.56\%}_{6.71\%}$	$15.86 \pm {}^{6.44\%}_{6.60\%}$	$9.41 \pm {}^{6.39\%}_{6.46\%}$	$6.17 \pm {}^{6.43\%}_{6.46\%}$

Table B.8: Systematic on the signal event rate.

Parameter	T200 GeV	T225 GeV	T250 GeV	T290 GeV	T300 GeV	T350 GeV	T400 GeV
JES Down	−0.87	−1.07	−1.18	−1.74	−1.58	−1.87	−2.72
JES Up	0.88	1.04	0.84	0.98	1.11	1.73	1.79
LES Down	−0.07	−0.09	−0.10	−0.15	−0.21	−0.20	−0.08
LES Up	0.03	0.08	0.31	0.17	0.05	0.51	0.16
eID Down	−0.03	−0.04	−0.03	−0.02	−0.01	−0.02	−0.01
eID Up	0.03	0.04	0.03	0.02	0.01	0.01	0.02
PES Down	−0.07	−0.01	−0.04	−0.04	−0.04	−0.17	−0.02
PES Up	0.09	0.21	0.01	0.33	0.57	0.16	0.17
OTX Down	−0.01	−0.05	−0.02	−0.01	−0.01	−0.05	−0.01
OTX Up	0.01	0.01	0.01	0.02	0.02	0.01	0.01
γID U-D	±0.001	±0.001	±0.001	±0.001	±0.001	±0.001	±0.001
Lumi	0	0	0	0	0	0	0
Nominal value (GeV)	$215.11 \pm {}^{0.90}_{0.89}$	$242.81 \pm {}^{1.07}_{1.08}$	$269.47 \pm {}^{0.91}_{1.18}$	$321.11 \pm {}^{1.05}_{1.75}$	$330.74 \pm {}^{1.25}_{1.60}$	$375.06 \pm {}^{1.78}_{1.89}$	$440.02 \pm {}^{1.81}_{2.71}$

Table B.9: Systematic on the signal peak position reconstruction.

B.10 Confidence level background hypothesis

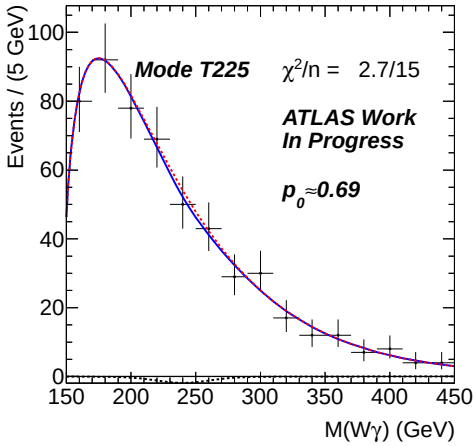

(a) T225

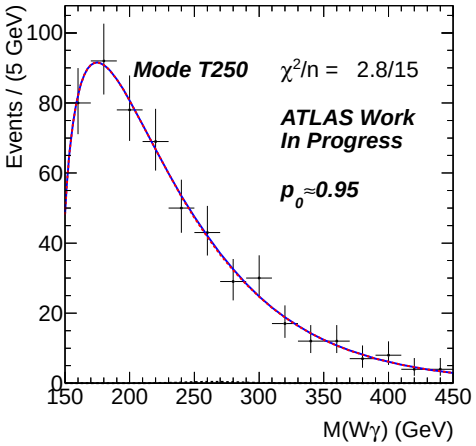

(b) T250

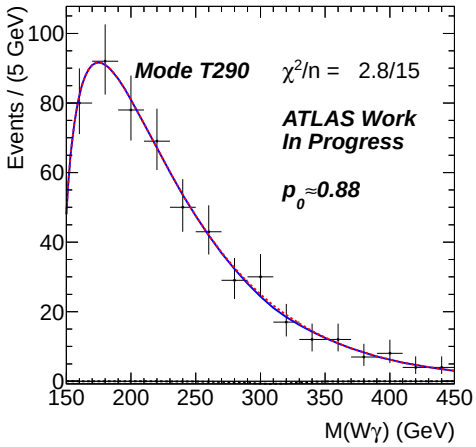

(c) T290

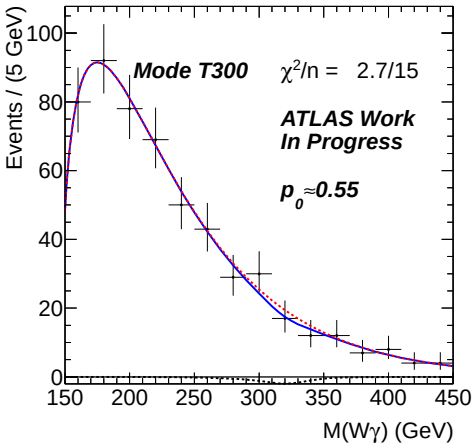

(d) T300

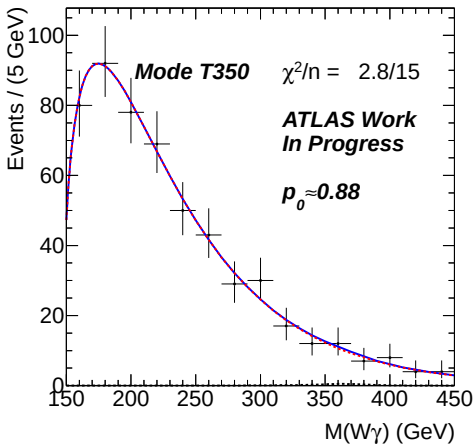

(e) T350

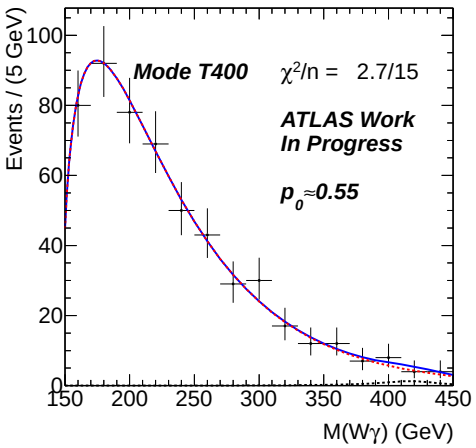

(f) T400

Figure B.9: Fit of the model on the data.

Bibliography

[1] M. E. Peskin and D. V. Schroeder. *An introduction to quantum field theory.* Westview Press, 1995.

[2] G. Chanfray and G. Smadja. *Les particules et leurs symétries.* Masson, 1997.

[3] F. Halzen and A. D. Martin. *Quarks and leptons.* Wiley, 1984.

[4] D. Griffiths. *Introduction to Elementary Particles.* Wiley, 1987.

[5] J-P. Derendinger. *Théorie quantique des champs.* PPUR, 2001.

[6] S. L. Glashow. Partial-symmetries of weak interactions. *Nuclear Physics*, 22(4):579–588, 1961.

[7] S. Weinberg. A model of leptons. *Physical Review Letters*, 19(21):1264–1266, 1967.

[8] A. Salam. Weak and Electromagnetic Interactions. Originally printed in Svartholm: Elementary Particle Theory. In *Proceedings of the Nobel Symposium held*, pages 367–377, 1968.

[9] E. Noether. Invariant variation problems. *Transport Theory and Statistical Physics*, 1:186–207, 1971.

[10] S. Abachi, B. Abbott, M. Abolins, BS Acharya, I. Adam, DL Adams, M. Adams, S. Ahn, H. Aihara, J. Alitti, et al. Observation of the top quark. *Physical Review Letters*, 74(14):2632–2637, 1995.

[11] F. Abe, H. Akimoto, A. Akopian, MG Albrow, SR Amendolia, D. Amidei, J. Antos, C. Anway-Wiese, S. Aota, G. Apollinari, et al. Observation of Top Quark Production in $p - \bar{p}$ Collisions with the Collider Detector at Fermilab. *Physical review letters*, 74(14):2626–2631, 1995.

[12] K. Kodama et al. *Observation of tau-neutrino interactions. Phys. Lett.*, B504:218–224, 2001.

[13] K. Nakamura et al. (Particle Data Group). *J. Phys. G 37, 075021*, 2010.

[14] N. Cabibbo. Unitary symmetry and leptonic decays. *Physical Review Letters*, 10(12):531–533, 1963.

[15] M. Kobayashi and T. Maskawa. CP-violation in the renormalizable theory of weak interaction. 1973.

[16] U. Arnison, A. Astbury, B. Aubert, C. Bacci, G. Bauer, A. Bezaguet, R. Böck, T. J. V. Bowcock, M. Calvetti, P. Catz, et al. Experimental observation of lepton pairs of invariant mass around 95 GeV/c2 at the CERN SPS collider. *Physics Letters B*, 126(5):398–410, 1983.

[17] U. Arnison, A. Astbury, B. Aubert, C. Bacci, G. Bauer, A. Bezaguet, R. Böck, T. J. V. Bowcock, M. Calvetti, T. Carroll, et al. Experimental observation of isolated large transverse energy electrons with associated missing energy at $\sqrt{(}s)$= 540 GeV. *Europhys Lett*, 1:327–345, 1986.

[18] R. Brandelik et al. Evidence for Planar Events in e+ e- Annihilation at High-Energies. *Phys.Lett.*, B86:243, 1979.

[19] F. Englert and R. Brout. Broken symmetry and the mass of gauge vector mesons. *Physical Review Letters*, 13(9):321–323, 1964.

[20] P. W. Higgs. Broken symmetries and the masses of gauge bosons. *Physical Review Letters*, 13(16):508–509, 1964.

[21] G. S. Guralnik, C. R. Hagen, and T. W. B. Kibble. Global conservation laws and massless particles. *Phys. Rev. Lett.*, 13(20):585–587, Nov 1964.

[22] J. Goldstone. Field theories with «Superconductor» solutions. *Il Nuovo Cimento (1955-1965)*, 19(1):154–164, 1961.

[23] J. Goldstone, A. Salam, and S. Weinberg. Broken symmetries. *Physical Review*, 127(3):965–970, 1962.

[24] Mathieu Aurousseau, Sandrine Laplace, and Isabelle Wingerter-Seez. *Mesure in situ de l'uniformité du calorimètre électromagnétique et recherche des premiers événements di-photons dans ATLAS. oai:cds.cern.ch:1307098.* PhD thesis, Annecy, Université de Savoie, Annecy-le-Vieux, 2010. Presented on 30 Sep 2010.

[25] Chris Quigg and Robert Shrock. Gedanken Worlds without Higgs: QCD-Induced Electroweak Symmetry Breaking. *Phys.Rev.*, D79:096002, 2009.

[26] Christopher T. Hill and Elizabeth H. Simmons. Strong dynamics and electroweak symmetry breaking. *Phys.Rept.*, 381:235–402, 2003.

[27] J. Ferland. *Potentiel d'observation de la technicouleur à l'aide de l'expérience ATLAS.* PhD thesis, Université de Montréal, 2009.

[28] N. Gollub. *Search for Technicolor with the OPAL Detector in e^+e^- Collisions at the Highest LEP Energies.* PhD thesis, Institut für Experimentalphysik Universität Hamburg, 2001.

[29] F. Zwicky. On the Masses of Nebulae and of Clusters of Nebulae. *APJ*, 86:217–+, October 1937.

[30] F. Zwicky. Die Rotverschiebung von extragalaktischen Nebeln. *Helvetica Physica Acta*, 6:110–127, 1933.

[31] Y. Fukuda and All. Measurements of the solar neutrino flux from super-kamiokande's first 300 days. *Phys. Rev. Lett.*, 81(6):1158–1162, Aug 1998.

[32] Steven Weinberg. Implications of Dynamical Symmetry Breaking: An Addendum. *Phys.Rev.*, D19:1277–1280, 1979. (For original paper see Phys.Rev.D13:974-996,1976).

[33] Leonard Susskind. Dynamics of Spontaneous Symmetry Breaking in the Weinberg-Salam Theory. *Phys.Rev.*, D20:2619–2625, 1979.

[34] Michael E. Peskin and Tatsu Takeuchi. A New constraint on a strongly interacting Higgs sector. *Phys.Rev.Lett.*, 65:964–967, 1990.

[35] Michael E. Peskin and Tatsu Takeuchi. Estimation of oblique electroweak corrections. *Phys.Rev.*, D46:381–409, 1992.

[36] Kenneth Lane. Two lectures on technicolor. 2002.

[37] Kenneth D. Lane. Technicolor and precision tests of the electroweak interactions. 1994.

[38] Gustaaf H. Brooijmans et al. New Physics at the LHC: A Les Houches Report. Physics at Tev Colliders 2007 – New Physics Working Group. 2008.

[39] G. Brooijmans et al. New Physics at the LHC. A Les Houches Report: Physics at TeV Colliders 2009 - New Physics Working Group. 2010.

[40] Kenneth Lane and Stephen Mrenna. The Collider phenomenology of technihadrons in the technicolor straw man model. *Phys.Rev.*, D67:115011, 2003.

[41] T. Sjöstrand, S. Mrenna, and P. Skands. PYTHIA 6.4 physics and manual. *Journal of High Energy Physics*, 2006:026, 2006.

[42] Louis Helary. Looking for technicolor in ATLAS. *Acta Phys.Polon.Supp.*, 3:867–872, 2010.

[43] CERN. *oai:cds.cern.ch:270200. European School of High-Energy Physics, addendum*, Geneva, 1994. CERN. Addendum to proceedings.

[44] The GFitter Collaboration. http://project-gfitter.web.cern.ch/project-gfitter/.

[45] Henning Flacher, Martin Goebel, Johannes Haller, Andreas Hocker, Klaus Monig, et al. Gfitter - Revisiting the Global Electroweak Fit of the Standard Model and Beyond. *Eur.Phys.J.*, C60:543–583, 2009.

[46] Search for technihadrons in pp collisions at $\sqrt{s}$=7 tev with the atlas detector. Technical Report ATLAS-CONF-2011-125, CERN, Geneva, Sep 2011.

[47] V.M. Abazov et al. Search for a resonance decaying into WZ boson pairs in $p\bar{p}$ collisions. *Phys.Rev.Lett.*, 104:061801, 2010.

[48] T. Aaltonen et al. Search for Technicolor Particles Produced in Association with a W Boson at CDF. *Phys.Rev.Lett.*, 104:111802, 2010.

[49] T. Aaltonen et al. Invariant Mass Distribution of Jet Pairs Produced in Association with a W boson in $p\bar{p}$ Collisions at $\sqrt{s} = 1.96$ TeV. *Phys.Rev.Lett.*, 106:171801, 2011.

[50] Viviana Cavaliere. Measurement of ww + wz production cross section and study of the dijet mass spectrum in the lnu + jets final state at CDF. 2010. Ph.D. thesis (advisor: Maria Agnese Ciocci).

[51] Estia J. Eichten, Kenneth Lane, and Adam Martin. Technicolor at the Tevatron. 2011.

[52] Victor Mukhamedovich Abazov et al. Bounds on an anomalous dijet resonance in W+jets production in ppbar collisions at sqrts =1.96 TeV. *Phys.Rev.Lett.*, 107:011804, 2011.

[53] C ATLAS, P Catastini, M Franklin, J Guimaraes da Costa, J Huth, F Nuti, C Roda, F Ruehr, A Solodkov, P Wells, and G Zevi Della Porta. Invariant mass distribution of jet pairs produced in association with a leptonically decaying w in the atlas experiment with 0.93 fb^{-1}. Technical Report ATLAS-COM-CONF-2011-114, CERN, Geneva, Jul 2011.

[54] http://public.web.cern.ch/public/en/research/AccelComplex-en.html.

[55] The ALEPH, DELPHI, L3, OPAL, SLD Collaborations, the LEP Electroweak Working Group, the SLD Electroweak and Heavy Flavour Groups. Precision Electroweak Measurements on the Z Resonance. *Phys. Rept.*, 427:257, 2006.

[56] http://press.web.cern.ch/press/PressReleases/Releases2008/PR08.08E.html.

[57] http://press.web.cern.ch/press/PressReleases/Releases2008/PR10.08E.html.

[58] (ed.) Carli, Christian. LHC performance. Proceedings, Workshop, Chamonix, France, January 24-28, 2011. 2011.

[59] (ed.) Evans, Lyndon and (ed.) Bryant, Philip. LHC Machine. *JINST*, 3:S08001, 2008.

[60] http://public.web.cern.ch/public/en/LHC/LHC-en.html.

[61] J Butterworth, E Dobson, U Klein, B Mellado Garcia, T Nunnemann, J Qian, D Rebuzzi, and R Tanaka. Single boson and diboson production cross sections in pp collisions at $\sqrt{s}$=7 tev. Technical Report ATL-COM-PHYS-2010-695, CERN, Geneva, Aug 2010.

[62] https://twiki.cern.ch/twiki/bin/view/AtlasPublic.

[63] http://www.fnal.gov/pub/now/tevlum.html.

[64] (ed.) Carli, Christian. LHC performance. Proceedings, Workshop, Chamonix, France, January 25-29, 2010. 2010.

[65] The ATLAS Collaboration, G. Aad, et al. Expected Performance of the ATLAS Experiment: Detector, Trigger and Physics,(CERN, Geneva, 2008). Technical report, CERN-OPEN-2008-020.

[66] The ATLAS Collaboration, G. Aad, et al. The ATLAS experiment at the CERN large hadron collider. *Journal of Instrumentation*, 2008.

[67] The ATLAS Collaboration. Inner Detector Technical Design Report, Vol. I. Technical report, CERN/LHCC/97-16, 1997.

[68] The ATLAS Collaboration. Inner Detector Technical Design Report, Vol. II. Technical report, CERN/LHCC/97-17, 1997.

[69] Alignment of the atlas inner detector tracking system with 2010 lhc proton-proton collisions at $sqrts = 7$ tev. Technical Report ATLAS-CONF-2011-012, CERN, Geneva, Mar 2011.

[70] Performance of primary vertex reconstruction in proton-proton collisions at $\sqrt{s}$ =7 tev in the atlas experiment. Technical Report ATLAS-CONF-2010-069, CERN, Geneva, Jul 2010.

[71] Georges Aad and all. The atlas inner detector commissioning and calibration. oai:cds.cern.ch:1262789. *Eur. Phys. J. C*, 70(arXiv:1004.5293. CERN-PH-EP-2010-043):787–821. 34 p, Jun 2010. Comments: 34 pages, 25 figures.

[72] Muon momentum resolution in first pass reconstruction of pp collision data recorded by atlas in 2010. (ATLAS-CONF-2011-046), Mar 2011.

[73] J B De Vivie de Régie. Update of inter-alignment between the electromagnetic calorimeter and the inner detector. Technical Report ATL-COM-PHYS-2011-671, CERN, Geneva, Jun 2011.

[74] https://twiki.cern.ch/twiki/bin/view/AtlasPublic/ApprovedPlotsATLASDetector.

[75] The ATLAS Collaboration. Calorimeter Performance Technical Design Report. Technical report, CERN/LHCC/96-40, 1996.

[76] G Pasztor, F Hubaut, and A Bocci. In-situ electron performance measurements with the atlas detector using the 2010 lhc proton-proton collision data. (ATL-COM-PHYS-2011-546), May 2011.

[77] The ATLAS Collaboration. Tile Calorimeter Technical Design Report. Technical report, CERN/LHCC/96-42, 1996.

[78] Jet energy resolution and selection efficiency relative to track jets from in-situ techniques with the atlas detector using proton-proton collisions at a center of mass energy $sqrts = 7$ tev. (ATLAS-CONF-2010-054), Jul 2010.

[79] G Romeo, A Schwartzman, R Piegaia, T Carli, and R Teuscher. Jet energy resolution from in-situ techniques with the atlas detector using proton-proton collisions at a center of mass energy $\sqrt{s} = 7$ tev. (ATL-COM-PHYS-2011-240), Mar 2011.

[80] The ATLAS Collaboration. Muon Spectrometer Technical Design Report. Technical report, CERN/LHCC/97-22, 1997.

[81] Muon reconstruction efficiency in reprocessed 2010 lhc proton-proton collision data recorded with the atlas detector. Technical Report ATLAS-CONF-2011-063, CERN, Geneva, Apr 2011.

[82] https://twiki.cern.ch/twiki/bin/view/AtlasPublic/TriggerPublicResults.

[83] The ATLAS Collaboration. Liquid Argon Calorimeter Technical Design Report. Technical report, CERN/LHCC/96-41, 1996.

[84] B. Aubert et al. Construction, assembly and tests of the ATLAS electromagnetic barrel calorimeter. *Nuclear Instruments and Methods in Physics Research A*, 558(2):388–418, 2006.

[85] B. Aubert et al. Performance of a liquid argon electromagnetic calorimeter with an" accordion" geometry. 1991. CERN-PPE-91-73.

[86] M. L. Andrieux et al. Construction and test of the first two sectors of the ATLAS liquid argon presampler. *Nuclear Instruments and Methods in Physics Research A*, 479(2):316–333, 2002.

[87] J. F. Marchand. *Etude de la recherche du boson de Higgs en deux photons dans l'expérience ATLAS au LHC et calibration du calorimètre à Argon liquide*. PhD thesis, Université de Savoie, 2009. CERN-THESIS-2009-127.

[88] B. Aubert et al. Development and construction of large size signal electrodes for the ATLAS electromagnetic calorimeter. *Nuclear Instruments and Methods in Physics Research A*, 539(3):558–594, 2005.

[89] M. Aleksa et al. Construction, assembly and tests of the ATLAS electromagnetic end-cap calorimeters. *Journal of Instrumentation*, 3, 2008. P06002.

[90] D. M. Gingrich et al. Construction, Assembly and Testing of the ATLAS Hadronic End-cap Calorimeter. *Journal of Instrumentation*, 2, 2007. P05005.

[91] A. Artamonovh et al. The ATLAS Forward Calorimeter. *Journal of Instrumentation*, 3, 2008. P02010.

[92] H. Abreu et al. Performance of the Electronic Readout of the ATLAS Liquid Argon Calorimeters. *Accepted by Journal of Instrumentation*, 2010.

[93] N. J. Buchanan et al. ATLAS liquid argon calorimeter front end electronics. *Journal of Instrumentation*, 3:P09003, 2008.

[94] A. Bazan et al. ATLAS liquid argon calorimeter back end electronics. *Journal of Instrumentation*, 2:06002, 2007.

[95] N. J. Buchanan et al. Design and implementation of the Front End Board for the readout of the ATLAS liquid argon calorimeters. *Journal of Instrumentation*, 3:P03004, 2008.

[96] J. Prast. The ATLAS Liquid Argon Calorimeters Read Out Drivers (ROD). 2008. https://edms.in2p3.fr/document/I-005698/4.0.

[97] J. Colas et al. Electronics calibration board for the ATLAS liquid argon calorimeters. *Nuclear Instruments and Methods in Physics Research A*, 593(3):269–291, 2008.

[98] L. Di Ciaccio, D. Fournier, and F. Hubaut. High Voltage corrections for the electromagnetic calorimeter. 2005. ATL-COM-LARG-2005-003, CERN, Geneva.

[99] S. Arfaoui. *The ATLAS liquid argon calorimeter high-voltage system: commissioning, optimisation, and LHC relative luminosity measurement.* PhD thesis, Université de la Méditerrannée Aix Marseille II, 2011. CERN-THESIS-2011-146.

[100] Geant4 Collaboration, S. Agostinelli, et al. A simulation toolkit. *Nuclear Instruments and Methods in Physics Research A*, 506(250):13, 2003.

[101] The ATLAS Liquid Argon Calorimeter Collaboration. The data quality policy of liquid argon calorimeter. April 2009.

[102] The ATLAS Collaboration, G. Aad, et al. Readiness of the ATLAS Liquid Argon Calorimeter for LHC Collisions. *Arxiv preprint arXiv:0912.2642*, 2009.

[103] CERN. *oai:cds.cern.ch:1119304. 2009 European School of High-energy Physics*, Geneva, 2010. CERN. Comments: 7 lectures, 234 pages, published as CERN Yellow Report http://cdsweb.cern.ch/record/1119304.

[104] Gavin P. Salam. Towards Jetography. *Eur. Phys. J.*, C67:637–686, 2010.

[105] Matteo Cacciari, Gavin P. Salam, and Gregory Soyez. The Anti-k(t) jet clustering algorithm. *JHEP*, 0804:063, 2008.

[106] R. Wigmans. *Calorimetry ? Energy Measurement in Particle Physics.* Clarendon Press, Oxford, 2000.

[107] M. Aharrouche, C. Adam-Bourdarios, M. Aleksa, D. Banfi, D. Benchekroun, et al. Measurement of the response of the ATLAS liquid argon barrel calorimeter to electrons at the 2004 combined test-beam. *Nucl.Instrum.Meth.*, A614:400–432, 2010.

[108] E. Abat et al. Study of energy response and resolution of the ATLAS barrel calorimeter to hadrons of energies from 20-GeV to 350-GeV. *Nucl.Instrum.Meth.*, A621:134–150, 2010.

[109] Jet energy scale and its systematic uncertainty for jets produced in proton-proton collisions at sqrt(s) = 7 tev and measured with the atlas detector. Technical Report ATLAS-CONF-2010-056, CERN, Geneva, Jul 2010.

[110] B. Abbott et al. High p(T) jets in anti-p p collisions at $\sqrt{s}$ = 630- GeV and 1800-GeV. *Phys. Rev.*, D64:032003, 2001.

[111] P. Bagnaia et al. Measurement of Jet Production Properties at the CERN anti- p p Collider. *Phys. Lett.*, B144:283, 1984.

[112] Luminosity Determination in pp Collisions at $\sqrt{s} = 7$ TeV Using the ATLAS Detector at the LHC. *Eur. Phys. J.*, C71:1630, 2011. ATLAS Collaboration, *Updated Luminosity Determination in pp Collisions at* $\sqrt{s} = 7$ *TeV using the ATLAS Detector*, ATLAS conference note: ATLAS-CONF-2011-011, http://cdsweb.cern.ch/record/1334563.

[113] Updated Luminosity Determination in pp Collisions at $\sqrt{s} = 7$ TeV using the ATLAS Detector. ATLAS conference note: ATLAS-CONF-2011-011, http://cdsweb.cern.ch/record/1334563.

[114] Data-quality requirements and event cleaning for jets and missing transverse energy reconstruction with the atlas detector in proton-proton collisions at a center-of-mass energy of *sqrts* = 7 tev. Technical Report ATLAS-CONF-2010-038, CERN, Geneva, Jul 2010.

[115] M Agustoni, M Aharrouche, A Ahmad, N Besson, M Boonekamp, L Carminati, JB de Vivie, H De La Torre, J Del Peso, J Farley, V Gallo, S Glazov, C Handel, S Haug, M Karnevskiy, I Koletsou, N Lorenzo Martinez, N Makovec, L Mandelli, Y Nakahama, R Turra, and G Unal. Electromagnetic energy scale in-situ calibration and performance: Supporting document for the egamma performance paper. Technical Report ATL-COM-PHYS-2011-263, CERN, Geneva, Mar 2011.

[116] The ATLAS Collaboration. Luminosity determination using the atlas detector. *ATLAS-CONF-2010-060, CERN, Geneva*, 2010.

[117] Georges Aad et al. Measurement of Wgamma and Zgamma production in proton- proton collisions at sqrt(s)=7 TeV with the ATLAS Detector. *JHEP*, 09:072, 2011.

[118] L Helary and N Berger. Searches for technicolor resonance decays to two electroweak gauge bosons using the atlas detector. Technical Report ATL-COM-PHYS-2010-866, CERN, Geneva, Oct 2010.

[119] H Wang and N Berger. Statistical studies for higgs to gamma gamma. Technical Report ATL-COM-PHYS-2011-783, CERN, Geneva, Jun 2011.

[120] Luminosity determination in pp collisions at $\sqrt{s} = 7$ tev using the atlas detector in 2011. Technical Report ATLAS-CONF-2011-116, CERN, Geneva, Aug 2011.

[121] A. Sherstnev and R.S. Thorne. Parton Distributions for LO Generators. *Eur.Phys.J.*, C55:553–575, 2008.

[122] Michelangelo L. Mangano, Mauro Moretti, Fulvio Piccinini, Roberto Pittau, and Antonio D. Polosa. ALPGEN, a generator for hard multiparton processes in hadronic collisions. *JHEP*, 07:001, 2003.

[123] G. Marchesini and B.R. Webber. Monte Carlo Simulation of General Hard Processes with Coherent QCD Radiation. *Nucl.Phys.*, B310:461, 1988.

[124] G. Marchesini and B.R. Webber. Simulation of QCD initial state radiation at small x. *Nucl.Phys.*, B349:617–634, 1991.

[125] Stefano Frixione and Bryan R. Webber. Matching NLO QCD computations and parton shower simulations. *JHEP*, 0206:029, 2002.

[126] Stefano Frixione, Paolo Nason, and Bryan R. Webber. Matching NLO QCD and parton showers in heavy flavor production. *JHEP*, 0308:007, 2003.

[127] Stefano Frixione, Eric Laenen, Patrick Motylinski, and Bryan R. Webber. Single-top production in MC@NLO. *JHEP*, 0603:092, 2006.

[128] Frank Krauss, Andreas Schalicke, Steffen Schumann, and Gerhard Soff. Simulating W/Z+jets production at the CERN LHC. *Phys. Rev.*, D72:054017, 2005.

[129] Expected electron performance in the atlas experiment. Technical Report ATL-PHYS-PUB-2011-006, CERN, Geneva, Apr 2011.

[130] ATLAS Collaboration. Expected photon performance in the atlas experiment. Technical Report ATL-PHYS-PUB-2011-007, CERN, Geneva, Apr 2011.

[131] A. D. Martin, W. J. Stirling, R. S. Thorne, and G. Watt. Parton distributions for the LHC. *Eur. Phys. J.*, C63:189–285, 2009.

[132] D Bourilkov, R C Group, and M R Whalley. LHAPDF: PDF use from the Tevatron to the LHC. 2006.

[133] M. Aliev et al. – HATHOR – HAdronic Top and Heavy quarks crOss section calculatoR. *Comput. Phys. Commun.*, 182:1034–1046, 2011.

[134] ATLAS Collaboration. Search for the Standard Model Higgs boson in the two photon decay channel with the ATLAS detector at the LHC. 2011.

[135] Luminosity Determination in pp Collisions at sqrt(s)=7 TeV Using the ATLAS Detector at the LHC. 2011.

[136] Alexander L. Read. Presentation of search results: The CL(s) technique. *J.Phys.G*, G28:2693–2704, 2002.

[137] G. Cowan, K. Cranmer, E. Gross, and O. Vitells. Asymptotic formulae for likelihood-based tests of new physics. *European Physical Journal C*, 71:1554–+, February 2011.

[138] Romeo G. Update of jet energy resolution. Jet Calibration Task Force Meeting - 25-01-2011.

[139] A G Brandt. Atlas forward detectors. Technical Report ATL-LUM-PROC-2010-003, CERN, Geneva, Jul 2010.

[140] M. J. Oreglia. A study of the reactions $\psi' \to \gamma\gamma\psi$. Technical Report Ph.D. Thesis, SLAC-R-236 (1980), Appendix D., SLAC.

Résumé

"La langue de la République est le français."
République Française,
Article 2 de la constitution Française.

Introduction

Les trois dernières années ont été riches en développement pour la physique des hautes énergies sur collisionneurs. En 2008, la mise en service du Grand Collisionneur de Hadrons, ou LHC, a démarré, suivie rapidement par un incident qui a causé l'arrêt de la machine, la rendant inopérante pendant un an. En 2009-2010, le LHC a été redémarré, la phase de test fut très courte permettant d'atteindre une énergie dans le centre de masse de $\sqrt{s} = 7$ TeV. S'en est suivi 9 mois de prise de données, offrant une luminosité intégrée d'environ $\mathcal{L} \approx 50$ pb^{-1} aux expériences. En 2011, le premier fb^{-1} a été délivré aux expériences du LHC, tandis qu'aux Etats-Unis, le Tevatron a été fermé après presque 20 ans de prise de données, laissant le LHC seul dans la recherche du boson de Higgs.

Cette particule est la dernière pièce manquante du Modèle Standard (MS) de la Physique des Particules, un cadre théorique expliquant la physique à l'échelle subatomique. Le MS est une théorie couronnée de succès qui a notamment prédit l'existence de plusieurs particules avant que celles-ci ne soient effectivement découvertes. Une introduction au MS est donnée dans le premier chapitre de cette thèse. Cette introduction résume les succès du MS et explique la génération des masses dans le MS *via* le mécanisme de Higgs. Les lacunes du MS sont également présentées. En particulier, le boson de Higgs prédit par le MS n'a toujours pas été observé jusqu'à présent. Un modèle alternatif, appelé Technicouleur, permettant de générer les masses des particules sans boson de Higgs est présenté.

L'expérience ATLAS est l'une des six expériences placées autour de l'anneau du LHC. Elle a été conçue pour la recherche du boson de Higgs et de la nouvelle physique. Dans la première partie du deuxième chapitre de cette thèse l'accélérateur LHC est présenté. Les paramètres actuels et nominaux sont donnés. Dans la seconde partie de ce chapitre, l'expérience ATLAS est présentée. Le fonctionnement des différents sous-systèmes et leurs performances sont donnés.

Le début de ma thèse en 2008 correspond à la fin de l'installation du détecteur ATLAS dans la caverne. Ce calendrier m'a permis de participer à une grande partie des activités liées à l'expérimentation : mise en service du détecteur, la prise de données, la reconstruction et les performances du détecteur et enfin de mener une analyse sur la recherche de nouvelle physique.

Dans le troisième chapitre de cette thèse, les calorimètres à argon liquide sont introduits en détail. Une très bonne connaissance de ces calorimètres est nécessaire, car ils permettent de mesurer l'énergie des électrons, photons et jets et de l'énergie transverse manquante. La mise en service des calorimètres à argon liquide dans le détecteur ATLAS a débuté en 2008 et s'est poursuivie jusqu'au début des

collisions en 2010. La fin du chapitre est axée sur mon implication dans le contrôle de l'acquisition et de la qualité des données des calorimètres à argon liquide.

Dans le quatrième chapitre de cette thèse, la reconstruction des jets est détaillée. En utilisant l'intégralité des données collectés en 2010, correspondant à une luminosité intégrée de $\mathcal{L} \approx 50$ pb^{-1} de données de collision pp à $\sqrt{s} = 7$ TeV, la résolution en énergie des jets est évaluée avec deux méthodes dérivées des données. La résolution en énergie des jets est ensuite testée dans les régions non nominales du calorimètre afin de déterminer leur impact éventuel.

Enfin, le dernier chapitre de cette thèse présente une recherche de nouvelle physique dans l'état final $W\gamma$ en utilisant la première partie des données collectées durant l'année 2011, ce qui correspond à une luminosité intégrée de $\mathcal{L} = 2.04$ fb^{-1} de données de collisions pp à $\sqrt{s} = 7$ TeV. Puisqu'aucune recherche de résonances n'a été mené dans l'état final $W\gamma$ au LHC, le modèle LSTC est utilisé comme un test pour la découverte de résonance dans ce mode.

Le Modèle Standard

Le Modèle Standard permet d'expliquer toutes les interactions sensibles à l'échelle des particules : l'interaction électromagnétique, l'interaction forte et l'interaction faible. Il ne permet par contre pas d'expliquer l'interaction gravitationnelle.

Le Modèle Standard est une théorie des champs quantiques, c'est donc une théorie à la fois quantique et relativiste. Toutes les particules y sont représentées par des champs. Les particules vecteurs des interactions possèdent un spin entier et sont appelées bosons de jauges, tandis que les particules élémentaire sensibles à ces interactions sont dotées d'un spin demi-entier et sont appelées des fermions : quarks où leptons.

Les trois interactions qui composent ce modèle sont expliquées par la théorie QCD pour l'interaction forte et par la théorie électrofaible pour les interactions électromagnétique et faible. Le Modèle Standard est ainsi une théorie invariante sous le groupe de jauge $SU(3)_C \times SU(2)_L \times U(1)_Y$, produits des groupes de symétries associées à ces interactions.

La théorie électrofaible est basée sur l'invariance de jauge du groupe $SU(2)_L \times U(1)_Y$. Pour conserver cette invariance de jauge, quatres bosons sans masse sont introduits, trois sont associés au groupe $SU(2)_L$: $W^0; W^1; W^2$ et un au groupe $U(1)_Y$: B. Les champs physiques représentant le photon et les boson intermédiaire $W^\pm$ et Z^0 sont des combinaisons linéaires de ces trois champs. Dans ce modèle, toutes les particules physiques sont sans masse, car l'introduction d'un terme de masse briserait l'invariance du Lagrangien sous la symétrie locale $SU(2)_L \times U(1)_Y$.

Génération de masse dans le Modèle Standard

Le modèle standard pose donc un problème dans sa version initiale. Car même si le photon est prédit sans masse, car la portée de l'interaction électromagnétique est infinie, les bosons $W^\pm$ et Z^0 eux, doivent posséder une masse, car la portée de leurs interactions est finie.

La génération des masses dans le Modèle Standard est assurée par le mécanisme de Higgs. C'est un mécanisme de brisure spontanée de symétrie. C'est à dire que le système est invariant sous les transformations de jauge locales associées aux groupes $SU(2)_L \times U(1)_Y$, mais que l'état fondamental du système, donc le vide, ne respecte pas une telle invariance.

Le principe du mécanisme de Higgs est d'introduire un champs scalaire, dont la valeur moyenne du potentiel associé brise la symétrie dans le vide. Le boson de Higgs acquiert sa masse par l'intermédiaire de son auto-couplage avec le champ qu'il génère. Les termes de masses des bosons $W^\pm$ et Z^0, apparaissent automatiquement dans le lagrangien à l'issu de l'introduction du champ de Higgs. Enfin on peut donner une masse à l'ensemble des fermions par un couplage dit de Yukawa avec le champ de Higgs.

Même si le mécanisme de Higgs permet de donner une masse à l'ensemble des particules connues, le Modèle Standard reste insatisfaisant à plusieurs égards. Il ne permet en effet pas de répondre à plusieurs questions, telle que le nombre de générations de quarks et des leptons. Ou bien, le problème de hiérarchie : celui-ci est caractérisé par une dépendance théorique des masses prédites de certaines particules aux échelles d'unification des interactions, ce qui entraîne qu'elles sont bien plus élevées que celles observées expérimentalement. Ou encore le fait que si l'on extrapole les constantes de couplages des interactions forte et électrofaible vers les hautes énergies, celles-ci ne convergent pas, interdisant de fait au Modèle Standard d'être un candidat à une théorie de grande unification.

Enfin, si l'on considère que le Modèle Standard est englobé dans une théorie plus fondamentale, apparaît le problème de la naturalité de la masse du boson de Higgs.

La TechniCouleur

Un modèle alternatif au modèle standard a été introduit au début des années 1970. Ce modèle appelé Technicouleur, en référence à la QCD, part du modèle standard actuel, mais sans son secteur de Higgs. Cette théorie est invariante sous le groupe de jauge $SU(3)_C \times SU(2)_L \times U(1)_Y$. Par opposition avec le modèle de Higgs, c'est un mécanisme de rupture dynamique de la symétrie électrofaible. L'idée de base de la Technicouleur est de construire un modèle analogue à la dynamique de la théorie QCD, qui pourrait être utilisée pour expliquer la masse des bosons $W^{\pm}$ et Z^0. En QCD, les quarks ressentent l'interaction forte et l'interaction faible. L'interaction forte couple les quarks dans un condensat qui brise la symétrie électrofaible. La QCD permet donc de donner une masse aux bosons $W^{\pm}$ et Z^0, bien que celles-ci soient mille six cent fois plus faible que ce qui a été observé expérimentalement, mais qui possède le bon ratio des masses des bosons de jauge. $M_W = M_Z \cos(\theta_W) = \frac{1}{2}\sqrt{3} g f_\pi \approx 50$ MeV, Où f_π représente la constante de désintégration du pion.

La Technicouleur introduit donc une nouvelle interaction similaire à la QCD, qui permet de briser de manière dynamique la symétrie électrofaible. Cette théorie est invariante sous un groupe de jauge $SU(N_{TC})_{TC}$, et introduit l'existence de nouveaux fermions : les techni-quarks. En Technicouleur, la constante de couplage est α_{TC}. Elle devient forte aux alentours d'une centaine de GeV, ce qui a pour effet de briser spontanément l'équivalent de la symétrie chirale pour les techni-quarks, faisant apparaître des bosons de Goldstone, dont trois deviennent les composantes longitudinales de $W^{\pm}$ et Z^0. Et de manière équivalente à la QCD, font apparaître les masses de ces deux bosons. Les masses des fermions et des techni-pions sont assurées par un mécanisme de brisure spontanée de symétrie appelé Extended TechniColor, où Technicouleur étendue.

L'avantage de la Technicouleur est qu'elle dispose de la liberté assymptotique de la QCD, ce qui permet de résoudre les problèmes de naturalité et de hiérarchie évoqués précédemment. Le problème étant que de manière générale, les modèles issus de la Technicouleur vont à l'encontre des tests de précision réalisés sur le Modèle Standard. Le modèle étudié ici est appelé : "Low Scale Technicolor", où Technicouleur à basse échelle. Dans ce type de modèle, la constante de couplage est dite rampante ("*walking*"), à la différence de la QCD, où on considère que c'est une constante de couplage qui monte très rapidement ("*running*"). Les modèles de TC à basse échelle permettent de passer les tests de précision électrofaible sous certaines conditions.

Le modèle qui a été utilisé pour la simulation est une version simplifiée, mais réaliste, du modèle LSTC. Il est implémenté dans le générateur Monte Carlo PYTHIA. On impose un nombre important de doublets de techni-quarks : $N_D = 9$

Les particules recherchées sont des états liés de techni-quarks. Plus exactement, ce sont des techni-mesons vecteurs, formés par le doublet de techni-quarks le plus léger. Ces particules sont : ρ_{T} , ω_{T} et a_{T} . Elles sont attendues dans une gamme de masse comprise entre [200,600] GeV. Dans la simulation, les masses des particules sont des paramètres libres, les largeurs de désintégration attendues pour chaque résonance sont étroites, de l'ordre de $\lesssim 1$ GeV.

En effet, le modèle LSTC impose que les masses des techni-pions soient à des valeurs comparables à celle des différents meson ρ_{T},a_{T},ω_{T}. Ceci interdit cinématiquement les canaux de décompositions équivalent QCD type $\rho \to \pi\pi$.

Les désintégrations des techni-mesons sont donc uniquement dues à l'interaction faible. Au LHC, on espère pouvoir découvrir l'ensemble de ces particules, dans des modes de décomposition comprenant deux leptons, où deux bosons de jauges électrofaibles : (γ, $W^{\pm}$ où Z^0). Par exemple, l'état final étudié à la fin de ce manuscrit : $W\gamma$ est obtenu à l'aide des désintégrations des mésons a_{T} et ρ_{T}.

Le LHC et l'expérience ATLAS

Le Grand Collisionneur de Hadron (où LHC) est un collisionneur proton-proton situé au CERN. Dans ses caractéristiques nominales, il est censé fournir des collisions de protons toutes les 25 ns à une énergie dans le centre de masse de $\sqrt{s} = 14$ TeV. Suite à l'incident survenu en 2008, le LHC fonctionne en mode dégradé avec des collisions toutes les 50 ns et à une énergie dans le centre de masse de $\sqrt{s} = 7$ TeV. Deux périodes de prises de données se sont succédées en 2010 et 2011. La première a permis d'accumuler environ 50 pb^{-1} tandis-que la seconde a permis d'enregistrer de l'ordre de 5 fb^{-1}, permettant ainsi au LHC de surclasser définitivement le Tevatron pour la recherche du boson de Higgs et de la physique au-delà du Modèle Standard.

ATLAS est l'une des deux expériences généralistes présente autour du LHC. Elle est composée de plusieurs sous-détecteurs :

Au plus proche des faisceaux, se trouve le détecteur à trace. Il permet d'assurer la détection des particules chargées, de mesurer leurs impulsions et de reconstruire les vertex d'interaction primaire. Il est décomposé en un tonneau et deux bouchons , chacun contenant un détecteur à pixels, un détecteur à transition de radiation et un détecteur au Silicium. Le trajectographe est immergé dans un champs magnétique solénoïdal de 2 T qui permet de dévier les particules chargées et donc de mesurer leurs impulsions.

Au-dessus du trajectographe, se situent les calorimètres électromagnétiques puis hadroniques. Le calorimètre électromagnétique sert à identifier les photons et les électrons, tandis que le calorimètre hadronique sert à l'identification des hadrons. Les deux calorimètres sont constitués de deux demi-tonneaux séparés par un faible espace de 4mm au centre du détecteur (à z=0), de deux bouchons et très proche du faisceau de deux petits calorimètres permettant de mesurer les particules émises vers l'avant. L'ensemble des calorimètres électromagnétiques et les calorimètres hadroniques des bouchons utilisent de l'Argon liquide comme milieu ionisant. Ils seront présentés plus en détails dans la prochaine partie. Le calorimètre hadronique du tonneau est quant à lui constitué d'une alternance de tuiles scintillante, comme matériaux actif, et d'acier, comme matière absorbante.

L'ensemble du détecteur ATLAS a été construit autour de six aimants toroïdaux. Ces derniers, ainsi que d'autres aimants placés dans des bouchons situés après les calorimètres, permettent d'obtenir un champ magnétique variable, comprit entre 1 et 7.5 T, dans un très grand volume. Ce qui permet de mesurer les impulsions des muons, jusqu'à environ 1 TeV. Le système de détection à muons est constitué de quatre boucliers à muons répartis de part et d'autre du détecteur, et de deux plans parallèles de détecteurs entourant l'intégralité du tonneau.

Enfin, l'expérience ATLAS possède un système de déclenchement décomposé en trois niveaux permettant de réduire le taux d'interaction de 40 Mhz et de sélectionner seulement approximativement 300 hz d'événements intéressants.

Cette décomposition du détecteur permet d'avoir une grande couverture dans le plan transverse : (η, ϕ). Et devrait permettre d'obtenir une très grande précision, pour identifier et mesurer les caractéristiques des particules créées par les collisions.

Les calorimètres à argon liquide

Les calorimètres à argon liquide sont des calorimètres à échantillonnage. Ils regroupent l'intégralité des calorimètres électromagnétiques, les deux bouchons du calorimètres hadroniques et les deux calorimètres avant (FCAL).

Ils sont constitués pour le calorimètre électromagnétique d'un ensemble de plaques de plombs pliées en accordéons, et maintenues par un support en inox. Ces plaques servant de milieu absorbeur, et bai-

gnant dans de l'argon liquide, comme milieu ionisant. Pour les bouchons du calorimètre hadronique le plomb est remplacé par du cuivre. Enfin, pour les calorimètres avant, il sont constitués d'un ensemble de trois couches, la première servant à l'étude des particules électromagnétiques, avec un milieu absorbeur en cuivre, les deux autres servant aux particules hadroniques, avec des milieux absorbeurs en tungstène.

Le calorimètre électromagnétique est segmenté en trois compartiments, de granularité différente. Le premier compartiment possède une granularité très forte en η, servant essentiellement à la réjection γ/π^0. Les particules électromagnétiques déposent la majorité de leur énergie dans le second compartiment. Le troisième et dernier compartiment sert à différencier les particules hadroniques des particules électromagnétiques.

Les calorimètres à argon liquide sont constitués en tout de 182468 cellules. Les cellules sont connectées par groupes de 128 à des cartes électroniques de lecture avant (FEB). Ces cartes électroniques ont pour rôle la sommation de l'énergie recueillie dans les cellules, et de mettre en forme ce signal. Le signal échantillonné est ensuite envoyé à l'électronique de lecture arrière, où l'énergie, le temps d'arrivé du signal et un facteur de qualité sont calculés.

En prise de donnée, à chaque événement, chaque cellule du calorimètre à argon liquide est soumise à un échantillonnage de son énergie toutes les 25 ns. Puis ces échantillons sont convertis numériquement pour donner une valeur comprise entre 0 et 4095. Un mécanisme d'amplification avec trois gains permet d'éviter qu'une cellule ne sature, en changeant le gain à certaines valeurs d'énergie. Ce changement de gain, avec un ADC à 14 bits, permet de reconstruire l'énergie d'une cellule, de quelques MeV à environ un TeV, tout en gardant une bonne résolution.

Durant ma thèse j'ai été impliqué sur le contrôle de la qualité de l'échantillonnage des cellules du calorimètre à Argon liquide. J'ai développé un programme permettant de s'assurer que les quantités utilisées pour la reconstruction de l'énergie étaient en accord avec ceux attendus et en particulier verifier que :

. La forme de l'échantillonnage est correct.
. Le temps d'arrivé de l'échantillonnage est correct.
. Les échantillons ne sont pas saturés.

Ces histogrammes de contrôle de l'acquisition des données ont été utilisé de manière intensive durant la mise en service du détecteur, à une époque où la réponse du détecteur était peu connue. Ils ont en particulier été utilisés durant les campagnes de prises de données avec des cosmiques, des événements dit de "*beam splash*", et les premières collisions, permettant de régler finement les paramètres de la machine.

Maintenant que le détecteur est mieux connu et que plus de données sont enregistrées, le contrôle de l'acquisition des données des calorimètres à argon liquide sont axés sur des quantités qui ont un impact direct sur la reconstruction des objets physique comme les cellules bruyantes. Néanmoins, les outils de contrôle que j'ai développé sont toujours utilisés et ont permis de détecter récemment des problèmes de saturation liés à l'empilement des événements.

Résolution en énergie des jets

Lorsqu'un quark ou un gluon est créé durant une collision, du fait de la nature confinante de la QCD, celui ci doit s'hadroniser. L'hadronisation crée une gerbe de particules émise dans la direction de vol du parton incident. Un jet hadronique est le cône de particules issu de la désintégration d'un parton. Les jets sont donc des objets composites qui doivent être reconstruits à partir d'une définition permettant une comparaison entre prédictions théoriques et résultats expérimentaux.

Les jets utilisés dans ATLAS sont majoritairement reconstruits à partir des calorimètres. La création des jets se fait en deux étapes :

. La première consiste à obtenir une liste des amas d'énergie disséminés dans les calorimètres. Ces amas sont obtenus en recherchant des cellules ayant une énergie supérieure à 4 fois leur bruit, auxquelles sont agrégées les cellules ayant une énergie supérieure à 2 fois leur bruit, et toutes leurs voisines directes.

. La seconde étape consiste à partir de cette liste d'amas obtenus et à chercher à les combiner pour obtenir des jets. Plusieurs algorithmes d'agglomérations ont été développés et utilisés au fil du temps. Celui utilisé principalement au sein de la collaboration ATLAS est l'algorithme anti-K_T, qui permet d'obtenir des jets de formes régulières, tout en étant peu sensibles au effets de radiations douces de la QCD.

Une des caractéristiques clef des jets est leur résolution en énergie. Celle-ci peut être évaluée à partir des simulations Monte-Carlo à disposition. Néanmoins dans l'hypothèse ou la simulation ne reproduirait pas de manière fidèle les données, ou que l'on souhaiterait controler des effets du détecteurs non pris en compte dans la simulation, il est également utile de pouvoir déterminer cette résolution directement dans les données. Deux méthodes ont été développées par le passé afin d'évaluer la résolution en énergie des jets dans les données.

. La première méthode repose sur la balance en énergie des événements di-jets. Lorsqu'un événement ne contenant que deux jets est produit, ceux ci sont a priori émis dos-à-dos. Les deux jets doivent donc avoir une énergie dans le plan transverse égale, à leur résolution près. La résolution en énergie peut ainsi être reliée à la différence relative des impulsions transverses des deux jets.
. La seconde méthode utilisée est appellé méthode de la bisectrice. Elle repose également sur des événements di-jets. Le plan transverse est redéfini à l'aide de la bisectrice des impulsions transverses des deux jets. Le vecteur résultant de la somme des impulsions transverses des deux jets est alors projeté dans ce nouveau référentiel. La résolution en énergie des jets peut ainsi être reliée à la différence des résolutions de ces deux composantes.

La résolution en énergie des jets a été évaluée en utilisant l'intégralité des données prises durant l'année 2010 en utilisant la méthode de la balance des événements di-jets et la méthode de la bisectrice. Un accord relatif meilleur que 10% a été trouvé entre ces deux méthodes. Par ailleurs, cette étude a permis de montrer que la résolution dans les données est plus importante systématiquement de l'ordre de 10% que celle mesurée dans le Monte Carlo.

Certaines zones des calorimètres ne sont pas alimentées à la valeur nominale de la haute tension, de manière temporaire à cause de courts-circuits des alimentations haute tension, ou de manière permanente afin de limiter les bouffées de bruits enregistrées et protéger les détecteurs. Il est attendu que cette baisse de la haute tension ait un impact négatif sur la résolution en énergie des jets. Néanmoins, puisque l'effet de la haute tension n'est pas simulé dans le Monte Carlo, les deux méthodes introduites auparavant ont été utilisées afin d'évaluer la taille de cette dégradation.

La haute tension du pré-échantillonneur a été réduite de sa valeur nominale de 2 kV à 1.6 kV, au milieu de la prise de donnée 2010. L'étude de la résolution en énergie des jets n'a pas permis de mettre en évidence une quelconque dégradation lié à cette réduction, les mesures de la résolution en énergie des jets avant et après la réduction étant compatibles à leurs erreurs près.

L'impact des zones haute tension non-nominales liés à des courts-circuits des alimentations haute tension a été évalué en utilisant une approximation. La dégradation de la résolution due à ces zones non-nominales a été estimée de l'ordre de 1% pour des jets à basse impulsion transverse. Cette effet devrait a priori être négligeable lorsque l'impulsion transverse augmente.

Afin de tester cette hypothèse, une nouvelle variable a été introduite dans la reconstruction des données. Cette variable comptabilise le nombre de cellules présentes dans des zones où la haute tension est non-nominale et est normalisée par le nombre total de cellules présentes dans le jet. Cette variable est fortement corrélée à la dégradation de la résolution due à la réduction de haute tension. L'étude de la résolution en énergie des jets a été reconduite en divisant le lot de données par rapport à cette variable. Aucune augmentation significative de la résolution en énergie n'a été mesurée. Cette étude a néanmoins permis de fixer une limite sur l'augmentation du terme de bruit : $\Delta N \lesssim 1$ GeV, ce qui signifie qu'à 1σ l'effet des zones à haute tension non-nominales sur la résolution en énergie est plus basse que 3% pour des jets de $p_T \approx 30$ GeV, et de l'ordre de 0.1% pour des jets de $p_T \approx 500$ GeV. Cette mesure peut néanmoins être améliorée avec différentes approches :

. Une grande partie des erreurs systématiques liées à cette mesure sont dues à la statistique disponible du lot Monte Carlo. Augmenter celle-ci permettrait de réduire d'autant les erreurs systématiques.

. Cette étude pourrait par ailleurs être reconduite sur le lot de donnée prise en 2011. Mais du fait de l'augmentation de l'empilement des événements dans ces données, il est à craindre que l'augmentation de la résolution en énergie des jets due aux zones haute tension non-nominales ne soit noyée dans l'augmentation de résolution due au bruit d'empilement.
. Enfin, la méthode qui permettrait vraisemblablement d'améliorer le mieux la mesure de cet effet consisterait à reconduire cette étude en utilisant des événements gamma-jets où Z+jets, à la place d'événements di-jets. En effet, la résolution en énergie des électrons, muons et photons est bien meilleure que celle des jets et permettrait d'obtenir une mesure plus précise.

Recherche de TechniCouleur dans le canal $W\gamma$

Le modèle LSTC prédit l'existence de nouvelle particules se désintégrant en deux bosons de jauge électrofaible. Dans cette dernière partie, la recherche de telles particules est présentée dans l'état final $W\gamma$ où le boson W se désintègre en $W \rightarrow e\nu$. Cette recherche a été conduite en utilisant $\mathcal{L} = 2.04$ fb^{-1} de donnée de collision pp à une énergie dans le centre de masse de $\sqrt{s} = 7$ TeV.

L'état final $W\gamma$ est caractérisé par la présence d'un électron et d'un photon de haute énergie et d'énergie transverse manquante. Avant de conduire une recherche de nouvelle physique, il convient d'obtenir en premier lieu une bonne description des différents processus physiques qui contribuent à cet état final dans le modèle standard. Une partie des processus peuvent être étudiés à l'aide de générateur Monte Carlo et de la simulation, mais certains bruits de fond nécessitent une étude détaillée sur les données.

Les bruits de fond électrofaibles considérés dans cette étude telle que la production simple et de paire de quark top, $Z \rightarrow ee$, $Z \rightarrow \tau\tau$, $W \rightarrow \tau\nu$ et dibosons sont évalués en utilisant la simulation et sont normalisés par rapport à leurs section efficace de production. Le bruit de fond irréducible $W\gamma$ issu du MS est modélisé pour sa forme en utilisant la simulation et sa normalisation est obtenue en utilisant une méthode dérivée des données. Les deux bruits de fond résiduels, QCD multi-jet et W+jets sont quant à eux complètement déterminés à partir des données.

Deux techniques complémentaires ont été utilisées afin d'évaluer la contribution de ces deux bruits de fond à partir des données :

. La première est une méthode utilisant des régions de contrôles latérales à la région de sélection du signal à deux dimensions. Le lot de données est séparé en 4 zones dépendant de deux variables d'identification. Une de ces quatre zones est enrichie en signal, tandis que les trois zones restantes sont enrichies en bruits de fond. On obtient alors la normalisation du signal dans la zone enrichie en faisant un produit en croix des bruits de fond dans les zones de contrôle.
. La seconde méthode est une méthode d'ajustement contraint des lots de données. Il convient alors de chercher des variables ayant des distributions permettant de séparer le signal et les différents bruits de fond. On assigne alors au signal et aux différents bruits de fond des fonctions d'ajustement différentes qui permetteront d'obtenir leurs normalisations.

Ces deux méthodes ont donné des résultats compatibles pour l'évaluations des normalisations des bruits de fond QCD, W+jets et $W\gamma$. Les formes des bruits de fond W+jets et QCD ont été prises dans des zones sans signal en inversant des critères d'identification. A l'issue de cette procédure d'analyse de l'état final $W\gamma$, la modélisation obtenue décrit correctement les données dans différentes zones de contrôles.

Afin de réaliser la recherche de nouvelle physique dans cette état final $W\gamma$, il convient de trouver une variable permettant de discriminer le bruit de fond standard d'un éventuel signal due à la Technicouleur. Dans le modèle LSTC, les résonances sont censés se désintégrer dans l'état final $W\gamma$, avec une largeur de désintégration étroite. Si de telles particules existent réellement, la distribution de la masse invariante $W\gamma$ devrait donc être une variable très discriminante, puisqu'on attend un pic au-dessus d'un continuum dû au bruits de fond. Le problème est que du fait de la présence du neutrino dans la désintégration leptonique du W, la reconstruction exacte de la quadri-impulsion du W est a priori impossible. Il est néanmoins possible de reconstruire de manière approchée cette quadri-impulsion. Pour ce faire, l'énergie transverse manquante de l'événement est affectée à l'impulsion transverse du

neutrino, et l'équation de conservation de l'énergie du W est posée en fixant la masse du W à sa valeur connue. On obtient alors une équation du second degré permettant d'obtenir une solution à l'impulsion longitudinale du neutrino. La solution minimisant la valeur absolue de cette impulsion est conservée.

Il convient maintenant d'optimiser la sélection des événements afin d'améliorer la signification statistique du signal par rapport au bruits de fond du MS. Cette optimisation est conduite en utilisant d'une part la modélisation composée des différents échantillons Monte Carlo et des échantillons de données décrivant les bruits de fond QCD et W+jets et d'autre part en utilisant le premier point de l'étude : T200. La sélection donnant la meilleur signification statistique tout en permettant une bonne différenciation du pic de signal par rapport aux bruits de fond est obtenue en imposant de garder les événements où $p_{\mathrm{T}}(\gamma) > 50$ GeV et $p_{\mathrm{T}}(W) > 30$ GeV.

La recherche est conduite sur les données en utilisant une fonction d'ajustement décrivant les bruits de fond du MS, et une fonction d'ajustement représentant le signal. La fonction d'ajustement des bruits de fond est laissée complètement libre durant l'ajustement sur les données, tandis que pour la fonction d'ajustement du signal, seule la normalisation du signal et deux paramètres de nuisances limités à la taille des erreurs systématiques sont laissés libres, les autres paramètres étant fixés à ceux obtenus sur le Monte Carlo. Les résultats sont ensuite interprétés en utilisant la méthode statistique des CL_s.

La recherche a été conduite sur les données, mais aucune déviation significative des prédictions du Modèle Standard n'a été observée dans la distribution de masse $W\gamma$, pour des particules Technicouleur comprises dans un intervalle de masses [220,440] GeV. La déviation la plus importante observée est enregistrée à $M(a_{\mathsf{T}}) = 329$ GeV avec une signification statistique de 0.71σ. L'hypothèse d'un signal avec $M(\rho_{\mathsf{T}}) = 290$ GeV comme suggérée dans la Ref [51] a été investiguée, mais aucune déviation significative par rapport au Modèle Standard n'a été observée. Cette analyse a néanmoins permis de mettre une limite sur la production de particules TC dans l'état final $W\gamma$correspondant à : $M(a_{\mathsf{T}}) > 265$ GeV, où $M(\rho_{\mathsf{T}}) > 243$ GeV.

Cette analyse de l'état final $W\gamma$ peut être améliorée de différentes façons :

. Une meilleure analyse des erreurs systématiques de l'étude pourrait permettre d'obtenir une contrainte plus importante sur la production de particules TC, même si l'impact attendu est a priori limité.

. La statistique limitée des échantillons Monte Carlo apporte également une incertitude importante sur cet état final.

. Les coupures d'optimisation peuvent être obtenues pour chacun des points indépendamment afin d'obtenir une meilleur signification statistique et donc un meilleur pouvoir discriminant à haute masse.

. Mais la meilleur amélioration attendue vient de l'augmentation de luminosité. L'ajout du mode de désintégration $W \to \mu\nu$ permet de doubler la statistique disponible, ajouter l'intégralité de la prise de donnée 2011 ajoute un facteur 2.5. Par ailleurs, en ajoutant la luminosité attendue à la fin de l'année 2012, la sensibilité de cette étude permettrait d'atteindre des technihadrons jusqu'à $M(a_{\mathsf{T}}) \approx 500$ GeV.

Conclusion

Depuis le redémarrage du LHC en 2009 et jusqu'à la fin 2011, la quantité des données accumulées est passée de 50 pb^{-1} à près de 5 fb^{-1}. Le LHC est extrêmement performant, fournissant une quantité de données utilisées pour comprendre le détecteur et effectuer de nombreuses analyses de physique.

Pour les expériences, il est crucial que les données prises respectent des critères de qualité, afin d'éviter " *de découvrir de la nouvelle physique*" à cause d'effets du détecteur. Dans le troisième chapitre de cette thèse, il a été expliqué pourquoi il est important d'avoir un contrôle de l'acquisition et de la qualité des données fiable qui permet d'identifier rapidement les problèmes et de les corriger. Le contrôle de l'acquisition des données qui a été développé durant ma thèse permet en particulier

d'effectuer des vérifications de base qui assurent que la reconstruction de l'énergie, du temps d'arrivée du signal et du facteur de qualité des cellules du calorimètre sont correctes.

Pour les analyses de physique, il est important d'avoir une bonne connaissance de l'impact du détecteur sur la reconstruction des objets. Dans le quatrième chapitre, la résolution en énergie des jets a été estimée en utilisant deux techniques dérivées des données, en utilisant l'intégralité des données de collisions pp à $\sqrt{s} = 7$ TeV, collectées durant l'année 2010.

Cette étude a montré qu'en 2010, la résolution en énergie des jets était sous-estimée dans le Monte-Carlo d'un facteur relatif d'environ 10% par rapport aux données. Cet écart n'est pas encore compris et toujours sous investigation.

Les méthodes utilisées pour mesurer la résolution en énergie des jets ont ensuite été appliquées pour évaluer l'impact des zones à haute tension réduite du calorimètre à argon liquide. L'étude n'a été conduite que sur la partie centrale du détecteur à cause des statistiques limitées disponibles. L'impact des zones à haute tension réduite a été mesurée comme négligeable. Pour des jets produits avec une rapidité $|y| < 0.8$, l'augmentation de la résolution en énergie due à la réduction de HV, est évaluée à moins de 3 % pour un jet de $p_{\mathrm{T}} = 30$ GeV, et moins de 0,1 % pour un jet de $p_{\mathrm{T}} = 500$ GeV.

Enfin, une recherche de résonances étroites dans l'état final $W\gamma$ a été effectuée. Les différent processus du MS contribuant à cette état final ont été évalués à l'aide du Monte Carlo et des données. En particulier, les bruits de fond QCD multi-jets et W + jets ont été estimés en utilisant des techniques dérivées des données pour leurs formes et normalisations. La normalisation de l'échantillon $W\gamma$ a été estimée à partir des données, et sa forme à partir du Monte Carlo. Les échantillons électrofaibles restants ont été estimés à partir du Monte Carlo.

En utilisant cette modélisation, l'analyse a été menée en aveugle par rapport à la variable masse invariante du système $W\gamma$. Un bon accord entre les données et le Monte Carlo a été trouvé dans deux régions de contrôle proche du signal. La sélection des événements a été optimisée afin de distinguer de manière optimale les bruits de fond du MS d'un éventuel pic de signal. L'optimisation permettant d'augmenter la signification statistique a été trouvée en imposant que $p_{\mathrm{T}}(\gamma) > 50$ GeV et $p_{\mathrm{T}}(W) > 30$ GeV.

Le système de masse invariante $W\gamma$ a finalement été découvert dans la région du signal. Un bon accord entre les données et la modélisation a été trouvé. La recherche a ensuite été menée sur les données. Aucun excès significatif des prédictions du Modèle Standard n'a été observée dans le spectre de masse $W\gamma$ dans l'intervalle [220,440] GeV. L'excès le plus important observé a été trouvé pour une masse $M(a_{\mathsf{T}}) = 329$ GeV avec une signication statistique de $0{,}71\sigma$.

L'hypothèse de signal à M $(\rho_{\mathsf{T}}) = 290$ GeV tel que suggéré dans la Ref [51] a été étudié, mais aucune déviation évidente du MS n'a été observée. Enfin, cette sélection a été utilisée pour définir une limite d'exclusion sur la production de particules TC dans cet état final : M $(a_{\mathsf{T}}) > 265$ GeV. Cette limite peut être exprimée en terme de la masse du méson ρ_{T}, on obtient alors M$(\rho_{\mathsf{T}}) > 243$ GeV. Cette limite est en bon accord avec les limites précédemment fixées par la collaboration ATLAS dans le canal dilepton puisque le meson ρ_{T}est exclu jusqu'à près de $M(\rho_{\mathsf{T}}) = 450$ GeV [46].

Résumé :

En 2011, le LHC a fourni près de 5 fb^{-1} de données aux expériences. Ces données ont été utilisées pour comprendre plus avant les détecteurs, leurs performances et effectuer des analyses de physique. Cette thèse est organisée en cinq chapitres. Le premier est une introduction théorique au Modèle Standard et à une de ses extensions possible : la TechniCouleur. Le deuxième chapitre donne un bref aperçu de l'accélérateur LHC et de l'expérience ATLAS. Dans le troisième chapitre, l'un des principaux sous-système de l'expérience ATLAS est présenté : le calorimètre à argon liquide. L'algorithme de contrôle de l'acquisition et de la qualité des données que j'ai développé au cours de ma thèse est également présenté. Le quatrième chapitre présente une étude des performances de la reconstruction des jets basée sur l'ensemble des données acquises en 2010. Cette étude a montré qu'en 2010, la résolution en énergie des jets dans le Monte-Carlo a été sous-estimée d'un facteur relatif d'environ 10% par rapport aux données. Cette étude a été ensuite reconduite pour évaluer l'impact de la réduction de la HV dans des zones du calorimètre sur la résolution en énergie des jets. Cet impact a été jugée négligeable. Pour des jets produits avec une rapidité $|y| < 0.8$, l'augmentation de la résolution en énergie due à la réduction de la HV, est évaluée à moins de 3 % pour un jet de $p_{\mathrm{T}} = 30$ GeV jet, et moins de 0,1 % pour un jet de $p_{\mathrm{T}} = 500$ GeV. Enfin, le dernier chapitre de cette thèse présente une étude de l'état final $W\gamma$. La contribution des différents processus du MS participant à cet état final a été estimée à partir du Monte Carlo et des données. Une recherche de résonances étroites a ensuite été effectuée en utilisant la distribution M($W\gamma$) dans un intervalle [220,440] GeV, mais aucun écart significatif des prédictions du MS n'a été observé. Cette étude a permis de fixer des limites sur la production de particules TC correspondant à $M(a_{\mathsf{T}}) > 265$ GeV ou $M(\rho_{\mathsf{T}}) > 243$ GeV.

Mots-clés : LHC, ATLAS, calorimètre à argon liquide, contrôle de la qualité des données, Haute Tension, résolution en énergie des jets, technicouleur, di-boson, $W\gamma$.

Abstract : In 2011 the LHC has provided almost 5 fb^{-1} of data to the experiments. These data have been used to perform a deep commissioning of the detectors, understand the performances of the detector and perform physics analysis. This thesis is organized in five chapter. The first one is a theoretical introduction to the Standard Model and to one of its possible extension : the TechniColor. The second chapter gives a brief overview of the LHC and the ATLAS experiments. In the third chapter one of the key subsystem of the ATLAS experiment is presented : the LAr calorimeters. The monitoring of the data acquisition developed during my thesis is also presented in this chapter. The fourth chapter presents a study of the jet performances based on the data set acquired in 2010. This study has shown that in 2010, the Monte Carlo was underestimating the jet energy resolution by a relative factor of about 10%. This study was refocused to evaluate the impact of the reduced LAr HV area on the jet energy resolution. The impact of the HV reduced region was found to be negligible. For jets produced with a rapidity $|y| < 0.8$, the increase of energy resolution due to the HV reduction, is evaluated at less than 3% for a $p_{\mathrm{T}} = 30$ GeV jet, and less than 0.1% for a $p_{\mathrm{T}} = 500$ GeV jet. Finally the last chapter of this thesis present a study of the $W\gamma$ final state. The standard model backgrounds contributing to this final state were estimated from Monte Carlo and from data. A search for narrow resonances was then conducted using the M($W\gamma$) distribution in a range [220,440] GeV, but no significant deviation from the SM was observed. This study has allowed to set limits on the production of TC particles corresponding to $M(a_{\mathsf{T}}) > 265$ GeV or $M(\rho_{\mathsf{T}}) > 243$ GeV.

Key-words : LHC, ATLAS, LAr calorimeter, data quality, High Voltage, HV, jet energy resolution, technicolor, di-boson, $W\gamma$.